Interferometric Observations of the J(0,1) CO Line on Venus: Upper Mesospheric Winds and CO Abundance

Thesis by

Kathryn Pierce Shah

In Partial Fulfillment of the Requirements
for the Degree of
Doctor of Philosophy

California Institute of Technology
Pasadena, California

1992

(submitted September 16, 1991)

Dedicated with love to Mom and Alkesh

Acknowledgments

These acknowledgements cannot possibly express all of my appreciation and thanks to the people who have helped me during my years at Caltech. Most of all, I thank my thesis advisor, Professor Dewey Muhleman, for his true support, conscientious guidance and helpful criticism. I feel very fortunate to have learned careful scientific analysis from him and to have gained understanding from his entertaining, insightful (and yet succinct!) comments.

I also thank the other faculty in planetary science who have graced my years at Caltech: Andy Ingersoll for his intuitive comments on dynamics and for hosting the Thanksgiving and July 4th celebrations, Yuk Yung for the unexpected philosophy and jokes, Jim Westphal for cheerful hallway discussions (from weather to Pele stories), Bruce Murray for awareness of 'The Big Picture', Dave Stevenson for eloquent class lectures, and Peter Goldreich for innovative demonstrations in lectures and the secretaries' office.

Moving on to life outside the hallways of South Mudd... thank you, Alkesh, for being patient and impatient and for answering all those phone calls at 3 A.M., eastern time. I was also strengthened by my Mom - who might not have understood what I was doing, but who always gave me a bit of home (the joy of new ducklings and fighting goldfish).

To my two closest friends, Don Rudy and Eddie Garnero, endless thanks for unpredictable, outrageous, deep conversations that brought me back into the real (real??) world. Don, thanks for uncle-ing, pulling me to many Thursday Happy Hours and jacuzzi get-togethers and, later, nobly proofreading rough drafts of thesis chapters. Eddie, thanks for my new artistic awareness (from left quotes to postcards extraordinaire), victoriously fighting my initial dislike for this coast, and letting me teach Misha bad habits!

I'm also very grateful to Julie Moses who improved and passed along Don and Randy Kirks' TeX macros, each day gave helpful advice and quirky news, and (maybe) forgave me for never playing softball; to Arie Grossman who had *such* patience and help for beginners in AIPS and radio observations; to Ken Herkenhoff, Diane Michelangeli, Phil Ihinger, Laurie Watson and Cheryl Contopulos for the delight of gossip; to Michelle Santee for vegetarian hints and serial killers discussions; to Kay Campbell who always had the answer; to Glenn Berge for correct, careful answers and pointing out Indian arrowheads in Owens Valley; to Brad Woods for strange hallway noises; to Carol Polanskey who had to share a house with my roller-coaster moods these last months; and to Kim Tryka, Steve Leroy, Mark Gurwell (the optimist), Mark Hofstadter, Don Banfield, Bryan Butler, Jim Friedson, Randy Kirk, Pat Pickett, David Koerner, Rich Dissly, Rich Achterberg, Bruce Betts and everyone else for chat around the laser-printer and chat at Happy Hours.

Research for this thesis was funded by NASA Grant NAGW 1448 and NSF Grant AST-8919698. Chapter II and Chapter IV have been published in modified form in *Icarus* by Academic Press, Inc.

Abstract

In 1988, we observed Venus with the millimeter interferometer at the Owens Valley Radio Astronomy Observatory at 115.2712 GHz, the first rotational transition of ^{12}CO. The 33.″4 diameter disk was spatially resolved by a synthesized beam with a full-width-half-maximum of 2.″8. Local time ranged from afternoon on the planetary eastern limb, 2 PM, to just past local midnight on the western limb, 12:30 AM. Venus' millimeter continuum emission was measured in a 400 MHz broadband channel. More importantly, the CO absorption line was measured and finely resolved in frequency by two 32-channel filterbanks having channel widths of 50 kHz and 1 MHz.

The 400 MHz broadband channel visibility data yielded a continuum brightness map of Venus. Brightness variations across the disk were primarily caused by sidelobe beam effects associated with the incomplete (u,v) coverage of the OVRO array. However, after radial averaging, the continuum brightness map continued to show one significant trend – a nightside limb cooler than the dayside limb. The continuum channel has a weighting function which samples a wide layer in the atmosphere between 40-60 km at normal incidence and 55-75 km along the planet limb. A radiative transfer model roughly reproduced the increased nightside limb-darkening, when given a mesospheric temperature profile 40 K cooler than the nominal Pioneer Venus nightside temperature profile between 60-85 km. The strength of this result is undercut by strong uncertainties associated with the continuum map's absolute intensity values due to the small number of baselines in the OVRO array.

The 50 KHz filterbank resolved the inner core of the CO absorption line. This yielded the first measurement of doppler shifts across Venus due to strong winds in the upper mesosphere. It is the most important result presented in the thesis. Calculated weighting functions showed sampling of the mesosphere over a 12 km layer centered at roughly 99 km. The doppler shifts have a signature which matches westward, horizontal winds – being strongly "blue" on the east/dayside limb, zero near the center and strongly "red" on the west/nightside limb of the planet. Smoothed wind measurements were best fitted in a least squares sense for a mean zonal flow of 132±10 ms^{-1}. A smaller (≤ 40 ms^{-1}) subsolar-to-antisolar flow may have been superimposed on the dominant zonal flow in 1988. These measurements indicate either a reversal of the mesospheric cyclostrophic breakdown inferred by Pioneer Venus or the influence of uninvestigated dynamical forces.

The 1 MHz and 50 kHz filterbank spectra were merged to look at the entire 115 GHz CO line. These 1988 CO spectra show a decided local time dependency, becoming progressively deeper from the afternoon to the evening hours. A constrained least-squares inversion algorithm was used to solve for the local CO mixing ratio profile over local time and latitude. The resultant CO mixing ratio remains constant with height at a value of several 10^{-5} in the late afternoon hours but increases from 10^{-4} at 80 km to 10^{-3} at 100 km in the night hours. The highest CO abundances occurred after local 10 PM and centered about the equator between 40°N and 40°S. This distribution of CO abundance fulfills predictions from research based on disk-average CO spectra and photochemical models. Only the late afternoon profiles are surprising, showing essentially little CO rather than an expected moderate CO abundance from dayside photodissociation of CO_2.

Table of Contents

List of Figures

Chapter I:

Chapter II:

Chapter III:

Chapter IV:

Chapter V:

Appendix C:

Appendix D:

List of Tables

Chapter II:

Chapter IV:

Chapter V:

Chapter I Introduction.

Venus has had various descriptions through the centuries. The Babylonians were one of the earliest sky-watchers to mention Venus in their writings. They thought Venus followed a strange path across the sky compared to other bright stars. After the invention and spread of the telescope, Franceso Fontana was among the first to remark on dark markings spotting Venus' disk. Christian Huygens argued later that he found none of these changing, transient markings but hinted at an atmosphere for this planet. Mikhail Lomonosov, a century later in 1761, was the first to point out direct evidence for an atmosphere by noting a halo about Venus' limb during a transit of the sun (Cruikshank 1983).

The arguments about visual markings and the true rotational period of Venus continued up through the early 1900's. In the 1930's and 1950's, technology advanced and created the fields of radiometry, spectroscopy, radio and radar astronomy. The new fields quickly settled many arguments and speculations inspired by telescopic observations through the centuries, revealing a CO_2 dominated atmosphere with high surface temperatures over a very slowly rotating solid planet. Later spacecraft data would replace early qualitative descriptions of Venus such as "moist, swampy, teeming with life" (Colin 1983) and inspire the more accurate description "a secular version of Hell" (Pollack 1991). The analysis of such data established vertical transitions for dividing Venus' atmosphere into three regions: the troposphere, the mesosphere and the thermosphere/cryosphere. This thesis will focus upon the new observational results constraining the dynamics and CO abundance of the upper mesosphere.

1. An Overview of Venus' Atmosphere

The following quick review of the Venus' troposphere, thermosphere and its atmospheric composition sets up an appropriate background for the mesospheric results discussed in later chapters.

1.1 Composition

The atmosphere of Venus is dominated by CO_2 at a mixing ratio of 96.5±0.8%. The second most abundant gas is inert N_2 with a mixing ratio of 3.5±0.8% (von Zahn *et al.* 1983). These two gases, along with small amounts of the gases He, Ne, Ar, and Kr, are expected to have constant mixing ratios throughout the atmosphere. The third most abundant species, CO, is produced during photolysis of CO_2 and, along with the reactive species H_2O, SO_2, H_2S, HCl, HF, C_2H_6 and O_2, has an abundance dependent upon altitude.

The influx of solar ultraviolet radiation gets absorbed primarily above the sulfuric acid cloudtops (45-70 km). Photons with wavelengths shorter then 2075 Å photodissociate the dominant gas into CO and O

$$CO_2 + h\nu \quad \rightarrow \quad CO + O. \tag{1}$$

The products CO and O cannot recombine easily through collisions into CO_2 because the three-body recombination reaction is spin-forbidden. Instead atomic oxygen is lost to formation of O_2. This latter molecule and CO were thus expected to be abundant in Venus' mesosphere. Instead, Connes *et al.* (1968) found a low CO abundance of 4×10^{-5} and Traub and Carleton placed a low upper limit for O_2 abundance of 10^{-6} with groundbased observations of reflected infrared absorption and scattered solar radiation from Venus. This motivated photochemical modellers to re-examine recombination of CO_2. The first suggestion was that hydroxyl radicals might drive a catalytic reaction

$$CO + OH \quad \rightarrow \quad CO_2 + H, \tag{2}$$

wherein the hydroxyl radicals are derived from photolysis of HCl (Prinn 1971). This catalytic reaction had actually been proposed originally to explain Mars' similar depletion of CO (McElroy and Donahue 1972). The second suggestion was also a catalytic reaction but depended upon chlorine radicals

$$ClCO + O_2 \rightarrow CO_2 + ClO \tag{3}$$

which, unlike the hydroxyl reaction, does not involve a further breakdown of O_2 to generate the needed catalytic molecule (Krasnopolsk and Parshev 1981; Yung and Demore 1982). In models, both of these recombination reactions peaked at heights between roughly 70-90 km. The photodissociation reaction of CO_2, on the other hand, peaked over the range of 70-100 km. Consequently the CO abundance profile over height decreased from a mixing ratio of 10^{-3} at 100 km to 10^{-4} at 80 km in photochemical models in agreement with observed CO abundances. The low observed O_2 abundance was not matched by simply the increased recombination of CO_2 and required further loss by efficient oxidation of sulfur compounds into H_2SO_4 in the lower atmosphere (Yung and DeMore 1982).

Deeper in the atmosphere, atmospheric chemistry is dominated by the sulfuric acid clouds (45-70 km) which enshroud Venus with essentially 100% coverage. This main clouddeck is sandwiched between thinner haze layers 10-20 km wide and has a multimodal particle size distribution dominated by spherical H_2SO_4 droplets 2 μm in diameter (Hansen and Hovenier 1974; Knollenburg and Hunten 1980). The liquid sulfuric acid-water cloud droplets form through oxidation of SO_2 into H_2SO_4 vapor. The sulfuric acid vapor probably nucleates and condenses in the cloudtop's low temperatures and evaporates at the cloud base's higher temperatures (Esposito *et al.* 1983). Vapors believed present in the cloud include H_2SO_4, SO_3 and H_2O though only H_2O has been measured. The Venus atmosphere is very dry above the clouds, with water abundance at 1 ppm (Yung and Demore 1982). Water vapor abundance increases to 200 ppm within the clouds (Moroz *et al.* 1979) and to several 1000 pm below the clouds (Oyama *et al.* 1980).

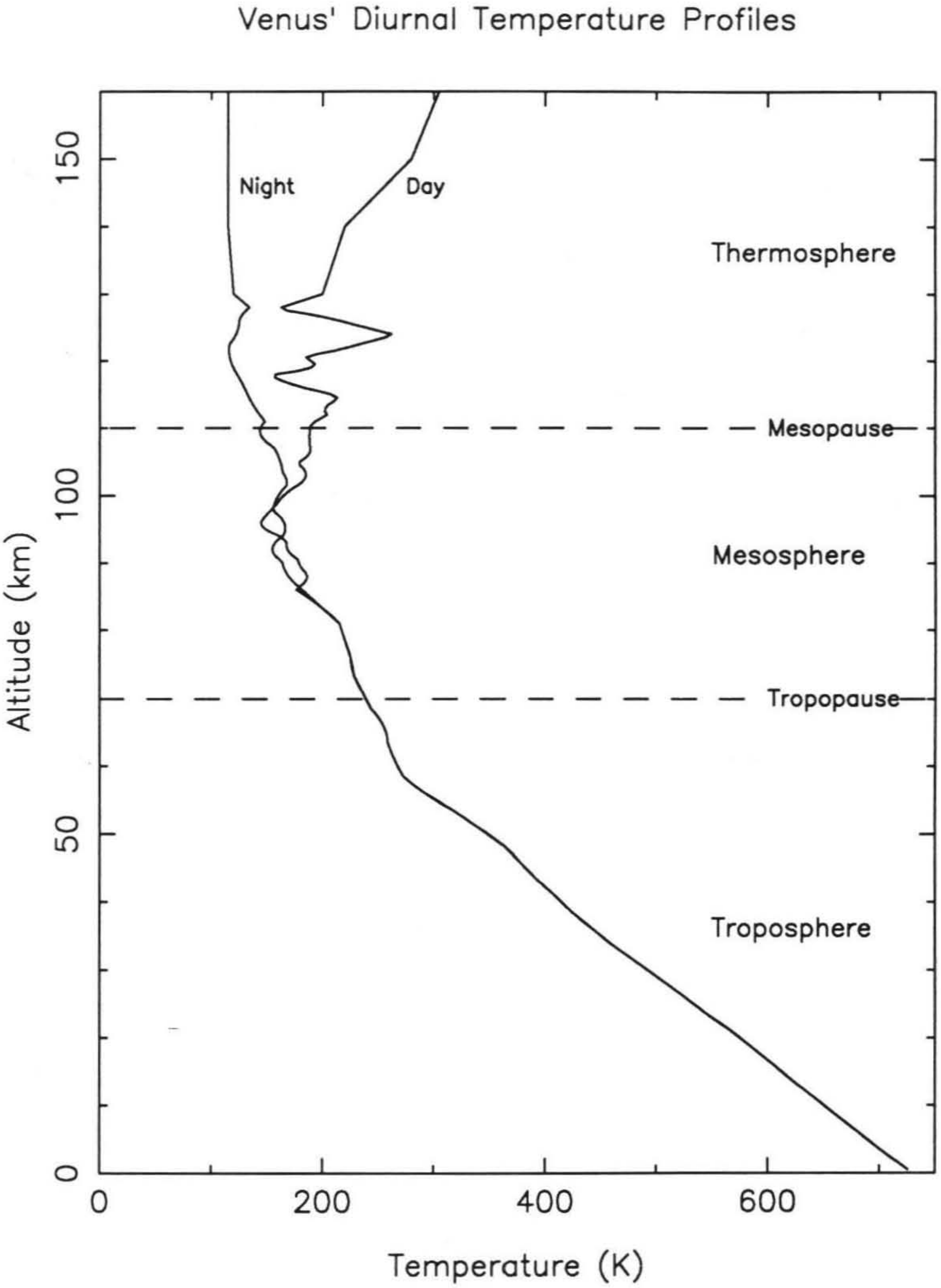

Figure 1. Day and night temperature profiles for Venus' atmosphere with associated nomenclature.

1.2 Troposphere

The troposphere (below 70 km) is noteworthy for its immense mass, having a surface pressure of 92 bars and a single temperature profile independent of local time of day. This temperature profiles increases downward to a surface temperature of 740 K (Figure 1). The high surface temperature is maintained by the greenhouse effect active in and below the cloud decks (45-70 km). The dense lower atmosphere is even more noteworthy for its motion – the retrograde zonal superrotation, popularly referred to as the '4-day winds', incongruously set above the solid planet's slow rotation period of 243 days. The superrotation has been measured for altitudes below 70 km by ground-based doppler tracking of the Venera probes (see Schubert 1983) and interferometric tracking of the Pioneer Venus (PV) probes (Counselman *et al.* 1980). The westward zonal superrotation generally decreases linearly in speed from 100 ms^{-1} at 70 km to a few ms^{-1} above the planet surface.

Tracking of UV cloud features in spacecraft photopolarimeter images has provided insight into the latitudinal variation of the zonal superrotation and into the smaller meridional flow in the cloud tops (Suomi 1974; Limaye 1977; Limaye and Suomi 1981; Rossow *et al.* 1980; Limaye *et al.* 1982; Limaye *et al.* 1988: Rossow *et al.* 1990). Mariner 10 UV images from 1974 and Pioneer Venus UV images gathered over 1979-1985 consistently found zonal speeds between 85 and 100 ms^{-1} in the low latitudes about the equator. The equatorial zonal speeds fall off at latitudes poleward of 40° to speeds between 70 and 90 ms^{-1} (Limaye *et al.* 1988; Rossow *et al.* 1990). During some years these latitudinal profiles of the zonal flow also showed mid-latitude jets, 5-15 ms^{-1} stronger than the ambient flow. The meridional winds of the clouds' Hadley cell measured in these studies move poleward with average speeds between 5-15 ms^{-1}. Both the zonal and meridional flows have exhibited latitudinal changes during the decade that these photopolarimeter images were taken. The zonal winds, in particular, have recently been described as cyclic due to the similarities between images taken for 1985-1986 and 1979-1980 versus the years 1982-1983 (Del Genio and Rossow 1989).

Theoretically, the troposphere's zonal superrotation is still not understood. The mid-latitude jets in the cloud top zonal flow are believed due to poleward advection of angular momentum by a Hadley cell driven by solar heating. This feature of the zonal circulation has been simulated in several models (Del Genio and Suozzo 1987; Covey *et al.* 1986; Rossow 1983). Yet, the mechanism which maintains the zonal superrotation is still uncertain. Current hypotheses employ eddy transport to supply necessary angular momentum to the zonal flow. The first hypothesis uses barotropic instability of the jets by combining the Hadley cell with large scale waves to generate eddies (Gierasch 1975; Rossow and Williams 1979). The second hypothesis uses vertically propagating solar-locked thermal tides or vertical momentum transport off a "moving flame" to generate eddies (Young and Schubert 1973; Fels and Lindzen 1974; Pechmann and Ingersoll 1984; Baker and Leovy 1987). The "moving flame" label comes from laboratory studies of the effects moving heat sources upon the motion of rotating fluids. The laboratory tests simulate the eastward motion of the Sun, the "moving flame". The Sun's motion crosses over the ongoing diffusion of solar heating within the troposphere's westward superrotation (Schubert and Whitehead 1969). The last hypothesis employs a spectrum of transient or topography-related gravity waves to cause vertical momentum transport (Leovy 1973; Hou and Farrell 1987; Gierasch 1987). However these hypothesis are acknowledged as incomplete and unable to account for the observed complexity of the Venus troposphere (Rossow *et al.* 1990).

1.3 Thermosphere

The second region, the thermosphere above 110 km, has an extreme temperature gradient between a dayside exobase temperature at approximately 300 K and a nightside exobase at approximately 130 K. The dayside thermosphere appeared to be very similar to the terrestrial thermosphere with increasing temperatures with height through solar heating. The severely low nightside temperature above 100 km was considered to be one of the major discoveries by Pioneer Venus mission and inspired the label of " cryosphere" for the nightside thermosphere on Venus. The associated diurnal pressure and number density gradients measured by Pioneer Venus fell roughly two orders of magnitude across the terminators at altitudes near and above 150 km (Seiff and Kirk 1982; Seiff 1983). This drives an axisymmetric subsolar-to-antisolar flow with speeds strongest over the terminators – up to several hundred ms^{-1} as calculated by two and three dimensional hydrodynamical models of the thermosphere (Bougher *et al.* 1988; Dickinson and Ridley 1977; Dickinson and Ridley 1975).

These models predict that air masses would rise in the thermosphere's subsolar area with vertical speeds on the order of tens of cms^{-1}, travel with increasing horizontal speed across the terminators and then subside in the nightside's cryosphere. The early models' low extreme ultraviolet (EUV) heating rates for the dayside's high atmosphere reproduced the dayside thermosphere temperatures. These models, though, originally predicted nightside temperatures a factor of two larger than observed temperatures. The nightside thermosphere would receive energy from the dayside via advection and conduction over the terminators and compression of the descending subsolar-to-antisolar flow. To achieve the observed thermospheric temperatures, more recent models employed enhanced 15 μm CO_2 radiative cooling during this molecule's collisions with ambient atomic oxygen in combination with a 10% EUV heating efficiency and a minimal eddy coefficient for cooling by eddy mixing. In these recent thermospheric models, the subsolar-to-antisolar winds reach maximum speeds of 230 ms^{-1} over the terminators.

The same models predicted that the subsolar-to-antisolar flow would transport light constituents away from the dayside photochemical regime to the nightside – creating a reversal phenomena with higher nightside than dayside abundances. Observations of such light species did find such a diurnal variation in abundances. However, these light constituents had nightside abundance maxima which were distinctly offset from local midnight towards the morning terminator. Such post-midnight maxima for O, H, and He number densities (Niemann *et al.* 1980; Brinton *et al.* 1979), post-midnight NO and O_2 airglow maxima (Stewart and Barth 1979) and a longitudinal displacement of the nightside minimum in temperature (Mayr *et al.* 1980; Keating *et al.* 1980) pointed to the existence of a 50-75 ms^{-1} zonal flow at low latitudes and altitudes around 150 km (Mayr *et al.* 1980, 1985; Schubert *et al.* 1980). Recently Goldstein and others (Goldstein 1990; Goldstein 1989; Goldstein *et al.* 1988) reported detection of a zonal flow superimposed on the expected subsolar-to-antisolar flow in their 1985 CO_2 infrared heterodyne observations of the lower thermosphere. Their measurements of doppler shifts of the nonthermal emission core of CO_2 at 10.33 μm found best-fit values of 120 ms^{-1} for cross terminator winds associated with the subsolar-to-antisolar flow and a 25 ms^{-1} retrograde zonal flow at 110±10 km. Thus, the thermosphere/cryosphere appears to contain a strong subsolar-to-antisolar flow with possibly a smaller zonal component superimposed.

2. Previous Observations of Venus' Mesosphere

These next sections focus on Venus' middle atmosphere (70-110 km). The mesosphere's dynamical structure is described only by theory and its thermal structure is sketchily measured in comparison with the troposphere. The best tool for exploring this region has been through observations of the rotational transitions by CO, a trace molecule residing in the upper mesosphere.

2.1 Continuum Brightness

Thermal radio emission from Venus was first measured in 1956 by Mayr *et al.* who found a disk-average brightness temperature of 560±73 K at 3.15 cm wavelength and the first indication of unexpectedly high surface temperatures. Figure 2 shows some of the microwave observations made over the subsequent three decades (Lowenstein *et al.* 1977; Whitcomb *et al.* 1979; Werner *et al.* 1978; Rather *et al.* 1974; Rowan-Robinson *et al.* 1978; Ulich *et al.* 1973; Hobbs and Knapp 1971; Ulich *et al.* 1974; Tolbert and Straiton 1964; Kuz'min and Salomonovich 1962; Steffes *et al.* 1990; Janssen and Klein 1981; Vetukhnovskaya *et al.* 1963; Yefanov *et al.* 1969). Venus' 2.6 millimeter emission originates in the troposphere's clouddeck around 50 km with a brightness temperature of roughly 335 K. Opacity occurs through continuum absorption by CO_2, SO_2 and, possibly, gaseous H_2SO_4.

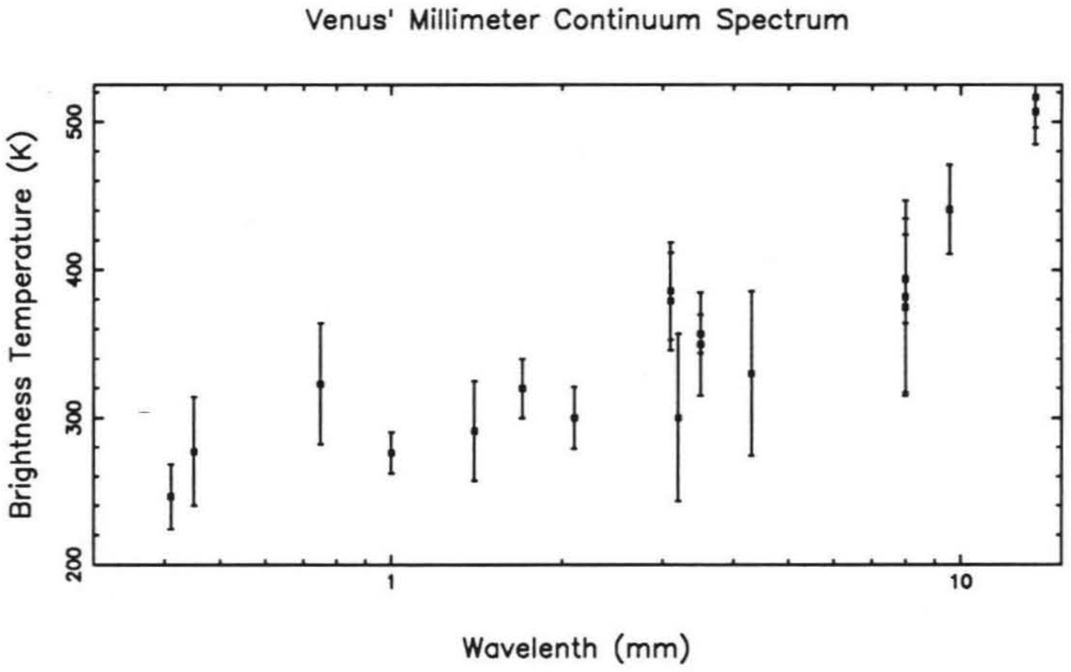

Figure 2. Observed disk-average brightness temperatures for Venus.

The normally nonpolar CO_2 undergoes pressure-induced microwave absorption in Venus' lower atmosphere. It develops a transient dipole during molecular collisions induced by its molecular electric quadropole fields (Maryott and Birnbaum 1962). This provides nearly all of the atmospheric opacity at 2.6 mm except at the cloud base and below. SO_2, the second source of opacity, has a large measured abundance below the clouds, $\geq$100 ppm, which decreases with height to $\leq$1 ppm at the cloud tops. This molecule has a complex rotational spectrum in the microwave which blends into continuum opacity at cloud and subcloud pressures, $\geq$1 bar (Janssen and Poynter 1981). At 2.6 mm SO_2 can provide 50% of the opacity given an abundance of 185 ppm, but it resides in the lower and sub- cloud altitudes below the peak sensitivity of the 2.6 mm wavelength. The last absorber, gaseous H_2SO_4, is a much more uncertain source of millimeter opacity. It is believed to exist in saturation densities below the main cloud layer above concentrated sulfuric acid-water cloud droplets and has a well known permanent dipole moment with resonances measured in the 60-120 GHz range (Kuczkowski *et al.* 1981). However, only a few laboratory measurements exist to constrain the molecule's uncertain vapor pressure characteristics (Gmitro and Vermeulen 1964; Ayers *et al.* 1980) needed to calculate cloud abundances. A preliminary, theoretical millimeter and microwave spectrum from Janssen and Poynter yielded high absorption coefficients for gaseous sulfuric acid (Cimino 1982; Steffes and Eschelman 1982; Steffes 1985). Later work, though, revealed mistakes in the partition function used to produce the theoretical line data. The incorrect partition function overestimated line intensities by a factor of 18 and, as yet, has not been resolved (Poynter 1989). The abundance and the continuum opacity of gaseous sulfuric acid in Venus' atmosphere is extremely uncertain. Consequently, gaseous sulfuric acid is left out of the analysis of the continuum data in Chapter III.

2.2 Mesospheric Winds

For over a decade, a significant gap has existed in the observations of Venus' atmosphere. Although the Venera, Vega, Mariner and Pioneer Venus missions and numerous ground-based observers have provided excellent quantitative constraints on circulation within this atmosphere's troposphere and thermosphere, no measurements have been made within Venus' mesosphere.

Circulation at the edge of the mesosphere was measured above the cloud deck at about 75 km by Betz *et al.* (1977), using doppler shifts of 10 μm $^{13}C^{16}O_2$ spectra. However, their data indicated 90 ms^{-1} zonal velocities along with 45 ms^{-1} *vertical* velocities. These high vertical velocities would have been unsupportable physically by the lower mesosphere's pressures of tens of millibars and in face of the cloud top's high zonal velocities. This cast doubt on the experiment's results.

The only other observations which suggest strong winds in the mesosphere are $^{12}C^{16}O$ microwave spectroscopic observations by Clancy and Muhleman (1985). Their synthetic spectra fits for CO mixing ratio profiles found a displacement of CO between 80-90 km from an expected midnight maximum towards the morning. Photochemical and vertical eddy diffusion models were tested to explain this displacement of the CO profile without success. Instead they proposed that the zonal winds extended at least up to approximately 90 km with velocities of several tens of meters per second, shifting the CO number density maximum.

Dynamics for the mesosphere have primarily been studied through models assuming cyclostrophic balance above 70 km and using latitudinal temperature gradients returned by the Pioneer Venus (PV) probes, the Pioneer Venus Orbiter infrared radiometer (OIR) and the Pioneer Venus Orbiter (PVO) radio occultations. With an assumed mean cloud top velocity of 150 ms^{-1}, early researchers using the 1978 North and Day PV entry probe data found strong zonal speeds of roughly 100 ms^{-1} at

100 km (Seiff *et al.* 1980). On the other hand, the models using concurrent OIR data and allowing for frictional effects from eddy viscosity found a rapid decrease in zonal velocities with height due to the different temperature gradients in these data (Elson 1979; Taylor et al. 1980). The OIR models also found a simultaneous increase in mean meridional circulation to speeds on the order of several tens of meters per second, adding yet another possible scenario for the mesospheric circulation pattern. Later PVO radio occultation temperature data gathered through 1981 (Newman *et al.* 1984) continued to find positive poleward temperature gradients and a decrease in the lower atmosphere's superrotation with altitude using cyclostrophic balance. However, subsequent PVO radio occultation data for the 1984-1986 period found cooler temperatures at high latitudes for altitudes from 60 to 90 km, reversing temperature gradients seen in the 1979-1981 data (Kliore and Mullen 1988). Obviously the question remained open on the existence of strong zonal or meridional or, even, subsolar-to-antisolar winds in the mesosphere of Venus.

2.3 Mesospheric CO

The 115.2712 GHz, J=0-1 transition of CO was first observed in Venus' spectrum by Kakar *et al.* (1976). Subsequent single-dish observations of this absorption line (Gulkis *et al.* 1977; Schloerb *et al.* 1980; Wilson *et al.* 1981; Clancy and Muhleman 1985ab; Clancy and Muhleman 1991) found that it varied in lineshape and depth with planetary phase angle. The line is sensitive to the total column abundance of CO between 75-105 km and undergoes doppler and pressure broadening. The contrast between the nightside phase angles' very deep, narrow absorption lines and the dayside phase angles' shallow, wide lines pointed to a diurnal dependence for CO abundance over altitude. At low altitudes, below 90 km, the CO abundance is greater in the dayside than the nightside hours. At higher altitude, above 90 km, the reverse is true, with higher abundances in the nightside than the dayside hours.

Tests of photochemical and dynamical models by Clancy and Muhleman (1985ab) found that dayside CO, formed through photodissociation of CO_2, is most likely transported via vertical eddy mixing and the subsolar-to-antisolar flow to local midnight. Furthermore, while disk-average spectra cannot directly determine the diurnal distribution of CO in detail, comparison of synthetic spectra, created from model CO distributions, to observed spectra pointed out a time offset for CO. Their comparison of spectra indicated a nightside CO bulge in the early morning hours rather than at local midnight. As in the case of He, H and O maxima offsets described in section 1.3, the researchers suggested an extension of the lower atmosphere's zonal flow into the upper mesosphere which would displace the CO maxima from local midnight.

Simultaneous observations of other rotational transitions by CO, the optically thin ^{13}CO line at 220 GHz and the optically thick ^{12}CO line at 230 GHz, have also been used to determine temperature profiles along with CO mixing ratio profile (Clancy *et al.* 1990; Clancy and Muhleman 1991). Recent work by Clancy and Muhleman compared disk-average CO lines from five Venus inferior conjunctions (1982, 1985, 1986, 1988 and 1990) to study interannual variations in nightside mesospheric temperatures and CO abundance. They found that the 1985 and 1986 years had exceptional upper mesospheric temperature profiles with temperatures 20-40 K higher than the 1979 Pioneer Venus temperature measurements. The other inferior conjunctions' temperature profiles agreed with the Pioneer Venus temperature profiles. CO mixing ratios also showed this interannual pattern, being increased by a factor of 4 in 1985 and 1986 relative to other inferior conjunction years. Clancy and Muhleman suggested that these unexpected 1985-1986 mesospheric temperature and CO increases, the 1975 increase in mesospheric temperatures as observed by the Venera 10 probe (Avduevskiy *et al.* 1983), the cooler high latitude temperatures measured by PV radio occultations in late 1984 (Kliore and Mullen 1988), the 5-10 year variations in UV cloud top features (Del Genio and Rossow 1989) and a 1979 decay in cloudtop SO_2 abundance (Esposito *et al.* 1988) are related. They suggest that these different observations are effects of an interannual variation of the global dynamics, thermal structure and composition of Venus' mesosphere having a timescale of roughly 10 years.

3. Millimeter Interferometry

The current observations were made using the OVRO millimeter interferometer. These measurements yielded higher spatial resolution than any previous ground-based observations of Venus CO. An interferometer operating in the mm-wavelengths is an array of radio antennas which gather visibilities – complex numbers measured in units of flux density usually stated in terms of a Jansky (= 10^{-26} Watts per square meter per Hertz). A visibility is the correlation between the signals received at each possible pair of antennas in the array

$$\begin{aligned} V_{ij} &= \langle\, V_i(t) V_j(t)\, \rangle \\ &= \langle\, v_i cos 2\pi\nu(t - \tau_g)\, v_j cos 2\pi\nu t\, \rangle \\ &\equiv |V| e^{i\phi_V}, \end{aligned} \tag{4}$$

where v_i is the voltage at an individual antenna, |V| the visibility amplitude, ϕ_V the visibility phase, ν frequency, angular brackets a time average and τ_g the geometrical delay. The geometrical delay measures the time delay between a wavefront's arrival at the antennas due to the baseline separating the antennas. The source's visibilities are measured in spatial frequency space with coordinates (u,v) corresponding to the instantaneous baselines projected on Venus (east-west, north-south). Coverage of the source's visibility function in the (u,v) plane is filled in by the Earth's rotation or physical repositioning of the antennas on the ground. This is referred to as aperture synthesis. A fourier transform relationship links the visibility, V(u,v), and brightness, B(x,y), of an object

$$V(u,v) = \int_{-\infty}^{\infty}\int_{-\infty}^{\infty} B(x,y)e^{-2\pi i(ux+vy)}\,dx\,dy. \tag{5}$$

Given extensive sampling of the source's visibility $V(u,v)$, brightness maps $B(x,y)$ with higher spatial resolution than from a single antenna can be constructed through the fourier transform relationship (see, e.g., Born and Wolf 1980; Thompson *et al.* 1986; Schloerb *et al.* 1979; Rudy *et al.* 1987). These brightness maps will have intensity described in terms of the solid angle of the resolving beam and, so, will be in units of Jy/beam. If a radio array is equipped with frequency filterbanks and tuned to a molecule's transition frequency, then brightness maps can be made in each frequency channel of the filterbanks. The change in brightness from channel map to channel map is equivalent to the molecule's absorption line. Thus an interferometer can yield local absorption lines in beam-sized spatial steps across the observed object.

The question of the existence of strong winds in Venus' upper mesospheric could be answered in observations of CO's first rotational transition given a frequency resolution of 50 kHz. Doppler shifts due to wind speeds of even 100 ms^{-1} (e.g., 38 kHz) are small relative to the transition frequency involved, 115,271,204.0 kHz, and relative to the Voigt line broadening effect, which is on the order of 1 MHz. The Voigt lineshape is a convolution of the Lorentzian pressure broadening Van Vleck-Weisskopf function and the Gaussian thermal broadening function. Nonetheless, given a sufficiently abundant trace molecule, a spectral line in the millimeter area of the spectrum where lines are isolated and a heterodyne receiving system using a precisely known local oscillator (LO) frequency, such measurements are possible. The lineshape functions for these rotational lines are symmetric so shifts due to only a few ms^{-1} can be extracted with a least-squares fitting to the center absorption frequency channels of the line provided that the observations have an adequate signal-to-noise ratio.

By fitting the shape of the absorption line over inner frequency channels, one can determine the frequency center of the absorption line and escape limitations due to channel widths greater than the absolute doppler shift observed. Our observations matched the above qualifications: CO exists between 70 to 110 km with corresponding abundances of 10^{-5} to 10^{-3}, its J(0,1) transition at 2.6 mm lies far apart from any other strong transitions and the receivers' LO frequency had an accuracy to 1 part in 650777580 or better than 3/4 of a kHz at the J(0,1) transition frequency. Therefore, since a shift of 384 Hz corresponds to a speed of 1 ms^{-1}, the rest frequency used in the observations had a precision to better than 2 ms^{-1}. However, since our knowledge of the CO transition frequency may be as poor as ± 5 kHz, the absolute error in all the velocities could be as large as ± 13 ms^{-1} (Poynter 1990).

This thesis will focus on observations of Venus' middle atmosphere, the mesosphere. It presents the analysis and results of our interferometric observations of the CO 2.6 mm line – the broadband 400 MHz data, the 50 kHz filterbank data and the 1 MHz filterbank data. The following chapter reviews the characteristics of the observations and summarizes the intensive reduction of all of the visibility data. The third chapter contains the analysis of features in the broadband continuum map and discussion of the associated atmospheric properties. The fourth chapter consists of the analysis of the 50 kHz filterbank data for doppler shifts to the CO absorption line and, equivalently, radial wind measurements. The fifth chapter presents the analysis which combined the 50 kHz and 1 MHz data sets and inverted the resultant absorption lines for CO mixing ratio profiles to find trends in the CO abundance distribution over local time and latitude. Finally the thesis ends with a summary of results from the different frequency resolution data sets and their implications.

Chapter II Observations and Data Reduction.

Observations of the ^{12}CO J=0-1 transition in Venus' upper mesosphere were made on April 26, April 28, May 2 and May 4, 1988. We used the Caltech Millimeter Wave Interferometer at the Owens Valley Radio Observatory (OVRO) located near Big Pine, California. Similar experiments were carried out in 1986 using the OVRO 1 MHz and 5 MHz frequency filterbanks (Muhleman *et al.* 1987) and the Hat Creek millimeter array's 625 kHz and 20 kHz correlators (de Pater *et al.* 1987; de Pater *et al.* 1991) to study the CO distribution on the planet.

1. OVRO

The OVRO millimeter interferometer consists of three 10.4 meter diameter antennas moveable to fixed stations along T-shaped tracks. To increase (u,v) coverage and consequently improve the synthesized beam, these antennas were moved out along the tracks to new spacings on days between observation runs. The antennas were moved into four array configurations. The antenna stations on the east-west and north tracks are separated by tens of meters and denoted as (meters east, meters north, meters west). The array was moved from (10e,20n,10w) to (30e,30n,30w) to (50e,80n,50w) and, finally, to the maximum baselines (100e,140n,100w). The synthesized beam thus had a size of 2.8 arcseconds at full-width-half-maximum (Fig. 3).

Each antenna used a low-noise superconductor-insulator-superconductor (SIS) heterodyne receiver cryogenically cooled to a total system temperature of 600 K at a wavelength of 2.6 mm in single sideband mode (Woody *et al.* 1985). The rest frequency was set at the ^{12}CO transition frequency of 115,271,204.0 kHz and then modified to a sky frequency, correcting for motion of the source relative to the mm array. The receivers used a local oscillator (LO) frequency maintained by a system consisting of three synthesizers, phase locked to a hydrogen maser and sent to each

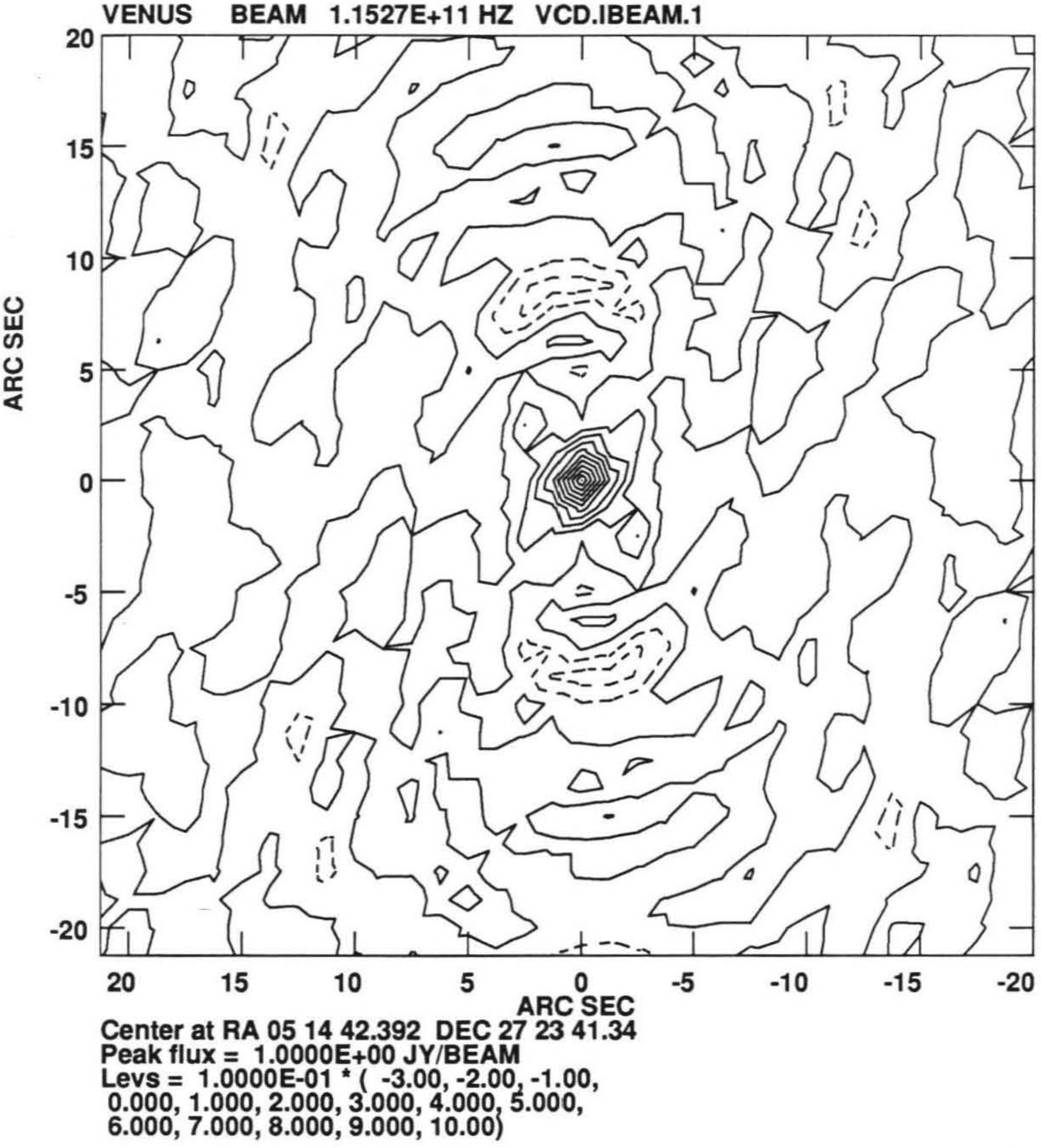

Figure 3. The 1988 OVRO synthesized beam with contours separated by .1 normalized response.

TABLE I

Parameters for Spring 1988 OVRO Observations

Reference Date April 30 15^h TDT

Right Ascension		5 hr 26 min
Declination		27° 37'
Geocentric Distance		.4995 AU
Apparent Diameter		33.14"
Fraction of illumination		.33
Phase Angle		108°
Subearth	Latitude	-5.20°
	Longitude	265.13°
	Local Time	7:20 PM
Subsolar	Latitude	-1.84°
	Longitude	15.50°
Subearth resolution	synthesized beam 2.8"	1050 km
	map pixel 1.25"	470 km
Bandwidths		400 MHz, 1 MHz and 50 kHz

antenna via a line stabilizer system. The first of these synthesizers provided the primary phase reference, operating at 600 MHz and composed of a Fluke synthesizer with a 4-fold multiplier. Signals from this synthesizer are phase locked to a hydrogen maser and sent to each antenna via a line stabilizer system. The ninth harmonic of this 600 MHz tone then acts as the basis for the second synthesizer. This operates at 5.4 GHz and uses a Yttrium Iron Garnet (YIG) tuned oscillator phase locked to the 600 MHz tone. Finally, a third synthesizer generates the mm-wave LO signal. It consists of doubled output from a 53- to 59-GHz Gunn oscillator which is phase locked to the signal from the YIG oscillator. This local oscillator system has an interreceiver phase jitter of only 7° at 115 GHz and an accuracy to under 750 Hz at this rotational transition (see, e.g., Padin *et al.* 1988).

The signal at each antenna was detected in two sidebands which have broadband continuum channel widths of 400 MHz. The standard operating procedure optimizes the receiver gains to favor one sideband in order to improve the signal-to-noise ratio. The upper sideband contained the CO absorption line so it received the higher gain. Its continuum signal was divided down into to two filterbanks – one with 32 channels of 1 MHz resolution and the other with 32 channels of 50 kHz resolution. The filterbanks and the broadband channel were aligned about the transition frequency. In the case of the broadband channel of 400 MHz, the channel was sampling essentially the continuum radiation of Venus at 2.6 mm. The filterbanks, on the other hand, sampled the resonant CO absorption line. The 2.6 mm ^{12}CO line typically has a width of 5 MHz. Therefore, the 1 MHz filterbank saw the entire line within its range of ±16 MHz from the line center. The channels of the 1 MHz filterbank were a tuned-inductor system. Each channel had a response shape that was flat over the inner 60% of the channel, falling off to -3 dB at the channel edges. The second filterbank, 50 kHz, saw the inner ±.8 MHz, or inner core, of the absorption line. For the 50 kHz filterbank, each channel was a crystal filter with a response shape that had less than ±1 dB variation along the peak and fell off by 3 dB at 50±3 kHz from the filter center (Seling 1989). A visibility point for each baseline was recorded after an integration period, called a record, of 30 seconds. After the four days of observations, 7143 visibility points were collected in the continuum channel and in each channel of the two filterbanks.

2. Venus' Aspect in Spring 1988

Venus was approaching its 1988 June inferior conjunction during our observations with a phase angle of 108°. Since the observations occurred over nine days, the data were corrected to the center reference day of April 30th. The aspect characteristics listed in Table I and described in detail below are exact for this reference day. These characteristics differ by less than half the size of the synthesized beam (2.8 arcseconds at FWHM) on the specific observing days. The directions east and west cited in the thesis are planetary directions and are not Astronomical directions. Therefore, in Figure 4 which shows Venus' aspect, east refers to the right side of the disk and west refers to the left side of the disk. Planetary longitude, by convention, increases across the disk eastward towards the dayside limb from 175° to 355° due to Venus' retrograde rotation.

The disk had a diameter of 33.4 arcseconds with an evening terminator separating the dayside crescent along the east limb from the evening hours covering the remaining 66% of the disk. The subearth point occurred at -5° latitude and 265°

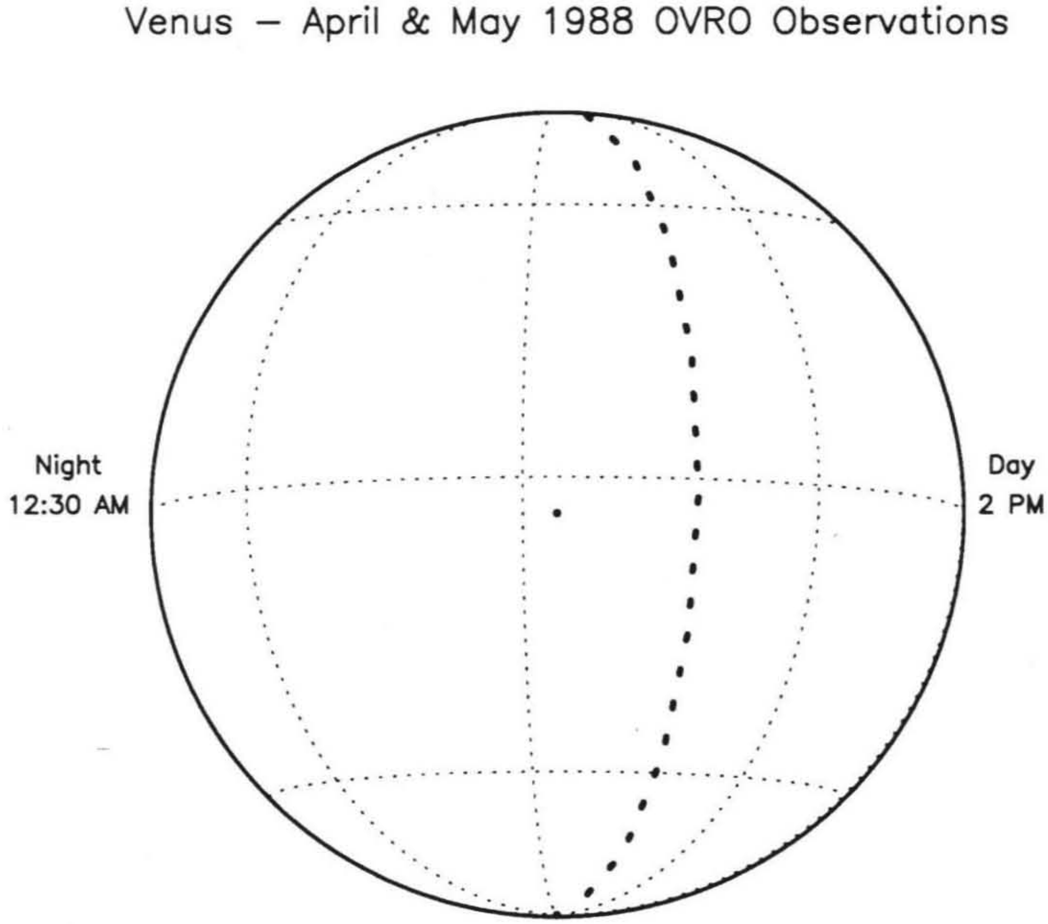

Subearth Lat: −5.2 Subearth Lon: 265.1
Evening Terminator Phase (% Day): .33
Local Time at Subearth Point: 7:20 PM
Range in Local Time: 2 PM to 12:30 AM

Figure 4.

longitude in planetographic coordinates. This translates into a subearth location at 19.3 hours local Venus time (LVT) and a range in viewable local time from approximately 14 hours LVT on the afternoon limb to 0.5 hours LVT on the nightside limb. The expected full twelve hours of coverage across Venus' disk appears limited to only 10.5 hours due to averaging over more local time in limb pixels than pixels near the center of the planet. Because of Venus' high declination of 27°, it was possible to collect data over approximately ten hours each day at OVRO and achieve excellent baseline rotation on Venus.

3. Calibration

Since visibility data are complex values, radio observers use quasi-stellar radio sources as calibrators. These compact radio sources have known flux amplitudes and known point positions which provide constant amplitudes and phases benchmarks over sufficiently long periods of time. These relatively constant point positions and amplitudes are needed to monitor instrumental variations that create amplitude and phase gain changes during the observations. After the observations are completed, scans on these compact radio sources are used to determine and correct these amplitude and phase gain variations in the Venus visibility data.

Even before the observations, basic parameters such as antenna positions, individual antenna gains and delays on signal lines between the antennas and correlators had to be determined for each array configuration by observing standard OVRO calibrators. This was satisfactorily accomplished for each array configuration except in the (100e,140n,100w) configuration. This wide configuration is rarely used at OVRO and, so, our observations uncovered a problem with its delay lines. The details of the additional calibration needed to correct the delay line problem, done during the post-observations data reduction, are described below. Finally, use of the filterbanks for spectral data required careful calibration of the filterbanks' passbands before be-

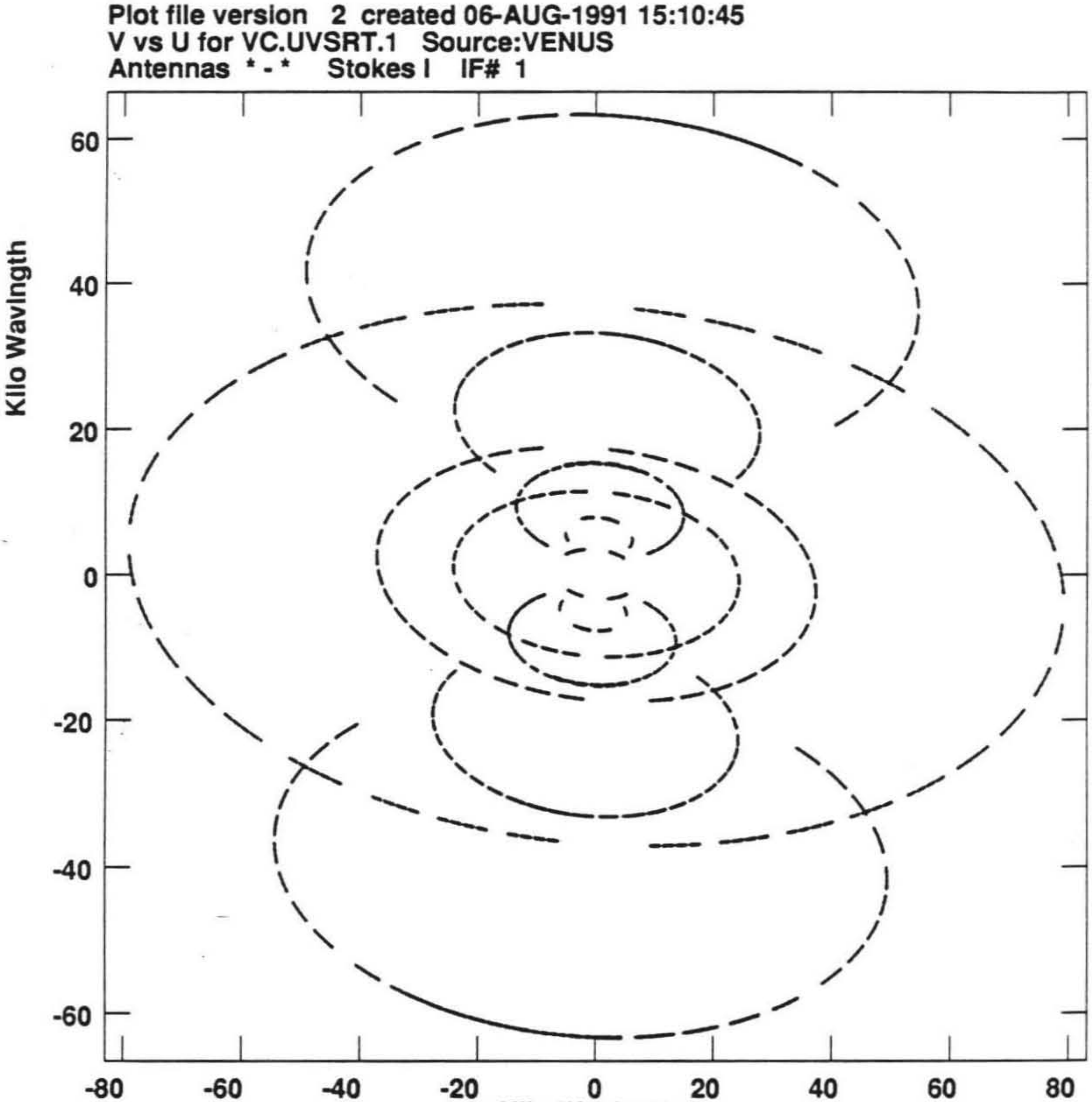

Figure 5. Coverage of the u-v spatial frequency plane during 1988 OVRO observations.

ginning the observations. In a passband calibration, a strong continuum source is observed to adjust channel amplitude and phase gains until both appear flat across the channels of the filterbank. For our observations, we adjusted the passband gains by observing the limb of the Moon in the short spacing configuration (10e,20n,10w). This lunar continuum source provided a strong signal to correct irregularity in the passbands' flatness to under 5%. The resultant sets of amplitude and phase gains for the filterbanks' passbands were used in each array configuration during the observations.

3.1 Delay Line Calibration

In order to understand the delay line problem in the (100e,140n,100w) configuration, it is necessary to return to Equation (4) and interferometry theory. This equation describes the output from a correlator which time averages the signals received at two antenna. Carrying through the time average, the two-element interferometer response is then

$$V_{ij} = |V| cos(2\pi \nu_\circ \tau_g - \phi_V). \tag{6}$$

This does not include the effects of observing with a finite bandwidth $\delta\nu$. A finite rectangular bandwidth places a sinc-function envelope about the cosine fringes in the above expression

$$V_{ij} = |V| \Delta\nu \frac{sin \pi \Delta\nu \tau_g}{\pi \Delta\nu \tau_g} cos(2\pi \nu_\circ \tau_g - \phi_V). \tag{7}$$

Looking at this expression for the response of an interferometer, the full amplitude is only observed when τ_g is zero – that is, when the source is normal to the baseline separating the antennas and wavefronts reach the antennas at the same time. During observations with an interferometer this geometric delay is therefore cancelled by physically delaying the arrival of one antenna's signal at the correlator. This is accomplished by adding a cable for the signal to travel on before reaching the correlator. Then the correlator outputs the full amplitude |V| as given by equation (4).

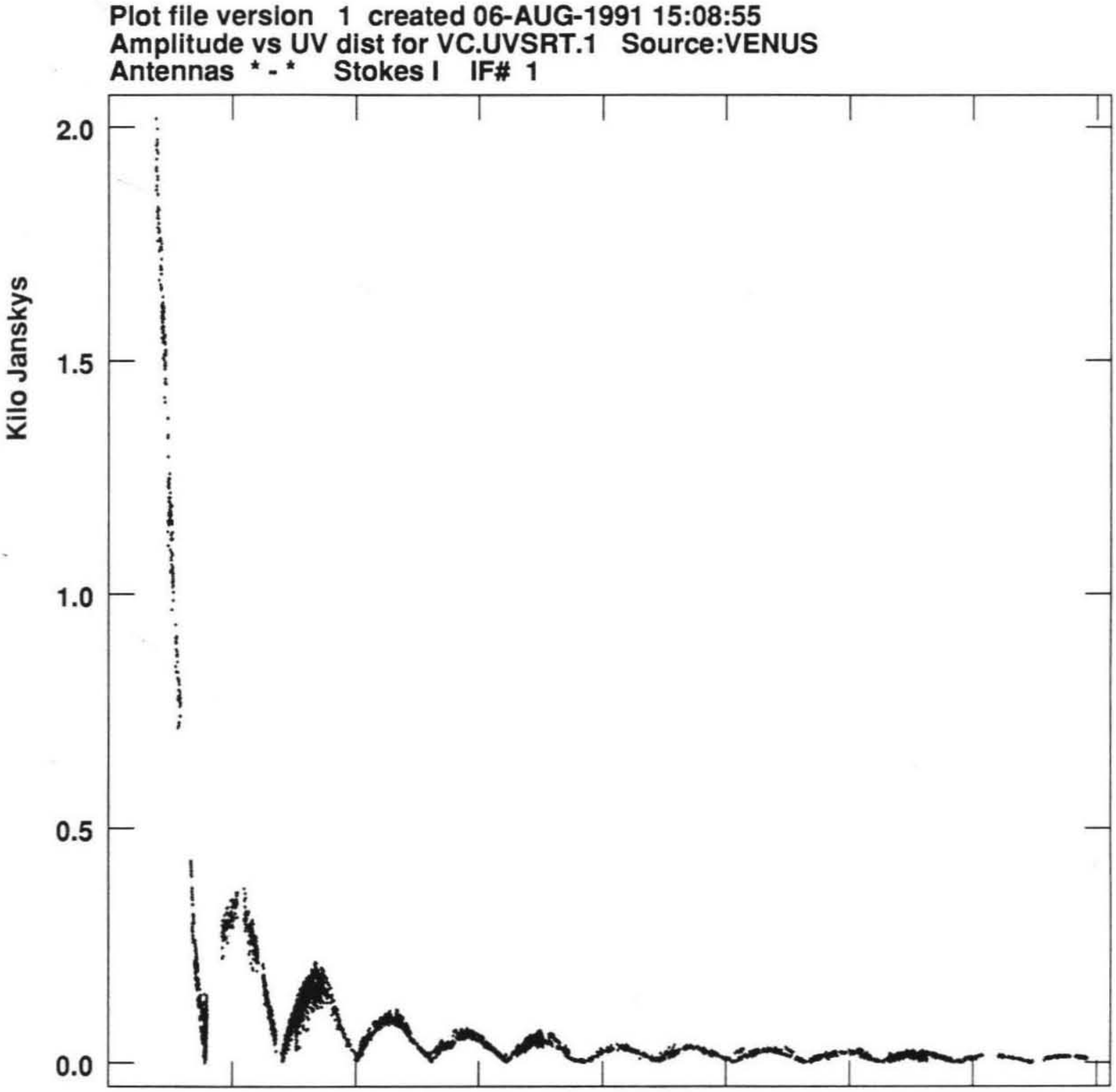

Figure 6. The broadband's visibility data is plotted in Bessel function form with visibility amplitude in kJy versus u-v distance in kilowavelength.

TABLE II

Delay Line Phase Corrections for the (100e,140n,100w) Track

Baseline	Delay 1<512 ns and Delay 2<512 ns	D1>512 ns and D2<512 ns	D1<512 ns and D2>512 ns	D1>512 ns and D2>512 ns
B12	0°	+12°	-73°	Did Not Occur
B23	0°	-83°	+63°	
B31	0°	+51°	0°	

Note. On notation, antenna 1 is at station 100 meters east, antenna 2 at 100 meters west and antenna 3 at 140 meters north. The delay on antenna 3 never exceeded 512 nanoseconds during the track, so this antenna's cables never added to the phase error.

Unfortunately the delay cables for the (100e,140n,100w) configuration were off by 0.3 m in length. Baseline lengths could not be solved for after the antennas were moved into this configuration. Instead, data was gathered to do the calculations after the observations and the delays recorded for each scan during the track. Baselines were later calculated by Dr Glenn Berge and each scan of the visibility phase data corrected by the phase corrections listed in Table II based on the combination of delay cables employed. Only the continuum band's visibility amplitude data required a correction factor due to its wide bandwidth. This correction factor was

$$factor = \left[\frac{\sin A\Delta\phi}{A\Delta\phi}\right]^{-1}, \tag{8}$$

where the constant A equalled 0.1481 and $\Delta\phi$ is the baseline dependent phase correction. The corresponding amplitude correction factors for the channel data were negligible given their much smaller bandwidths and were not applied.

3.2 Amplitude and Phase Calibration

During the observations, 3C84 served as the primary calibrator and, when this compact radio source fell below the horizon, P0851+202. The antennas were pointed to the calibrators for a scan (equal to 10 records or 5 minutes) after every four scans (equal to 20 minutes) on Venus. Both of the radio sources were used to

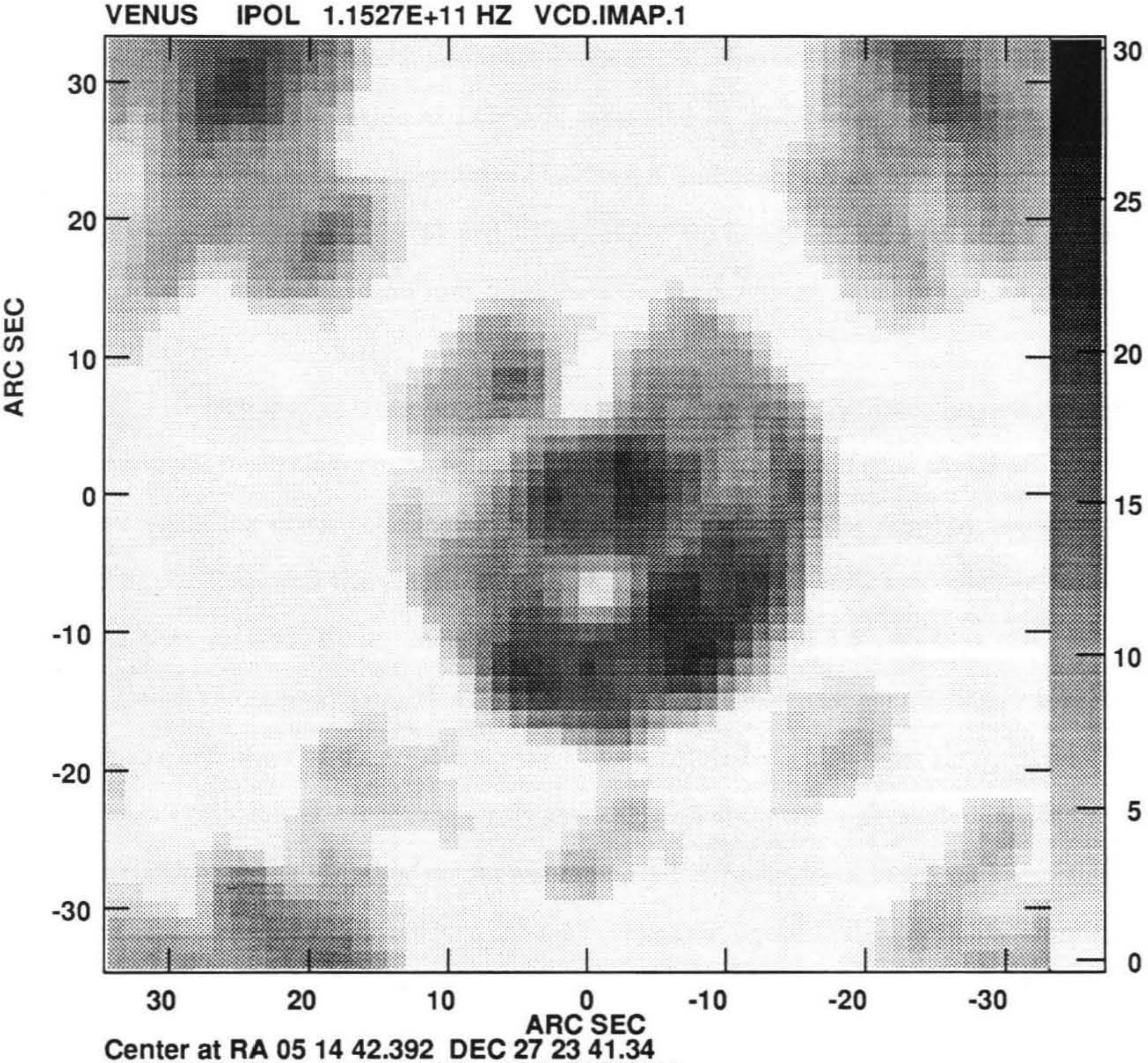

Figure 7. The dirty continuum brightness map in Jy/beam brightness units is plotted against right ascension and declination in arcseconds.

do phase calibration. Only 3C84 was used for amplitude calibration. It had a flux density of 15±.3 Jansky as calculated from bootstrapping with scans on Mars. Mars' brightness temperature of 204±5 K (99.2 Jansky) at 2.6 mm and at a planetocentric orbital longitude of 187 L_s came from the thermal model described by Rudy (1987). As a further check on amplitude calibration, Uranus had a brightness temperature of 116±10 K based on the scans made during this observation period, providing good agreement with the value of 122±5 K measured by Muhleman and Berge (1991) at 2.66 mm. Brightness temperatures of 125±9 K and 134±4 K at 3.33 mm as measured by Ulich and Conklin (1976) and Ulich (1981) are in agreement with the Muhleman and Berge value based on mm-brightness curves for this planet presented in Orton *et al.* (1986).

Before fourier transforming the visibility data into brightness images, the data from each observing run were normalized to the reference day of April 30 and the corresponding distance of 0.4995 AU. This normalization was done by rescaling the (u,v) positions and the amplitude of each visibility to this distance. Each set of data was then rotated, by an angle which ranged from 3.3° to 5.5°, so that the position angle of Venus was zero. Hence, Figure 5, which shows the complete u-v sampling for the four days of observations, has ellipses rotated slightly from the vertical. The planet's rotation axis is consequently vertical in all of the maps presented in this thesis. Next, 43 extreme visibility points were removed from the data based on inspection of the continuum data plotted as a Bessel function or, equivalently, visibility amplitude versus u-v distance (Fig. 6). This is a standard method of examining planetary data since the visibility function of an ellipse of uniform brightness is given by

$$V(\beta) = \frac{J_1(2\pi\beta)}{\pi\beta} F_\circ, \tag{9}$$

where J_1 if the first Bessel function, $F_\circ$ the total flux density of the disk and β a dimensionless parameter. β expresses the spacing of the interferometer and the angular radius of the planet

$$\beta = \frac{R}{d}(u^2 + v^2)^{1/2}, \tag{10}$$

with $(u^2 + v^2)^{1/2}$ the u-v distance, R the planet radius and d the distance from the array to the planet. Clipping spurious visibility points by this inspection method left 7100 visibility points in the continuum and in each channel to transform into brightness maps.

4. Mapping with CLEAN deconvolution

When doing the fourier transform from visibility u-v space to brightness x-y space, an algorithm works with a limited sampling of noisy u-v visibility points to create the brightness map in x-y space. The fourier transform of the visibility weighted by the u-v sampling, S(u,v), gives the "dirty" brightness map of the observed object

$$B_D(x,y) = \int_{-\infty}^{\infty}\int_{-\infty}^{\infty} S(u,v)\,V(u,v)e^{2\pi i(ux+vy)}\,du\,dv. \tag{11}$$

This dirty map will have features restricted in size from a minimum on the order of 1/maximum(u,v) to a maximum on the order of 1/minimum(u,v). The "dirty" brightness map of the object is related to the "true" brightness map, B(x,y), by the convolution

$$B_D(x,y), = B(x,y) * b(x,y), \tag{12}$$

where b(x,y) is the synthesized beam of the observations. A less mathematical look at this problem uses the fact that the transform of u-v sampling is the synthesized "dirty" beam of the array. This beam has sidelobes around the central peak response which distort the "true" brightness map of the source. Our synthesized beam, for example, had sidelobes as strong as 25% (see Fig. 3). The positive and negative sidelobes move flux from one point on the disk to a second point on the disk or a second point off the disk in empty space (see Fig. 7 of dirty continuum map).

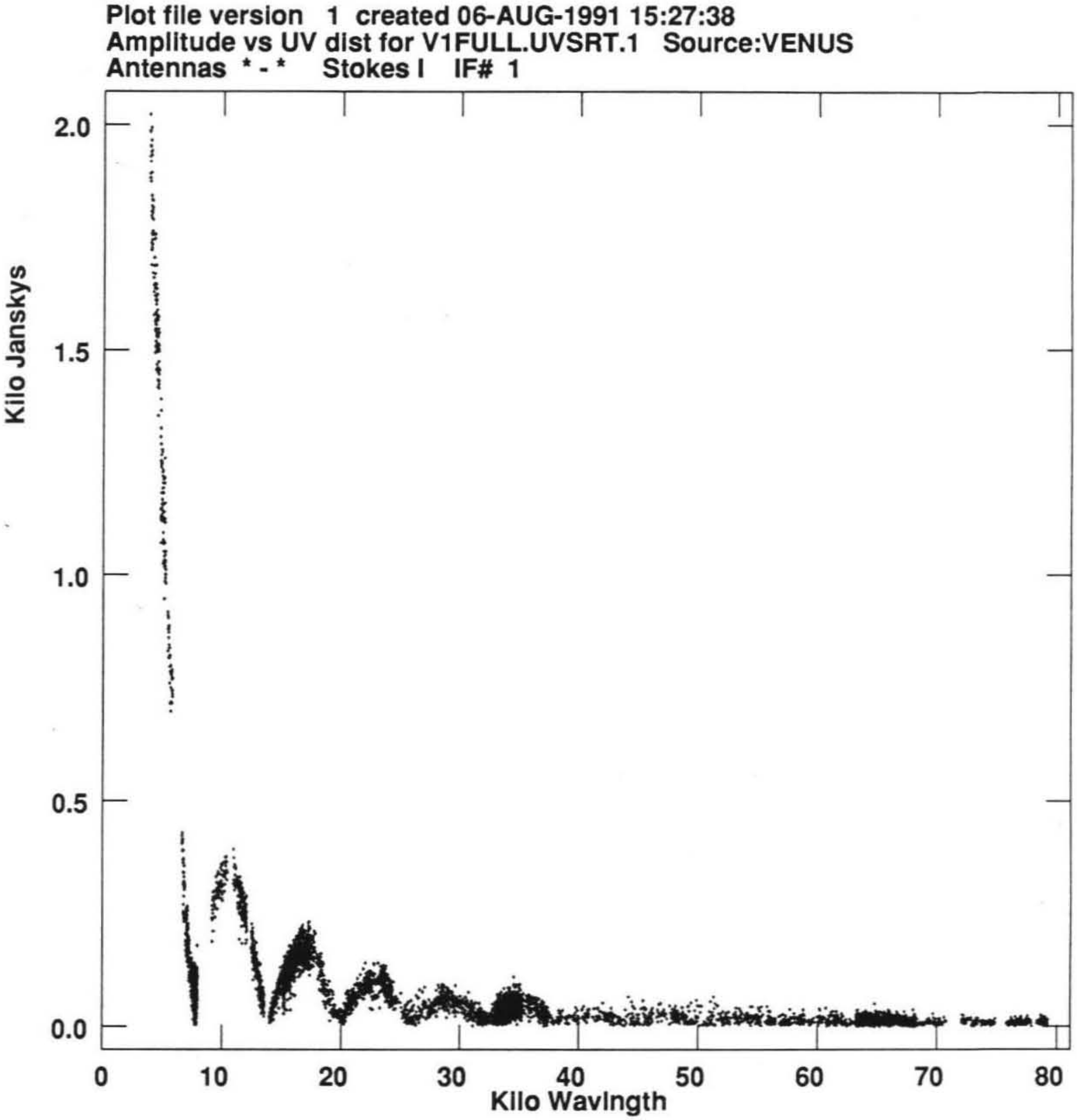

Figure 8. The 1 MHz channel 1 visibility data plotted as a Bessel function – the 50 kHz channels' Bessel functions are less distinct.

One typically removes these dirty beam effects with an algorithm such as CLEAN, available in the National Radio Astronomy Observatory's software the Astronomical Image Process System (AIPS). This is a widely accepted algorithm which uses known information, the shape of the synthesized dirty beam, to deconvolve the dirty beam from the true map. The deconvolution proceeds iteratively, pulling out peaks in a map's flux distribution (called CLEAN components) until a noise-level residual map is reached. The CLEAN components are then convolved with a Gaussian beam (a CLEAN beam) and added together to produce the brightness map of the observed source.

Though originally designed for point sources, the algorithm can be applied successfully to extended sources given an initial model of the object – in our case, a uniform bright disk at Venus' known position in the map. The bright model disk has a total flux equal to the flux which would be measured by a single dish antenna, called the "zero-spacing" flux. Thus, the model effectively fills in the zero-spacing flux missing from an interferometer's u-v visibility distribution (i.e., the hole in coverage at small u-v values in Fig. 5 and the breakoff to the Bessel function at small kilowavelength values in Fig. 6).

It is conventional, when working with multi-frequency radio data, to first develop optimal CLEAN parameters with the continuum, broadband data set and then use the same parameters on channel data. The broadband data has much less random thermal noise attached to it (see, e.g., the relatively distinct continuum Bessel function in Figure 6 versus the channel Bessel functions of Figure 8). Similarly, the phase self-calibration, discussed below, was calculated with the continuum data.

We applied CLEAN to our continuum visibility data with an initial model of a uniform, 2700 Jy (330 K) disk for the iterative removal of CLEAN components. The iterations continued until even numbers of positive and negative, noise-magnitude

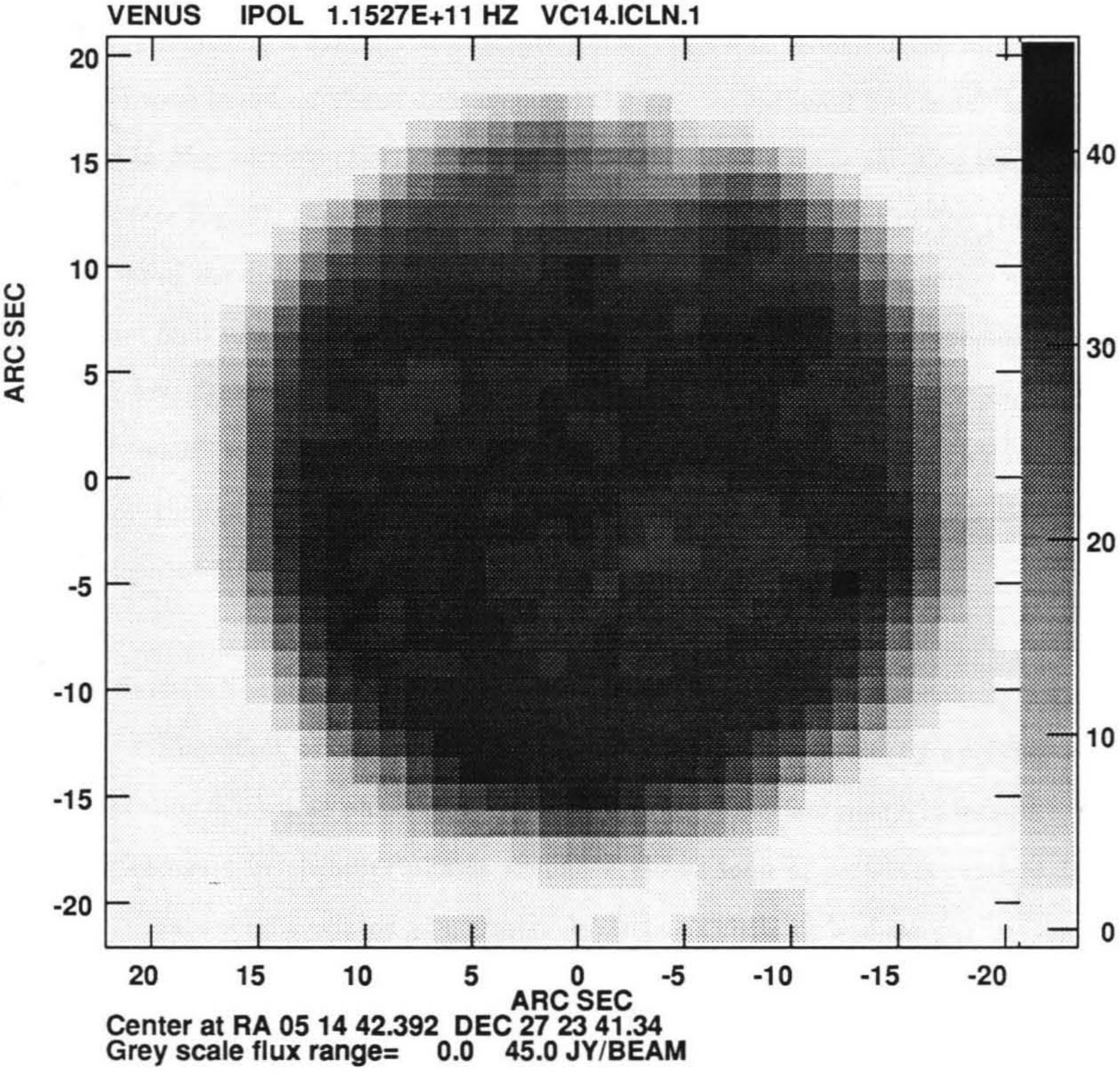

Figure 9. The CLEAN continuum map before self-calibration was applied.

components were being pulled out of the data. The CLEAN components were added to this residual map at the spatial resolution, or pixel size, of 1."25 and weighted with a Gaussian CLEAN beam of 3" FWHM. The same CLEAN procedure was then used on the 50 kHz and 1 MHz filterbank channel visibility data. The channels' inputed uniform disks decreased in flux from the outermost channels to the innermost channels, simulating a symmetric absorption line. The flux levels for the initial uniform disks were based on Venus disk-averaged CO spectra gathered by Clancy and Muhleman in May of 1988 (1991). CLEAN yielded brightness maps showing the planetary disk (see Fig. 9). However, in each map, there was small amount of flux (roughly 100 Jy) off of the disk (roughly 3100 Jy) where there should have been empty space. The higher final total flux of 3100 Jy for the continuum disk was not unexpected since the CLEAN algorithm is not highly constrained by the zero-spacing flux provided and can "walk" to higher total fluxes. The displacement of flux off the disk into empty space, though, indicated that unknown and relatively small phase noise was present in the visibility data, creating residual beam effects.

5. Self-Calibration

The effect of noise in the visibility data can be reduced by applying a self-calibration known as phase closure. Early in radio interferometry, it was recognized that the sum of visibility phases around a closed loop of baselines remains free of individual antenna-related gain errors. A baseline's visibility's phase can be expressed as

$$\phi_{ij,obs}(t) = \phi_{ij,true}(t) + \theta_i(t) + \theta_j(t) + noise, \tag{13}$$

where i, j denote individual antennas and θ_i(t) is the phase gain from an individual antenna. A loop of baselines with antennas i, j, k is then characterized by a quantity

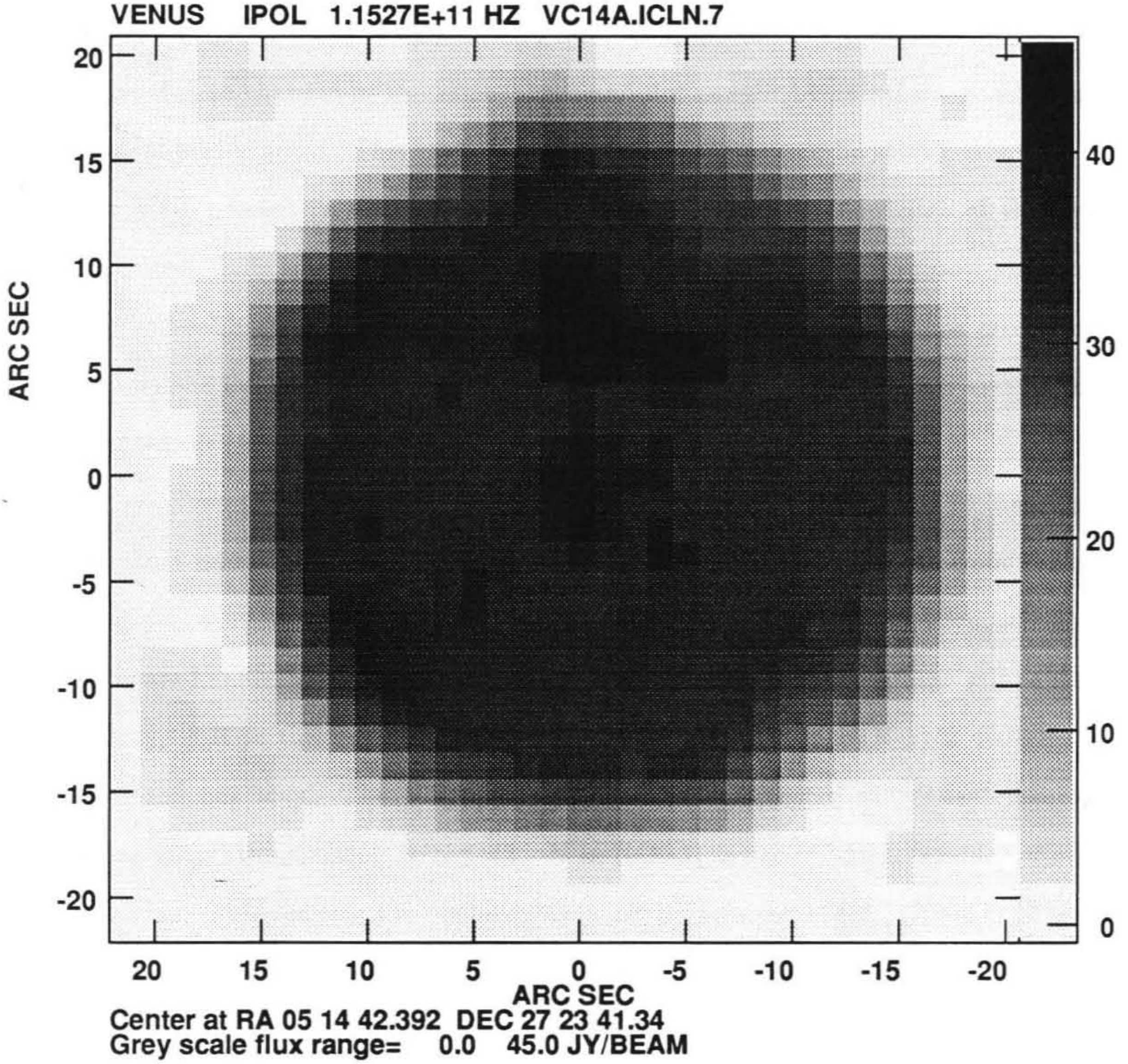

Figure 10. The CLEAN continuum map after self-calibration was applied.

called closure phase $C_{ijk,obs}(t)$

$$\begin{aligned} C_{ijk,obs}(t) &= \phi_{ij,obs}(t) + \phi_{jk,obs}(t) + \phi_{ki,obs}(t) \\ &= \phi_{ij,true}(t) + \phi_{jk,true}(t) + \phi_{ki,true}(t) + noise \\ &= C_{ijk,true}(t) + noise \end{aligned} \tag{14}$$

(Jennison 1953, 1958). Phase closure removes short term variations in antenna phase gains due to changes in the atmosphere and not caught by gain corrections based on the calibrator scans. This method requires that the source be strong compared with the noise present in the map and that there be a priori knowledge of the source's structure. This is easy with a planet as its structure is mainly a smooth, bright disk. We self-calibrated only the phase portion of the data – since phase errors usually distort the final map much more than amplitude errors and since our array had only 3 antennas (too few for amplitude calibration).

Even though the OVRO array has only 3 antennas and seems to just meet the required number of antennas, it is possible to phase calibrate data from this array. One gets around the problem of the smallness of the OVRO array because computer software handles visibility data at the record, not scan, level. In phase self-calibration theory, if N is the number of antennas in an array, then N(N-1)/2 visibilities are recorded per scan. The N antenna gains can be corrected via phase closure with these visibilities, leaving N(N-1)/2 - N = N(N-3)/2 "good" and "usable" visibilities per scan. This reduces the visibility data set by a factor of (N-3)/(N-1). Given only 3 antennas in the array, then there are no "good", "usable" visibilities left after the gain calculations - if one works at the scan level. In the AIPS software, though, one can work with the visibility points at the record level and set up a time interval over which visibility points are averaged together to do the gain calculation. During our phase self-calibration, a time interval of 8 minutes was used for the gain corrections. The records were 30 seconds long, so the self-calibration method used 16 visibility measurements to calculate 3 antenna gain corrections. Therefore, we reduced our "usable" visibility data by a factor of (16-3)/16 or by 18.8%. Furthermore, we only changed the phase component of the complex visibility data. The "usable" visibility data is then actually reduced by 9.4%, safely leaving behind a considerable amount of "usable" visibility data.

Besides using enough visibility points in doing correction of the antenna gains and having a priori knowledge of the source, it's necessary to have a strong source or, more specifically, a high signal-to-noise ratio to do the self-calibration correctly. As mentioned above, Venus had 3100 Jy total flux in the continuum brightness map with only 10-15 Jy of noise in empty space about it. The self-calibration used a simple model of a uniform disk with the same total flux in the phase corrections. Only 235 points of the 7100 visibility points had antenna phase gain corrections calculated in the first self-calibration iteration – only 3.4% of the data. The second and third iterations had 10-15 antenna phase gain corrections with small sizes under 5° on average. These relatively limited changes to the phase visibility data evened the edges of the planetary disk in the new CLEAN map and pulled more flux onto the disk from known empty space (see Fig. 10). As the gain corrections improved the image slightly, they were then applied to the channel visibility data. The channel data were then re-CLEANed into brightness maps. Further detailed discussion of phase noise, CLEAN and self-calibration with respect to planetary sources is given in Berge *et al.* (1988), Rudy *et al.* (1987), Schloerb *et al.* (1979) and the NRAO handbook on synthesis imaging edited by Perley *et al.* (1989).

6. Spectral Cubes

At this point in the data reduction, the 400 MHz broadband channel's continuum map was a "finished" result. The 1 MHz and 50 kHz channel maps, however, went through several more reduction steps. The particular steps depended on whether

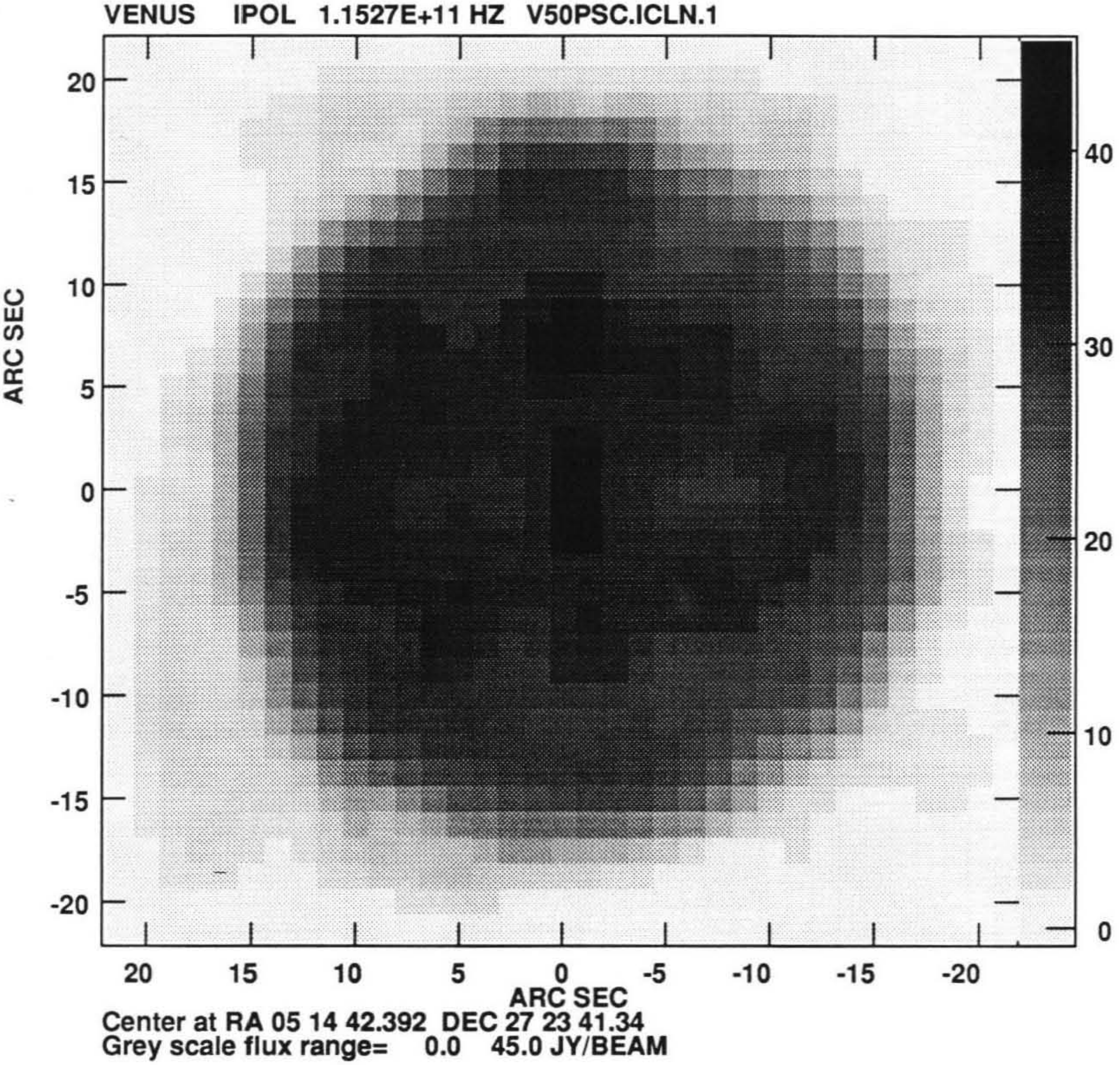

Figure 11. This pseudo-continuum map is an average of 50 kHz filterbank's channel 1, 2 ,30 and 32 brightness maps.

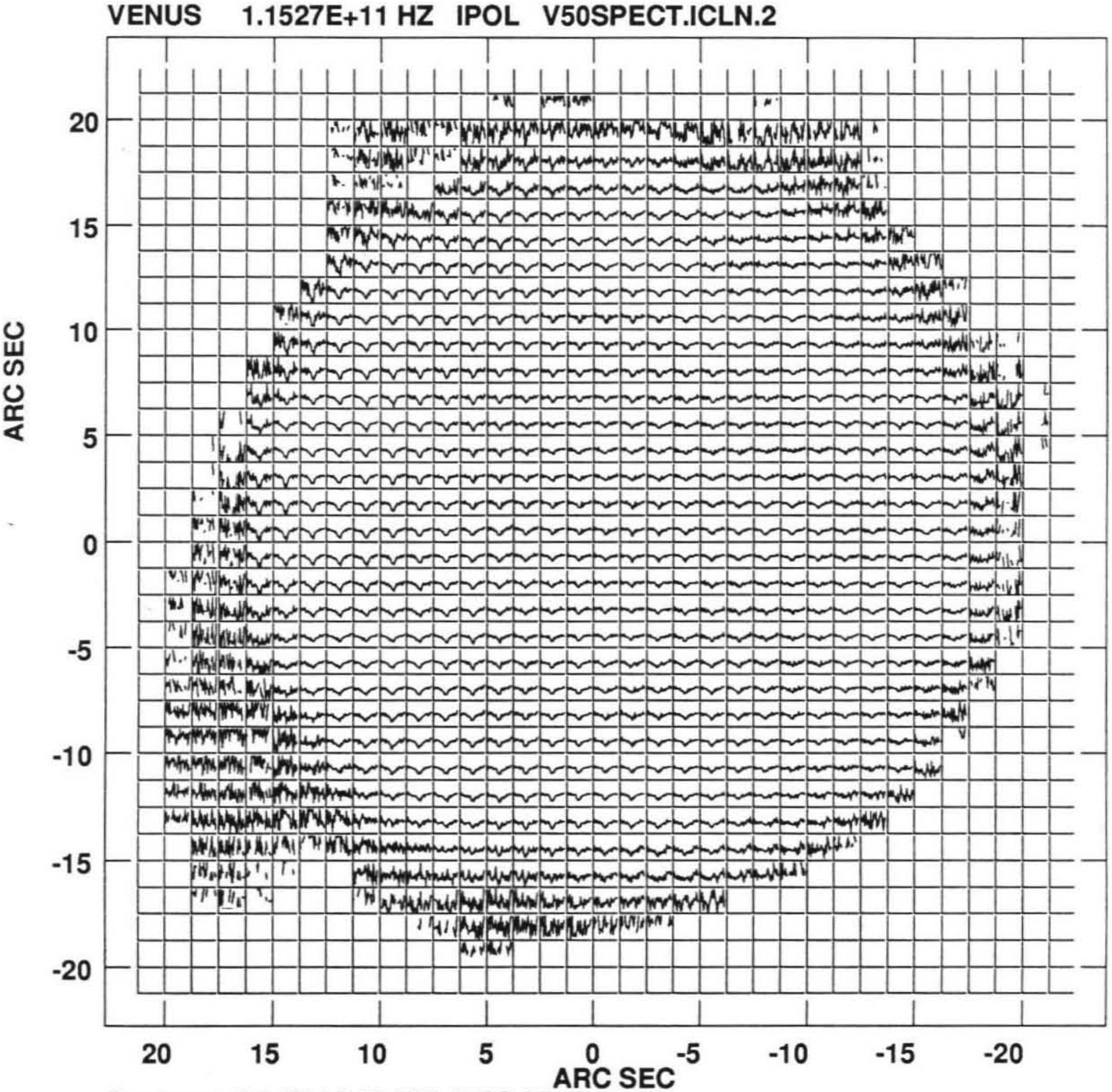

Figure 12. Each cell across the planet contains the CO absorption line at that cell's latitude and local time of day in 1988.

the final goal was the doppler shift analysis of Chapter IV or the CO abundance analysis of Chapter V. The filterbanks' maps were pulled into spectral cubes (described below), then any baseline ramping was possibly corrected, then the CO lines were possibly normalized for conventional line-to-continuum units, then local CO absorption lines were possibly extracted with averaging over declination (latitude) and right ascension (longitude or local time) from these cubes and then the extracted 1 MHz and 50 kHz lines were possibly merged together.

With a brightness map from each of the 32 narrowband channels, it was possible with the NRAO software to manipulate these maps into a cube. Each of the two dimensional, channel brightness maps with axes of declination versus right ascension were "lined up" by frequency. This three dimensional cube then had axes of frequency, right ascension and declination. The brightness could then be sampled along the frequency axis at a specific right ascension (local time) and declination (latitude) point. The brightness distribution over frequency at a point would be the CO absorption line at that point. This method of sampling the cube could thus generate a plot of the disk of Venus filled with cells at the pixel size of $1.''25$. Each cell would contain the local CO absorption line against axes of line-to-continuum ratio versus frequency.

For the wind analysis of Chapter IV, the 50 kHz channel maps were normalized by a pseudo-continuum map formed from an average of the four end channel maps, channels 1, 2, 31 and 32 from the filterbank. The pseudo-continuum map, shown in Fig. 11, has some uneven patches of higher flux on top of the typical limb-darkened disk. These roughly 10% higher flux patches were created partly from residual sidelobe effects and partly from organized noise in the filterbank data hidden by the random thermal noise associated with narrower frequency channels. This brightness distribution characterizes each 50 kHz channel brightness map and is not as smooth

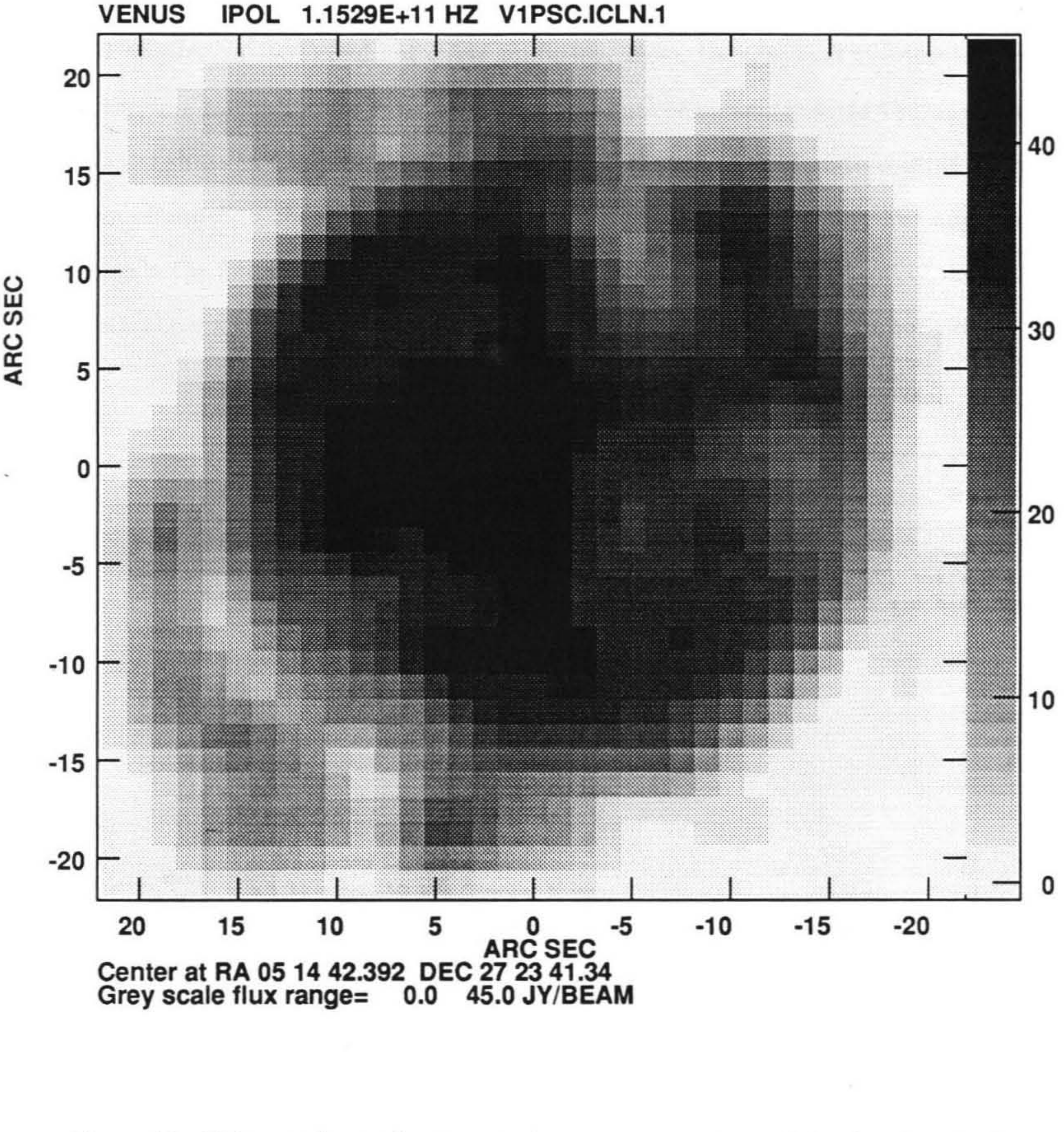

Figure 13. This pseudo-continuum map is an average of the 1 MHz filterbank's channel 1, 2, 30 and 32 brightness maps.

as the broadband continuum map. Hence, a pseudo-continuum map and not the broadband continuum map was used to normalize the channel brightness maps into the conventional, dimensionless line-to-continuum ratio for spectra. The maps were then scaled down by a factor of 0.88 so that the end channels at $\nu_o \pm .4$ MHz would have line-to-continuum ratios consistent with the disk-averaged CO spectra (Clancy and Muhleman 1991) and not cause confusion. Note, though, that the absolute value of the line-to-continuum ratio in a given channel is meaningless to the analysis for doppler shifts in Chapter IV. Only the relative change of the line-to-continuum ratio from channel to channel or, equivalently, the absorption lineshape has any significance in the following analysis. The local CO line cores were pulled out of the 50 kHz spectral data cube with a running average over three cells applied in both right

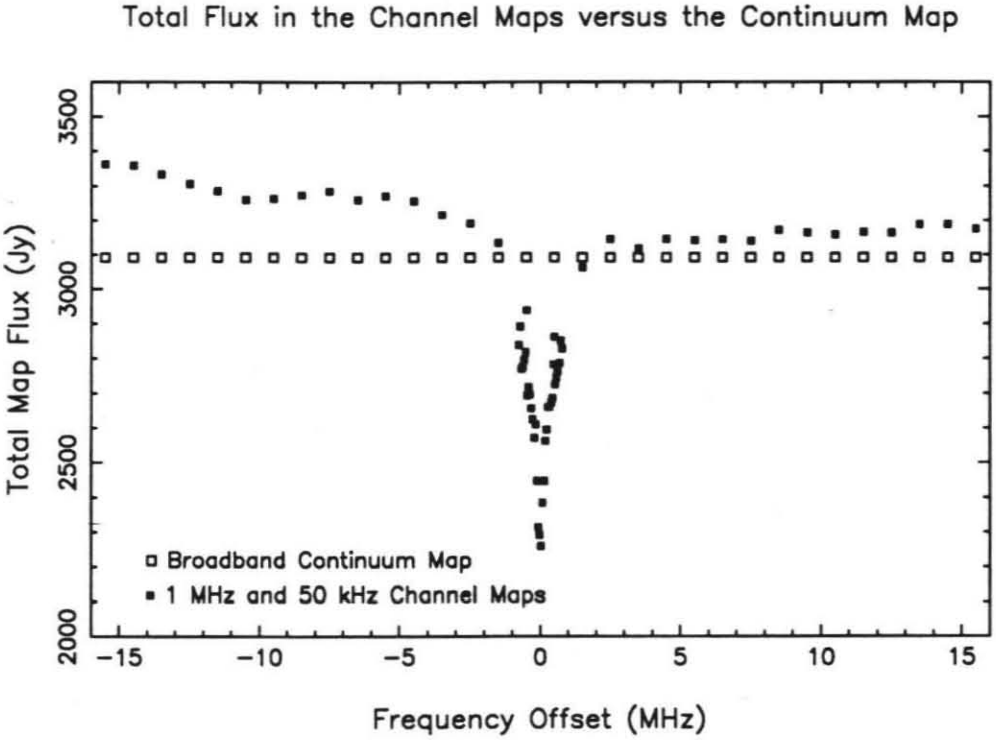

Figure 14. Total flux in the brightness maps.

ascension and declination. A normalized triangular filter was used in this running average to achieve a spatial resolution approximately matching that of the synthesized beam, but sampling at the finer pixel level of 1."25. This yielded 533 spectra across the planet as shown in Figure 12 which were then analyzed for doppler shifts (see Chapter IV).

For the CO abundance work of Chapter V, the 1 MHz and 50 kHz spectra had to be correctly merged. There were two complications to overcome in order to merge the channel data. First, the channel brightness maps, as discussed in the previous paragraph, had patchy brightness distributions caused by beam effects and thermal noise in the filterbank channels. Moreover, this noise brightness distribution was different for the two filterbanks. Figure 11 shows a pseudo-continuum map formed from the end channel maps of the 50 kHz filterbank and Figure 13 shows the counterpart from the 1 MHz filterbank. Secondly, the total fluxes in the different bandwidth maps were not in agreement. The total flux in these channels maps fall sensibly together over frequency as shown in Figure 14 and have a disk-average linedepth of 31%. This agrees roughly with Clancy and Muhleman's (1991) single-dish linedepth of 26% since the single-dish observations used wider channels of 250 kHz which would average the inner 5 channels' fluxes of the OVRO 50 kHz filterbank data. The baseline ramping present in Figure 14 came from the 1 MHz channel maps. 19% of CO lines across the planet disk had to be corrected for baseline ramping by doing a linear fit and subtracting out the baseline slope. The largest baseline ramp was 13% over the 32 channels or 7 Jy/beam on a dc level of 55 Jy/beam. For this worst case, a slope of 220±26 nanoJy/beam/Hz was removed. The 50 kHz spectra did not suffer any baseline ramping. More importantly, though, the total map fluxes were roughly 6% higher in channels out on the wings of the absorption line, channels experiencing mainly nonresonant absorption, than the total flux of the broadband's continuum map. This 6% difference in total flux corresponds to roughly 23 K in brightness temperature – significantly outside the uncertainty range of 5-10 K allowed Venus' brightness temperature at 2.6mm.

The channel maps could not be normalized into line-to-continuum ratios with either the continuum map, a pseudo-continuum map from 1 MHz channels or a rescaled pseudo-continuum map from 50 kHz channels without introducing artifacts due to the lower total continuum flux and the filterbank-dependent noise brightness structure. Instead, the 1 MHz channel maps were rescaled to the line-to-continuum ratio in the 2.6 mm, single-dish CO absorption line gathered in 1988 at Kitt Peak Observatory by Clancy and Muhleman, 1991. This disk average CO line had an average line -to-continuum ratio of 0.9957 in the channels 15.5 MHz offset from line center. The OVRO 1 MHz absorption lines were pinned to this absorption value at $\nu_\circ \pm 15.5$ MHz. Then the 50 kHz lines were tied into the rescaled 1 MHz lines by averaging the 4 channels at ±0.575, 0.525, 0.475 and 0.425 MHz from the line center and rescaling by the ratio of the averaged 50 kHz channels to the 1 MHz channel at ±0.5 MHz from line center. The merged CO lines were then binned in 2.5 by 2.5 arcsecond cells (or 9° latitude by 40 minutes local time at the equator) and averaged to give 121 spectra across the planet for the CO inversion analysis (see Chapter V).

Chapter III Broadband Data: Continuum Brightness Map.

Continuum observations of a planet with a radio antenna(s) in a single polarization can yield either a disk-average brightness temperature (see Fig. 2), u-v visibility data described by equation (9) or, with enough sampling of the u-v plane, brightness maps. Disk-average brightness temperatures have been used to determine global absorber abundances. The first zero crossing of u-v visibility data, i.e., the first J_1 crossing reflects the apparent disk diameter and estimates the limb-darkening of the planet. Holding the greatest amount of spatial information, brightness maps can yield local distributions of continuum absorbers over latitude and longitude given an accurate microwave model of the atmosphere.

1. Continuum Map Brightness Features

A reliable brightness map of Venus' millimeter emission would be timely since Crisp *et al.* (1989) has just repeated Allen and Crawford's breakthrough near-infrared photometric observations of Venus' nightside (1984). These first maps of the nightside in narrow atmospheric windows enclosed by CO_2 and H_2O bands at wavelengths between 1 and 5 μm shows bright features moving with the cloudtop's zonal wind. These near-infrared features are brightest at 480 K and darkest at $\leq$430 K. It was suggested that these high contrast features originated in the hot lower atmosphere below 35 km and then passed through the cooler, higher atmosphere which had horizontal patchiness in opacity. The contrast features moved about the planet with a rotation period of roughly 6 days or at 70 ms^{-1} which indicated that the features formed in the middle region of the clouddeck. Therefore, the nightside features indicated that the Venus clouddeck may have partial clearings – a controversial idea upsetting conventional models of Venus' atmosphere. Partial clearings in the clouddeck would, for example, create leaks for thermal radiation in greenhouse models of

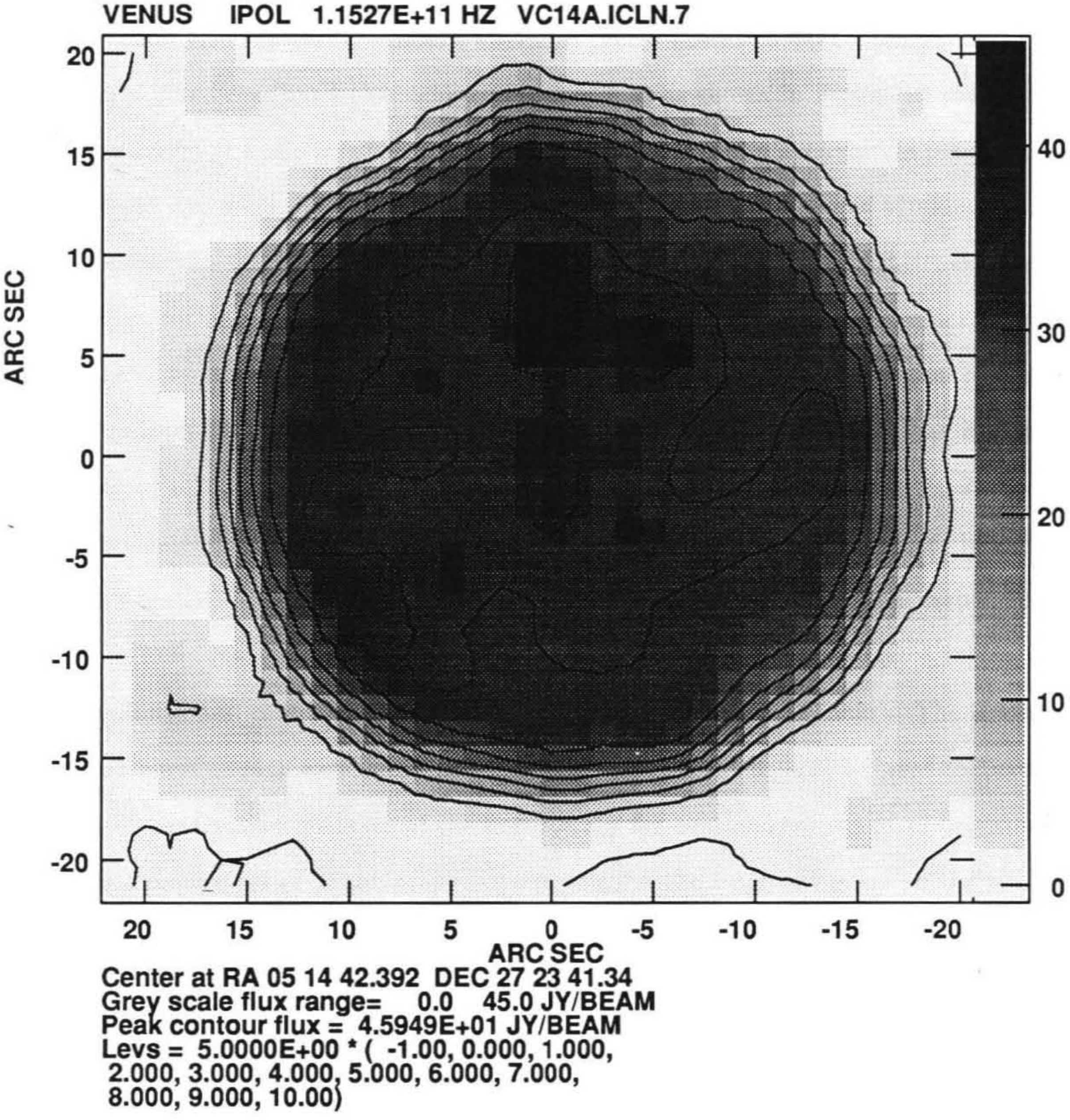

Figure 15. The broadband channel's 2.6 mm continuum map of Venus with contours at every 5 Jy/beam or, equivalently, every 51.1 K.

Venus' high surface temperature. Venus' thermal radiation is usually assumed, except in the ultraviolet, to be as smooth as a pool cue ball. Departures from a smooth, limb darkened disk in a millimeter brightness map of Venus would, therefore, add support to this idea of a horizontally-variable Venus clouddeck if the 2.6 mm continuum radiation also samples clouddeck altitudes over a limited height interval.

The broadband channel's continuum map is shown in Figure 15 with contour lines drawn at every 5 Jy/beam or at every 11% of the map's maximum pixel intensity of 45.95 Jy/beam. The 1.25" map pixels have a spatial footprint of 470 km at normal incidence on the planet which is convolved by the guassian 3" CLEAN beam present and smoothing map intensities over a footprint of 1050 km. The standard error on brightness in an aperture synthesis map is the rms deviations in a region of the map away from the observed object. The OVRO 1988 continuum map has a standard error of 0.703 Jy/beam or, equivalently, 7.2 K as 1 Jy/beam equals 10.22 K. This formal standard error of the map of 7 K is pleasingly low. However, it averages the negative and positive fluxes from residual beam effects in the map's "empty space" regions. These non-zero intensities in the maps' empty space region reach maximum and minimum flux densities of -2.07 and +1.95 Jy/beam. The average of these empty space extremes, ±2.01 Jy/beam or ±20.5 K, will be used instead as a more conservative estimate of the uncertainty for continuum map pixel brightnesses. The dynamic range of the map, i.e., the ratio of the brightest point to the standard error is 65 and is by definition an estimate of the quality of the map.

The continuum map does show deviations from a smooth, circularly-symmetric limb-darkened disk. The continuum disk has a high 40 Jy/beam peak north of the equator about the subearth longitude or local time of 7:20 PM and a second lower 40 Jy/beam peak south of the equator about 7:20 PM on top of a flat 35 Jy/beam, non-circular plateau. Also, the disk appears to be asymmetric. The nightside limb

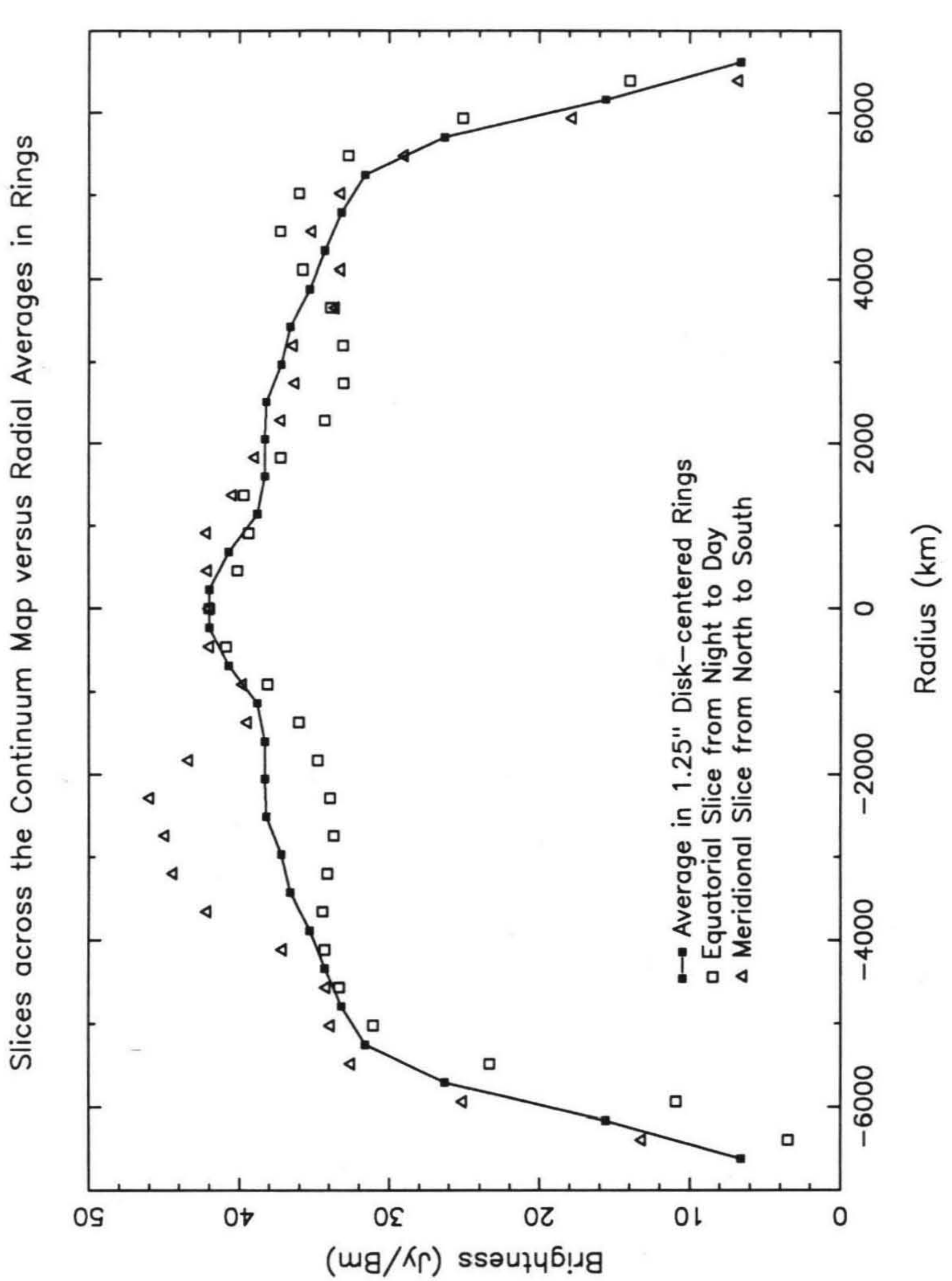

Figure 16. Sampling of the continuum map pixels in slices from night to day limb and from northern to southern limb versus map brightness azimuthally averaged.

appears to be more limb-darkened than the afternoon limb of the planet. To a lesser degree, the southern limb is also limb-darkened relative to the northern limb.

Figure 16 shows a plot of radial averages of the continuum map's intensity in disk-centered rings 1.25" wide versus slices across the map from night to day and from north to south. A slice is a line across the map which picks off the intensity in each pixel crossed without any averaging with surrounding pixels and is symmetric about zero radius. Negative radii correspond to nightside and northern radii while positive radii correspond to afternoon and southern radii. This view of the continuum map's brightness distribution emphasizes the strong local variations over radius versus the map's average intensities over radius. These localized surges and dips in brightness correspond to changes as large as 40-80 K from average brightness temperatures.

These brightness contrasts may seem, at first glance, to be in agreement with the near-infrared features. However, the nature of this continuum map must first be considered further - in particular, the small size of the array used to create this aperture synthesis map. With only three antennas in the array, residual beam effects form the synthesized beam's strong sidelobes (see Fig. 3) may still be present in the maps despite the CLEAN algorithm and self-calibration. Such artifacts are notable by their beam-related size and their symmetrical radial placement from the map center. The strong intensity features in the map are roughly 1-2 synthesized beams in size which may be real. However, the slices' 40-80 K intensity deviations do occur in suspiciously symmetrical placement about the disk center and, hence, appear to be brightness fluctuations due to residual beam effects which disappear in radial averaging.

The asymmetry of night versus afternoon limb-darkening is the second notable aspect of the continuum map. Unlike the northern versus southern limb-darkening contrast, the diurnal contrast in limb-darkening is present after averaging map pixels

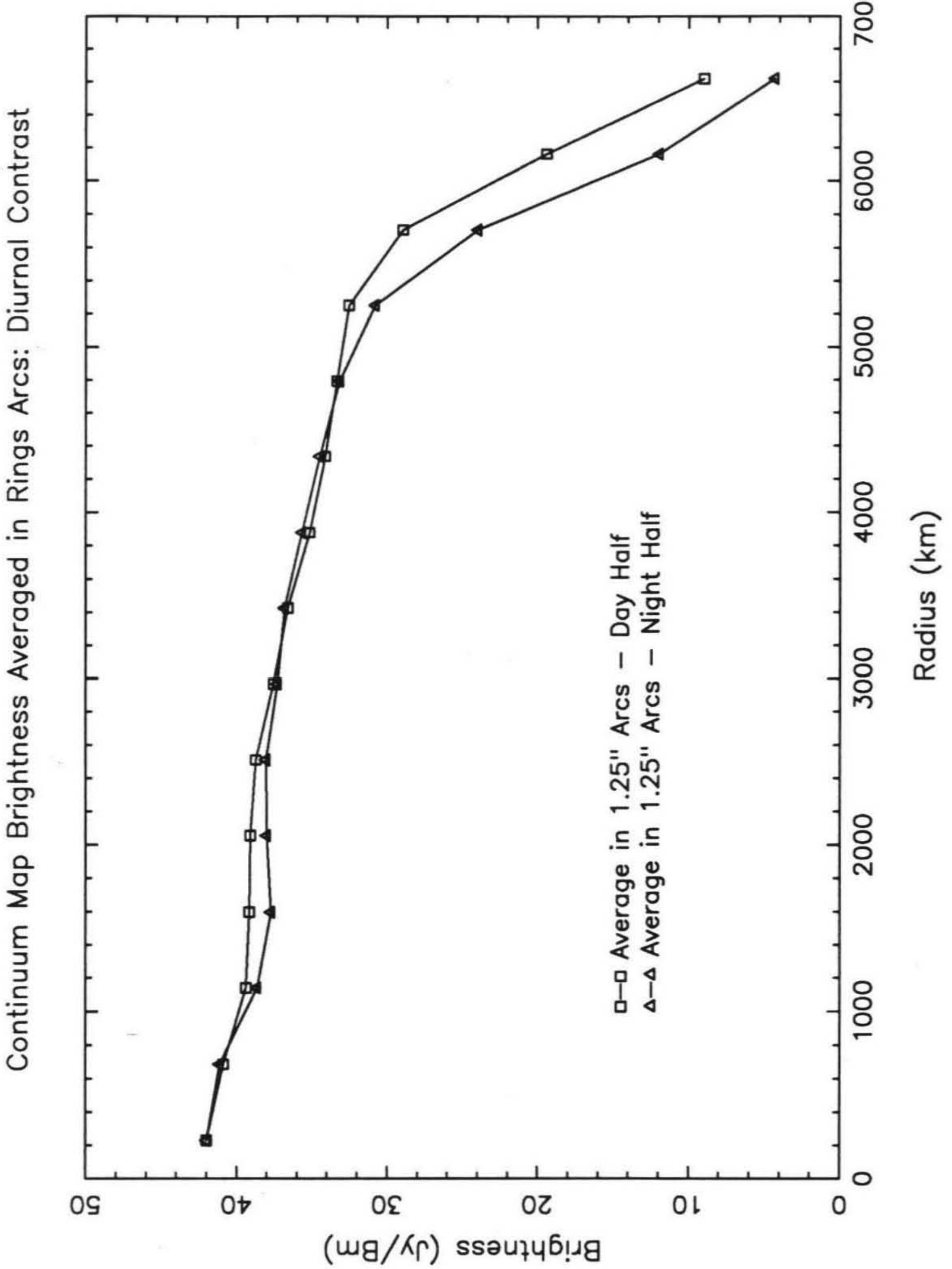

Figure 17. Diurnal differences in limb-darkening in the continuum map as measured in arcs 1.25" wide from the disk center.

in 1.25" wide half-rings or arcs with apexes at the equator. Figure 17 shows the average brightness in these arcs in the day half, i.e., the eastern hemisphere of the planet containing the evening and afternoon hours versus the night half, i.e., the western half of the planet containing nighttime hours. The difference in limb-darkening becomes pronounced at radii larger then 5000 km with, for example, a nightside limb brightness cooler by 18% than the afternoon limb brightness at a radius of 5700 km. In order to understand this difference in limb darkening further, 2.6 mm continuum weighting functions and limb-darkening curves were investigated with a radiative transfer model of Venus atmosphere.

2. Radiative Transfer Model with Continuum Absorption

The radiative transfer model used to calculate brightness temperature limb darkening curves and associated atmospheric weighting functions assumed a nonscattering atmosphere in local thermodynamic equilibrium. The haze and cloud particles observed by Pioneer Venus polarimetry do not effectively interact with millimeter radiation due to their small particle size of $\leq 8\mu$m (Kawabata *et al.* 1980; Knollenberg *et al.* 1980) so scattering can be neglected. In the millimeter wavelengths, a Rayleigh-Jeans approximation for the Planck source function B_ν can be used since $h\nu \ll kT$. The Planck function for a radiating object is then

$$B_\nu \equiv \frac{2h\nu^3}{c^2}\Big[\frac{1}{e^{\frac{h\nu}{kT}}-1}\Big] \simeq \frac{2kT\nu^2}{c^2}, \tag{15}$$

where B_ν is the brightness of the object at a frequency ν, k the Boltzmann constant, c the speed of light, and T the object's temperature. The Rayleigh-Jeans approximation overestimates thermal radiation by only 1% at 2.6mm. The equation of radiative transfer for a non-scattering atmosphere can therefore be simplified to

$$T_B(\nu,\mu) = T_\circ exp\Big(-\int_0^\infty k_{\nu,z}\frac{dz}{\mu}\Big) + \int_0^\infty k_{\nu,z}T(z)exp\Big(-\int_z^\infty k_{\nu,z'}\frac{dz'}{\mu}\Big)\frac{dz}{\mu}, \tag{16}$$

where μ is the atmospheric path length, $T_\circ$ the lower boundary brightness temperature and $k(\nu, z)$ the atmospheric absorption coefficient. Equation 16 expresses the thermal radiation from an atmosphere as a weighted average of the vertical temperature profile. The first term on the rightside is the surface continuum thermal emission transmitted through the atmosphere and the second term the thermal emission from the atmospheric layers. Quadrature of this brightness temperature integral was done along a ray path by dividing the atmosphere into layers of Δz thickness so

$$T_B(\nu,\mu) = T_\circ \prod_{n=1}^{nmax} exp(-k_n(\nu)\frac{\Delta z}{\mu}) + \sum_{n=1}^{nmax} T_n k_n(\nu)\frac{\Delta z}{\mu} \Pi_{i=n+1}^{nmax} exp(-k_n(\nu)\frac{\Delta z}{\mu}), \tag{17}$$

with

$$\mu(r) = \left[((\frac{r}{\Delta z})^2 cos^2\theta + 2\frac{r}{\Delta z} + 1)^{1/2} - \frac{r}{\Delta z}cos\theta\right]^{-1} \tag{18}$$

as the pathlength for each layer n with $nmax$ the top layer of the model atmosphere, r the radius on the planet and θ the angle from local normal.

This atmospheric model was based on a radiative transfer model of the Venus atmosphere developed by Duane Muhleman, Glenn Orton and Glenn Berge (1979) which was modified to correctly describe the atmosphere in the millimeter wavelengths and to include weighting of brightness temperatures by the 3" FWHM gaussian CLEAN beam. Appendix A gives details on the beam weight calculations. The model is circularly symmetric. Two models, one dayside and one nightside, were used to calculate T_B over the entire disk. Thus, any model results are referred to as "nightside" or "dayside" values. The model atmosphere includes pressure-induced continuum absorption by the primary constituent CO_2, continuum absorption by a cloud of SO_2 and resonant absorption by CO at its first rotational transition. The resonant CO absorption is unimportant for this chapter's analysis of the broadband continuum map and will be addressed later in Chapter IV and Chapter V. The CO_2

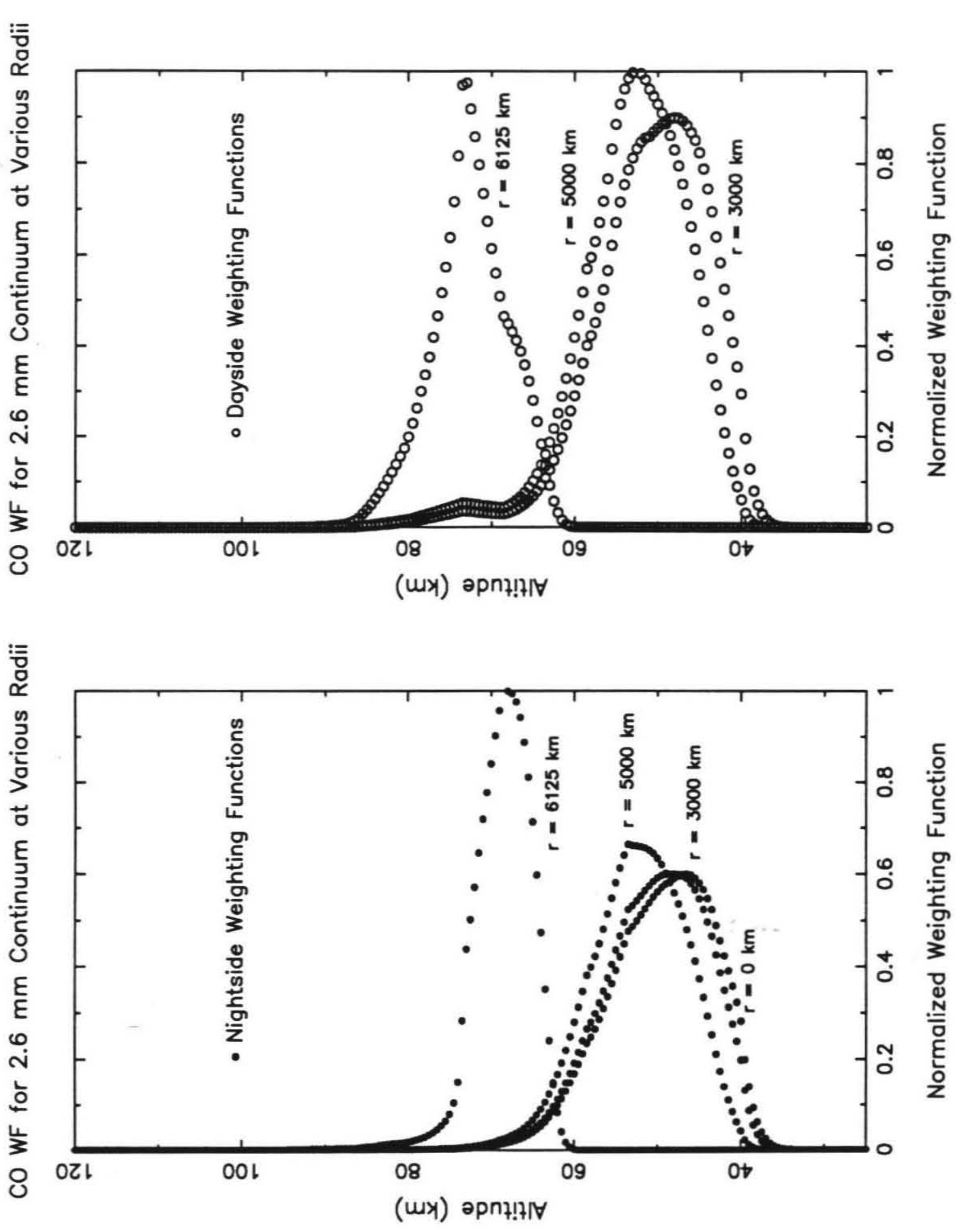

Figure 18. Model weighting functions averaged over the 400 MHz broadband channel and calculated with PV night and day atmospheric profiles at various radii.

absorption coefficient (km^{-1}) in the model,

$$k(\nu) = 1.57 \times 10^{-2} (\frac{p}{1\,\mathrm{atm}})^2 (\frac{273^\circ K}{T})^5 \nu^2 \tag{19}$$

came from high temperature and pressure laboratory measurements by Ho *et al.* (1966). The SO_2 absorption coefficient (km^{-1}) in the model is given by

$$k = 3.69 \times 10^6 \, q \, \nu^2 \, \frac{p^{1.22}}{T^{3.1}}, \tag{20}$$

with q the SO_2 volume mixing ratio and ν in GHz, coming from Janssen and Poynter's model of SO_2's rotational spectrum in moderate to high pressures (1981). A constant abundance of 185 ppm of SO_2 between 20 and 40 km which decreased exponentially with height above 40 km was assumed. Absorption coefficients were determined in each 0.5 km layer from the surface to 129 km with diurnal temperature, density and pressure profiles from Mariner 5 data below 85 km and from PV probe deceleration data above 85 km (see Fig. 1). The PV dayside data are from the 31°N, 6:46 AM probe and the nightside data from the 27°S, 0:07 AM probe.

The model calculates the brightness temperature at a given radius by radiation down through the atmosphere to the continuum or surface height and then upwards through the atmosphere until it exits. This method of integration over height is referred to as tracing the ray path of radiation through a non-scattering atmosphere. Refraction of radiation passing through the atmospheric layers was taken into account with Snell's law,

$$s = r\, n(r)\, sin(\phi(r)), \tag{21}$$

where s is the apparent distance from the disk center where a ray enters the atmosphere, $n(r)$ the local index of refraction given by the Lorentz-Lorenz relationship and $\phi(r)$ the angle of the ray from local normal in a layer. Venus' atmosphere critically refracts radiation entering at large radii near the planet limb with ϕ becoming $\pi/2$ in equation (21) and the radiation's ray only passing through outer atmospheric layers.

Radiation following this particular incoming ray gets bent increasingly until reaching the critically refracting layer. The ray skims through the critically refracting layer and then moves back up through high altitude layers, leaving the atmosphere. Using this ray-tracing of radiation, the brightness temperature was integrated at each radial gridpoint from the center of the disk to 5700 km with steps of 200 km, from 5700 km to 6085 km with steps of 100 km, and, at the limb, from 6085 to 6180 km with steps of 10 km.

The model gives a full-disk brightness temperature of 336 K for the nightside model and 334 K for the dayside model with an uncertainty of approximately ±10 K. The uncertainty arises from the uncertainty in atmospheric profiles, absorption coefficients and the Rayleigh-Jeans approximation. These disk average brightness temperatures are in agreement with the millimeter observations of Venus shown in Figure 2.

3. Models of Diurnal Limb-Darkening

The temperature weighting functions calculated with this radiative transfer model are described by

$$W_\nu(z,r) = k_\nu(z) exp(-\int_\infty^z k_\nu(z')\frac{dz'}{\mu}) \quad km^{-1} \tag{22}$$

and vary with frequency, height z, and radius from the disk center r with the pathlength μ given by equation (18). Figure 18 shows nightside and dayside average weighting functions over 400 MHz centered about μ_o at various radii. Across most of the disk, continuum radiation comes from a wide layer between 40-60 km containing most of the clouddeck and peaking at heights close to 50 km. Only along the planet limb, where critical refraction occurs, does the weighting function sample altitudes above the clouds and peak at heights around 70 km. This wide vertical sampling of the lower atmosphere, besides the smallness of the OVRO array, may have pre-

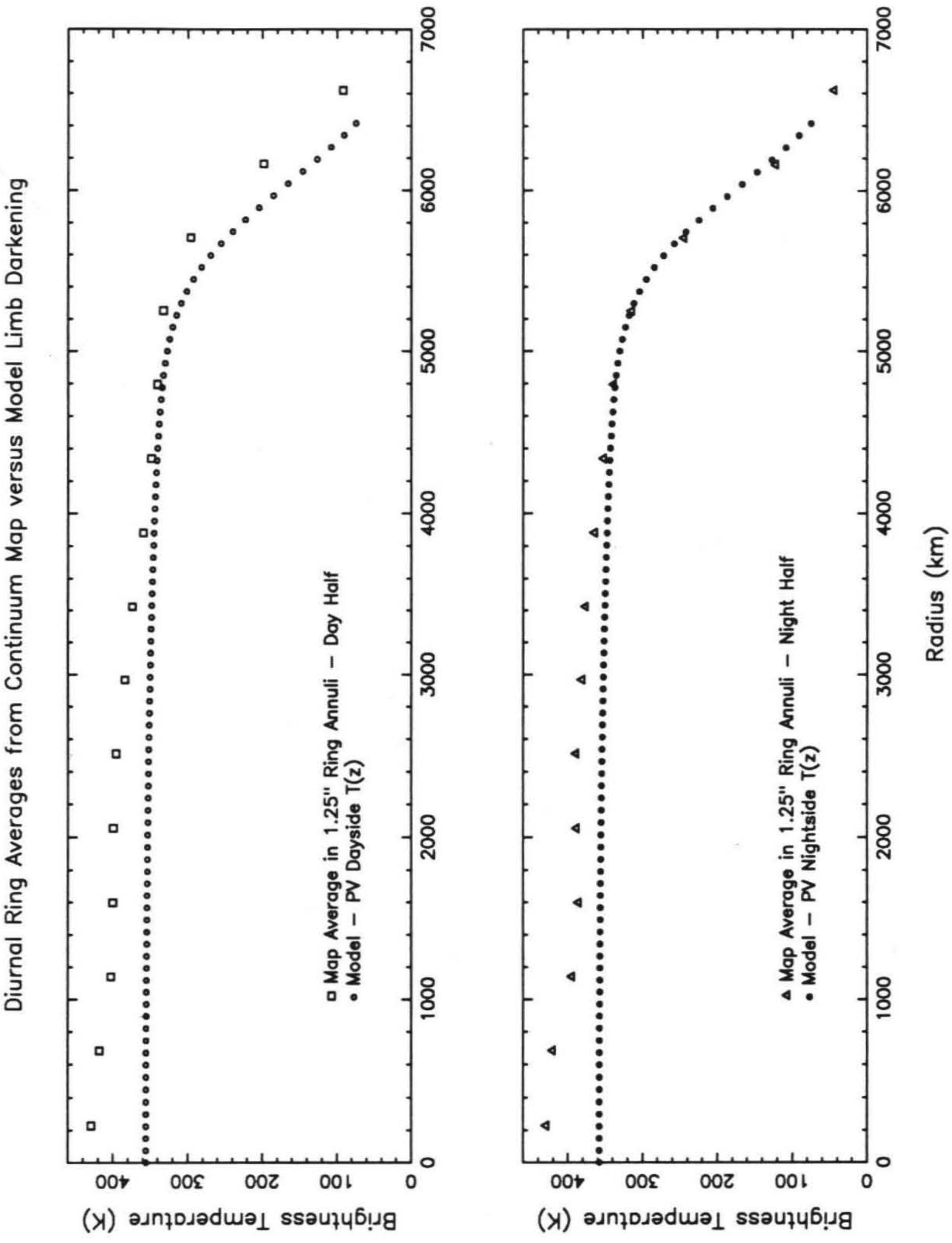

Figure 19. Model limb-darkening curves for both a PV nightside or dayside atmosphere are compared to 1.25" arc averages of the nightside and afternoon hemisphere of the continuum map.

vented detection of any resolved millimeter continuum brightness features similar to the near-infrared features mentioned earlier. In any case, the continuum map's limb-darkening can be expected to reflect mean conditions over a very wide crossection of the atmosphere between 45 and 75 km based on these weighting functions.

Figure 19 compares the model's brightness limb-darkening curves for nightside and dayside conditions to the 1.25" arc averages of the continuum map's nightside and afternoon hemispheres. The continuum map averages have been converted from Jy/beam to degrees Kelvin. The nightside and dayside map brightness temperatures are higher than the model temperatures despite map temperature uncertainties of ±20.5 K and model uncertainties of ±10 K. This was not unexpected as the absolute total flux value in an aperture synthesis map formed with CLEAN can drift as mentioned in section 4 on Mapping in Chapter II. The shape of the continuum map's limb-darkening, rather than the absolute value, provides a more useful comparison. The model dayside limb-darkening curve remains consistently lower than the map's afternoon averages unlike the model nightside limb-darkening curve. The continuum map's nightside radial averages, on the other hand, intersect the lower-valued nightside model limb-darkening at radii greater then 5000 km from disk center. The simplest interpretation of the model versus observed limb-darkening curves of Figure 19 is that the nightside limb of Venus experienced increased limb-darkening in the spring of 1988. While other interpretations may be viable, this one is the most straightforward and will be considered further.

The atmospheric model was next used to determine changes to the temperature profile in order to intensify the nightside limb-darkening at radii greater than 5000 km. Figure 20 compares the initial PV nightside model limb darkening in the top panel and a nightside model with increased limb darkening in the bottom panel to the continuum map's nightside average limb-darkening. The nightside temperature

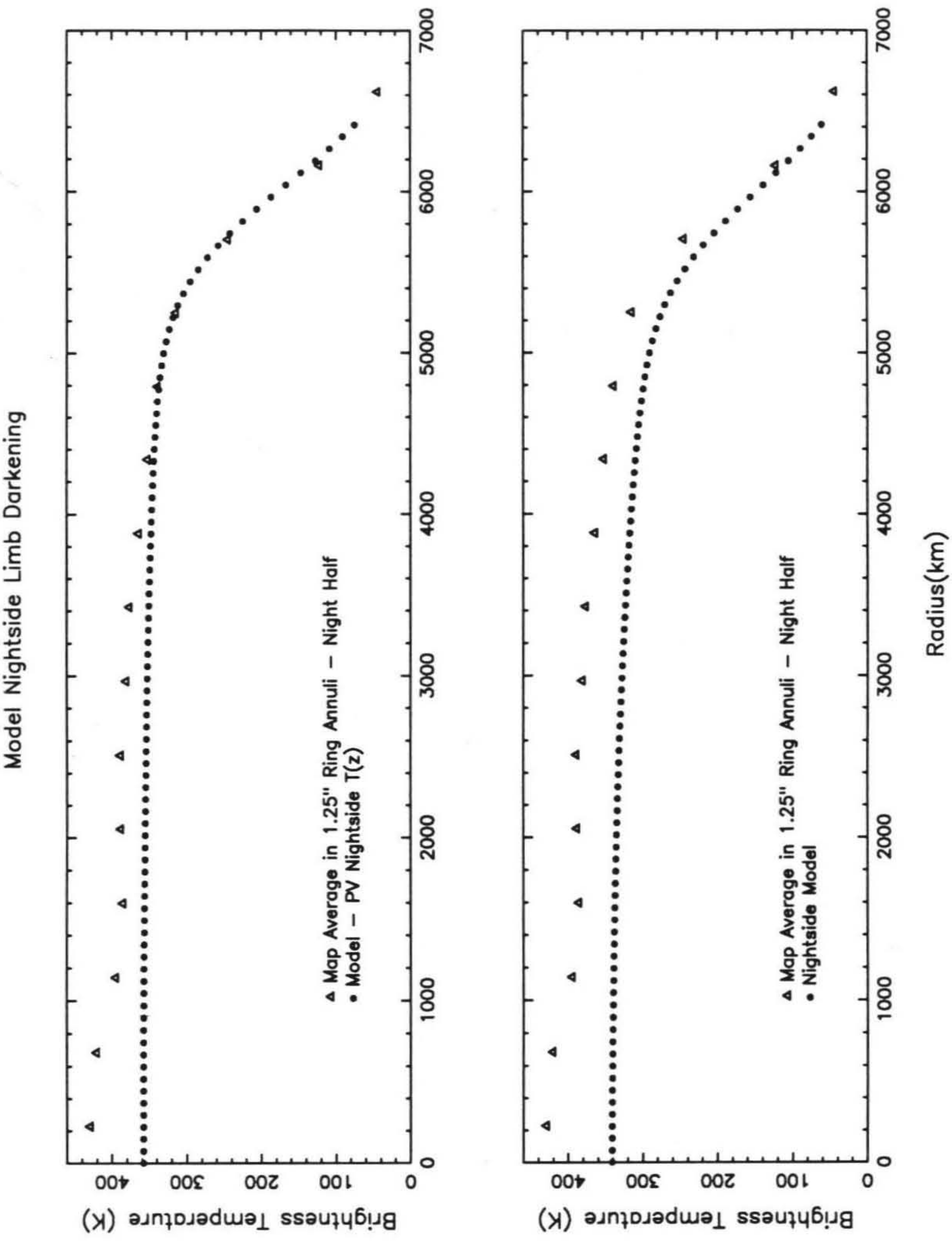

Figure 20. A nightside model with increased limb-darkening is compared to the initial PV nightside model in the top panel and to the continuum map's average nightside limb-darkening in the bottom panel.

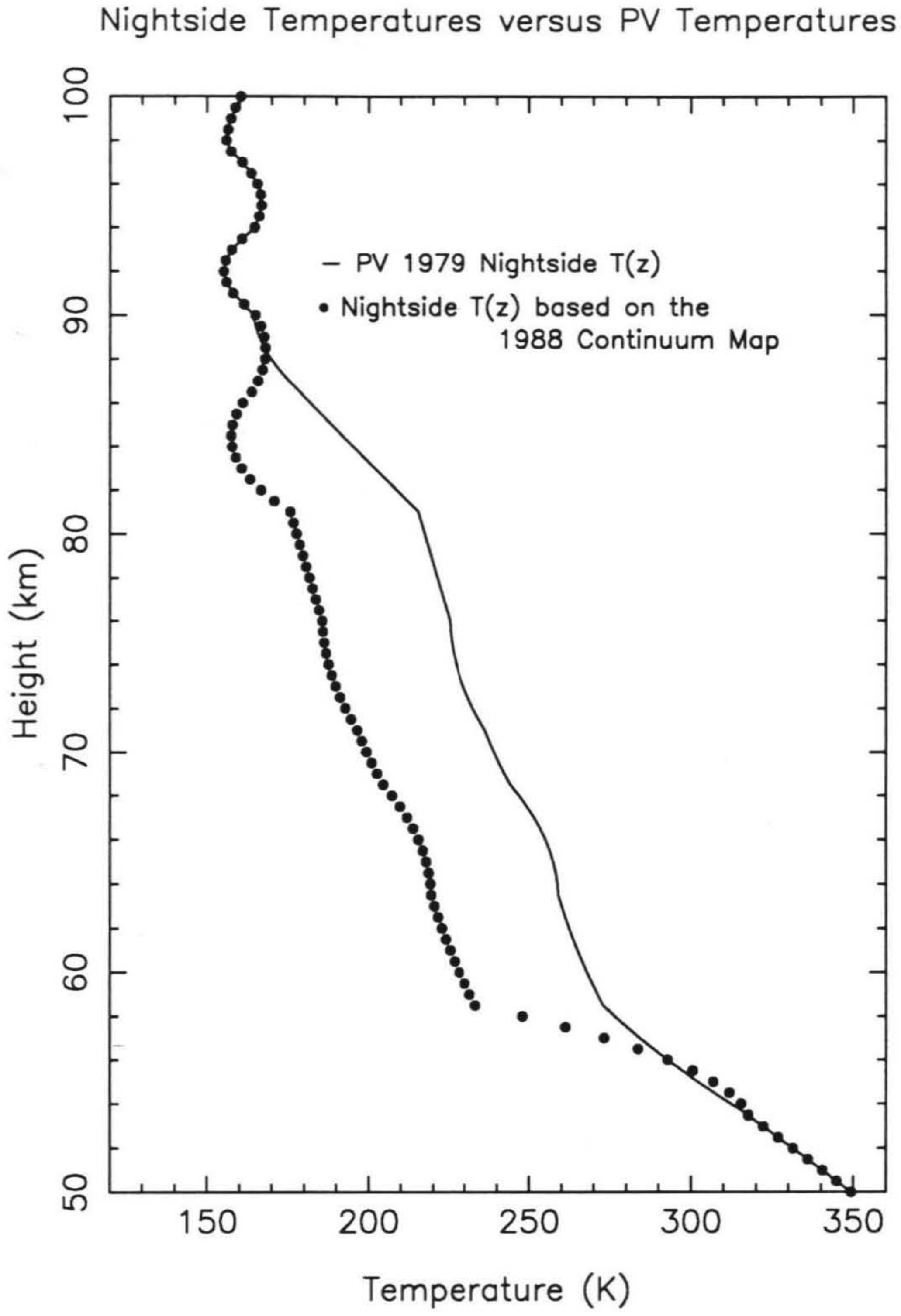

Figure 21. This cooler nightside temperature profile created the strong limb-darkening shown in the lower panel of Figure 20.

profile used to create increased limb-darkening is shown in Figure 21 and is cooler than the PV profile by roughly 40 K between 60-85 km. This cooler temperature profile does intensify the limb-darkening, but the total brightness curve is also lowered by 20 K and the continuum map's average temperatures at radii $\geq$6000 km are still more limb-darkened than the model's temperatures. A more reliable fit of a temperature structure to the continuum map's limb-darkening requires a means of pinning down the continuum map's absolute brightness values - essentially requiring a larger antenna array for the millimeter continuum observations. The temperature profile of Figure 21, therefore, can only be considered a crude estimate of the temperature profile at local midnight in Venus' atmosphere in spring 1988.

Chapter IV 50 kHz Data: Upper Mesospheric Winds.

The 50 kHz spectra immediately showed doppler shifts indicative of a zonal and/or subsolar-to-antisolar flow in the upper mesosphere of Venus. Figure 22 shows several of the equatorial 50 kHz spectra in panels at specified local times with a dotted vertical line indicating the center of the filterbank and the center of an unshifted absorption line. Careful inspection of the shape of these lines as positioned against frequency revealed shifts about one or two channel wide. Both the zonal and subsolar-to-antisolar flows would move in a westward direction over the evening terminator in the low latitudes. Therefore, such winds would approach the subearth point from the afternoon limb and move away from the subearth point to the nightside limb. This matches the blue shifts in observed CO spectra along the afternoon limb, zero shifts near the center of the planet, and red shifts along the nightside limb. The next step in the analysis was to extract values for these shifts or, equivalently, these components of the wind velocities in the Earth or line of sight (LOS) direction within each of the 533 usable cells on the planet. Here after, we call this LOS components the "radial wind".

1. Lorentzian Cross-Correlation for Doppler Shifts

In this analysis, the 50 kHz CO absorption lines were hand fitted by Lorentzian lines in order to measure the doppler line shifts. The center 16 channels of the CO absorption line in a given cell were cross-correlated over frequency with a Lorentz line shape. It was not possible to generate model synthetic spectra for the cross-correlation, since the CO mixing ratio and temperature profiles are not known at this spatial resolution. The CO absorption line typically changes greatly in width and depth with local time on Venus, becoming narrower and deeper in the nightside hours (Schloerb *et al.* 1980; Wilson *et al.* 1981; Clancy and Muhleman 1985ab). Our

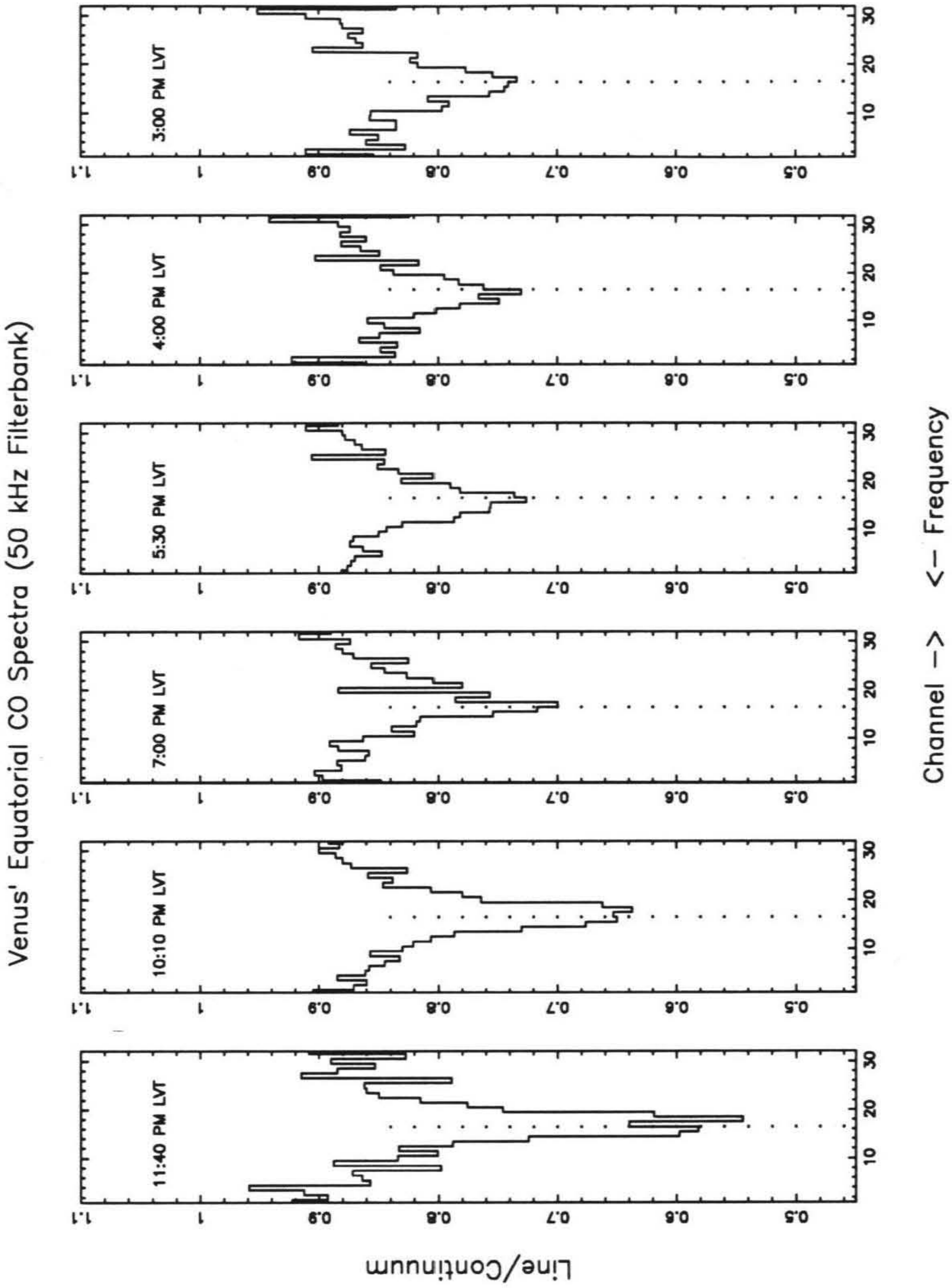

Figure 22. These 50 kHz filterbank CO lines lie along the equator at noted local times. The dotted line marks ν_o's location.

50 kHz spectra show the same trend, deepening of the line in the evening hours (see Fig. 22). However, since the observed absorption lines do change shape significantly across the planet, it was necessary to determine "by eye" a Lorentzian shape for each of the 533 CO lines.

1.1 Cross-Correlation Analysis

Each Lorentzian was defined by inspection with a depth and full-width-half-maximum width. Figure 23a shows a typical fitted Lorentzian line shape against an observed CO spectrum. The Lorentzian and the observed line were cross correlated, moving the Lorentzian across the CO line by channel-sized frequency steps, or channel lags. By calculating the sum of squared residuals between the two lineshapes over

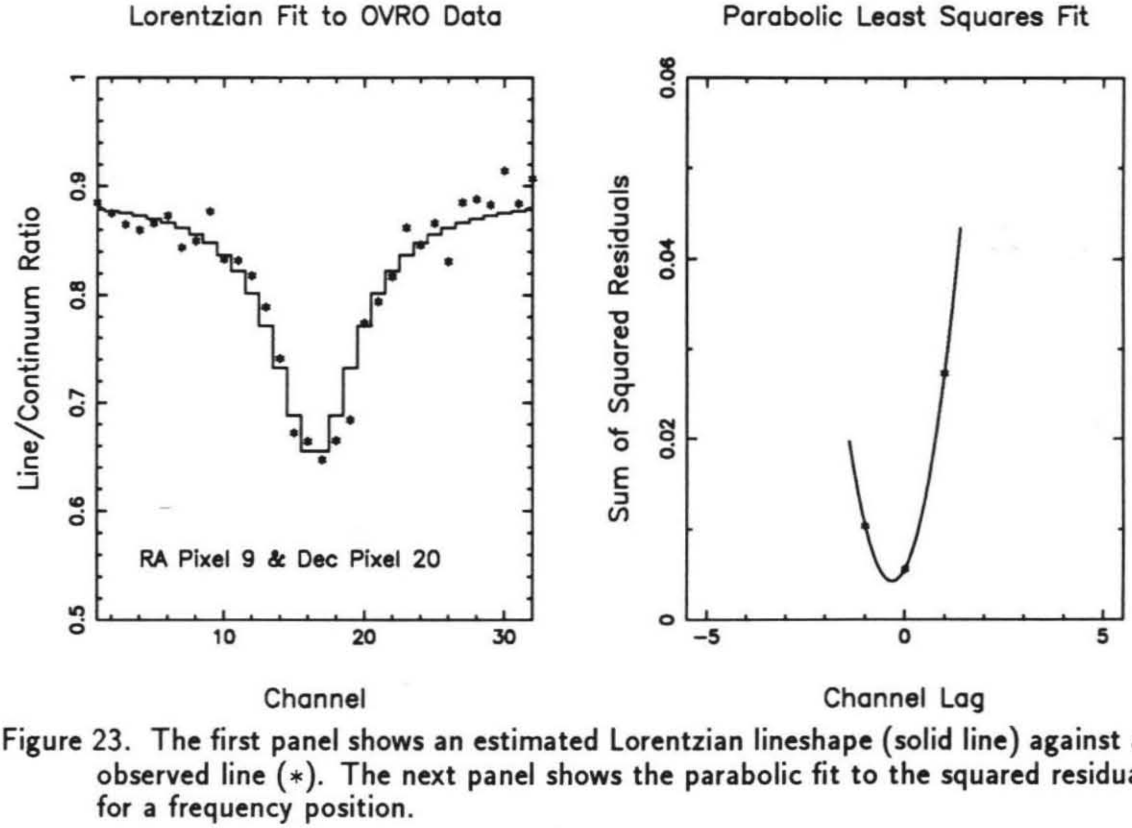

Figure 23. The first panel shows an estimated Lorentzian lineshape (solid line) against an observed line (∗). The next panel shows the parabolic fit to the squared residuals for a frequency position.

the inner 16 channels at each channel lag, one measures how well the Lorentzian's frequency location matches the frequency location of the observed CO line. These cross-correlation residuals change quickly in magnitude as seen in Figure 23b, clearly indicating the frequency center of the observed CO line. The summed residuals ranged in size, for example, from 0.241 at a large lag of 4-5 channels to 0.006 at a lag of 0-1 channels. The smallest size of the summed residuals acted as a check on the quality of the hand-fitted Lorentzian whose depth and FWHM were varied until the minimum residual was brought down to roughly .01.

The three smallest sum-of-squared residuals were then fitted in a least-squares sense to a parabola (Fig. 23b). Since the exact frequency center of the Lorentzian was known as it was moved across the observed CO line, the minimum of this parabola formed of the three smallest residuals then specified the frequency center of the observed CO lineshape and, consequently, the doppler shift to the CO line center. It can be seen from Fig. 23 that the shift can be estimated to a fraction of a channel width. This method also provided standard deviations for the measured doppler shift (see Appendix B for further details) which reflected the amount of noise in the CO line and, to a lesser degree, subtle differences between the Lorentzian and the CO line.

1.2 Radial Wind Measurements

The resulting radial wind measurements sample the upper mesospheric circulation from 74°N to 84°S in latitude and from 13.9 hours LVT in the afternoon to 0.9 hours LVT just past midnight. Figure 24 presents these radial wind measurements with their standard deviations plotted at specified latitudes with coordinates of radial wind speed in ms^{-1} versus local time. At a given latitude, radial wind velocities progress from blue shifts, positive velocities, on the dayside through zero to red shifts, negative velocities, on the nightside. However small-scale structure in the radial wind

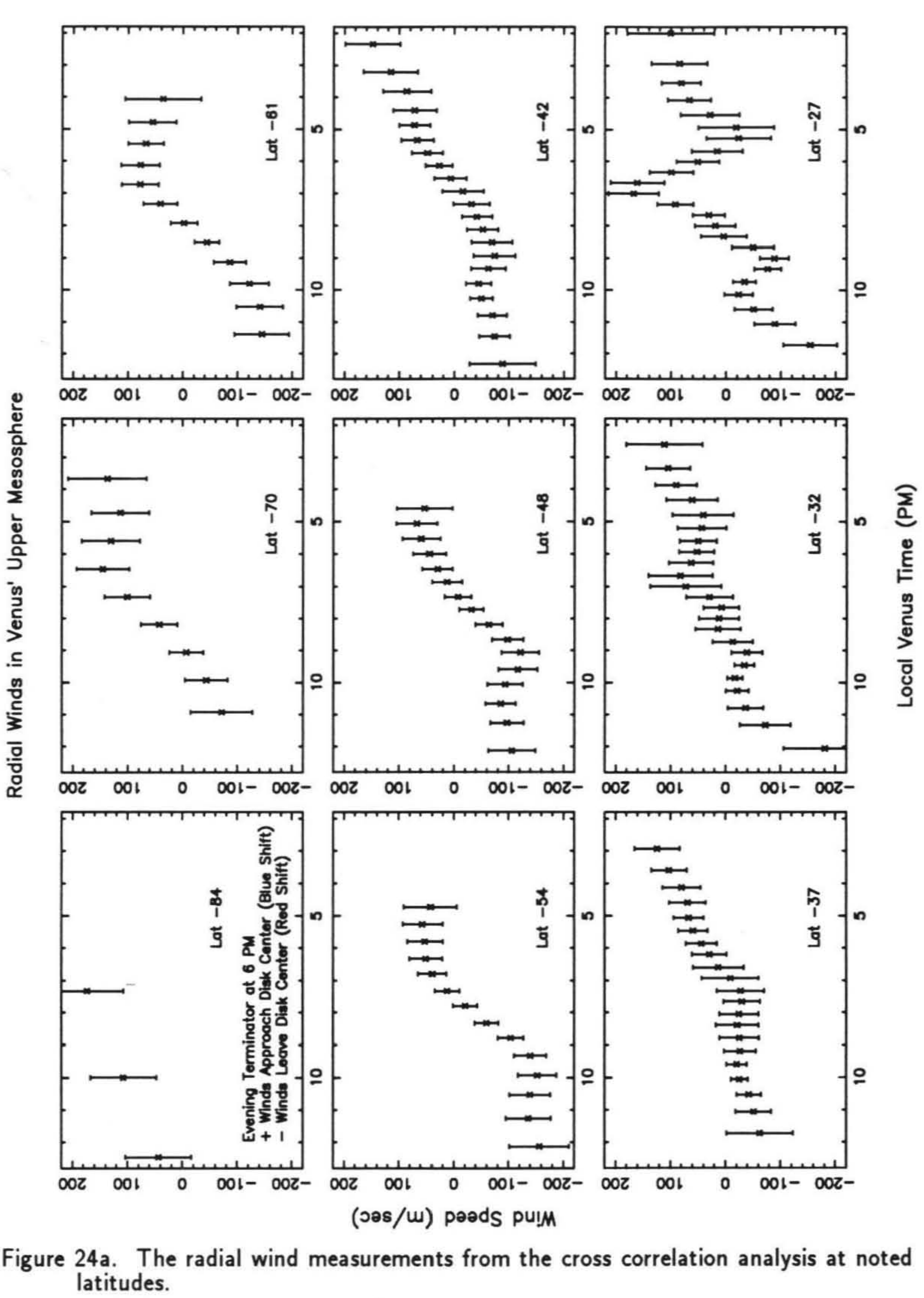

Figure 24a. The radial wind measurements from the cross correlation analysis at noted latitudes.

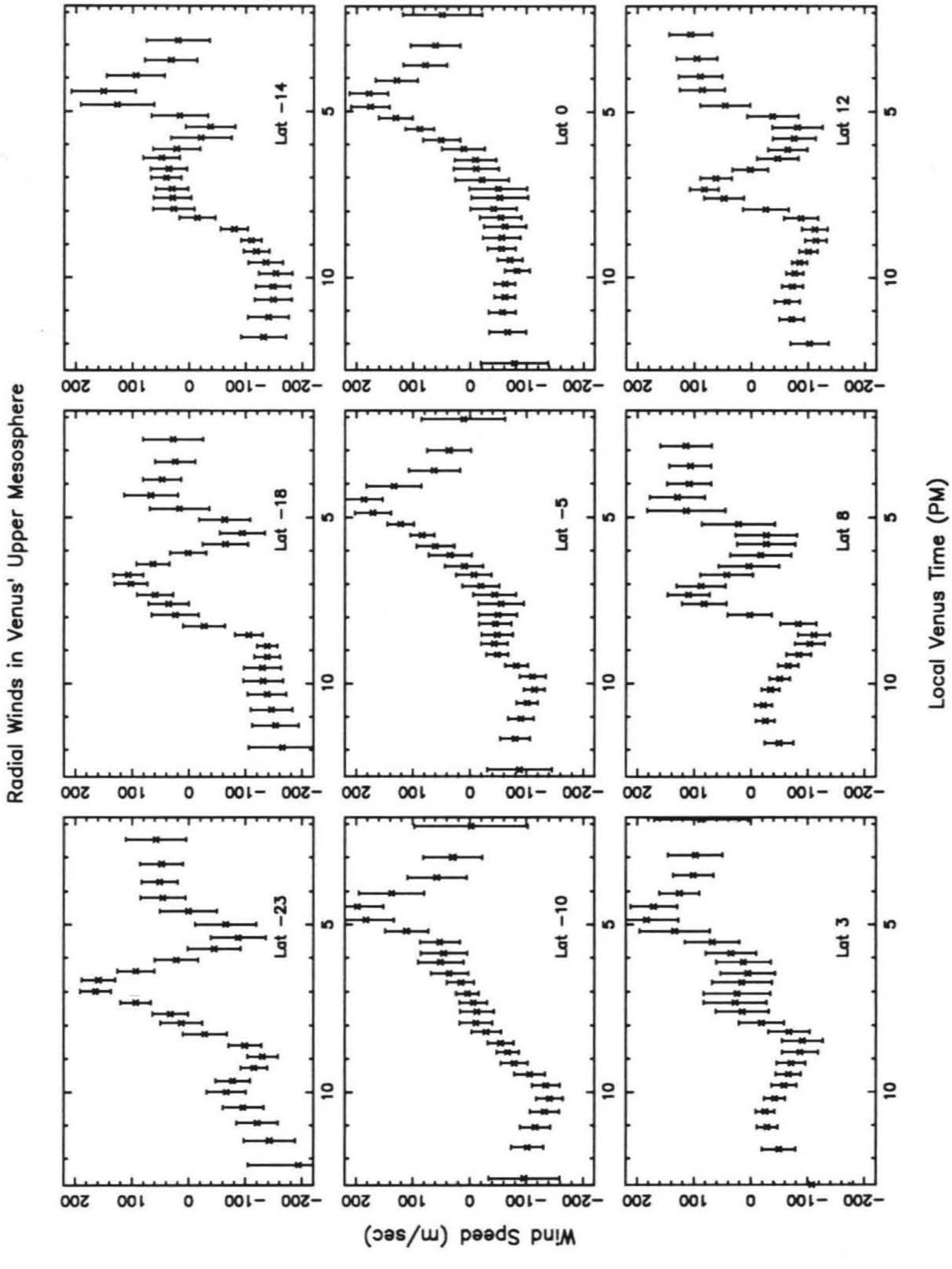
Radial Winds in Venus' Upper Mesosphere
Lat −23
Lat −18
Lat −14
Lat −10
Lat −5
Lat 0
Lat 3
Lat 8
Lat 12
5
10
−200
−100
0
100
200
Wind Speed (m/sec)
Local Venus Time (PM)

Figure 24b.

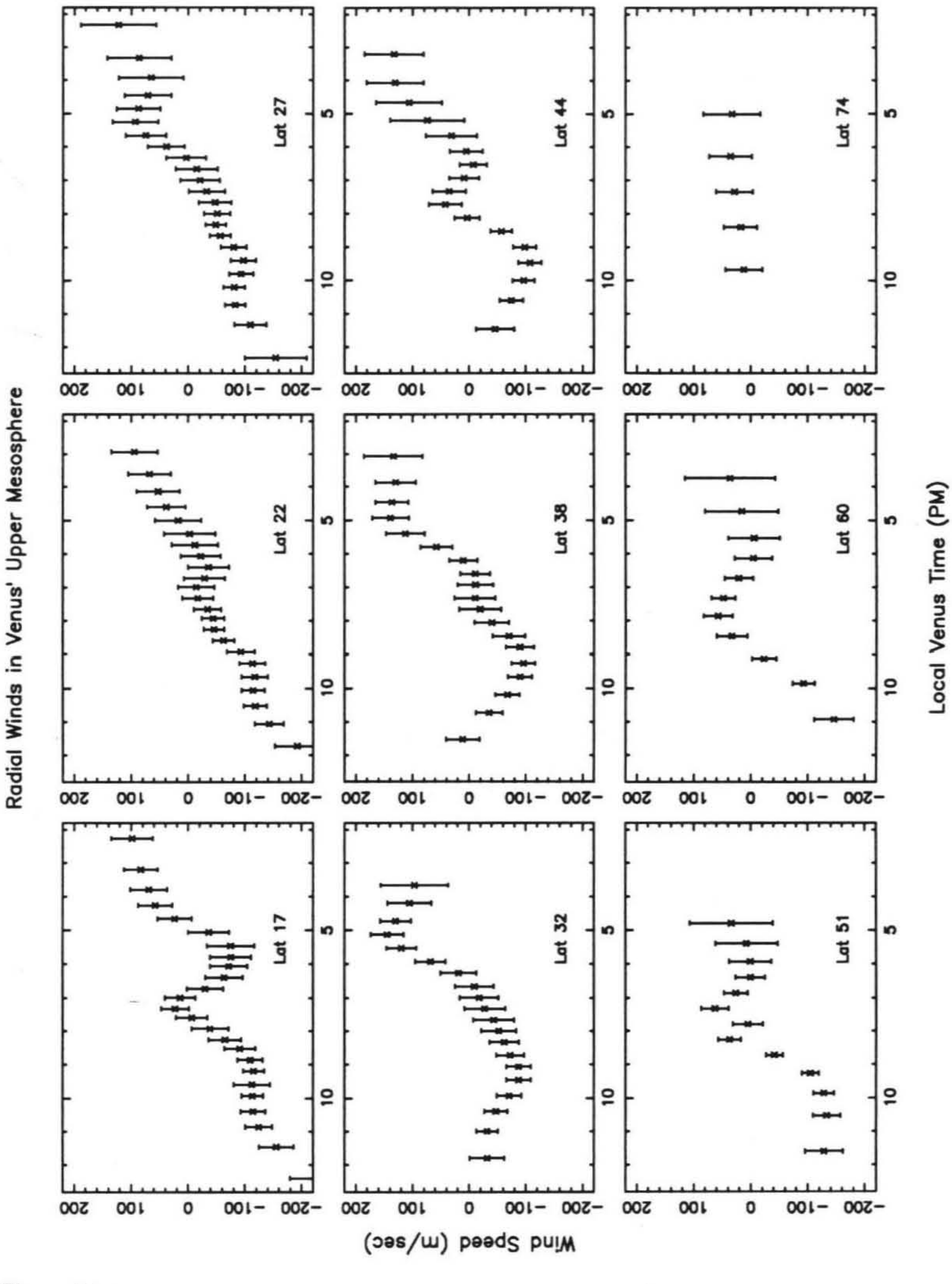
Radial Winds in Venus' Upper Mesosphere
Lat 17
Lat 22
Lat 27
Lat 32
Lat 38
Lat 44
Lat 51
Lat 60
Lat 74
200
100
0
−100
−200
10
5
Wind Speed (m/sec)
Local Venus Time (PM)

Figure 24c.

measurements is apparent at several latitudes. Clear examples of this small-scale structure can be seen in the panels at latitudes near 54°S, 23°S, 18°S, 12°N, 32°N and 44°N. At these latitudes, a smooth transition from dayside approaching velocities to nightside, receding velocities has been distorted and the passage through zero wind speed has been displaced from the subearth time of 19.3 LVT. These small scale surges in the wind measurements appear symmetrically across Venus' disk with a size similar to that of the dirty beam. This can be seen more clearly in the grey scale map and corresponding contour map of the radial winds in Figures 25 and 26. The spatial size and symmetry of these small-scale features argues against a "real" origin.

As discussed earlier, the synthesized dirty beam of an interferometer will distort the true map of a source and displace flux from one point to another in a map. When flux is moved by the dirty beam, it is moved in each channel map and the continuum map since the data are gathered by the same synthesized dirty beam. This displaced flux will retain the signature of the doppler shift of the original "true" position and put this signature at the second "dirty" position, eventually causing small to moderate errors in radial wind measurements. We believe that the small scale surges in the radial wind measurement map are caused by relatively small, unknown phase noise in the visibility data. This phase noise was not corrected by CLEAN and self-calibration and left residual dirty beam effects in the maps.

Returning to discussion of the radial wind measurements, the standard deviations tied to the velocity measurements are generally larger by a factor of two near the planet limb compared to standard deviations near the disk center. This is due simply to a lower signal to noise ratio associated with the lower brightness temperatures along the planet limb. The standard deviations are also typically larger on the dayside compared to the nightside by a factor of 1.3 as the CO line is deeper and narrower in the evening hours. The narrower, deeper lines make measurement of any

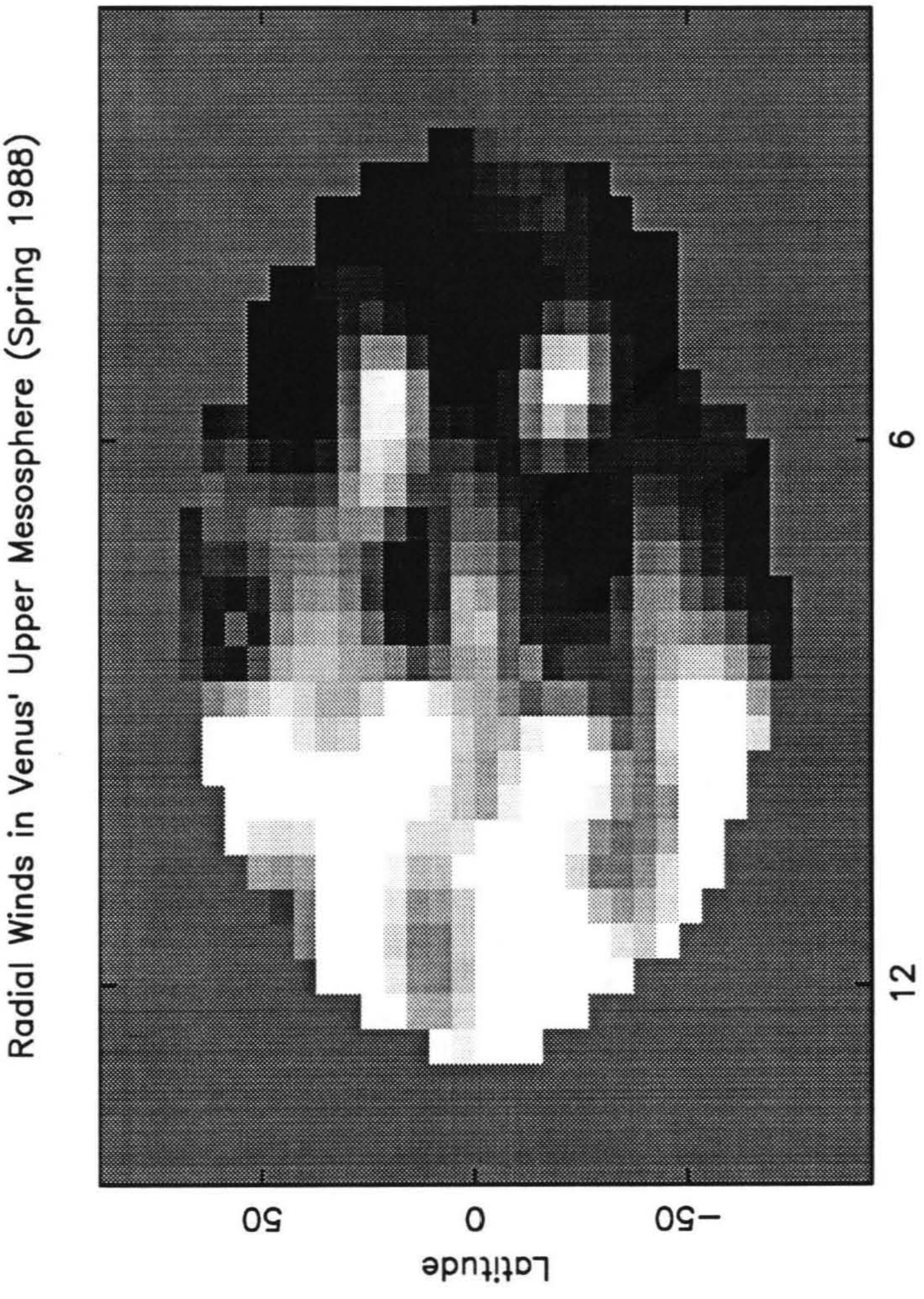

Figure 25. Radial winds across Venus are are plotted as shades between white for -80 ms^{-1} and black for 80 ms^{-1}.

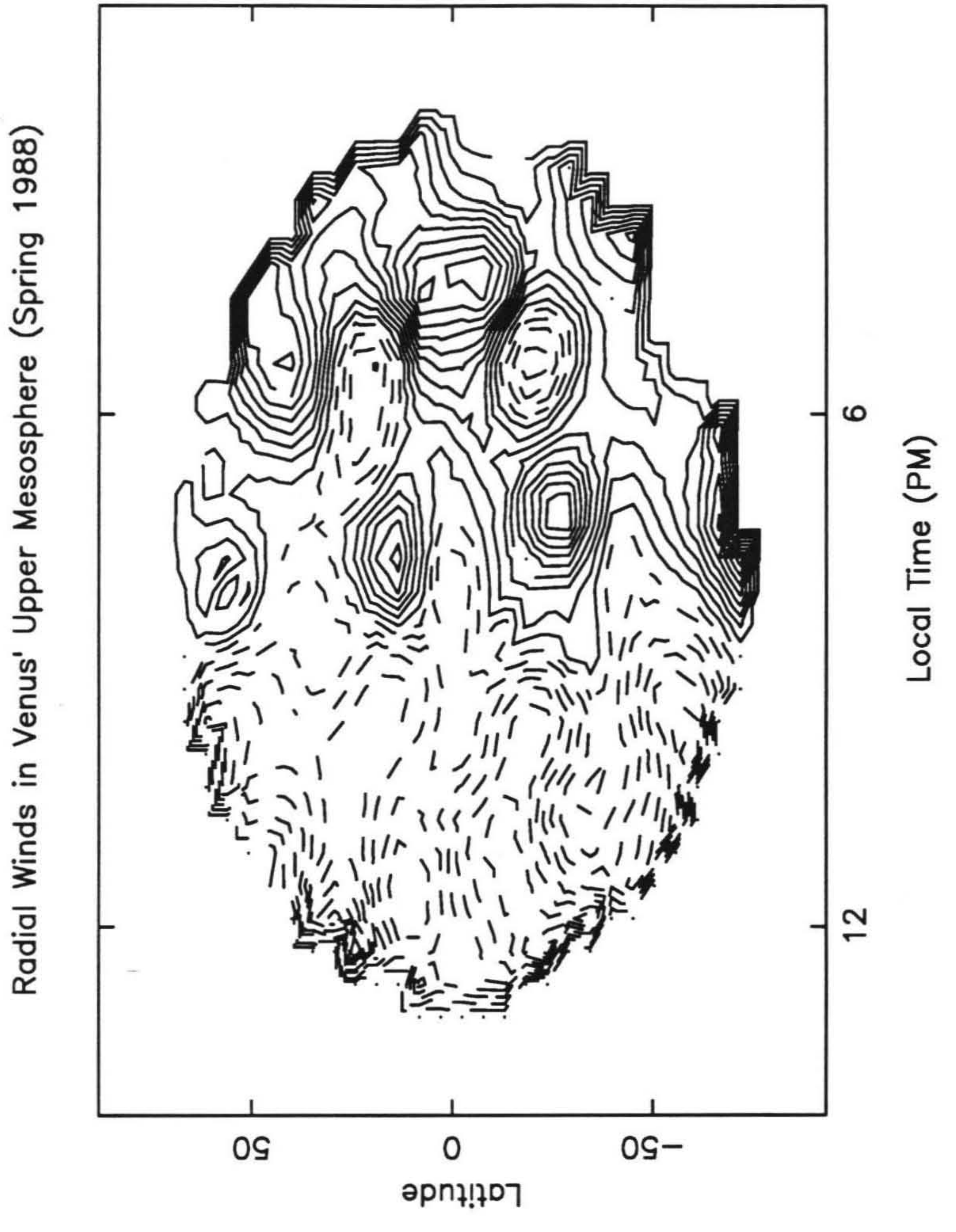

Figure 26. Radial winds across Venus with contours separated by 20 ms^{-1} and negative speeds indicated by dashed contour lines.

TABLE III

	Nightside Limb				Dayside Limb			
Lat°	Lon°	Time	Speed (ms^{-1})	σ	Lon°	Time	Speed (ms^{-1})	σ
-68	218.0	10.4	-54.98	34.0	312.0	4.2	128.21	45.0
-60	210.0	11.0	-151.65	34.8	308.0	4.4	55.94	40.7
-53	199.0	11.7	-150.71	34.6	300.0	5.0	61.65	34.5
-47	199.0	11.7	-106.62	26.2	302.0	4.8	77.32	37.2
-39	196.0	11.9	-81.17	27.3	333.0	2.8	138.92	37.2
-34	204.0	11.4	-60.20	31.9	326.0	3.3	124.45	28.1
-29	199.0	11.7	-113.53	43.1	330.0	3.0	117.78	38.2
-23	204.0	11.4	-129.53	33.6	338.0	2.5	94.42	45.5
-19	197.0	11.8	-168.80	44.3	332.0	2.8	56.30	33.2
-15	201.0	11.6	-176.86	38.2	330.0	3.0	29.09	33.3
-11	190.0	12.3	-133.09	38.5	327.0	3.2	31.29	40.5
-5	193.0	12.1	-109.62	27.7	337.0	2.5	25.85	49.3
-1	193.0	12.1	-88.45	25.7	337.0	2.5	33.00	36.7
3	193.0	12.1	-74.45	31.1	337.0	2.5	61.93	39.5
8	191.0	12.3	-64.15	29.3	339.0	2.4	101.82	44.4
11	203.0	11.5	-36.63	15.6	327.0	3.2	124.42	32.2
16	200.0	11.6	-89.76	20.6	329.0	3.0	110.30	28.7
20	196.0	11.9	-191.05	27.1	334.0	2.7	95.97	25.0
25	204.0	11.4	-177.67	24.2	326.0	3.3	89.67	30.1
31	197.0	11.8	-128.33	27.0	332.0	2.8	108.99	45.9
34	204.0	11.4	-34.73	17.7	316.0	3.9	118.73	37.7
41	208.0	11.1	-17.88	20.4	323.0	3.5	143.12	31.7
47	209.0	11.0	-71.02	19.3	320.0	3.6	141.31	38.6
52	209.0	11.1	-138.17	20.4	298.0	5.1	19.77	49.4
62	219.0	10.4	-110.57	18.2	311.0	4.2	25.49	51.9

Nightside Mean Speed= -106±10 ms^{-1} Dayside Mean Speed= 85±8 ms^{-1}

Note. Negative speeds are winds receding from the subearth point and positive speeds are approaching winds. Also tabulated are corresponding planetary latitudes, longitudes, local PM times and standard deviations for the wind measurements.

doppler shift to the line easier with the quicker change in line depth over frequency channels. Overall, the standard deviations on these radial wind velocities have an approximate mean of 35 ms^{-1}, ranging from a minimum of 13 ms^{-1} at an evening hour near the disk center to a maximum of 79 ms^{-1} near the north pole.

The signature of strong westward winds across Venus' disk is apparent in these radial wind measurements. Table III lists wind measurements and associated standard

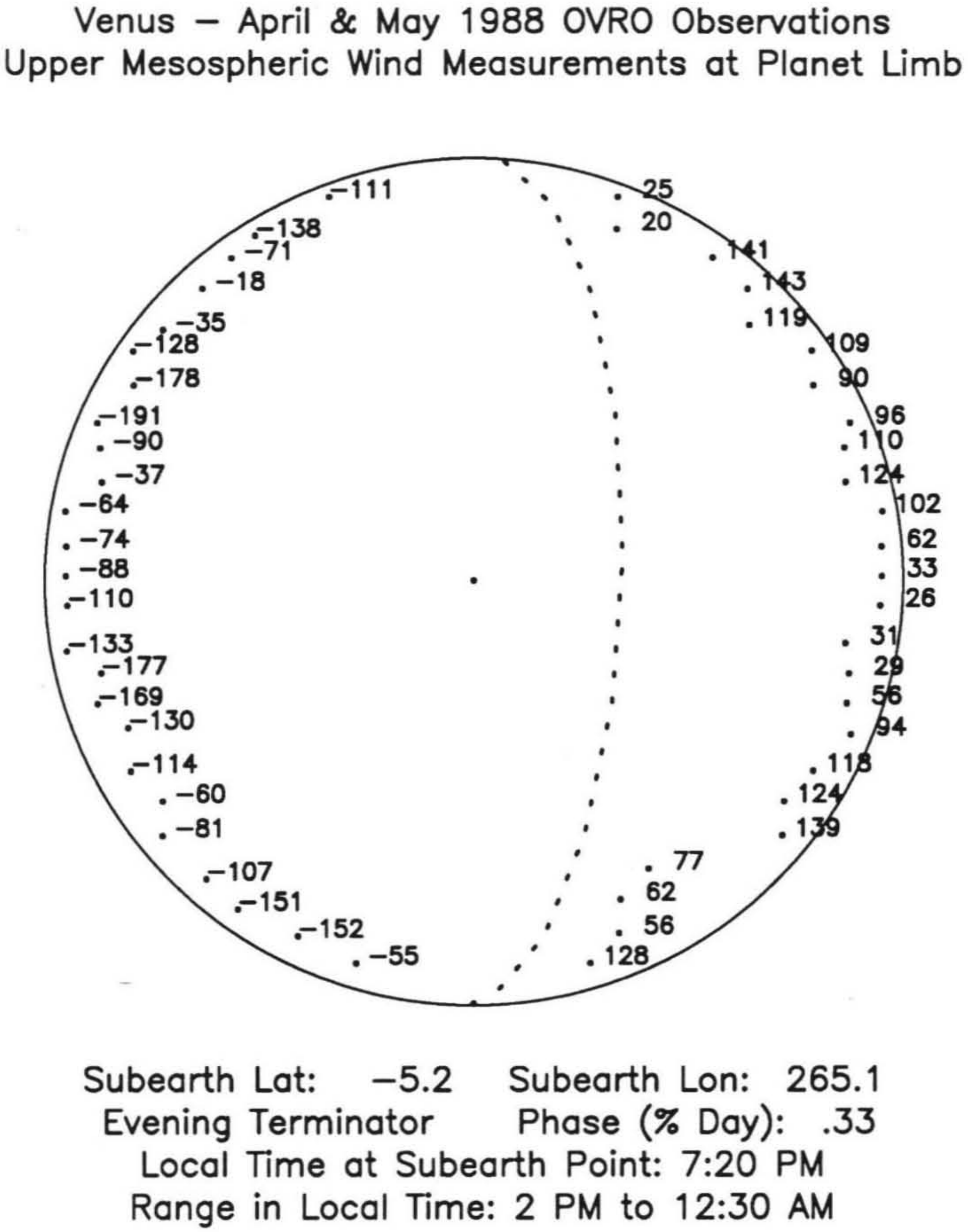

Figure 27. Incidence angle-corrected limb wind measurements of Table III in ms^{-1} with positive speeds denoting winds approaching the disk center and negative speeds winds receding.

deviations along the night and day planet limbs corrected for incidence angle ι

$$\iota = acos\Big(cos(\beta')cos(\lambda')\Big), \tag{23}$$

where β' and λ' are a measurement's latitude and longitude from the subearth point and averaged over two longitude pixels at a given latitude. These measurements nearly directly measure horizontal wind speeds in the upper mesosphere given their large wind component along the line of sight. The positions for the limb measurements correspond to incidence angles ranging from approximately 55° to 75° or a correction factor of 1.22 to 1.04. The latitudinal variations in these speeds arise mainly from the small scale artifacts described above and also from differences in longitudinal sampling as shown in the schematic of Figure 27. A simple mean value along each limb is 106 ± 10 ms^{-1} on the west, nightside edge and 85 ± 8 ms^{-1} on the east, dayside edge. The nightside limb velocities appear to be larger than the dayside velocities, lying outside the means' standard deviations by a few ms^{-1}. Essentially, though, these mean speeds for the east and west limbs of the planet are equally strong and indicate a dominant westward wind flow in Venus' upper mesosphere over the evening terminator.

2. Smoothing Radial Wind Measurements

In order to test simple models of global circulation, it was necessary to smooth the data spatially. It was impossible to improve the signal-to-noise ratio of the individual CO spectra and remove the small-scale artifacts by folding of the absorption line or smoothing through the frequency channels. That method would alter the frequency position of the CO lines. It was necessary to de-resolve the data spatially in order to solve for first-order fits to models of the zonal and subsolar-to-antisolar flow. A simple running average could not be applied to the measurements as the smaller nightside standard deviations would bias the disk center values towards red doppler

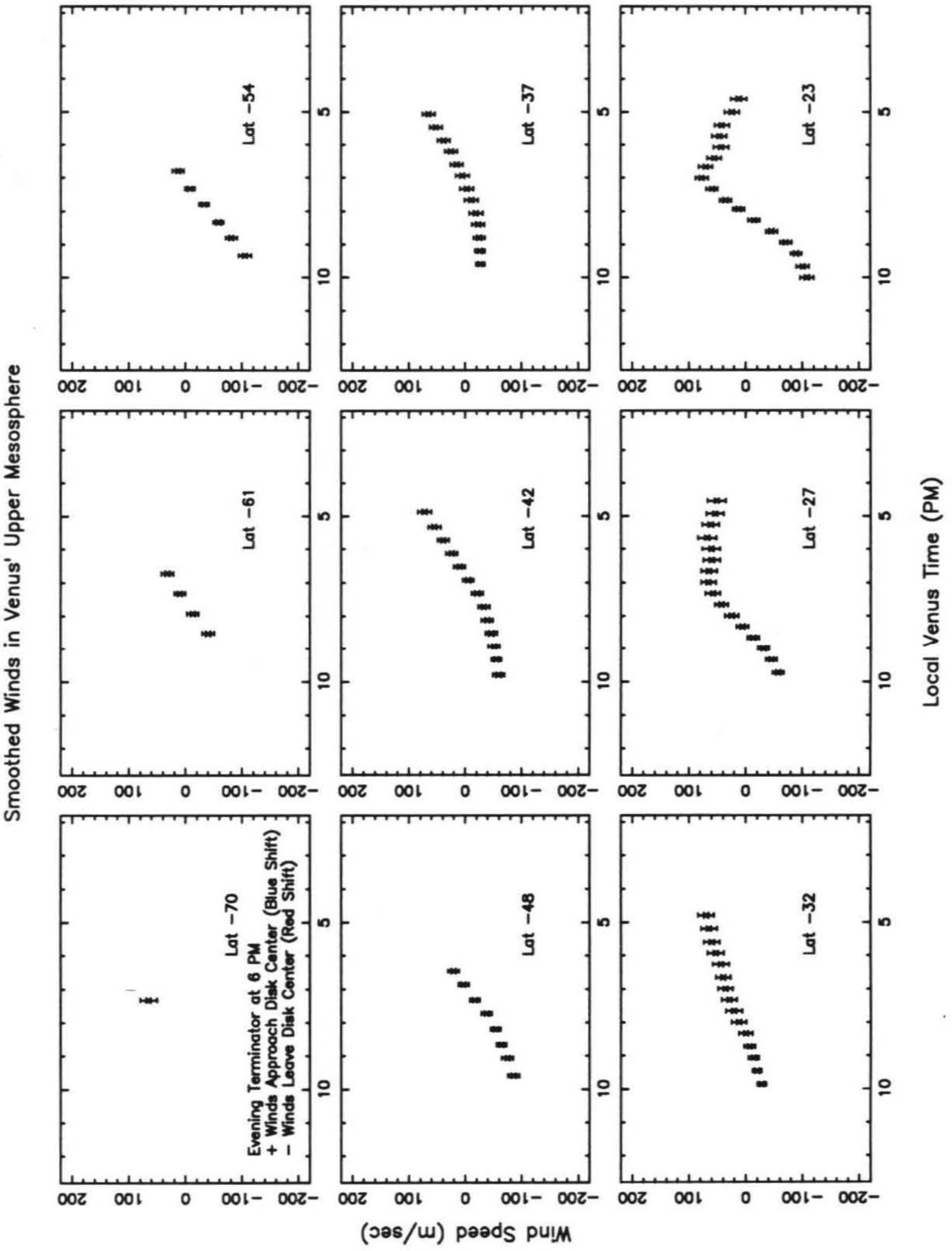

Figure 28a. Smoothed radial wind measurements at the noted latitudes.

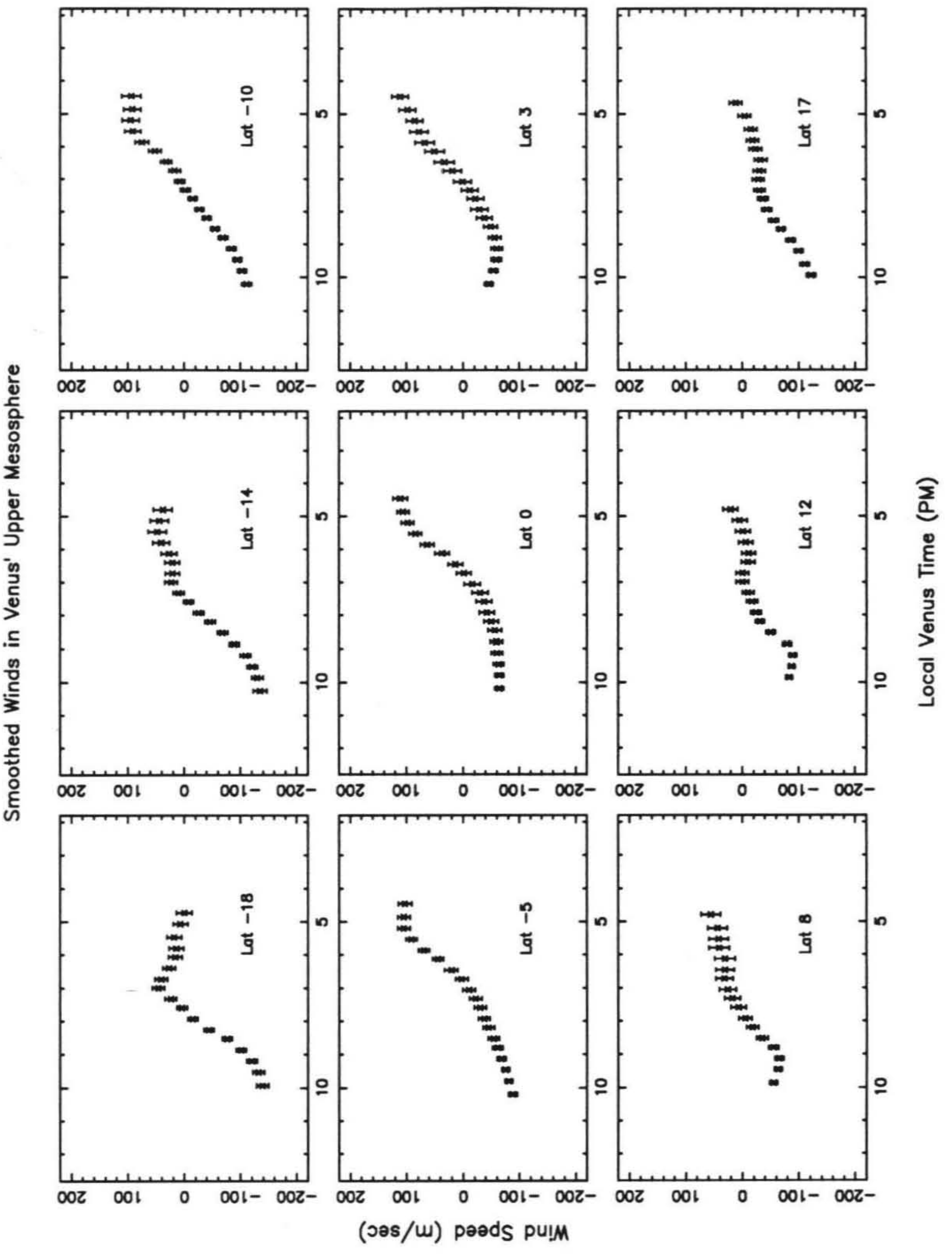
Smoothed Winds in Venus' Upper Mesosphere
Lat −18
Lat −14
Lat −10
Lat −5
Lat 0
Lat 3
Lat 8
Lat 12
Lat 17
Wind Speed (m/sec)
Local Venus Time (PM)
−200
−100
0
100
200
5
10

Figure 28b.

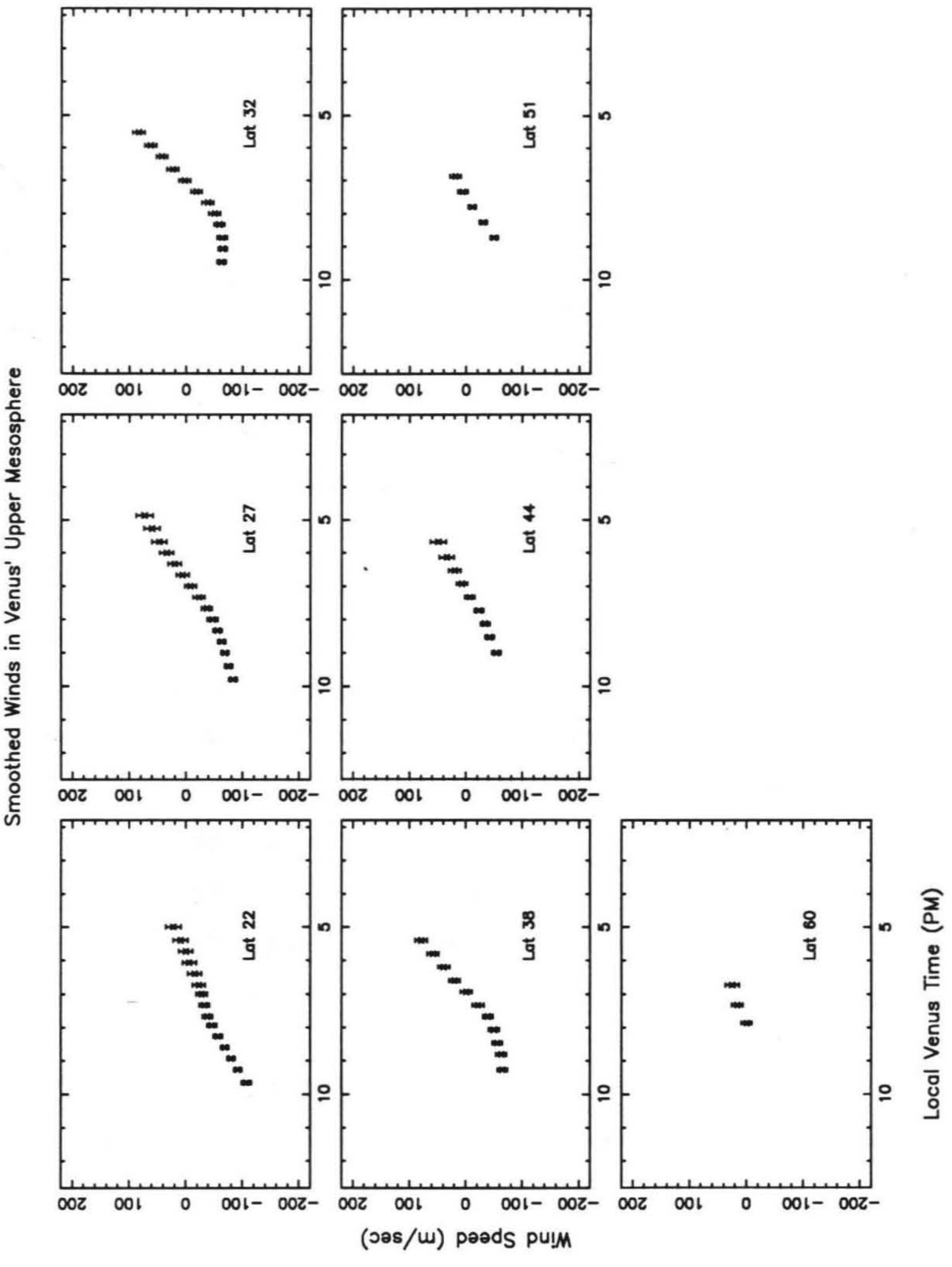
Smoothed Winds in Venus' Upper Mesosphere
Lat 22
Lat 27
Lat 32
Lat 38
Lat 44
Lat 51
Lat 60
Wind Speed (m/sec)
Local Venus Time (PM)
-200
-100
0
100
200
10
5

Figure 28c.

shifts. A running average would also not take into account the slope in the original latitudinal profiles of the radial wind measurements. Instead, a linear polynomial fit was calculated over an appropriate number of pixels and the midpoint pixel was reassigned to the corresponding fit value. The appropriate number of pixels to minimize the systematic small-scale features turned out to be nine pixels. This smoothing was applied only through longitude in an attempt to retain some of the latitudinal coverage.

Figure 29 and Figure 30 present the 324 smoothed radial wind measurements in the form of a grey scale map and corresponding contour map. The small-scale beam artifacts have indeed been damped so that the smoothed measurements reflect only the first order circulation in Venus' upper mesosphere. The distribution in smoothed radial wind measurements extends from 60°N to -70°S and from 16.5 LVT in the late afternoon to 22.2 LVT in the evening. The standard deviation associated with these smoothed radial wind measurements range about an approximate mean of 10 ms^{-1} with a maximum of 17 ms^{-1} near the position of an original small-scale feature at 8°N and a minimum of 6 ms^{-1} at an equatorial, nightside hour. The transition from dayside blue doppler shifts to nightside red doppler shifts is less distorted by dirty beam-related surges in velocity as shown in the panels of Figure 28. In this form, the smoothed radial wind speeds can be fitted in a simple least-squares sense for model zonal and subsolar-to-antisolar flows.

3. Model Zonal and Subsolar-to-Antisolar Flows

It was assumed that winds in the mesosphere followed a pattern similar to some linear combination of the zonal and/or subsolar-to-antisolar flows. These two circulation patterns have been used to explain observations of this atmosphere at altitudes below and above the mesosphere through the past two decades. It seemed appropriate to search for these two flows in the mesosphere. Though previous re-

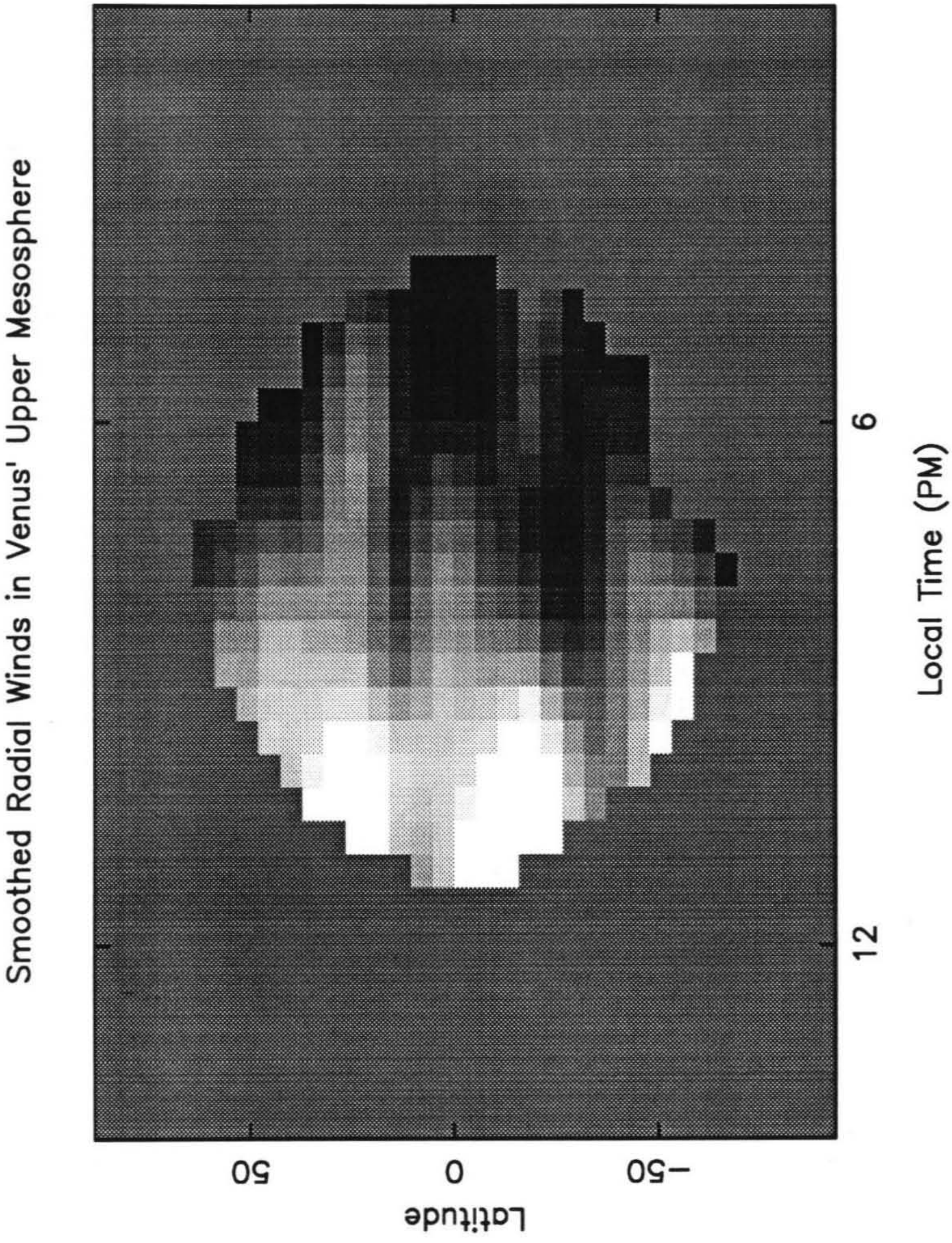

Figure 29. See description of Figure 25.

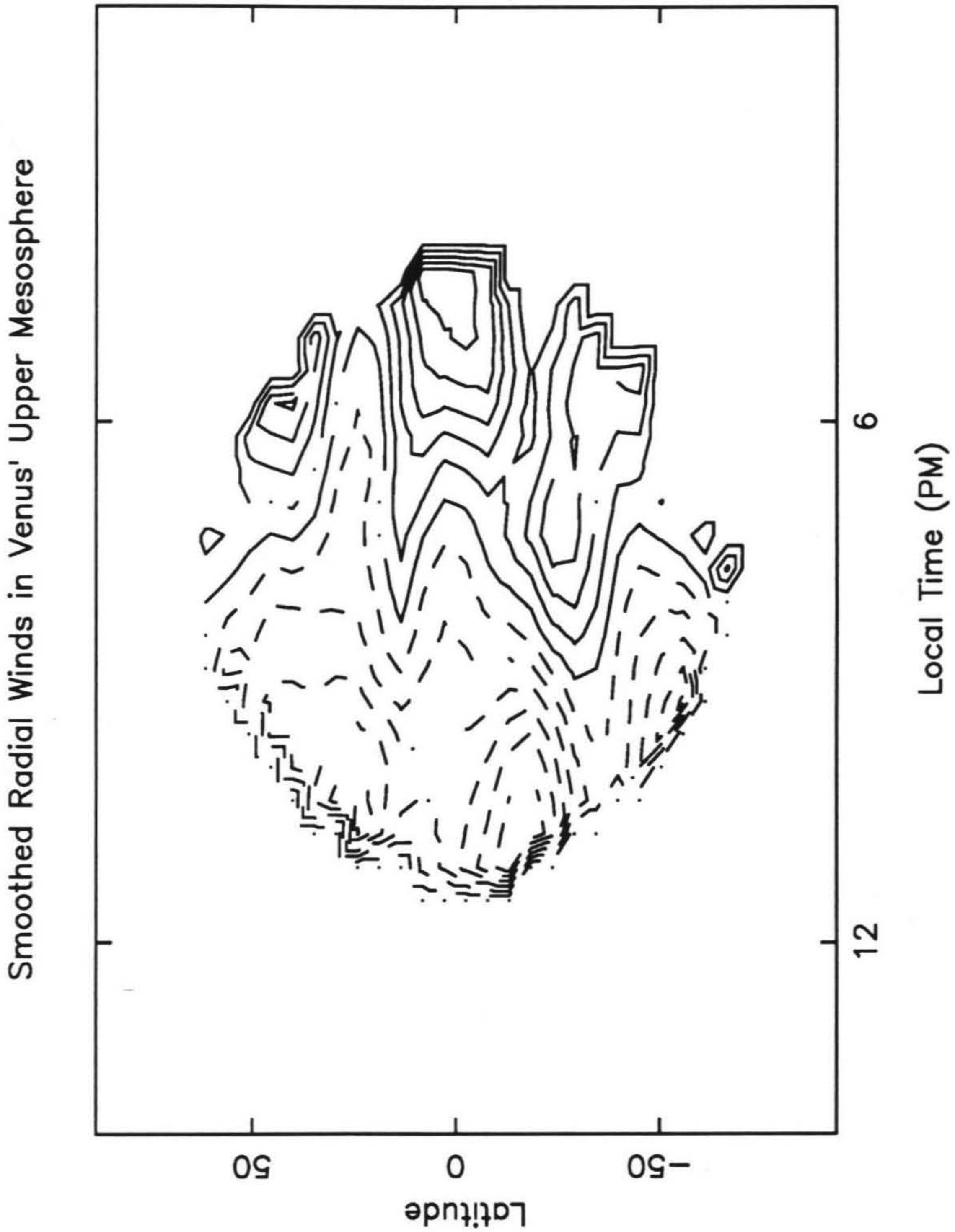

Figure 30. See description of Figure 26.

searchers (Elson 1979; Taylor *et al.* 1980) have developed dynamical models which can produce significant meridional flows at mesospheric altitudes, the OVRO 1988 data did not find evidence of such flows. This possible meridional motion or even a vertical motion was ignored in the modelling since the orientation of doppler shifts across the Venusian disk indicated a strong, westward, horizontal flow.

As mentioned earlier, the lower atmosphere's zonal flow moves westward at a

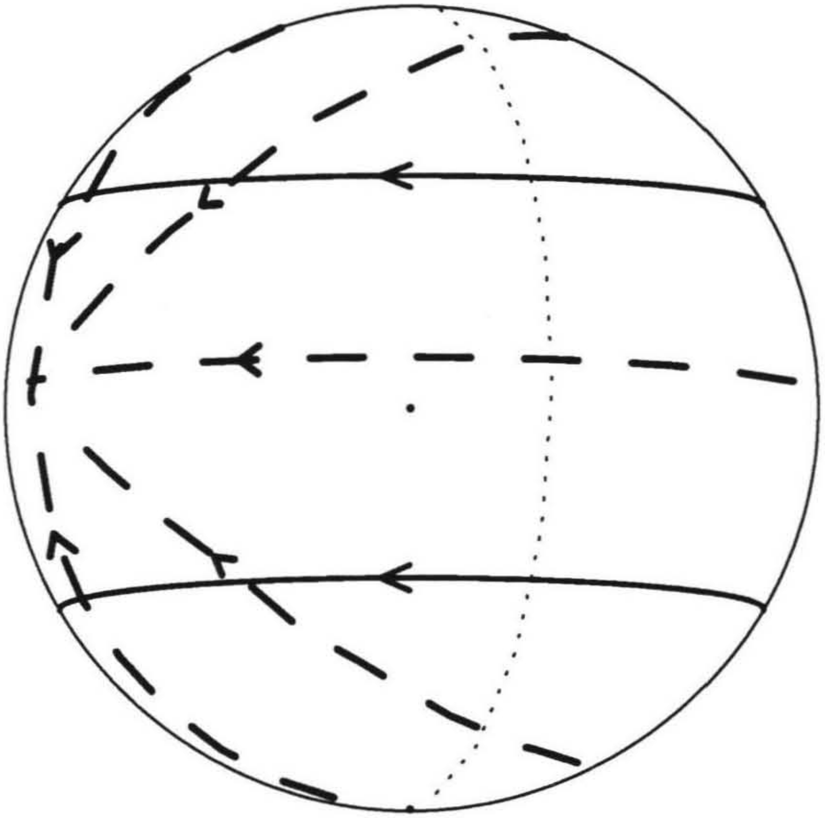

Zonal and Subsolar–to–Antisolar Flows Over The Evening Terminator

Figure 31. The zonal (solid line) and subsolar-to-antisolar flows (dashed line).

constant speed, given a narrow range in altitude and a short time interval. It has a latitude dependence of either 1/cos(latitude) away from the poles, if one assumes conservation of angular momentum as implied by Mariner 10 photopolarimeter images, or cos(latitude), if one assumes solid body rotation as implied by Pioneer Venus photopolarimeter images (Schubert *et al.* 1980). Given these two equally proven, very different theoretical descriptions of the zonal flow and given the variability in the latitudinal structure of the zonal flow as seen in the UV photopolarimeter data, a more simplistic approach was taken. The zonal flow was modelled as only a constant westward wind with no prescribed latitudinal dependence and with a trigonometric factor for the component seen along the line of sight

$$u_Z = a_1 sin\lambda cos\delta, \tag{24}$$

where a_1 is the constant speed in ms^{-1}, λ in the longitudinal angle from a given radial wind measurement to the subearth point, and δ is the latitude of the subearth point.

A simple form for the magnitude of the subsolar-to-antisolar flow was adopted from Goldstein (1989)

$$u'_{SA} = a_2\left[1 - \frac{|90^\circ - \theta|}{90^\circ}\right], \tag{25}$$

where a_2 is the maximum speed of the flow as it crosses the evening terminator and θ the angle in degrees between the terminator and a given radial wind measurement. This describes only the magnitude of the horizontal motion of the upper atmospheric flow, being zero at the subsolar and antisolar points on the planet and reaching maxima over the terminators at 6 and 18 hours LVT. As pointed out by Goldstein (1989), it provides qualitative agreement with current circulation models of Venus' thermosphere (Bougher *et al.* 1988). The flow, however, moves in an axisymmetric manner between the antisolar and subsolar points and so only a component of the subsolar-to-antisolar flow given by equation (25) was seen along the line of sight. Equation (26) builds on this basic description of the flow's magnitude, including trigonometric factors that account for the axisymmetric motion and provide the necessary components along the line of sight

$$\begin{aligned} u_{SA} &= a_2\Big[1 - \frac{|90^\circ - \theta|}{90^\circ}\Big] \\ &\Big[(cos\delta/sin\theta)[cos\lambda_{AS}cos\beta_{AS} - cos\lambda cos\beta cos\theta] \\ &+ (sin\delta/sin\theta)[sin\beta_{AS} - sin\beta cos\theta]\Big]. \end{aligned} \tag{26}$$

In equation (26), the angles introduced are latitude and longitude of the antisolar point β_{AS},λ_{AS} and latitude and longitude of given radial wind measurement β,λ as measured from the subearth latitude. Appendix C reviews the simple geometry behind the trigonometric factors of equations (24) and (26).

Figure 32 shows the model line of sight components for zonal and subsolar-to-antisolar flows versus planetary longitude at various latitudes as described by equations (24) and (26). In each panel, the unknown maximum speeds a_1 and a_2, characterizing the zonal and subsolar-to- antisolar flows respectively, have been set to a nominal value of 100 ms^{-1}. A positive speed denotes winds moving towards the subearth point and a negative speed moving away from the subearth point. The zonal flow creates a radial wind profile in the shape of an S-curve symmetric about the subearth point or line of sight position at planetary longitude 265° or, equivalently, 19.3 hours LVT. Radial winds from a westward horizontal flow appear strongest, of course, along limb of the planet or planetary longitudes of approximately 185° (.6 hours LVT) and 345° (14.1 hours LVT). Near the subearth point, radial zonal winds are forced to zero since the flow moves perpendicularly across the line of sight.

The radial wind components for the model subsolar-to-antisolar flow vary greatly with latitude. At equatorial latitudes, this flow appears strongest at a longitudes about 310° (16.1 hours LVT) – shifted off an expected maximum position at the evening terminator longitude of 285° due to the line of sight influence. A smaller

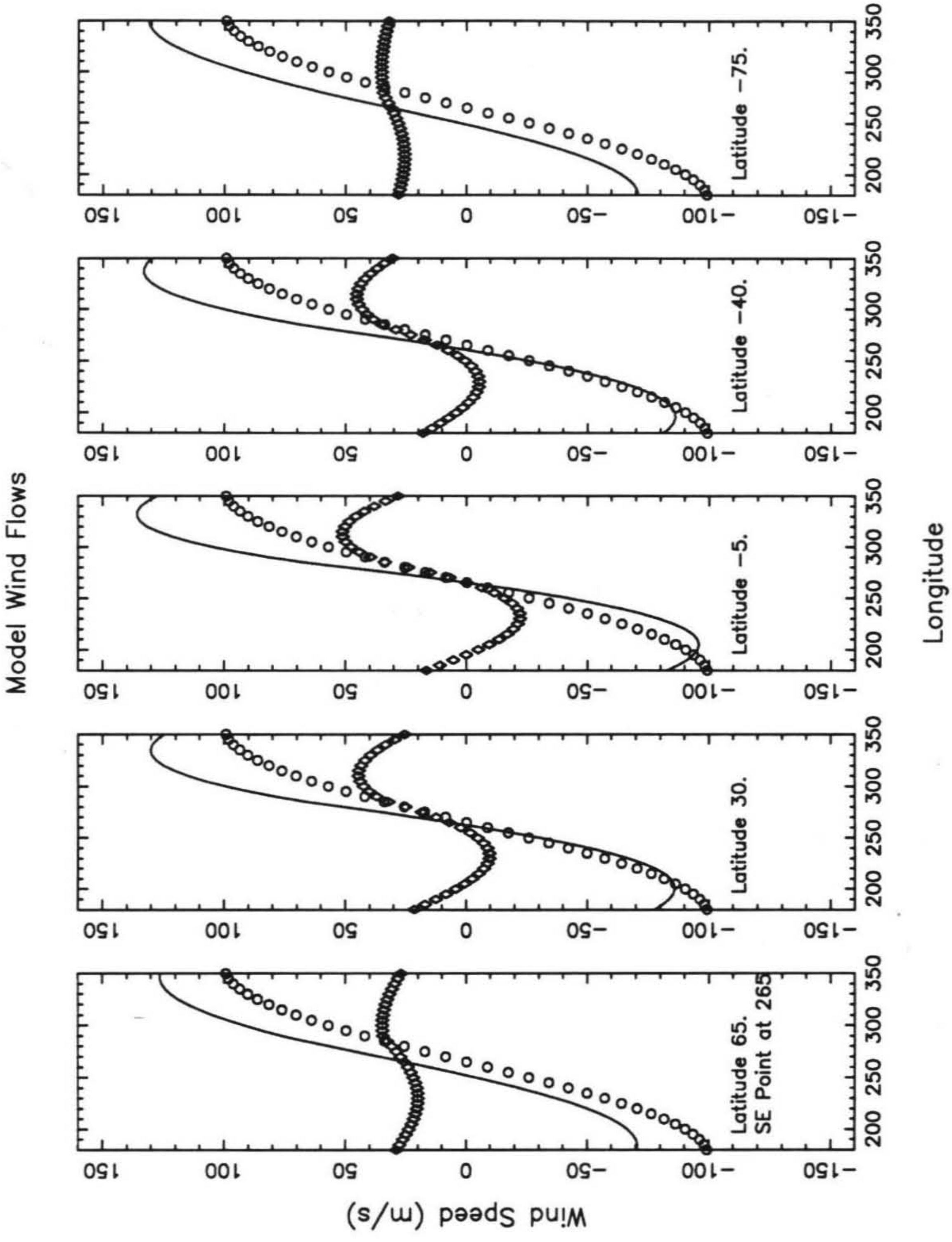

Figure 32. Model radial wind speeds for a zonal flow (○), a subsolar-to-antisolar flow (◇) and the sum of these flows (solid line) in panels at specified latitudes.

opposite extrema in wind speed occurs around longitude 230° (21.6 hours LVT) again due to the line of sight influence. This sinusoidal radial wind curve becomes flatter and shifted to positive wind speeds at poleward latitudes. Since the flow is moving over the terminator towards the antisolar point at longitude 195°, the subsolar-to-antisolar winds appear to move towards the subearth point and, near the poles, have positive radial speeds at all longitudes. The subsolar-to-antisolar components' maxima decrease in magnitude at higher latitudes because of smaller line of sight factors (see Equation (26)).

4. Least Squares Analysis

The 324 smoothed radial wind measurements were fitted in a least-squares sense for four cases: to a superposition of the zonal and subsolar-to-antisolar flow over all latitudes, to only a zonal flow over all latitudes, to a superposition of the two flows in 10° latitude bins and, finally, to only a zonal flow in 10° latitude bins.

A fit for a superposition of the two model flows with all of the smoothed radial wind measurements yielded a speed of 151 ± 3 ms^{-1} for the zonal constant a_1 and -35 ± 4 ms^{-1} for the subsolar-to-antisolar cross-terminator constant a_2. This least squares fit failed in three ways. First, it produced an unrealistic eastward subsolar-to-antisolar flow, indicated by the negative speed for a_2. Second, it was characterized by an unacceptably high reduced chi-squared value of 6.7, reflecting the poor quality of the fit. Third, the fitted values for a_1 and a_2 had a very high correlation coefficient of -0.8, reflecting the high instability and high inter-dependency of the fitted values. Obviously, our data could not provide good, uncorrelated fits for both a zonal and subsolar-to-antisolar flow over all latitudes. The two flows moved in a too similar direction over most of the planet during the time of our observations (see Figure 31). The aspect geometry of Venus (i.e., the evening terminator) combined with the noise on the data made it too difficult to separate out values for both flows.

Next, a least squares fit for a zonal flow speed with all of the measurements was tried. This test also failed conventional requirements for a good least-squares fit. It yielded a westward speed of 135±2 ms^{-1} for a single zonal speed a_1 over all latitudes. However, the reduced chi-square value of the fit was unacceptably high at 6.9. This chi-square value pointed to a poor agreement between this 135 ms^{-1} zonal flow and smoothed radial wind measurements at some latitudes. A single value for the zonal constant a_1, therefore, was not found to satisfactorily fit the radial wind measurements at all latitudes.

The smoothed radial wind measurements were then separated into bins of 10° of latitude and fitted for the final cases: first, for a superposition of the zonal and subsolar-to-antisolar model flows and, second, for only a zonal flow. Table IV presents results for both cases: the center latitude of the bin, the number of smoothed radial wind measurements in each bin, the values fitted for the flows' characteristic constants a_1 and a_2, the standard deviations for these constants, the reduced chi-square value for the fit in that bin, the correlation coefficient of the fitted constants and then similar columns for fitting the second case of only a zonal constant.

In the first case, the smoothed measurements were fitted to find a combination of the two circulation patterns. In equatorial latitudes, the correlation coefficient was again very high and the fitted characteristic constants large and unstable (columns 3, 5 and 7 of Table IV). In poleward latitudes, the correlation between the fitted flows became low and acceptable. The fitted subsolar-to-antisolar component at high latitudes was small with speeds of roughly 30-50 ms^{-1} compared to the zonal component speed of 80-140 ms^{-1} (see columns 3 and 5 of Table IV). However, the combination of too few measurements and larger standard deviations led to error estimates which were as large as the fitted subsolar-to-antisolar cross-terminator speeds (column 6 of Table IV). If a subsolar-to-antisolar component was present during the spring of

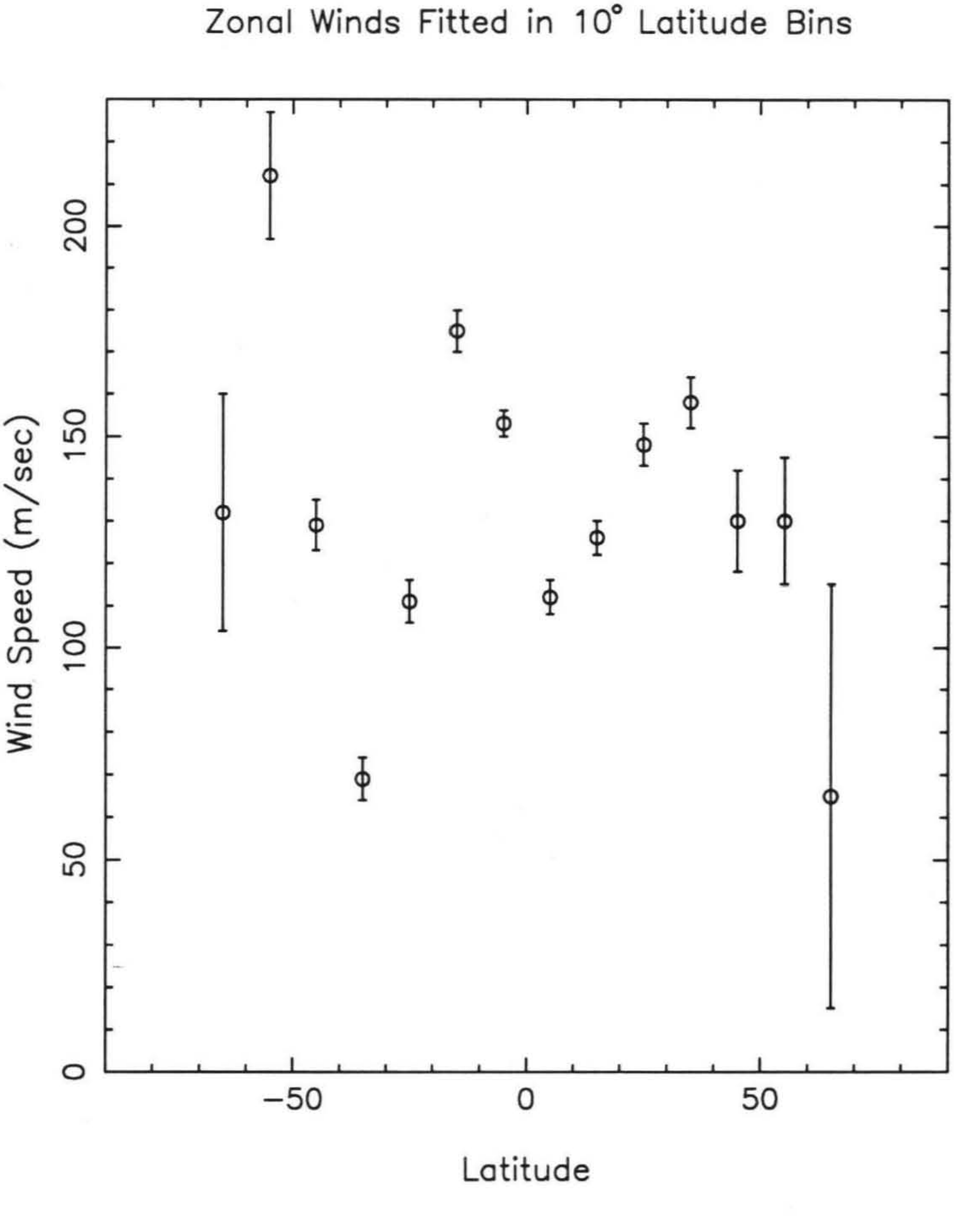

Figure 33. The fitted zonal speed constant a_1 with associated standard deviations (see Table IV) are plotted versus latitude.

1988, it cannot conclusively be pulled out or ruled out by our data. The best estimate of the size of such a subsolar-to-antisolar flow would be a rough upper limit on the cross-terminator speed, at approximately 40 ms^{-1} based on these high latitudes least-squares fits.

The smoothed radial wind measurements were then fitted for only the simple westward zonal flow in the same latitudinal bins. This was a lowest order fit to the data since the zonal constant a_1 is essentially the slope of the radial wind measurements over longitude or local Venus time. Columns 9 and 10 of Table IV list the fitted speeds for the zonal constant a_1 and their standard deviations in the 10° latitude bins. The fitted zonal speed ranged about a median value of 130 ms^{-1} from a maximum of 212 ± 15 ms^{-1} at 55°S to a minimum of 65 ± 50 ms^{-1} at 65°N. Some of the equatorial fits for a zonal speed had satisfactory chi-square values, but those at latitudes of 25°S, 15°S, 15°N and 25°N remained high. Agreement between the fitted zonal flow and the measurements was still best at latitudes where the small scale beam artifacts did not occur. The fitted zonal speeds in high latitude bins agreed with the zonal speeds found in the fit for a superposition of flows – as expected given the low correlation coefficient at these polar latitudes (see columns 3 and 9). A mean value of all the latitudinal-binned fitted zonal speeds was 132 ± 10 ms^{-1} (matching the zonal speed of 135 ± 2 ms^{-1} from the zonal fit over all latitude).

Figure 33 shows these fitted zonal speeds with their standard deviations versus latitude. The scatter over latitude in the fitted speeds is quite evident. Zonal speeds poleward of 35° might fall off from a equatorial plateau around 130 ms^{-1}. We view the variation of these latitudinal fitted zonal speeds and the absolute differences in fitted speeds from latitude to latitude with scepticism given the small scale artifacts in the maps of the radial wind measurements (Figures 25 and 26). However, the median and mean speeds for the zonal flow have proved to be consistent throughout the least squares analysis. Also the agreement between the latitudinal fits for high latitudes, as listed in Table IV, has led to a rough estimate of an upper limit for any subsolar-to-antisolar component. Therefore, our data has not only detected strong, westward winds over the evening terminator but has yielded a mean value of 132±10 ms^{-1} for the zonal flow and an upper limit of 40 ms^{-1} for a cross-terminator speed of a subsolar-to- antisolar component.

5. Line Core Weighting Functions

In order to assign altitude levels for these wind measurements, it was necessary to examine the weighting functions for the CO absorption lines, the atmospheric parameters which control the shape of the weighting functions and the variation of these weighting functions across the disk of Venus.

5.1 Radiative Transfer Model with Resonant Absorption

The radiative transfer model of Venus used to investigate the CO weighting function is the nonscattering, LTE, circularly symmetric model described in section 2 of Chapter III. For the frequency range used in the doppler shift analysis, only resonant CO absorption appears in the weighting function at altitudes in the upper mesosphere. The radiative transfer model used a CO absorption coefficient formulation by Waters (1976) with a more current value for the dipole moment of CO (0.112 Debye; Kolbe *et al.* 1977)

$$k(\nu) = (9.21 \times 10^{-9})\left[1 - \frac{2.769}{T}\right]\frac{N_{CO}}{T^2} f(\nu) \quad cm^{-1}, \tag{27}$$

where ν is frequency, T atmospheric temperature in K, N_{CO} the number density of CO molecules in cm^{-3}, and $f(\nu)$ the normalized Voigt lineshape function. Note that temperature and CO abundance are the two atmospheric parameters which control the absorption coefficient. Moreover, the Voigt lineshape function is a convolution of

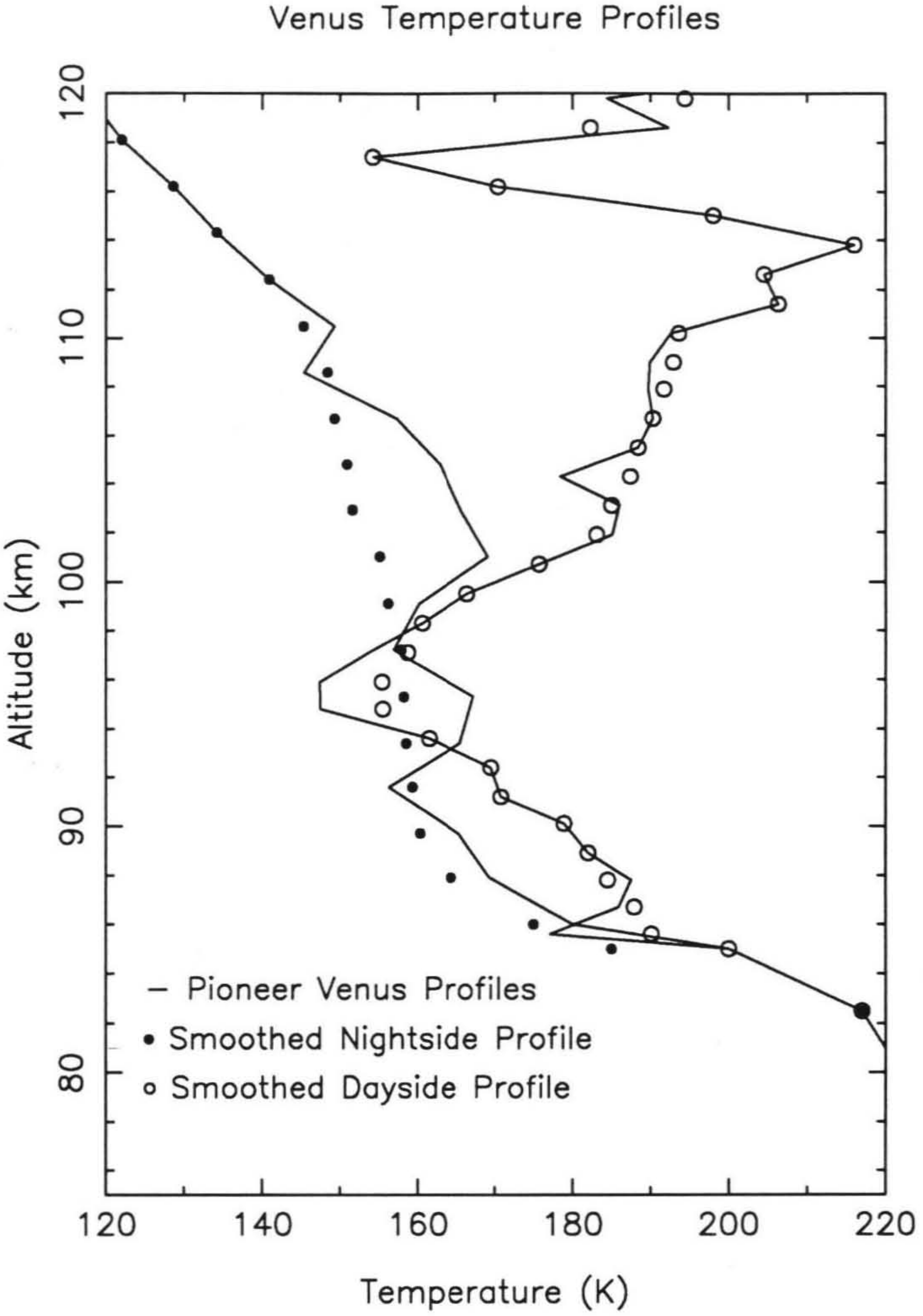

Figure 34. Diurnal temperature profiles used to calculate the CO core weighting functions against reference PV profiles.

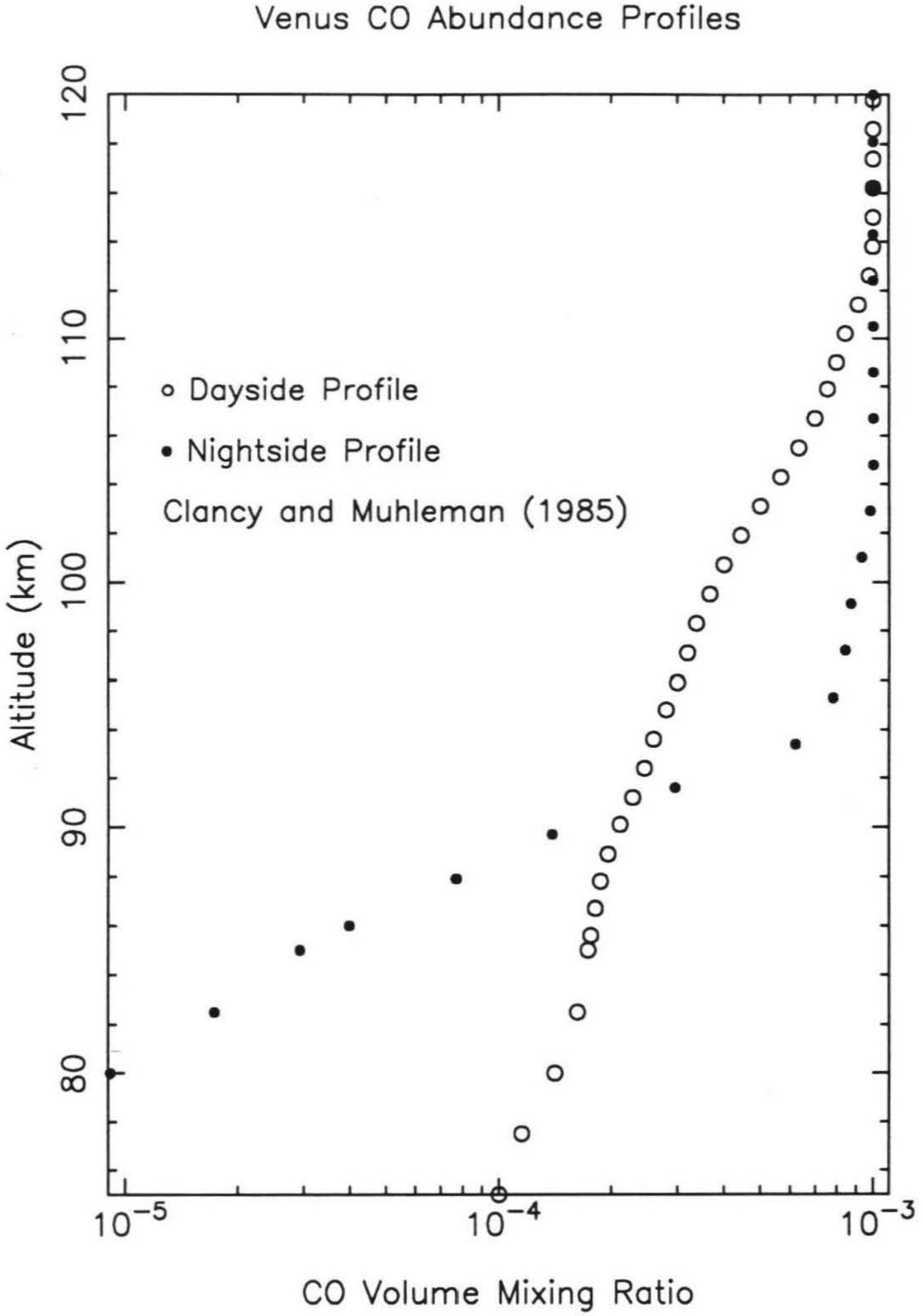

Figure 35. Diurnal CO mixing ratio profiles from single dish observations (Clancy and Muhleman 1985a) used in CO core weighting functions calculations.

the Van Vleck-Weisskopf, collisional broadening lineshape function and the doppler, thermal broadening lineshape function over frequency. The convolved lineshape function depends on both pressure and temperature as expressed by

$$f(\nu) = \int_{-\infty}^{\infty} \frac{1}{\pi} \frac{\Delta\nu_c}{(\nu_i - \nu_\circ - y)^2 + \Delta\nu_c^2)} \frac{ln2^{1/2}}{\pi} \frac{1}{\Delta\nu_d} e^{-ln2\frac{y^2}{\Delta\nu^2}}\, dy, \tag{28}$$

wherein y is a frequency variable, $\Delta\nu_c$ the collisional broadening width in Hz and $\Delta\nu_d$ the doppler broadening width in Hz. The collisional or pressure broadening width of an absorption line increases directly with pressure,

$$\Delta\nu_c = \gamma p(\frac{T_{ref}}{T})^{\alpha} \tag{29}$$

with γ the pressure broadening constant and the temperature exponent dependency α determined by laboratory measurements of the molecule within an ambient gas at references temperature T_{ref} and acting as a source of error in any atmospheric model. In this case, the reference temperature was at 300 °, α 0.75 and γ 0.122±.006 cm^{-1} atm^{-1} for CO molecules in a CO_2 gas (Varanasi 1975). Collisional broadening widths spread from 0.10 MHz at altitudes near 100 km to 20 MHz at altitudes about 80 km. The doppler broadening width is the half maximum power of a Maxwellian velocity distribution for a gas at temperature T

$$\Delta\nu_d = \frac{\nu_\circ}{c}(2R^{*}ln2)^{1/2}(\frac{T}{m})^{1/2} \tag{30}$$

with m the molecular weight of CO and R^{*} the universal gas constant. The doppler broadening width varies much less in Venus' upper mesosphere than the pressure broadening width since it depends only on temperature and is relatively dominant in the convolutional lineshape only at altitudes above 100 km. The doppler width increases from 0.10 MHz around 100 km to 0.11 MHz around 80 km.

Calculation of the absorption coefficient for a temperature weighting function given by equation (22) was done in each layer with either the nightside or dayside

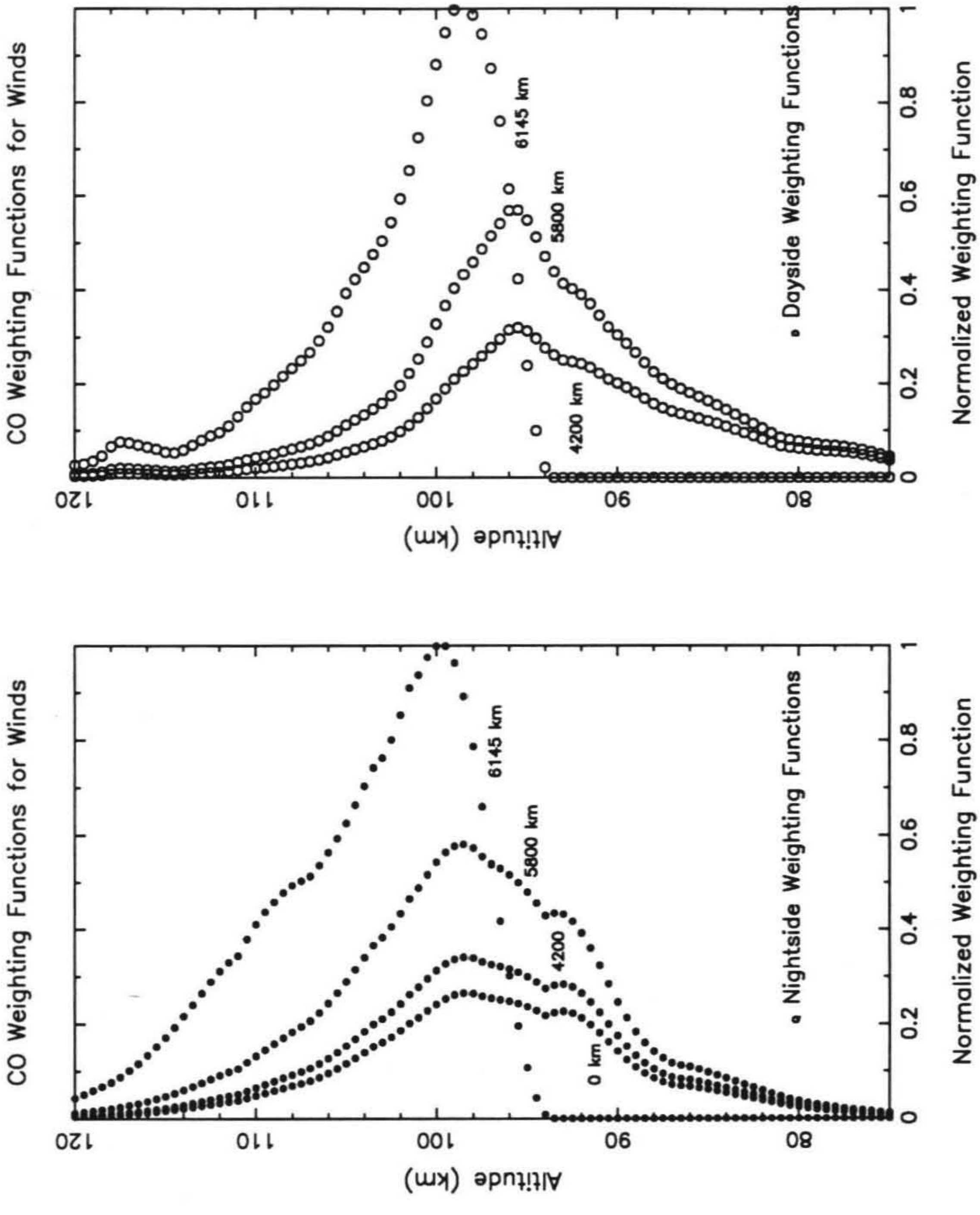

Figure 36. Normalized diurnal CO weighting functions at various radii for the inner 16 50kHz channels or over $\nu_o \pm 0.4$ MHz.

temperature, density, pressure and CO mixing ratio profiles as appropriate. The model does not assume any doppler shift to the absorption line's center and, so, does not include any wind shear effects. The weighting function was calculated and then averaged over the inner 16 channels of the 50 kHZ filterbank or $\nu_{\circ} \pm .4$ MHz since these frequency channels were used to do the radial wind measurements. Figures 34 and 35 show the smoothed Pioneer Venus profiles and diurnal CO abundance profiles (Clancy and Muhleman 1985ab) used in the calculations. Smoothed temperature profiles were used since the 92 km minimum in the nightside temperature profile and the 95 km minimum in the dayside temperature profile produced small maxima in the weighting function which, as discussed later in the chapter, are probably transient fluctuations.

5.2 Temperature Weighting Functions

Figure 36 shows the relevant normalized CO weighting functions at various radii for both the afternoon crescent across the disk and the remaining nightside portion. The weighting functions are, on average, 14 km wide at half-maximum on the nightside and 10 km wide at half-maximum on the dayside. The peak of the weighting function samples deeper into the atmosphere at the disk center than near the planet limb. On the dayside, for radii in the afternoon crescent, the center altitude moves from 95 km at a radius of 5700 km (approximately 15 hours and 23.7 hours LVT on the equator) to 99 km at a radius of 6145 km (approximately 14.1 hours and 0.6 hours LVT). On the nightside, the center altitude moves from 97 km at normal incidence to 103 km at a limb radius of 6145 km – higher altitudes than the dayside as the nightside CO abundance profile contains more CO above 96 km (see Figure 35). Even more interesting is the change in the weighting function's shape at the planet limb. About normal incidence near the planet center the CO opacity is less than one and the weighting function relatively broad. At limb incidence, the CO opacity is greater than one and the weighting function narrower, sampling mainly high mesospheric altitudes above a sharp cutoff at 95 km. The path length on the limb passes through only the outer atmospheric layers of the planet. Though these weighting functions will differ in shape with changes to the temperature and CO abundance profiles on Venus (see, e.g., Clancy and Muhleman 1991), such differences will not overturn the behavior of the weighting function as shown in Figure 36. These weighting functions are good estimates of where the 2.6 mm CO absorption line sampled the upper mesosphere of Venus. Therefore, the wind measurements are an average over roughly 12 km in altitude about a center at 97 km near normal incidence, moving upwards through the mesosphere to sample about 102 km along the planet limb above a sharp cutoff at 95 km.

6. Cyclostrophic Thermal Wind Equation

Early ground-based UV observations of cloud features revealed the cloudtop's large zonal speeds (Dollphus 1968; Boyer and Guerin 1969; Scott and Reese 1972). These large zonal speeds led Leovy (1973) to suggest a balance between the equator-to-pole pressure gradient from differential solar heating and the centrifugal force on a high zonal flow. With a decrease of average temperature from the equator to the poles, pressure surfaces in the atmosphere would have an equatorial bulge. A pressure gradient force would then be directed away from the bulge towards the poles. This pressure force could be balanced by the equatorward centrifugal force acting on a zonal flow that has a rotation rate increasing with height. This is called cyclostrophic balance.

Cyclostrophic balance is analogous to the Earth's geostrophic balance wherein the equator-to-pole pressure gradient is balanced by the Coriolis force acting on air parcels. Both balances come from the conservation of meridional momentum which

TABLE V

Equator-to-Pole Temperature Gradients

	1987			1985			Model
H(km)	ϕ:20-45°	ϕ:75-90°	$\delta T/\delta\phi$	ϕ:20-45°	ϕ:75-90°	$\delta T/\delta\phi$	$\delta T/\delta\phi$
60	240±5	238±5	-.04	250±5	230±5	-.06	-.22
70	218±5	230±5	+.24	220±5	238±5	+.16	-.11
80	188±5	214±5	+.52	200±10	210±5	-.50	-.02
90	164±20	175±10	+.22	180±30	155±50	-2.10	+.02

Note. Temperatures listed under 1987 and 1985 are from PV radio occultation measurements during those years (Clancy and Muhleman 1991). The temperature gradients are rough estimates based on the PV measurements except in the last column which contains a guessed poleward temperature gradient.

can be written in cartesian coordinates as

$$\frac{dv}{dt} - \frac{u^2 tan\phi}{a} + \frac{vw}{a} = -\frac{1}{\rho}\frac{\delta p}{\delta y} - fu + F_y \tag{31}$$

with the y-coordinate directed poleward, u, v, w the zonal, meridional, vertical velocities, ϕ latitude, a the planetary radius, F_y frictional forces and $f \equiv 2\Omega \sin\phi$ the Coriolis parameter with Ω the angular speed of rotation (Holton 1979). By assuming that the eddy (velocity products), meridional acceleration and friction terms are small, the pressure gradient term can be balanced by either the Coriolis force or, in Venus' case of a very small rotation Ω and large zonal speed u, the centrifugal force.

Cyclostrophic balance leads to a nonlinear equation for its thermal winds

$$\frac{u^2 tan\phi}{a} = -\frac{1}{\rho}\frac{\delta p}{\delta y}. \tag{32}$$

By using the definition of geopotential, the ideal gas law and the hydrostatic equation

$$\Phi \equiv g\,z$$

$$p = \rho R T$$

$$\frac{\delta p}{\delta z} = -\rho g, \tag{31}$$

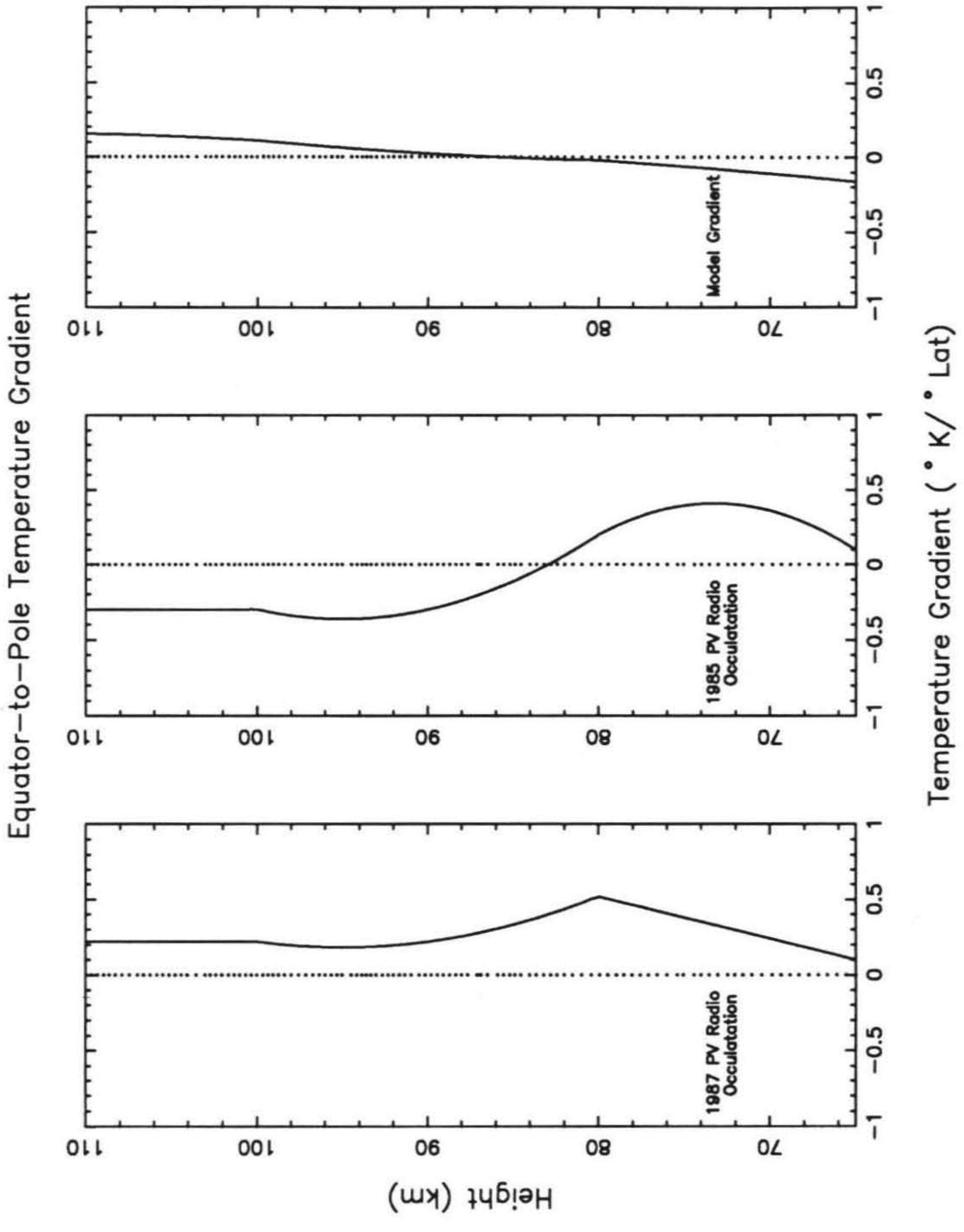

Figure 37. Equator-to-pole temperature gradients estimated from 1987 PV radio occultations, 1985 PV radio occultations and mean fitted zonal wind for spring 1988.

the cyclostrophic thermal wind equation can be rewritten in terms of a log pressure coordinate $\zeta \equiv \ln \frac{p_{ref}}{p}$ as

$$\frac{\delta (u^2)}{\delta \zeta} = - \frac{R}{tan\phi} \frac{\delta T}{\delta \phi}\bigg|_p, \tag{32}$$

where R is the gas constant of Venus (=191.4 J kg^{-1} K^{-1}) and p$_{ref}$ is the reference or lower boundary pressure (Schubert 1983). Thus, once assuming some lower boundary zonal speed profile over latitude, u($\zeta = 0$, ϕ), and temperature field, T(ζ,ϕ), it is possible to integrate equation (32) for vertical profiles of zonal speed over mid-latitudes. Obviously, cyclostrophic balance breaks down at the equator where tanϕ approaches zero and at the poles where tanϕ approaches infinity. Cyclostrophic balance would also break down when curvature and eddy terms become important to conservation of momentum.

Assuming that cyclostrophic balance could accurately describe the state of the mesosphere, equation (32) was integrated with the simple trapezoidal differencing formula

$$u^2_{z+1} = u^2_z - \frac{R\Delta\zeta}{2tan\phi}\Big(\frac{\delta T}{\delta \phi_{z+1}} + \frac{\delta T}{\delta \phi_z}\Big) \tag{33}$$

using z as a vertical index to examine the changes to a zonal flow over height. The vertical spacing in the calculations, $\Delta\zeta$, was equal to .1 and the latitudinal spacing was 2.5° from 15°-60° latitude. The lower boundary was at a cloudtop reference pressure of 98 mbars corresponding to roughly 65 km. The initial cloudtop zonal speed was assumed to be a constant 93 ms^{-1} over latitude based on the mean speeds found with PV ultraviolet images in five epochs between 1979 and 1985 (Rossow *et al.* 1990). Table V lists the most current temperature data for the Venus mesosphere – the Pioneer Venus radio occultation temperature measurements at four heights in the mesosphere in two wide latitude bands for 1985 and 1987. These temperature values were used to estimate temperature gradient profiles over height $\frac{\delta T}{\delta \phi}(\zeta)$. These 1985 and 1987 temperature gradient profiles (Fig. 37) were held constant over latitude

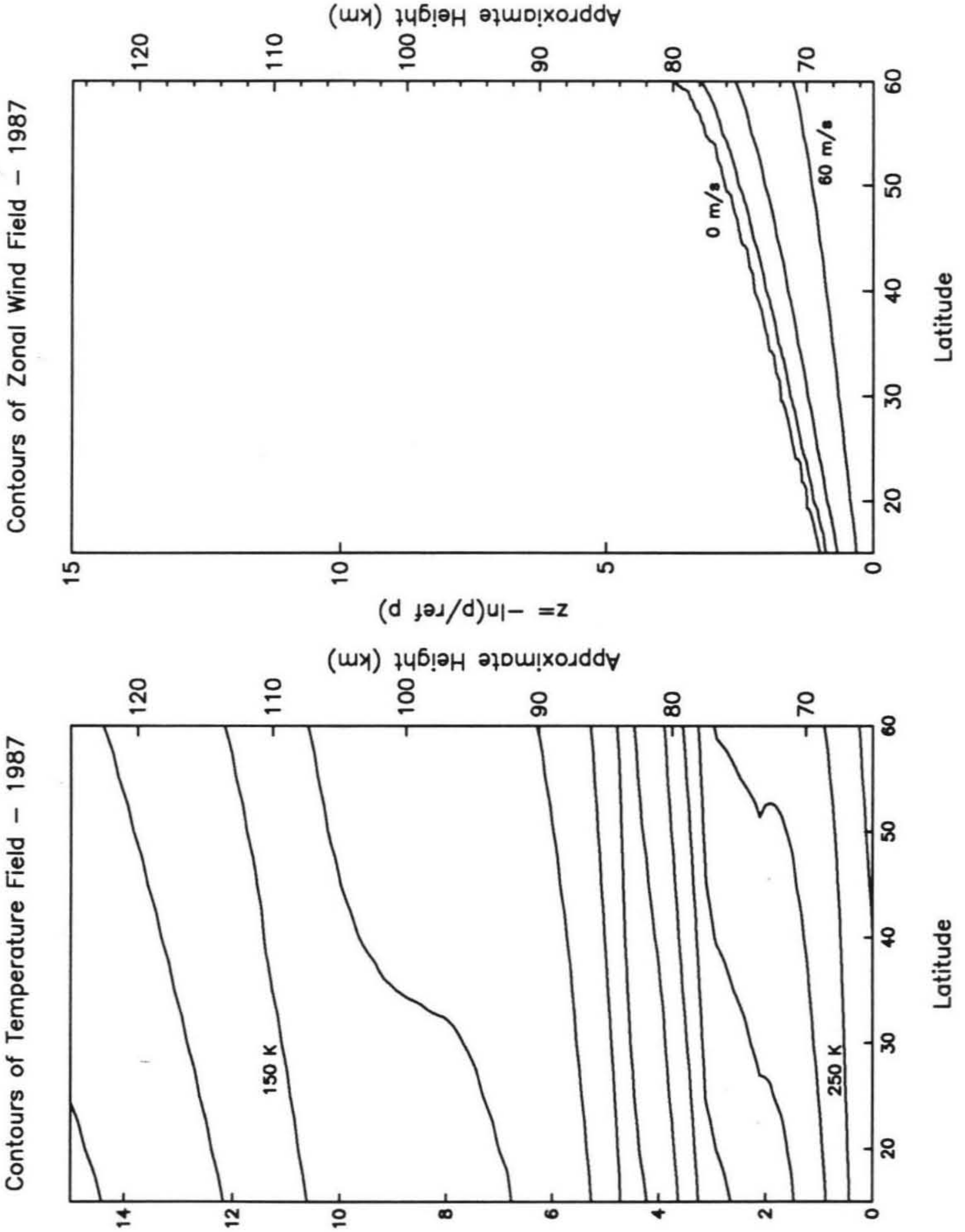

Figure 38a. The temperature field has contours every 10°K. It produces the wind field on the right (contours at 10 ms^{-1}) assuming cyclostrophic balance.

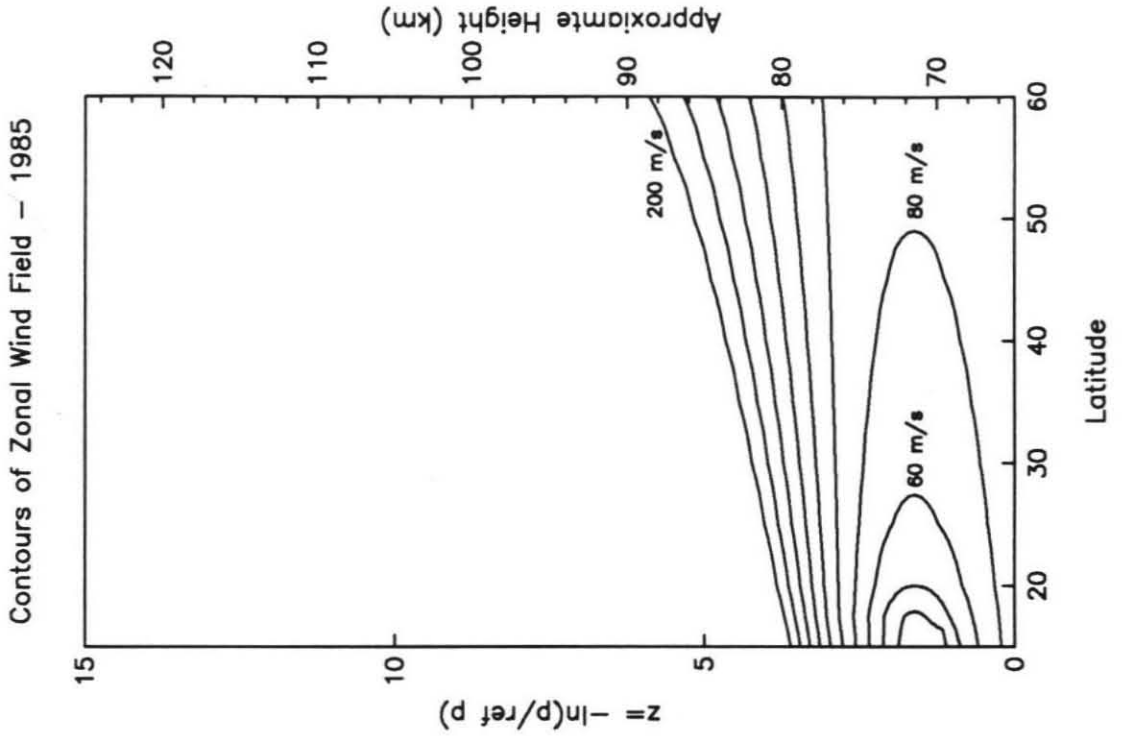
Contours of Zonal Wind Field – 1985
Approxiamte Height (km)
120
110
100
90
80
70
200 m/s
80 m/s
60 m/s
15
10
5
0
z= −ln(p/ref p)
20
30
40
50
60
Latitude

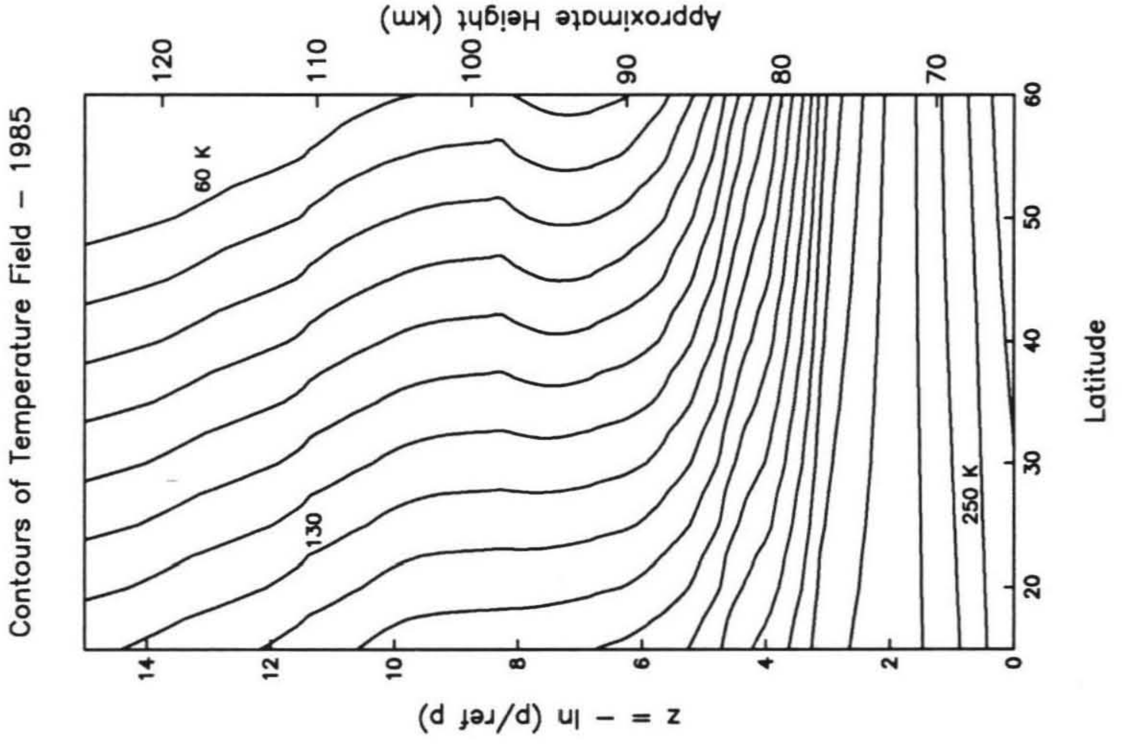
Contours of Temperature Field – 1985
Approximate Height (km)
120
110
100
90
80
70
60 K
130
250 K
14
12
10
8
6
4
2
0
z = − ln (p/ref p)
20
30
40
50
60
Latitude

Figure 38b.

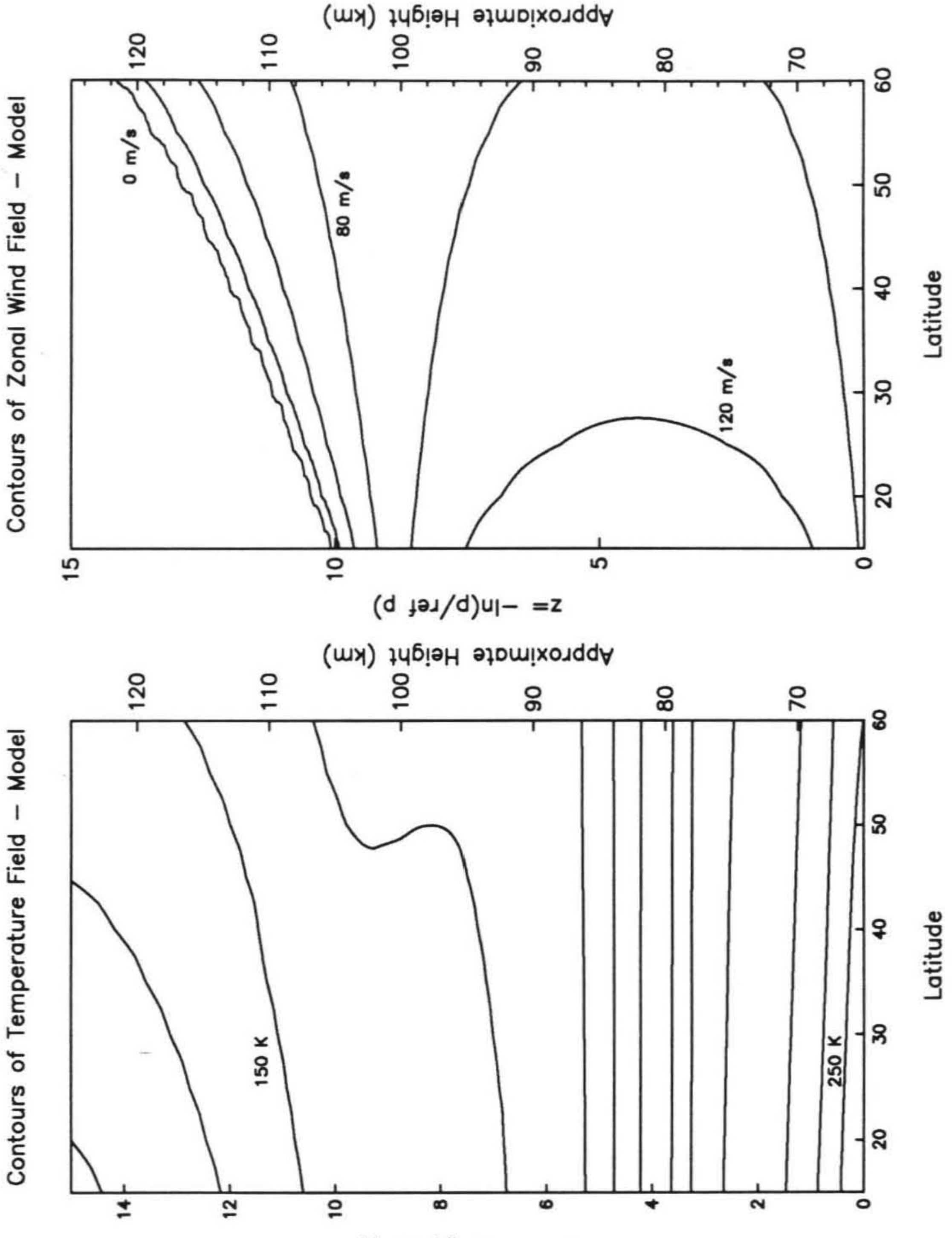
Contours of Zonal Wind Field – Model
Approxiamte Height (km)
120
110
100
90
80
70
0 m/s
80 m/s
120 m/s
15
10
5
0
z= −ln(p/ref p)
20
30
40
50
60
Latitude
Contours of Temperature Field – Model
Approximate Height (km)
120
110
100
90
80
70
150 K
250 K
14
12
10
8
6
4
2
0
z = − ln (p/ref p)
20
30
40
50
60
Latitude

Figure 38c.

given the limited temperature data and the wide latitude bands corresponding to the temperature measurements.

Figure 38 shows the resultant wind fields from the 1985 and 1987 temperature gradients. In both cases the positive temperature gradients at 70 km quickly damp the zonal flow over height and lead to breakdown of cyclostrophic balance. In the case of the estimated 1985 temperature gradients, zonal winds do build up again in the extremely negative temperature gradient at higher altitudes. In fact, the 1985 zonal winds reach high speeds under this extremely negative temperature gradient (Figure 38b). If the 70 km positive temperature gradient was reversed by changing the temperatures at 70 km by 10° or less, then the zonal winds would continue to persist to higher altitudes under a moderate temperature gradient profile (the rightmost panel of Figure 37). Figure 38c shows such a temperature gradient profile with height. The corresponding wind field in Figure 38c increases in zonal speed at 15° latitude to a maximum speed of 140 ms^{-1} at roughly 85 km and then decreases with height until zero speed at roughly 108 km. Applying a normal incidence nightside weighting function (see Figure 36) to the zonal profile at 15° latitude gives an averaged speed of 106 ms^{-1}. A moderate temperature gradient profile with height can, therefore, reproduce zonal speeds similar to those measured in 1988 at OVRO.

7. Discussion

A brief discussion of this chapter's results is given here. Chapter VI will give a fuller summary of the wind analysis' results and attempt to integrate with results from the other chapters.

7.1 Mesospheric Zonal Winds versus Cyclostrophic Models

Our analysis of 1988 2.6 mm CO lines found doppler shifts due to strong, horizontal winds moving westward across the Venusian evening terminator in the upper mesosphere of Venus near an altitude of roughly 99 km. Smoothed radial wind values best matched a zonal flow with a mean speed of 132±10 ms^{-1} based on least squares fits to model flows. This fitted value agrees relatively with unsmoothed limb measurements of the horizontal westward flow, characterized by mean speeds of 106±10 ms^{-1} on the nightside west limb and 85±8 ms^{-1} on the dayside east limb.

The difference of roughly 25 ms^{-1} between the fitted zonal speed and the more direct limb speeds may reflect the different altitudes sampled by the smoothed measurements and the limb measurements. The nightside and afternoon limb measurements correspond to local times of roughly 0.3 hours and 14.4 hours respectively (see Table III). The smoothed radial wind measurements, on the other hand, exclude local times along the limbs and sample between the hours of 22.2 and 16.5. These local times correspond to radii which range between 0 km and 4200 km for the smoothed measurements and between 5800 km and 6145 km for the limb measurements. As shown in Figure 36, the weighting function for the limb measurements see higher altitudes - several pressure scale heights above weighting functions for the smoothed measurements. The roughly 25 ms^{-1} difference between the fitted zonal speed and the limb speeds may then be a decrease to the zonal flow with increasing altitude in the upper mesosphere. However, this argument is speculative as the 25 ms^{-1} difference between the mean limb and fitted speeds is roughly equal to error bars on the unsmoothed radial wind measurements.

Our results disagreed with some earlier results from cyclostrophic models employed to constrain dynamics in the Venus mesosphere based on temperature profiles measured between 1979 to 1981 (Taylor *et al.* 1980; Newman *et al.* 1984). These cyclostrophic models assumed values for the zonal flow at the cloud tops and, in some, an eddy viscosity coefficient to predict the change in the zonal superrotation with increasing altitude given latitudinal temperature data. The models using OIR data and allowing for frictional effects from eddy viscosity found rapid decrease in zonal velocities with height (Elson 1979; Taylor *et al.* 1980). Yet, using the North (60.2°N and 3:35 AM) and Day (31.3°S, 6:46 AM) PV entry probe data, Seiff and others (1980) found strong zonal speeds reaching a maximum of 155 ms^{-1} near 68 km and decreasing rapidly after 120 ms^{-1} at 95 km. They had assumed a mean cloud top speed of 150 ms^{-1} at 70 km and no frictional eddy effects. Lower cloud top velocities would have led to lower zonal speeds from a cyclostrophic model (Schubert *et al.* 1980). Later PVO radio occultation temperature data analyzed through 1981 by Newman *et al.* (1984), however, again found a decrease to the lower atmosphere's superrotation with altitude. The outcome from these cyclostrophic models relies mainly on the direction of the meridional pressure or, equivalently, the temperature gradient. The Pioneer Venus OIR data's warmer north pole temperatures led to a rapid decrease in the zonal flow above the clouds and departure from cyclostrophic balance. The Pioneer Venus probes contrarily saw lower pressures versus altitude along the North probe's descent than along the Day probe's descent. This led to a negative temperature gradient with latitude and, consequently, to zonal winds and cyclostrophic balance above the cloud tops. Given that the probe data consisted of only two *insitu* measurements versus the zonally averaged temperature data from the OIR instrument, the wind estimates from the OIR data may have given a more accurate estimate of the mesospheric wind field during 1979. Yet, only a change of 10-15 K would have been needed to reverse the early PV OIR positive temperature gradients over latitude and find zonal velocities above the cloud tops.

Perhaps these cyclostrophic models' variables had different values in the spring of 1988 compared to the period of 1979-1981. Perhaps cyclostrophic balance does not sufficiently describe the dynamics in Venus' upper mesosphere. The relevant variables which may have changed with epoch are the horizontal eddy viscosity coefficient, the mean value for cloud top zonal velocities, and, most importantly, the latitudinal temperature gradient. For agreement with our wind measurements, cyclostrophic models would require a low viscosity coefficient, e.g., $\leq 2\times10^8$ m^{2}s^{-1}, a mean cloud top speed of roughly 120 ms^{-1}, and a negative or, at least, zero temperature gradient towards the poles (Elson 1979; Taylor *et al.* 1980; Seiff *et al.* 1980; Newman*et al.* 1984). These values for the models' parameters would produce the extension of the lower atmosphere's zonal velocities into the upper mesosphere and a dynamical explanation of our wind measurements.

The most controversial change required in parameter values would be the zero poleward temperature gradient. Only the few PV entry probe pressure profiles allowed for a negative gradient in 1979 (Seiff *et al.* 1980). Zonal averages of the PV OIR radiometric temperature profiles of the same year indicated a positive gradient (Taylor *et al.* 1980). More recent work by Newman *et al.*, 1984, used PV radio occultation data gathered between 1978 and 1981 sampled the atmosphere up to 80 km and found a positive poleward gradient. However, later radio occultation work by Kliore and Mullen (1988) spanned a period from 1979 to 1987 and indicated cooler polar mesospheric temperatures between 60 and 90 km during the solar minimum period of 1984 to 1987. This polar cooling was, in fact, accompanied by heating at some low latitudes and no cooling elsewhere at low latitudes, possibly setting up a zero or negative temperature gradient. Further indication for temporal variation of the temperature structure in Venus' upper mesosphere for low to mid-latitudes was documented by Clancy and Muhleman (1991). Their disk-averaged CO spectra from inferior conjunctions of Venus in 1982, 1985, 1986, 1988 and 1990 revealed large changes in temperature profiles for the upper mesosphere. The 1985 and 1986 profiles, in particular, appear warmed between 85-100 km by 20-40 K unlike the other inferior conjunctions which match the PV 1979 temperature profiles. Even though separate polar and low-latitude temperature profiles cannot be derived from their observations, these CO single-dish spectra clearly document the variable, possibly periodic, nature of the mesosphere's temperature structure. This variable nature admits a possible zero temperature gradient over latitude in the spring of 1988 and extension of the lower atmosphere' superrotation up into the upper mesosphere.

7.2 Possible Mesospheric Subsolar-to-Antisolar Component

The existence of a subsolar-to-antisolar flow in Venus' mesosphere has not been contradicted or supported by our observations. Earlier researchers have suggested a superposition of a zonal flow and a subsolar-to-antisolar flow in various thermospheric data sets. Most recently, Goldstein and others (Goldstein 1990; Goldstein 1989; Goldstein *et al.* 1988), with IR heterodyne observations, reported a 25 ms^{-1} zonal component mixed with a 120 ms^{-1} cross terminator, subsolar-to-antisolar component at altitudes spanning 110±10 km for the period of 1985-1987. Our 1988 measurements, sampling lower in the atmosphere by roughly 15 km, are instead dominated by a zonal flow pattern. A smaller subsolar-to-antisolar component may be present in our observations but obscured by Venus' unfavorable aspect and the beam artifacts in the map of radial wind speeds. Our measurements may place an upper limit on its cross terminator speeds at approximately 40 ms^{-1} based model results at high latitudes where correlation coefficients allowed least squares fits for a superposition of zonal and subsolar-to-antisolar flows. If a subsolar-to-antisolar component is present, our observations combined with the IR heterodyne observations may see *the* transitional region between the upper and lower atmospheres' circulation patterns over the altitudes of approximately 90-120 km.

Chapter V 1 MHz and 50 kHz Data: CO Abundance.

Analysis of CO rotational absorption lines has traditionally provided disk-averaged temperature and CO mixing ratio profiles in the upper mesosphere of Venus. Recent single-dish observations by Clancy and Muhleman (1991) are used in this chapter to constrain absolute absorption values for the OVRO lines. Their comprehensive disk-averaged CO and temperature results, obtained from observations made over the past decade, are the primary source of comparison. This work differs from their and others analyses in three respects. First, only one rotational absorption line was observed at OVRO in the spring of 1988. Consequently only one unknown parameter, the CO mixing ratio profile, can be determined with the data. The mesospheric temperature profile is assumed to be a "known" parameter. Secondly, the observed CO lines were not hand-fitted to a model atmosphere's synthetic line. The observed absorption lines were instead inverted with an iterative algorithm developed by Mark Gurwell using an analytical expression for the change in brightness temperature with CO abundance. Lastly, and most importantly, the OVRO data resolves the absorption line across the planet. The final inverted CO profiles are localized profiles, revealing the CO distribution over local time and latitude. This work was carried out in co-operation with Gurwell and Muhleman who have analyzed the 1986 OVRO synthesis data of Venus.

1. Kitt Peak Single Dish Lines

The nightside 2.6 mm CO line measured by Clancy and Muhleman (1991) during Venus' 1988 inferior conjunction with the NRAO millimeter observatory's 12-meter antenna at Kitt Peak, Arizona, is shown in Figure 39. Their absorption line was sampled in 250 kHz channels spanning a total bandwidth of 64 MHz about the line center. The line has an absorption depth of 26% and a width of several MHz

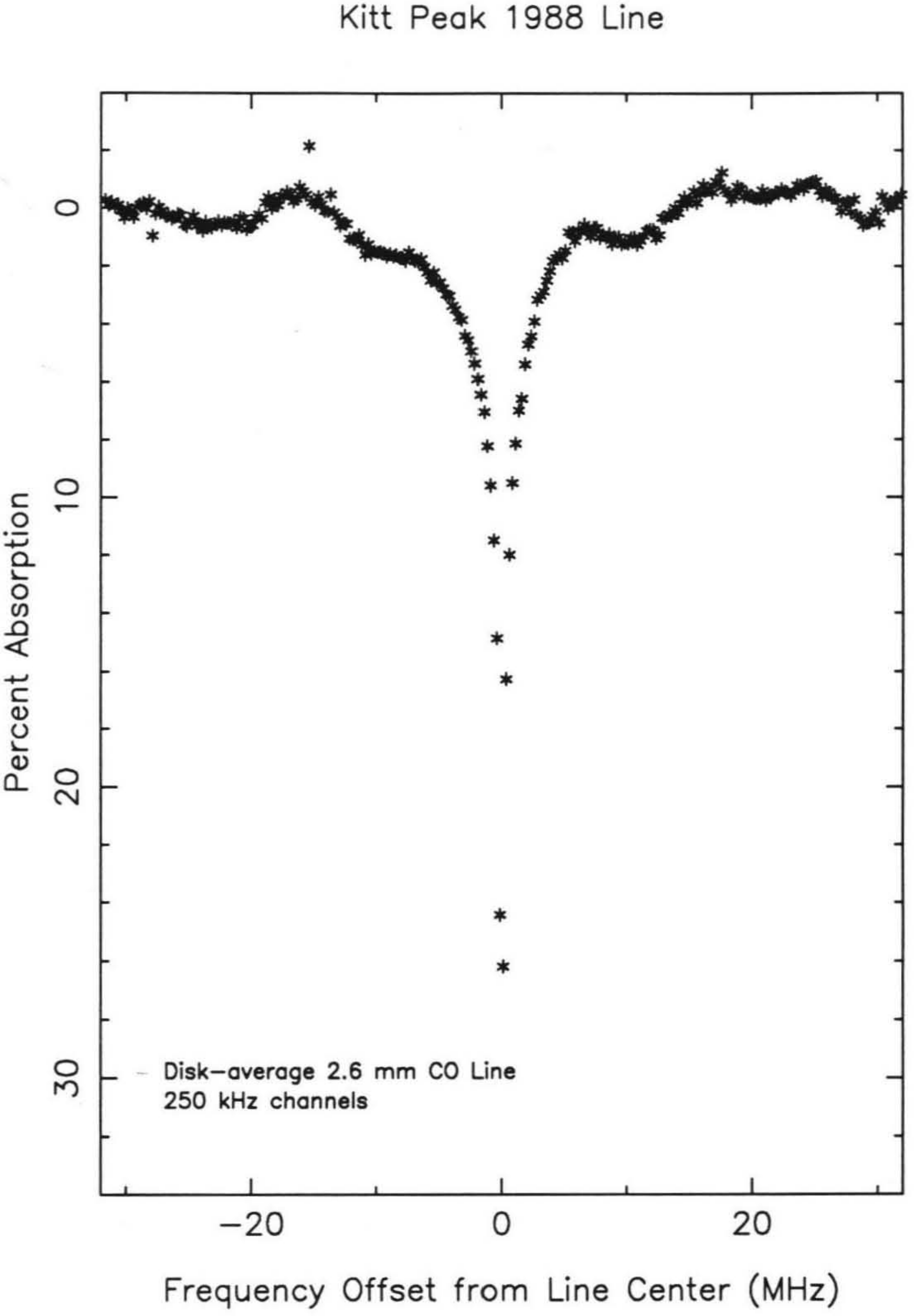

Figure 39. The disk-averaged nightside 2.6 mm CO line measured by Clancy and Muhleman (1991) at Kitt Peak in the spring of 1988.

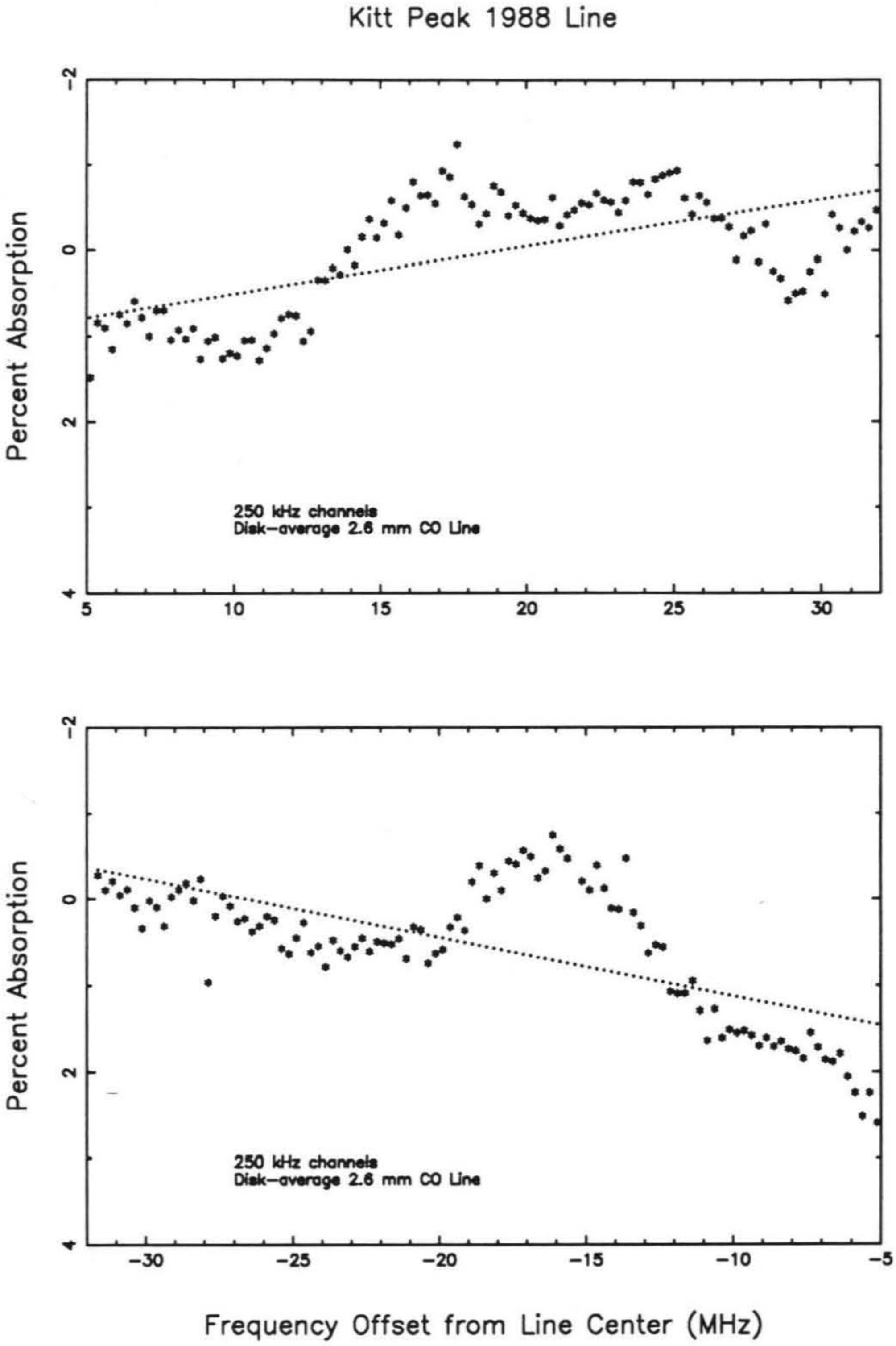

Figure 40. Linear fits to the wings of the disk-averaged 2.6 mm line which were averaged to get an absorption value of .43% at $\nu_\circ \pm 15.5$ MHz.

and is similar in lineshape to previously observed Venus nightside lines. The angular resolution of the antenna's beam was roughly 60" in diameter on a planetary disk 42" in diameter. Therefore, the results from their analysis reflect disk-averaged values for the Venus mesosphere over the low to mid-latitudes. During their 1988 observations, the subearth point was located at 8:30 PM Venus local time - an hour later than the subearth point of the OVRO data. Nonetheless, their observations are treated as coincident with the OVRO observations and are used to constrain the disk-resolved OVRO data.

As described in section 6 of Chapter II, the absolute values for the line-to-continuum ratios of the merged 1 MHz and 50 kHz lines had to be constrained by the single-dish CO line. Figure 40 shows linear fits to the near-continuum wings of the Kitt Peak line. A linear fit was not removed from the Kitt Peak line. Rather, the values of these linear fits were averaged to find a mean absorption value in the line wings at $\nu_\circ \pm 15.5$ MHz. A standing wave runs through the baseline of this single-dish line so a more sophisticated fit to the line was not attempted. An average absorption value based on these linear fits is 0.43% or, equivalently, a line-to-continuum ratio of 0.9957 at $\nu_\circ \pm 15.5$ MHz. The merged OVRO lines were pinned to this continuum value at $\nu_\circ \pm 15.5$ MHz in each cell so that the resultant lines and their depths could be used to determine the local CO profiles. This "pinning" was considered reasonable because the Kitt Peak observation was independent of and coincident with the OVRO observations. Furthermore, the OVRO 1 MHz filterbank spectra, before merging them with the 50 kHz filterbank spectra, were narrow. The 1MHz filterbank lines had resonant absorption only within a few MHz about the line center and showed minimal resonant absorption at frequencies about $\nu_\circ \pm 15.5$ MHz similar to the Kitt Peak line.

The Kitt Peak observations also measured the optically thick 1.3 mm ^{12}CO rotational line ($\tau \gg 1$ at line center) and the optically thin 1.4 mm ^{13}CO line ($\tau \ll 1$ at line center). The difference in the lines' optical thickness lends itself to determining both temperature and CO abundance. This can be seen by integrating the brightness temperature equation (16) of Chapter III for an atmosphere of only one layer at temperature T and using the definition of opacity τ

$$\tau(\nu, z) \equiv \int k(\nu, z)\, dz \tag{34}$$

and the proportionality

$$\tau \propto \frac{N_{CO}}{T^2} \tag{35}$$

for the resonant CO absorption coefficient which can be seen in equation (27) of section 5, Chapter IV. These expressions simplify the integrated solution of equation (16) for the brightness temperature of an isothermal atmosphere over a continuum temperature to

$$T_B(\nu) = T_c e^{-\tau} + T(1 - e^{-\tau}). \tag{36}$$

A description of the line formed in this layer is then

$$\frac{T_B}{T_c} = \frac{T}{T_c} + [1 - \frac{T}{T_c}]e^{-\tau(\nu)}, \tag{37}$$

where T_c is the continuum temperature. In the case of an optically thin line, the exponent can be simplified to the first two terms of the exponential series so

$$\frac{T_B}{T_c} = 1 + \tau(\frac{T - T_c}{T_c}) \tag{38}$$

This leads to the relationship

$$\frac{T_B}{T_c} \propto \frac{N_{CO}}{T^2}(\frac{T - T_c}{T_c}) \tag{39}$$

between the line emission and the layer's CO abundance and temperature.

In the case of Venus' mesosphere, T is typically less then T_c so absorption will occur according to equation (37). In optically thin areas of a line where τ is much

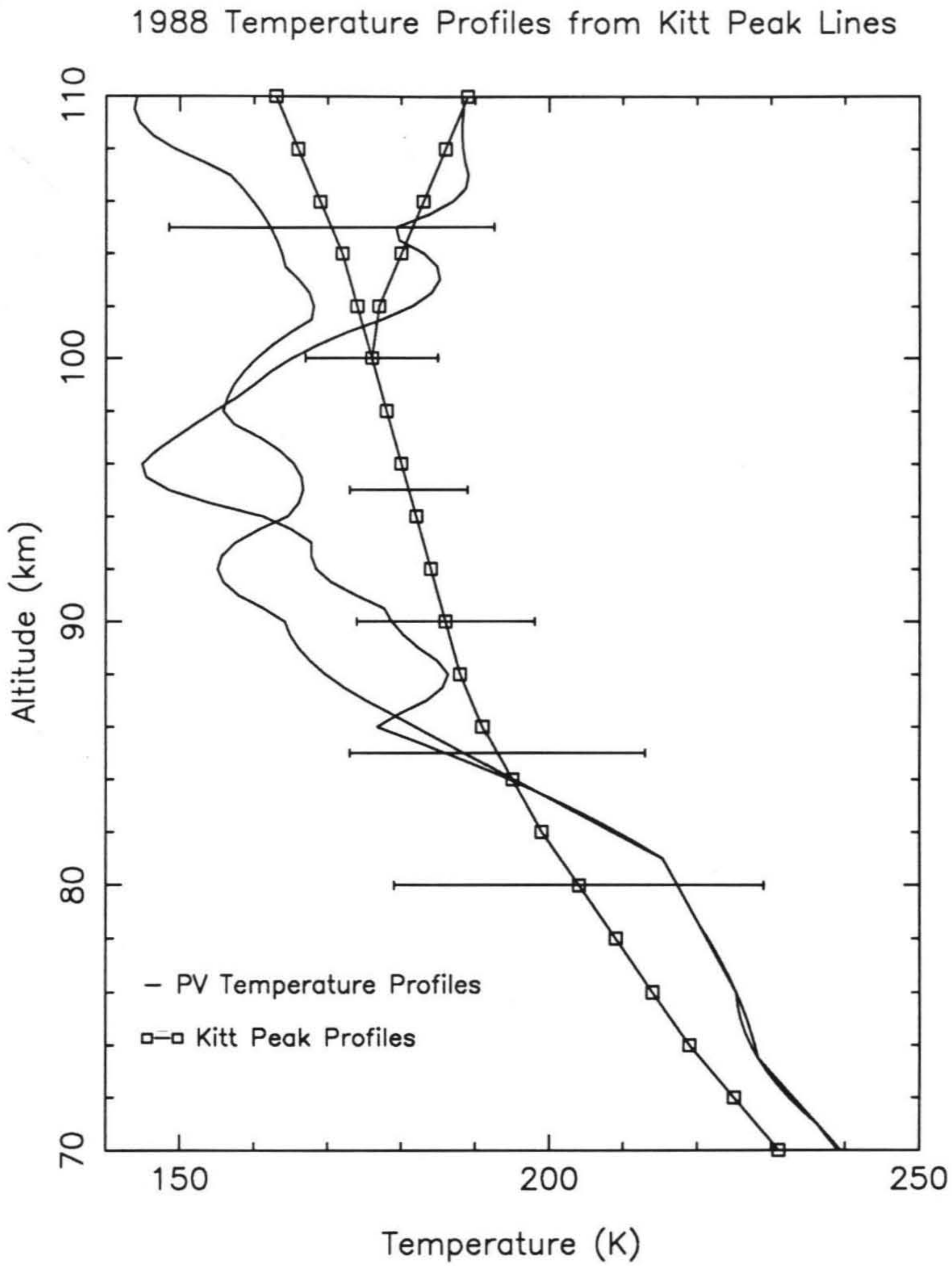

Figure 41. 1988 disk-averaged temperature profile from synthetic line fits to Kitt Peak data.

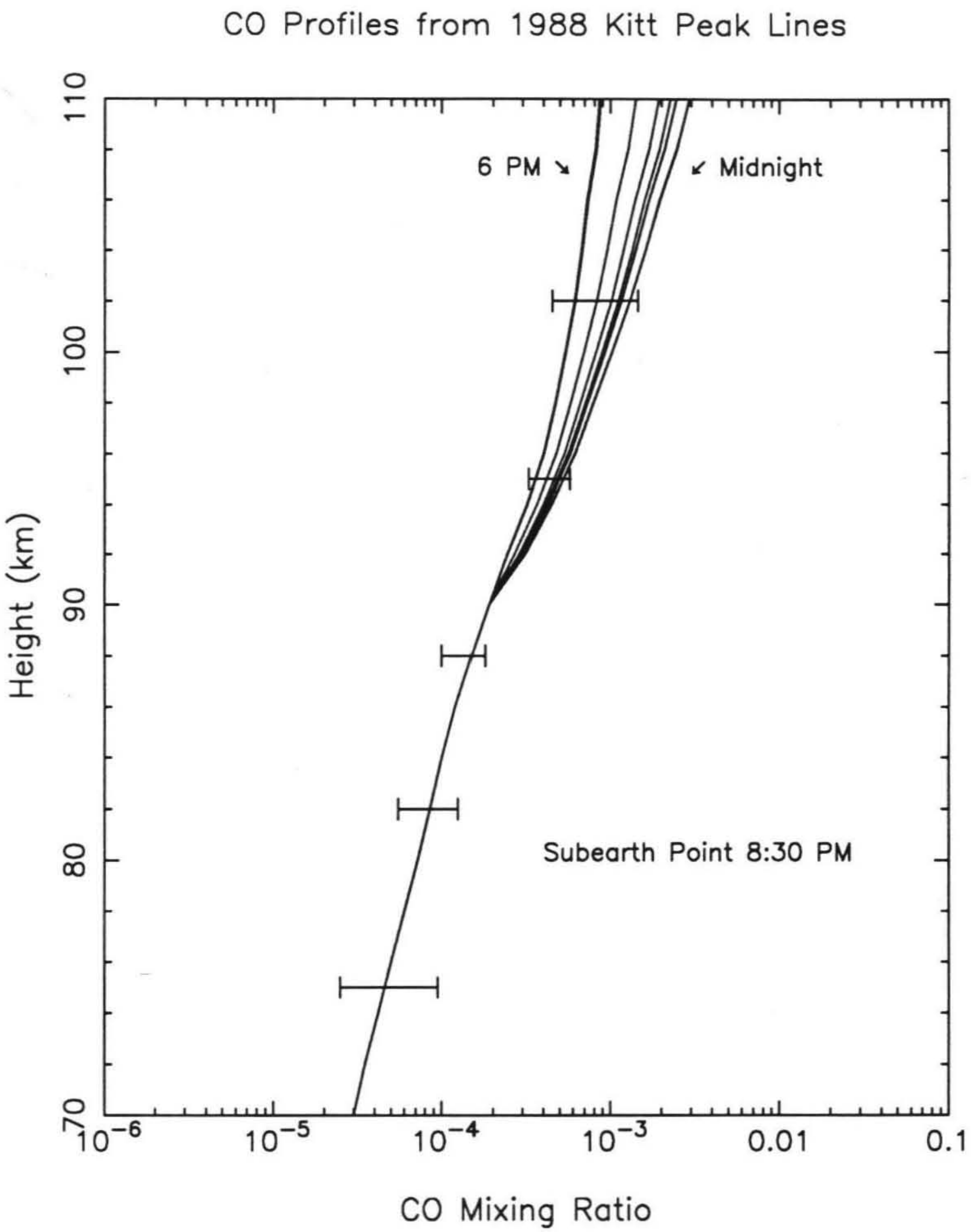

Figure 42. 1988 disk-averaged CO volume mixing ratio profile from synthetic line fits to Kitt Peak data.

less then one, the absorption will be more dependent upon CO abundance than on temperature (as described by equation (39)). In optically thick portions of a line, absorption will be more dependent upon the temperature of the layer (as described by equation (37)). The 2.6 mm CO line falls between these two extreme cases. It has an optical depth that almost reaches unity at line center and, so, responds mainly to the atmosphere's CO abundance. Therefore, coincident observations of the thick 1.3 mm CO line, the thin 1.4 mm CO line and the 2.6 mm CO line complement each other in sensitivity to atmospheric temperature and molecular abundance.

Clancy and Muhleman used the technique of coincidently observed absorption lines to determine both temperature and CO profiles. The single-dish CO lines were hand-fitted to synthetic spectra. The mesospheric CO and temperature profiles of the model atmosphere are varied until the synthetic lines match the observed lines. They used an atmospheric model based on the Muhleman *et al.* (1979) model described in section 2 of Chapter III. This model atmosphere was developed to allow variation of the CO profile over local time and to begin the atmosphere at a lower boundary height corresponding to a continuum temperature of 335 K rather than ray-tracing to the surface (Clancy and Muhleman 1985a). Figures 41 and 42 show the resultant temperature profile. This profile diverges above 100 km to agree with diurnal temperatures of thermospheric models, and CO mixing ratio distribution respectively. These figures also show estimated error bars for the temperature and CO profiles at relevant heights. The variation of the error bars over height indicate that this technique of measuring Venus mesosphere works best between 85 and 100 km. The following section provides formal weighting functions for the 2.6 mm CO line which will support this interpretation.

2. Full Line Weighting Functions

Figure 43 shows the diurnal temperature profiles used in the CO inversion

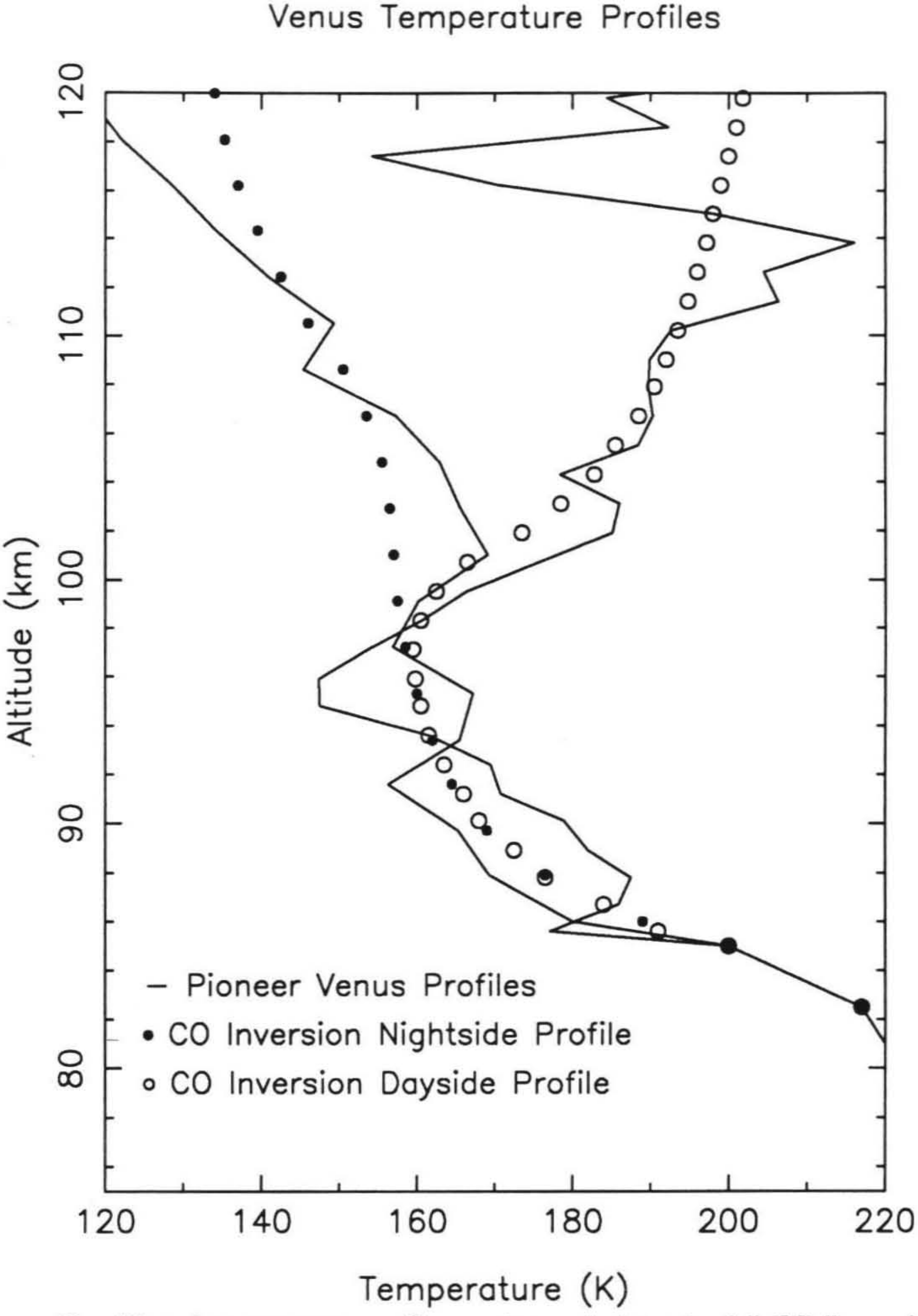

Figure 43. Diurnal temperature profiles used to calculate the full CO line weighting functions and used in CO inversion analysis. They are referred to as the 'smooth' profiles in contrast to the "fluctuating" temperature profiles in Figure 34.

analysis and in the calculations of weighting functions for both the 1 MHz and 50 kHz data. These temperature profiles are an average of the Pioneer Venus temperature profiles and were chosen by inspection by Gurwell and Muhleman. Unlike the "fluctuating" temperature profiles used to calculate weighting functions for the wind analysis (Figure 34), these profiles do not have transient inversion layers due to atmospheric waves. Also, these profiles are identical up to 98 km. Above 98 km, the dayside and nightside temperature profiles diverge as measured by the PV descent probes, approaching thermospheric models' temperatures of 130 K for the nightside and 300 K for the dayside around 150 km. This simple vertical structure for the diurnal temperature profiles was chosen to avoid introducing any vertical fluctuations to the CO profiles. The fine structure present in the PV temperature profiles is almost certainly incidental and probably created by transient atmospheric waves present during the isolated descents of the PV probes.

Normalized weighting functions for both nightside and dayside conditions are shown in Figure 44 at several radii. The weighting functions are temperature weighting functions, as described by equation (22) in section 3 of Chapter III. Resonant CO absorption in the upper mesosphere serves as the primary source of sensitivity to the atmosphere at 2.6 mm, as described in section 5 of Chapter IV. The standard diurnal CO mixing ratio profiles of Clancy and Muhleman (1985a), shown in Figure 35, were used to calculate the weighting functions. The calculations were done with the "smooth" temperature profiles (Figure 43) and with a frequency resolution of either 1 MHz or 50 kHz. These estimates of atmospheric sensitivity over height were averaged separately for both frequency resolutions to distinguish between the atmospheric sampling by the 1 MHz filterbank channels and the 50 kHz filterbank channels.

The 2.6 mm weighting functions of Figure 44 show behavior similar to the

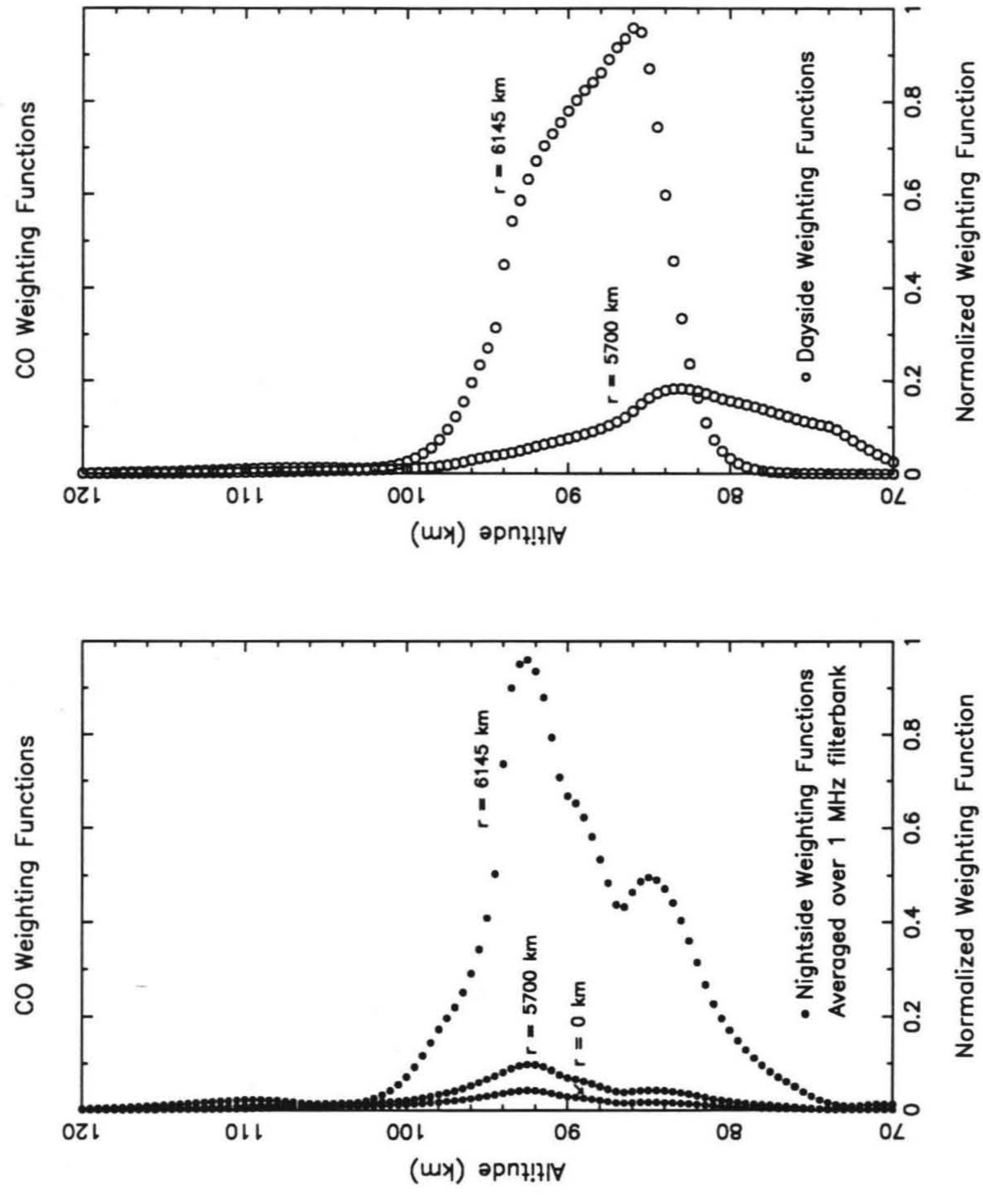

Figure 44a. Normalized diurnal CO weighting functions at various radii calculated with a 1 MHz frequency resolution and then averaged over $\nu_\circ \pm 15.5$ MHz.

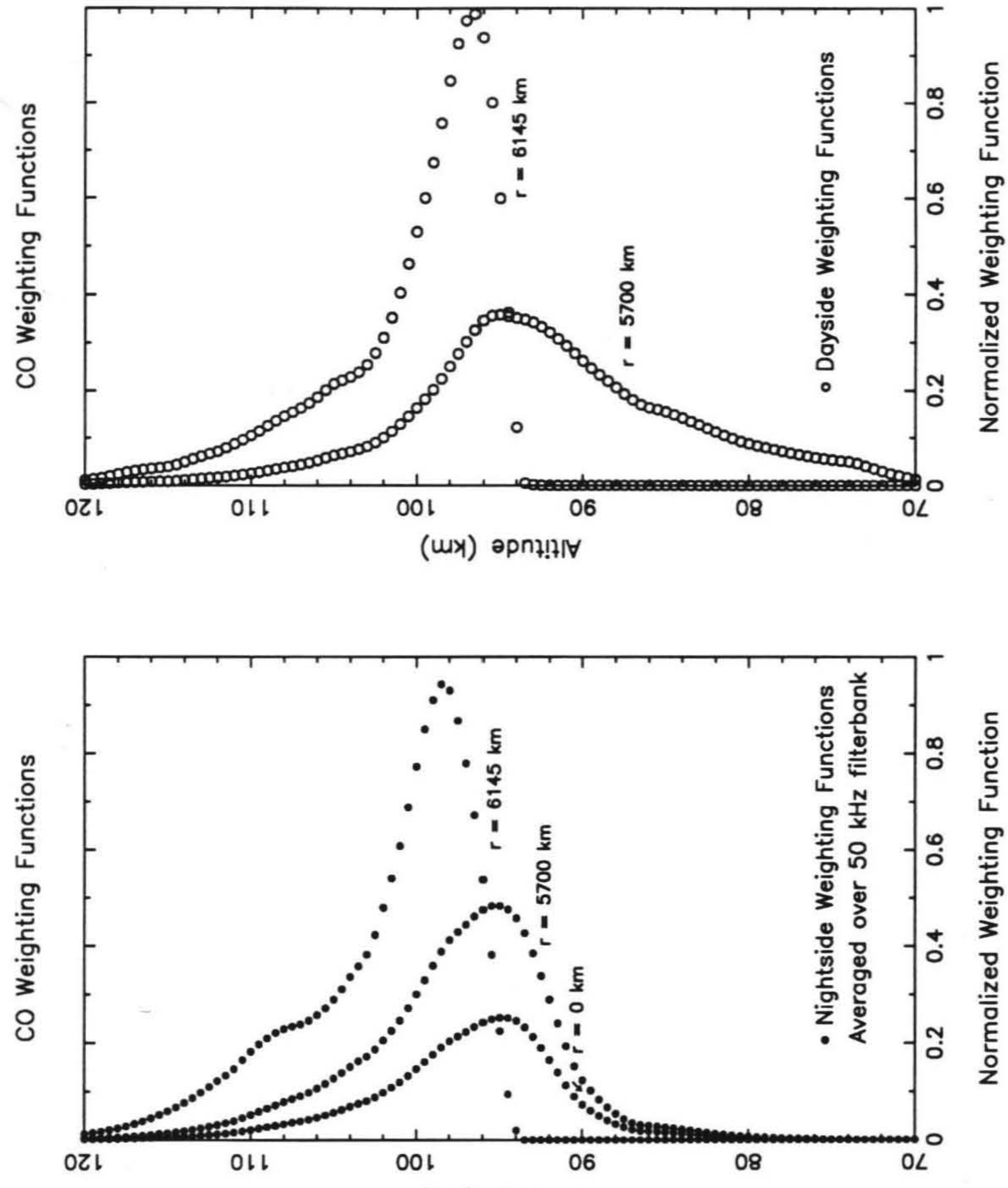

Figure 44b. Normalized diurnal CO weighting functions at various radii calculated with a 50 kHz frequency resolution and then averaged over $\nu_{\circ}\pm.775$ MHz.

weighting functions calculated for just the CO line core (i.e., for $\nu_\circ \pm 0.40$ MHz) in the wind analysis of Chapter IV (c.f. Figure 36). The atmospheric weighting peaks at higher altitudes for radii closer to the limb than at normal incidence. The pathlength through the upper mesosphere's interacting CO molecules is longer at larger radii, so the weighting functions at larger radii are greater than at normal incidence. The weighting functions averaged across the entire line are 5-10 km wider than those calculated for just the CO line core. The 1 MHz weighting functions display sensitivity to altitudes between 75 and 96 km. The 50 kHz weighting functions slightly overlap and then extend sensitivity to altitudes from 94 to 104 km. Thus, the volume mixing ratio profiles derived from the merged OVRO 2.6 mm CO lines will constrain CO abundance between roughly 75 and 104 km. The best CO abundance determination from the observed lines will occur between 90 and 100 km based on these theoretical weighting functions.

3. Inversion Algorithm for CO Profiles

I am greatly indebted to Mark Gurwell for much of the following material in this section.

The radiative transfer equation relates the thermal emission of an atmosphere at any frequency to its meteorological state

$$I_\nu = I_\circ e^{-\tau_\nu} + \int B_\nu e^{-\tau_\nu} k dz, \tag{40}$$

where I_ν is the atmosphere's intensity at a given frequency, B_ν the Planck function, τ_ν the atmospheric opacity at a given frequency and $I_\circ$ the lower boundary's intensity (Chandrasekhar 1960). This equation is dominated by the integrand's product of the Planck function and the derivative of the atmospheric transmittance. Therefore, it depends upon the atmosphere's temperature structure and the atmosphere's distribution of absorbers. With atmospheric profiles, the radiative transfer equation can be integrated numerically for the atmosphere's intensity at any frequency. That is referred to as the forward problem. The inverse problem is to estimate atmospheric conditions based on observed thermal emission. The inverse problem is much more complicated since the inverse solution of the radiative transfer equation is nonunique. There can be many combinations of temperature and absorber profiles which can create one set of observed intensities. The inverse problem is under-constrained and a solution will be dependent upon the algorithm employed to solve for atmospheric profiles within the radiative transfer equation's integrand. Such an algorithm will necessarily impose *apriori* constraints in order to solve the inverse problem.

The inversion methods used to retrieve temperature or absorber profiles generally fall into two categories: (1) statistical methods which linearize the Planck function using abundant climatological data (Wark and Fleming 1966) or (2) iterative methods which use analytical forms for the retrieved profile and/or assumption about the radiative transfer equation (Twomey 1963; Chahine 1970; Smith 1970). Statistical methods would be inappropriate as Venus' climatological data are too sparse to generate representative statistical functions. Therefore the latter method was used to determine CO abundance profiles based on the 1988 OVRO data. The iterative inversion that was used did not assume an analytical form for the CO profile. Instead, the iterative algorithm employed calculated partial derivatives for the brightness temperature at each frequency with respect to the CO mixing ratio. It compared the synthetic CO line (the model's brightness temperatures over frequency) associated with these partial derivatives to the observed CO line. Next it used the partial derivatives to estimate changes to the CO mixing ratio which will decrease the difference, or residuals, between the synthetic and observed brightness temperatures. The algorithm iteratively improved the CO mixing ratio profile until the residuals decrease to fall below the noise on the observed line. This inversion method is essentially a linearized least- squares problem wherein the measured spectrum is a weighted sum of an atmospheric parameter. This can be expressed as a set of linear equations

$$Residuals_m \;=\; Weights_{mn}\ \Delta CO_n. \tag{41}$$

with subscripts m, n denoting the size of the arrays. The linear weights of the problem are the partial derivatives. If the linear weights are known and if the number of equations do not greatly outnumber the number of measured brightnesses, a best-fit solution can be found.

At millimeter wavelengths, the radiative transfer equation for a nonscattering atmosphere is

$$T_B(\nu,\mu) \;=\; T_\circ exp\Big(-\int_0^\infty k_{\nu,z}\frac{dz}{\mu}\Big) \;+\; \int_0^\infty k_{\nu,z}T(z)exp\Big(-\int_z^\infty k_{\nu,z'}\frac{dz'}{\mu}\Big)\frac{dz}{\mu} \tag{16}$$

as discussed in detail in Chapter III. This can be numerically integrated over altitude by discretely summing the absorption pathlength $k_{\nu,z}dz/\mu$ over altitude layers. Switching notation from absorption coefficients to opacity and numerically integrating, the brightness temperature of an atmosphere at a frequency ν and an impact parameter μ is then

$$T_B(\nu,\mu) \;=\; T_\circ e^{-\Sigma_{i_\circ}^{imax}\frac{\tau_i}{\mu_i}} \;+\; \sum_{i_\circ}^{imax} T(i)\left[1-e^{-\frac{\tau_i}{\mu_i}}\right]e^{-\Sigma_{j=i+1}^{imax}\frac{\tau_j}{\mu_j}}, \tag{42}$$

with the subscript $\circ$ denoting a continuum level and the subscript i an altitude layer. Based on the weighting functions shown in Figure 44, the continuum level was placed at 65 km for the inversions.

The CO volume mixing ratio profile can be expressed as

$$log_{10}(f_{CO,n}) \;=\; c_n, \tag{43}$$

where c_n is a constant for the layer n. This c_n will be referred to as the CO mixing ratio parameter. The partial derivative for the brightness temperature with respect to the CO abundance is consequently

$$\begin{aligned}
\frac{\delta T_B(\nu,\mu)}{\delta c_n} &= -\,T_\circ\, e^{-\sum_{i_\circ}^{imax}\frac{\tau_i}{\mu_i}}\,\frac{\delta[\tau_n/\mu_n]}{\delta c_n} \\
&\quad -\sum_{i_\circ}^{n-1} T(i)\, e^{-\sum_{j=i+1}^{imax}\frac{\tau_j}{\mu_j}}\,\frac{\delta[\tau_n/\mu_n]}{\delta c_n} \\
&\quad +\sum_{i_\circ}^{n} T(i)\, e^{-\sum_{j=i}^{imax}\frac{\tau_j}{\mu_j}}\,\frac{\delta[\tau_n/\mu_n]}{\delta c_n}
\end{aligned} \tag{44}$$

for the layer n, at frequency ν, and at the radial position characterized by the path-length factor, or impact parameter, μ. The opacity τ_n is a sum of CO_2 continuum opacity and CO resonant opacity. If this total opacity for a layer is expressed as

$$\tau_n(\nu) \;=\; k_{CO_2}(\nu)\Delta z \;+\; cnst_n(\nu) f_{CO,n}\,, \tag{45}$$

then its partial derivative with respect to the mixing ratio parameter is simply

$$\frac{\delta[\tau_n/\mu_n]}{\delta c_n} \;=\; \frac{ln10\, cnst_n(\nu)\, 10^{c_n}}{\mu_n}. \tag{46}$$

The new variable $cnst_n$ remains constant through the algorithm's iterations and holds the lineshape and temperature dependencies for the CO opacity over altitude. Equations (27)-(30) of Chapter IV for the CO absorption coefficient and equation (34) for the definition of opacity can be mixed for the definition

$$\begin{aligned}
cnst_n &= (9.21\times 10^{-9})\Big[1-\frac{2.769}{T}\Big]\frac{\rho_n A_\circ}{amu\, T^2} \\
&\int_{-\infty}^{\infty}\frac{1}{\pi}\frac{\Delta\nu_c}{(\nu_i-\nu_\circ-y)^2+\Delta\nu_c^2)}\,\frac{ln2^{1/2}}{\pi}\,\frac{1}{\Delta\nu_d}e^{-ln2\frac{y^2}{\Delta\nu^2}}\,dy\;\Delta z,
\end{aligned} \tag{47}$$

where $A_\circ$ is Avagadro's number, *amu* the average molecular weight of the atmosphere, ρ the atmospheric density in the layer and the other variables as explained in Chapter IV. Only the mixing ratio parameter c_n, the synthetic line $T_B(\nu)$ and the temperature partial derivatives change with the algorithm's iterations.

Combining equation (44) and equation (46) gives an explicit expression for the partial derivative of the brightness temperature with respect to the mixing ratio parameter in a layer n

$$\begin{aligned}\frac{\delta T_B(\nu,\mu)}{\delta c_n} &= -\,T_\circ\, e^{-\Sigma_{i_\circ}^{imax} \frac{\tau_i}{\mu_i}}\, \frac{ln10\; cnst_n(\nu)\, 10^{c_n}}{\mu_n} \\ &\quad - \sum_{i_\circ}^{n-1} T(i)\, e^{-\Sigma_{j=i+1}^{imax} \frac{\tau_j}{\mu_j}}\, \frac{ln10\; cnst_n(\nu)\, 10^{c_n}}{\mu_n} \\ &\quad + \sum_{i_\circ}^{n} T(i)\, e^{-\Sigma_{j=i}^{imax} \frac{\tau_j}{\mu_j}}\, \frac{ln10\; cnst_n(\nu)\, 10^{c_n}}{\mu_n}. \end{aligned} \qquad (48)$$

The right side of equation (48) was calculated in the inversion algorithm. The inversion model had three grids: frequency, height and radius. The 32 frequency steps were at the center of the observed 1 MHz and 50 kHz channels. Only half of the 64 channels observed had to be calculated since the CO line is symmetric about its line center. The full radial grid is described in section 2 of Chapter III. The atmosphere had layers 0.5 km wide between the lower boundary at 65 km and a specified upper boundary $\leq$ 129 km. These thin layers were sandwiched into thicker "multi-levels" with the least-squares restriction that the number of multi-levels be $\leq$32 (the number of measured independent frequency steps). The layers within a given multi-level had the same mixing ratio parameter c_n. The temperature partial derivative for a multi-level was the sum of the temperature partial derivatives over the layers in that multi-level. The number of 0.5 km layers per multi-level was a specified input to the inversion and the total number of multi-levels another specified input. The combination of these inputs determined the upper boundary altitude.

A constraint was placed on the CO mixing ratio profile so that the algorithm would be stable. This "smoothing" constraint controlled the degree to which the CO profile could change between multilevels

$$c_{n+1} \;=\; c_n \pm \sigma. \qquad (49)$$

This constraint therefore added rows onto the weighting matrix in the set of linear equations in (41)

$$\Big[T_{Observed\,line}(\nu,\mu) \;-\; T_B(\nu,\mu)\Big]_m \;=\; \begin{bmatrix} Partials \\ Constraints \end{bmatrix}_{mn} \Big[\Delta CO\Big]_n. \qquad (50)$$

The absolute values of the constraint used in the inversions is discussed later in the chapter.

The last important feature of the inversion model is the inclusion of weighting by the 3" CLEAN gaussian beam and 70" primary beam. The beam weighting factors $b(r)$ were applied the entire right sides of equation (42) for the brightness temperature and equation (47) for the brightness temperature partial derivatives. These beam factors are independent of the CO mixing ratio profile and correctly average the calculated radial distribution of the brightness temperatures to the resolution of the observations. A simple expression for this area weighting is

$$T_B(\nu,\mu_r) \;=\; \sum_{\Delta r} b(r) T_B(\nu,\mu) \;=\; \sum_{\Delta r} \frac{\Delta A_i\, e^{-(r/HPBW)^2 ln2}}{\Sigma_i \Delta A_i\, e^{-(r/HPBW)^2 ln2}} T_B(\nu,\mu) \qquad (51)$$

given a radial range Δr, a gaussian beam with a half power beam width $HPBW$ and an area under the beam $\Sigma \Delta A_i$ corresponding to the radial range Δr. Further details on calculation of the beam weights are given in Appendix A.

4. Synthetic Spectra Test Inversions

The performance of the inversion algorithm was tested with two synthetic 2.6 mm CO spectra. The two spectra were generated with the same CO mixing ratio profile, shown in Figure 45, and the same nightside temperature profile, shown in Figure 43, but at different impact radii. These lines are shown in Figure 46. The two synthetic spectra were created with the atmospheric model described in the previous section and in section 5 of Chapter IV. Therefore, these brightness temperatures have been convolved with the beam weighting function. Random gaussian noise was added onto these lines with an amplitude of 5 K and different seeds for the random number generator. The normal incidence spectrum in the left panel of Figure 46 has a continuum brightness temperature of roughly 355 K in the line wings. This continuum temperature is typical of radii near the disk center. The absorption line in the right panel was calculated for a radius of 5800 km, closer to the planetary limb at approximately 6180 km. At this larger radius, the continuum temperature in the line wings experiences limb-darkening and is roughly 220 K. The synthetic line at an impact radii of 5800 km also experiences a longer pathlength through the upper mesosphere then the normal incidence line.

The CO profiles from inversion of the synthetic spectra are drawn as solid lines in the panels of Figure 47 against the "true" CO profile. The inversions were carried

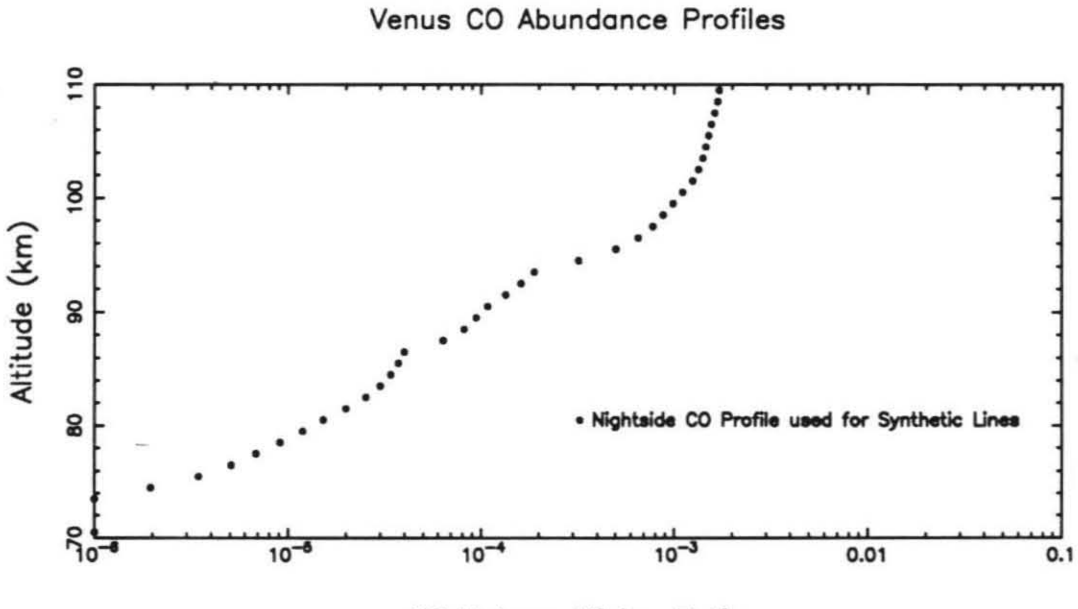

Figure 45. The CO profile used to generate synthetic spectra for testing the inversion algorithm.

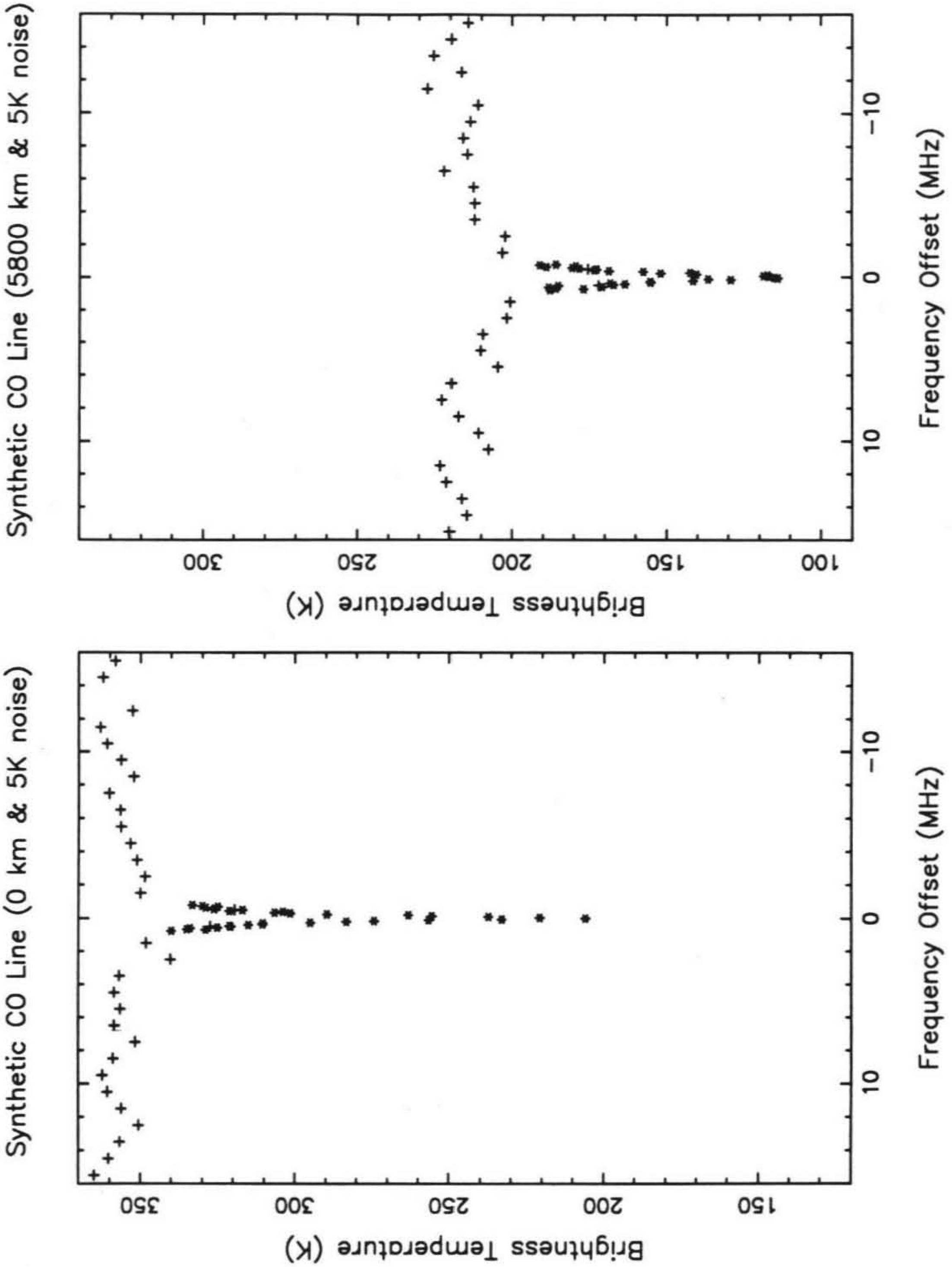

Figure 46. Noise-corrupted synthetic spectra at 0 km and 5800 km used to test the inversion algorithm.

out with an initial CO mixing ratio profile of $10^{-3.4}$, 26 multi-levels over height yielding an upper boundary at 116 km and a stability constraint on the CO profile between multilevels of 0.02. Iterations for these inverted CO profiles were stopped when residuals fell below a noise level of ±8 K. Only 4 iterations were needed to produce the CO profiles shown in Figure 47. The inversion algorithm appears to work best between 82 and 104 km for these particular lines and for this test CO profile. If the synthetic CO line has little sensitivity to the mixing ratio at an altitude, then the CO "smoothing" constraint forces a continuation of the CO abundance found in neighboring altitudes where there is sensitivity. Thus, at altitudes below 82 km, the inversion's final CO profile is a constant over height. If the CO profile used to generate the synthetic spectra had little CO at high altitudes, then the inversion's CO solution would have been constant as a function of height above ~104 km. Instead, these synthetic lines show little response to the CO abundance below 82 km. The inversion algorithm must therefore repeat its CO abundances from the neighboring multi-levels where the lines *are* sensitive to the CO abundance. Nonetheless, the inversion algorithm did satisfactorily find the CO profile behind the synthetic spectra across ~20 km in the upper mesosphere.

Convergence by the iterative algorithm and its final CO profile depend upon the parameters supplied to the algorithm. Parameters were varied to determine appropriate values for convergence and to determine their influence on the final CO solution. Such parameters include the initial CO profile for the iterations, the number of multi-levels over altitude (or,equivalently, the upper boundary for the model), and the CO smoothing constraint applied over altitude. The "standard" values for these parameters that lead to convergence and a correct CO solution were mentioned in the previous paragraph. The synthetic spectra were again inverted with different values for each of these parameters and the CO solutions compared to the standard inversion's CO solution shown in Figure 47.

The inversion begins with an intial estimate of the CO mixing ratio profile which, for simplicity, is constant over height. Subsequent iterations change this profile in order to minimize the residuals between the model's synthetic line and the observed line and reach a final CO solution. Based on previous observations (see Figure 35) and photochemical models of Venus, the CO volume mixing ratio should be on the order of 10^{-4} to 10^{-3} in the upper mesosphere. The standard initial CO mixing ratio for the inversions is $10^{-3.4}$. Figure 48 shows inversions of the synthetic spectra using iteration parameters identical to those of the standard inversion except for the initial CO profile which was placed at 10^{-3} and at $10^{-3.8}$. If the intial estimate of the CO mixing ratio was placed outside the range of 10^{-4} to 10^{-3}, the algorithm might not converge. Within this range of initial CO mixing ratios, however, changing the initial CO profile did not influence the final CO solution as shown in Figure 48.

During inversions of the spectra, four of the thin 0.5 km layers were placed in each multi-level. The standard number of these 2 km-wide multi-levels was 26. Consequently, the upper boundary of the calculations was 116 km. This satisfied the least-squares over determination requirement that the number of unknowns to be calculated (in this case, the number of CO abundances determined over height) be less than the number of known values in the problem (the 32 frequency measurements of the symmetric CO line). This upper boundary may appear to be unnecessarily high. However, as shown in Figure 49, decreasing the number of multi-levels and lowering the upper boundary worsens the solution. The CO profiles shown in the panels of Figure 49 were calculated with upper boundaries lowered to 94 and 104 km for the normal incidence synthetic line and to 100 and 104 km for the 5800 km line. The upper boundary for the latter spectrum could not be lowered below 100 km since critical refraction of the traced ray occurs in layers $\geq$100 km in the model for impact

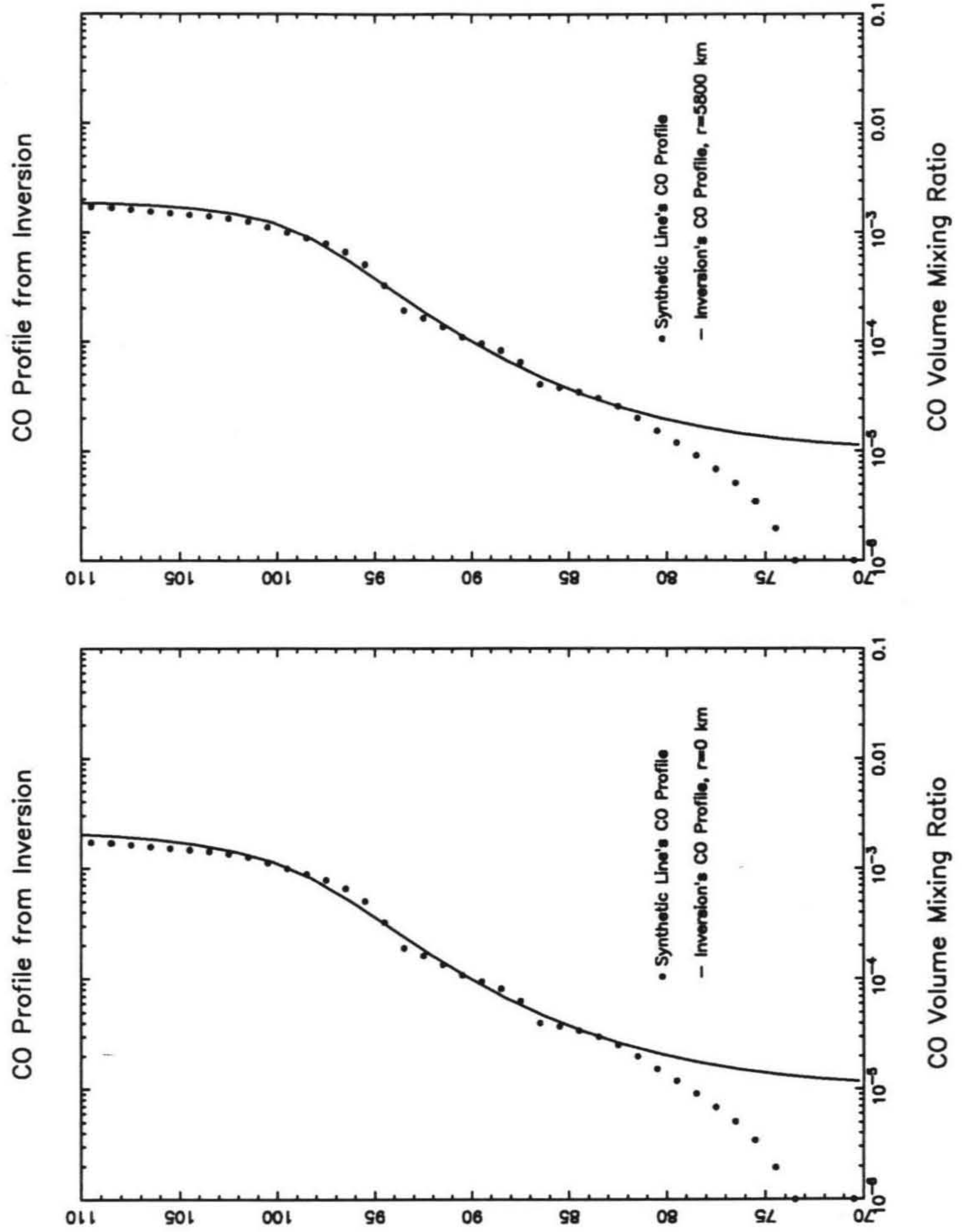

Figure 47. CO profiles from inversion of the synthetic spectra.

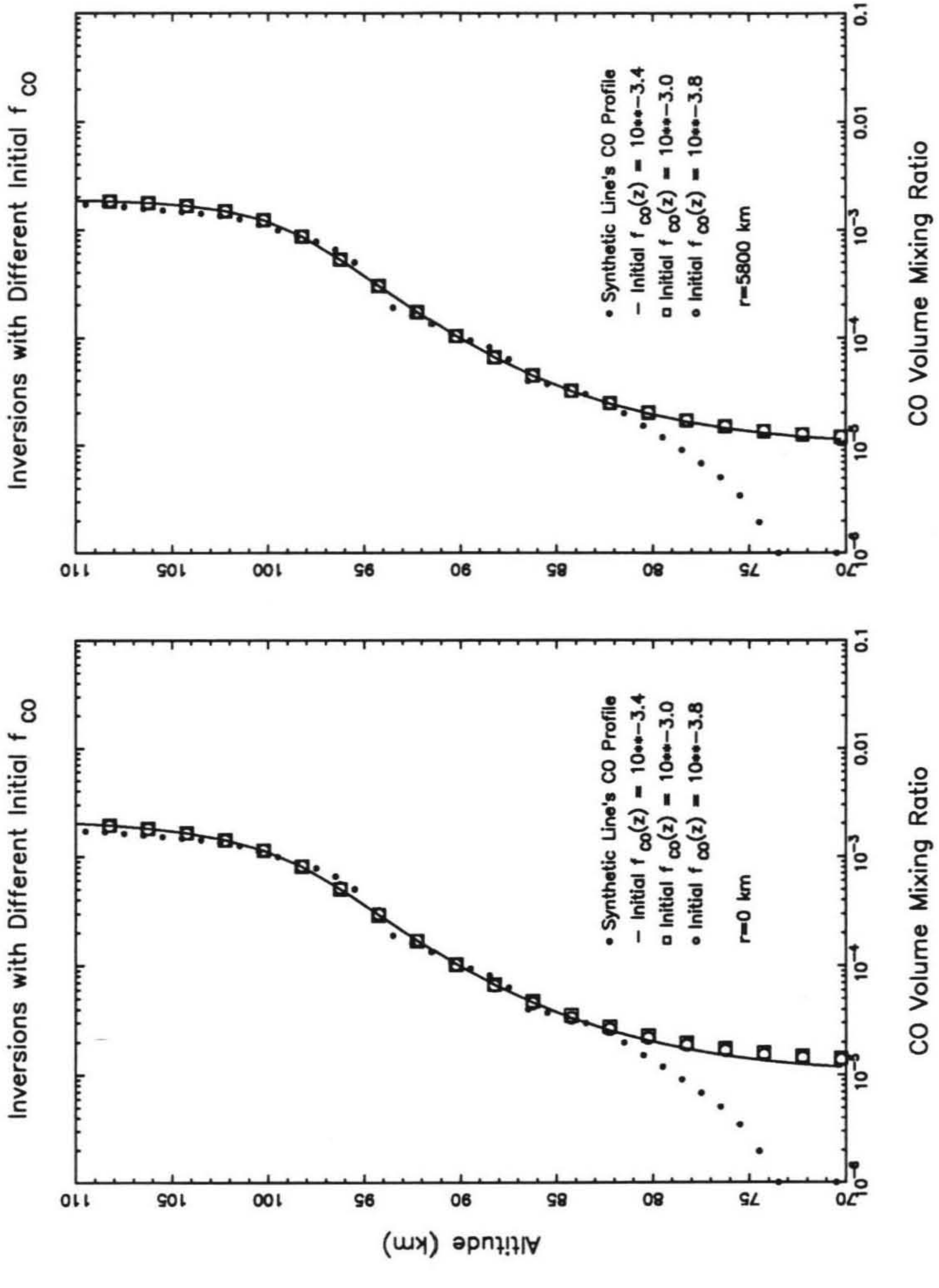

Figure 48. Inversions of the synthetic lines with different initial CO profiles.

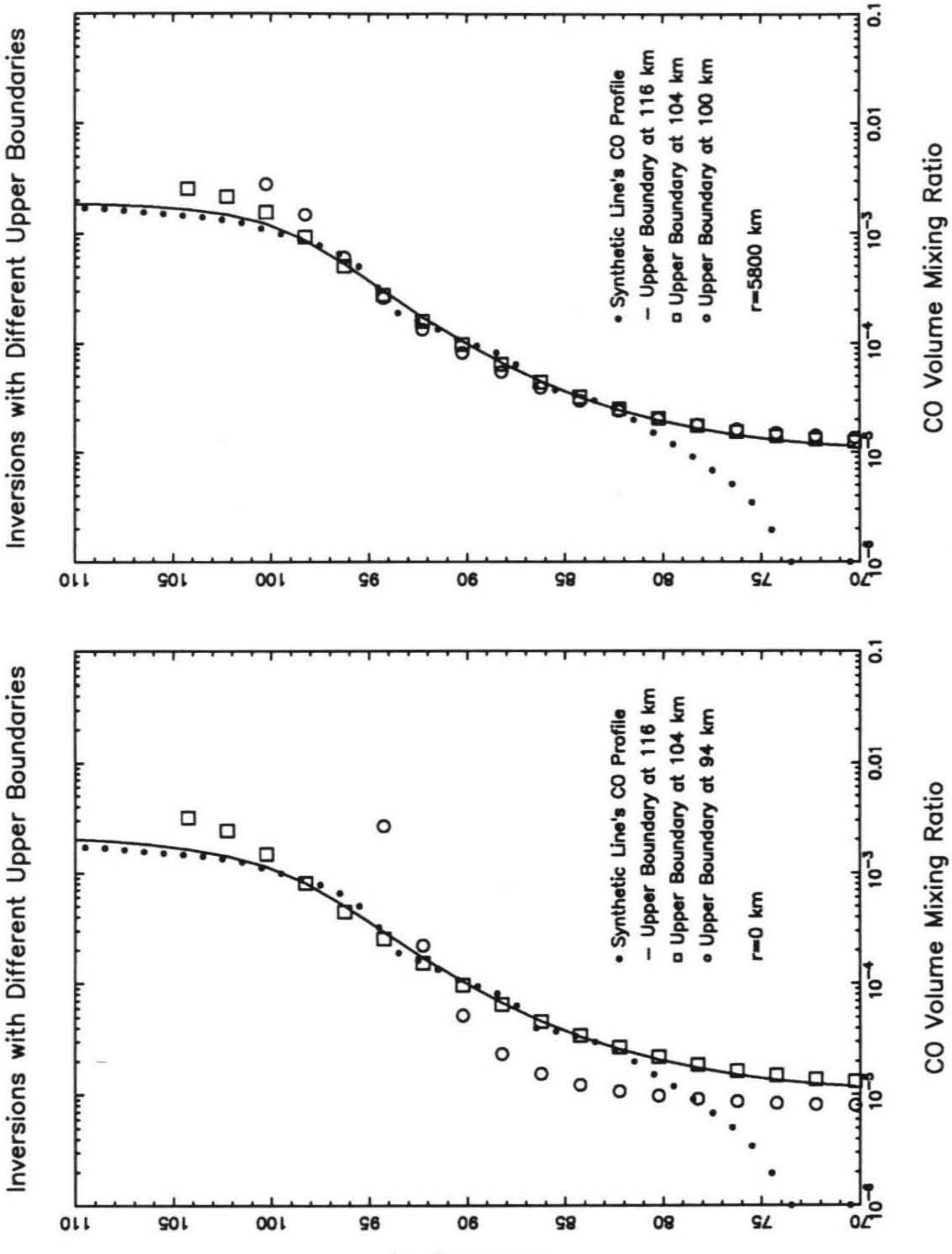

Figure 49. Inversions of the synthetic lines with different total multi-levels and, consequently, different upper boundaries.

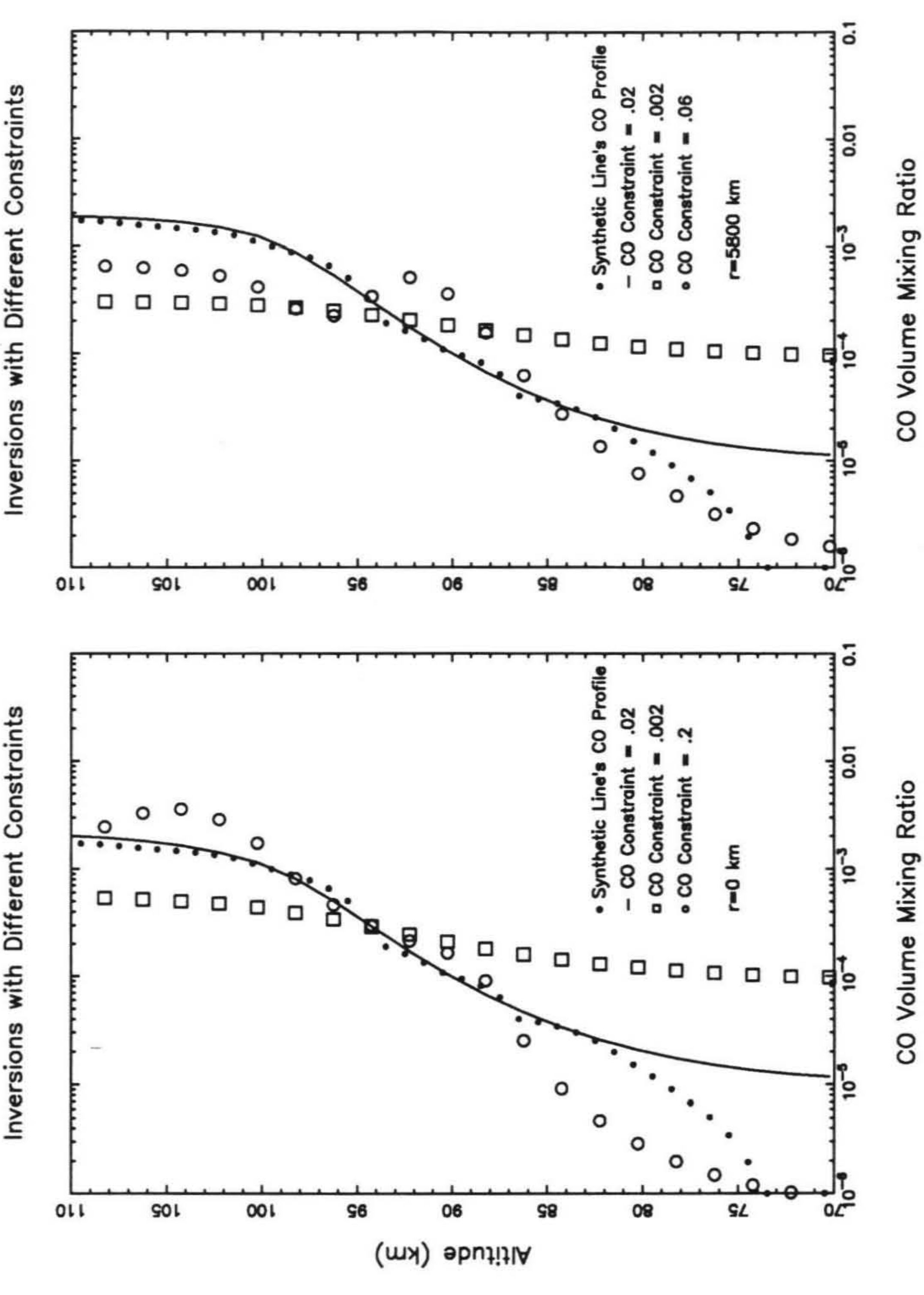

Figure 50. Inversions of the synthetic spectra with different CO constraints.

radii ≥ 6152 km. These radii are necessary for calculating the brightness temperatures at 5800 km because of the beam convolution.

Any "true" CO abundance at altitudes above 100 km becomes exaggerated and piled into the top multi-levels when the upper boundary is lowered in order to fit the measured linedepths. Lowering the number of multi-levels and the model's upper boundary furthermore required increased iterations and led to non-convergence for some of the observed, deep spectra. This problem occurred primarily with spectra along the limb of the planet which responded to higher altitudes more then normal incidence spectra. Therefore, the optimal number of multi-levels to reach convergence and yield CO profiles with reliable structure was 26.

The final and most important parameter is the "smoothing" constraint which restrained the structure of the calculated CO profile during the iterations. This constraint, as defined by equations (43) and (49), restricts the difference in the estimated CO exponent c_n between neighboring multi-levels. Therefore it controls the vertical structure of the CO profiles by limiting the gradient in CO abundance over height between two multi-levels. This, in turn, determines the stability of the algorithm: CO changes at a given iteration cannot be too extreme and lead the algorithm away from convergence.

For the standard inversion of the synthetic lines in Figure 47, the constraint was 0.02. The standard inversion reached convergence after 4 iterations. It had residuals below the noise limit of ±8 K and a solution whose vertical structure agreed with that of the "true" CO profile. CO solutions are shown in Figure 50 from iterations with constraints of 0.002 and 0.2 for the normal incidence line and 0.002 and 0.06 for the 5800 km line. For both lines, the tight constraint of 0.002 did not allow convergence and residuals remained at ±18 K. With a tight constraint on the CO vertical gradient, the algorithm could not change the CO profile and reduce residuals despite increased iterations. The algorithm, consequently, produced a nearly constant CO profile which is an approximate average of the "true" CO profile over height.

The CO solutions shown in Figure 50 and found with looser constraints of 0.2 and 0.06 did converge to residuals of ±10 K. The 5800 km synthetic line could not be inverted with a constraint larger then 0.06. Near-limb spectra typically required tighter constraints then lower incidence spectra in order to converge. The CO solutions found with loose constraints, however, have oscillatory structure not caused by "true" atmospheric conditions. When the inversions were tried with even looser constraints, the algorithm became even more unstable. The larger and looser constraints led to amplification of the residuals with each iteration in a runaway manner and to non-convergence. A moderate constraint near 0.02 was therefore used for the inversion work so that the algorithm would converge to a stable CO profile.

5. Inversions of the OVRO CO Spectra

As discussed in section 6 of Chapter II, the merged CO lines from the 1 MHz and 50 kHz filterbanks were binned in 2.5 by 2.5 arcsecond cells. These spatial bins correspond to 9° in latitude by 30 minutes in local time at normal incidence. This averaging yielded 121 spectra expressed in line-to-continuum ratio with noise of 2-3% for the CO inversion analysis. Typical spectra from the southernmost, the equatorial and the northernmost latitudes (i.e., -58°, 2° and 55°) are shown in Figure 51. The panels correspond to the spatial bins centered about these latitudes and the specified local times. All of the merged CO lines which were inverted for local CO mixing ratio profiles are provided in Appendix D.

These spectra readily reveal several trends. First, the observed spectra show a decided local time dependency, becoming progressively deeper from the afternoon hours to local midnight. Linedepths increase from roughly 20% in the afternoon hours to 40-45% in the hours near midnight. This trend agrees with results from previous

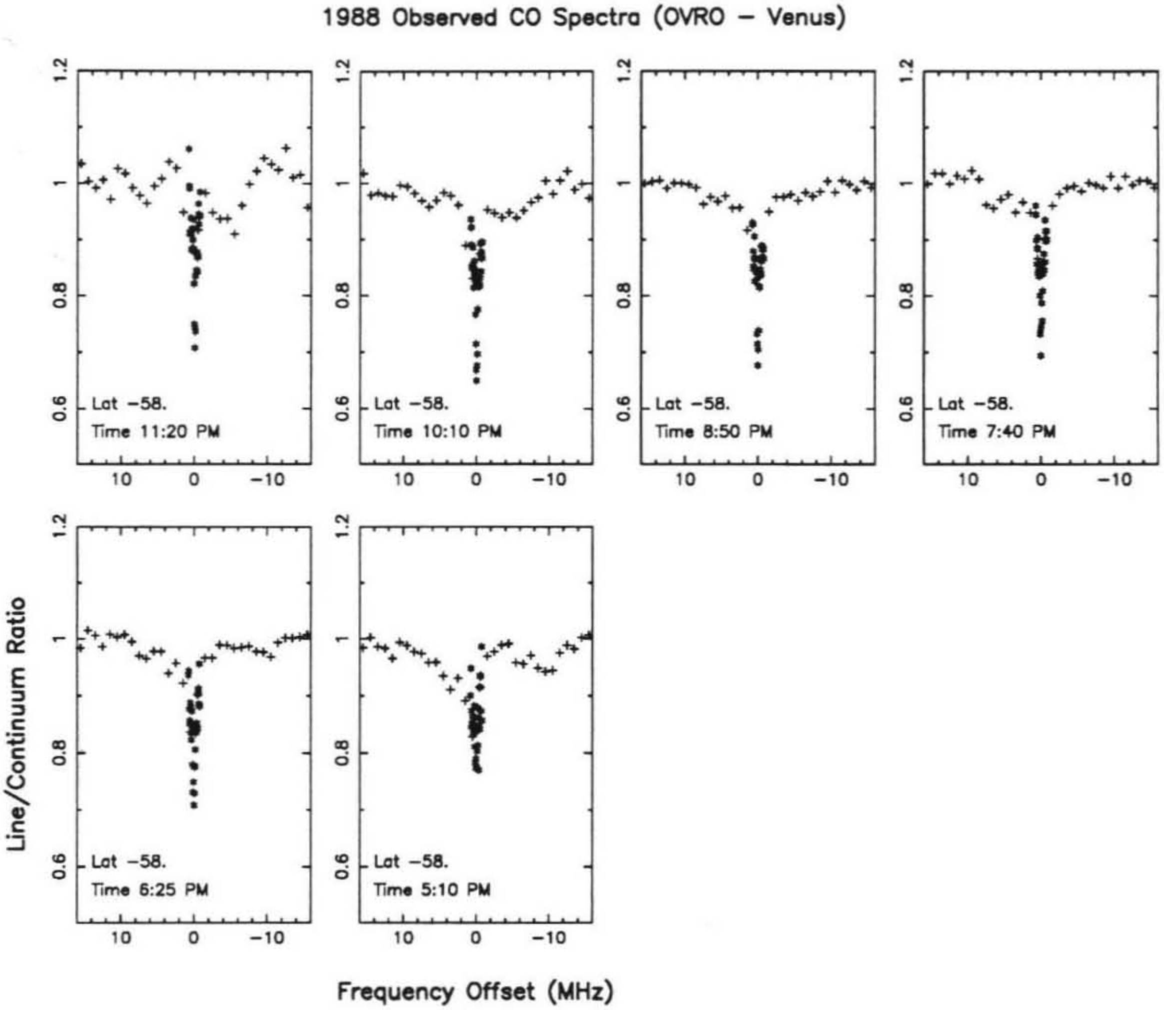

Figure 51a. The OVRO CO spectra in bins across Venus centered about the specified latitude and specified local times. The line-to-continuum ratios measured in the 1 MHz channels are denoted by crosses and the 50 kHz channels by asterisks.

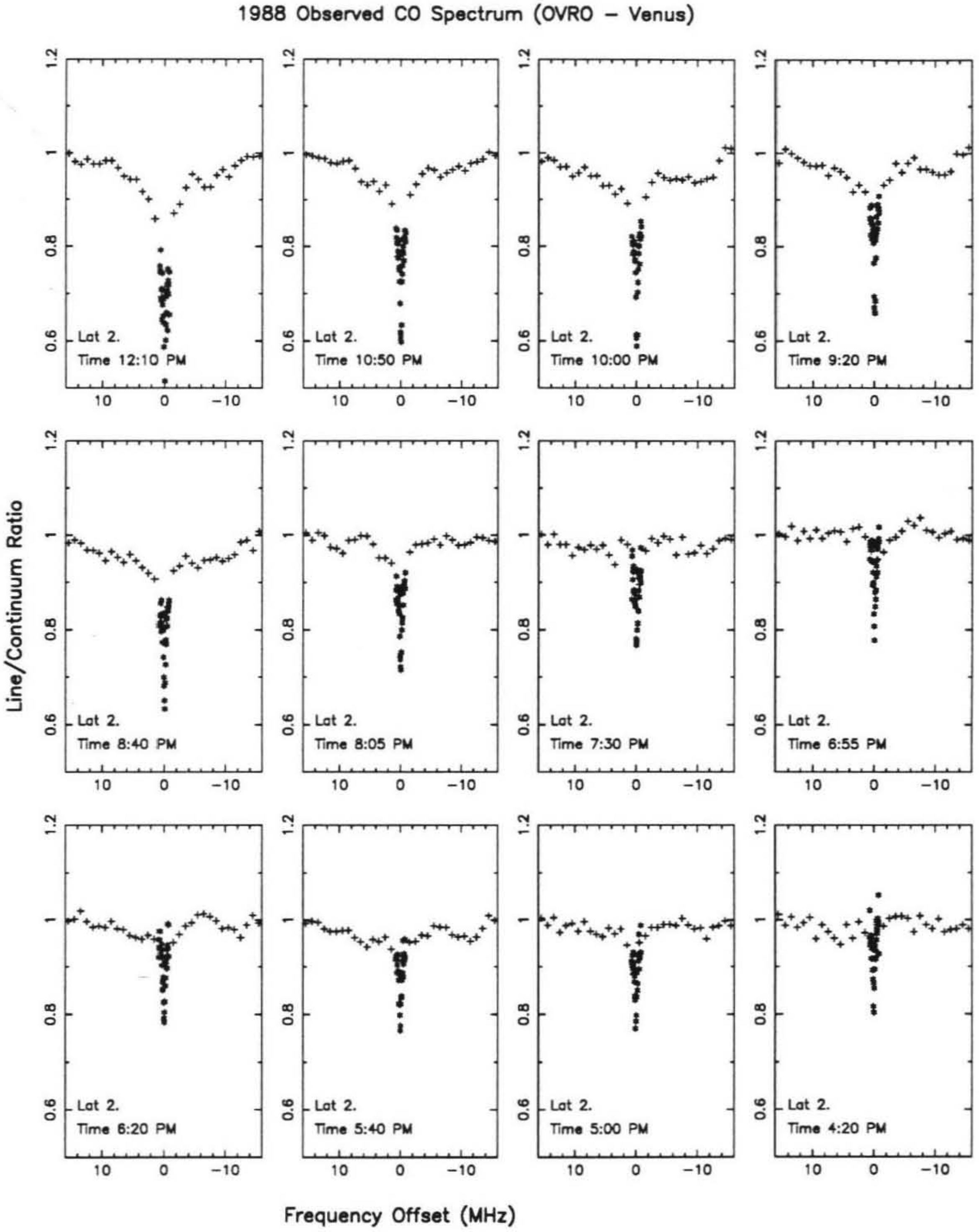
1988 Observed CO Spectrum (OVRO – Venus)
Line/Continuum Ratio
Frequency Offset (MHz)
1.2
1
0.8
0.6
10
0
−10
Lat 2.
Time 12:10 PM
Time 10:50 PM
Time 10:00 PM
Time 9:20 PM
Time 8:40 PM
Time 8:05 PM
Time 7:30 PM
Time 6:55 PM
Time 6:20 PM
Time 5:40 PM
Time 5:00 PM
Time 4:20 PM

Figure 51b.

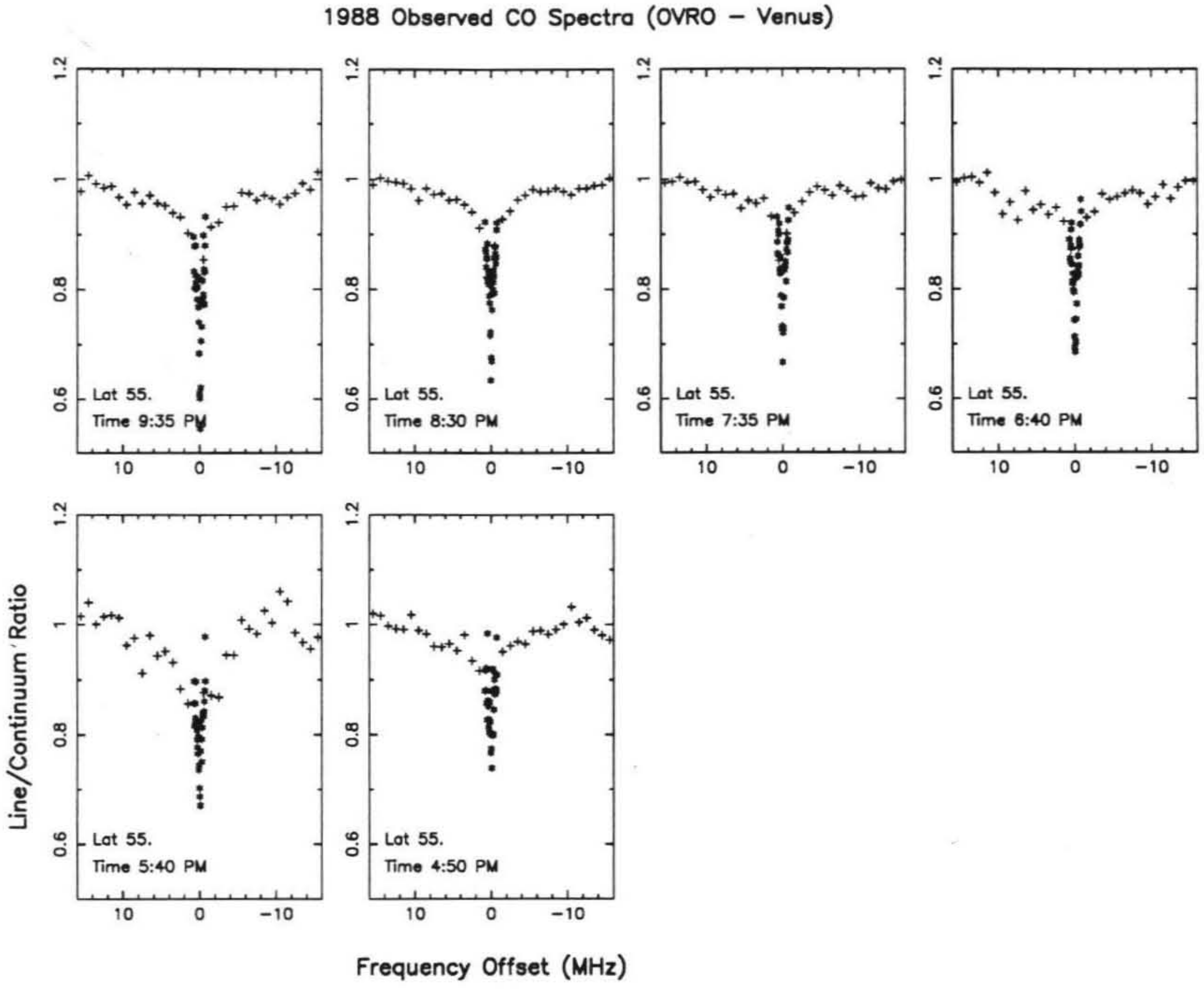
1988 Observed CO Spectra (OVRO – Venus)
Line/Continuum Ratio
Frequency Offset (MHz)
1.2
1
0.8
0.6
10
0
−10
Lat 55.
Time 9:35 PM
Lat 55.
Time 8:30 PM
Lat 55.
Time 7:35 PM
Lat 55.
Time 6:40 PM
Lat 55.
Time 5:40 PM
Lat 55.
Time 4:50 PM

Figure 51c.

disk-averaged observations of CO as discussed in section 2.3 of Chapter I. Secondly, the spectra for the northern high latitudes are similar to those for the southern high latitudes. There does not appear to be any asymmetry between the poleward latitudes in terms of CO absorption. Spectra at these poleward latitudes, though, are slightly shallower then equatorial spectra at a given local time near midnight. Finally, the CO lines appear to be most narrow near the disk center or, equivalently, local times about 7:20 PM. This might be either due to normal incidence, due to an real change in the mesospheric CO distribution, or due to merging of the observed spectra from 1 MHz and 50 kHz filterbanks. The two former possibilities are investigated with the inversion algorithm. The latter possibility is a concern given spectra such as those in the panels at 7:30 PM and 6:55 PM at latitude 2° in Figure 51b. Such spectra were formed from 1 MHz data which had shallow linedepths which are either

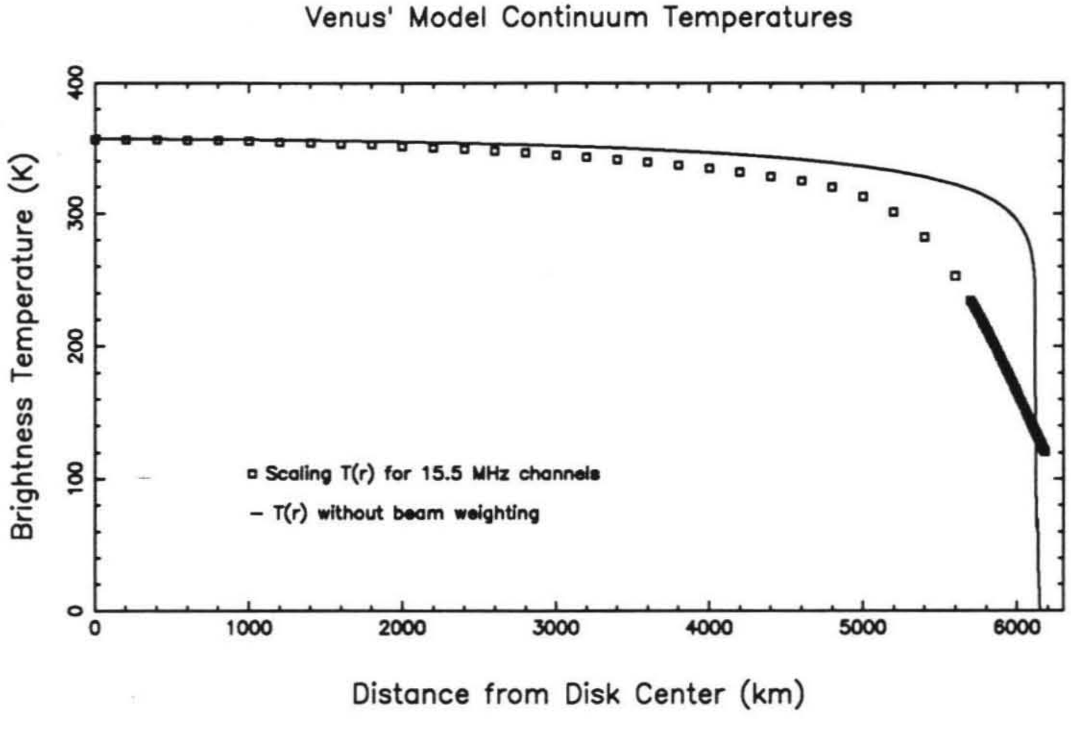

Figure 52. The beam-weighted limb-darkening curve for degrees Kelvin.

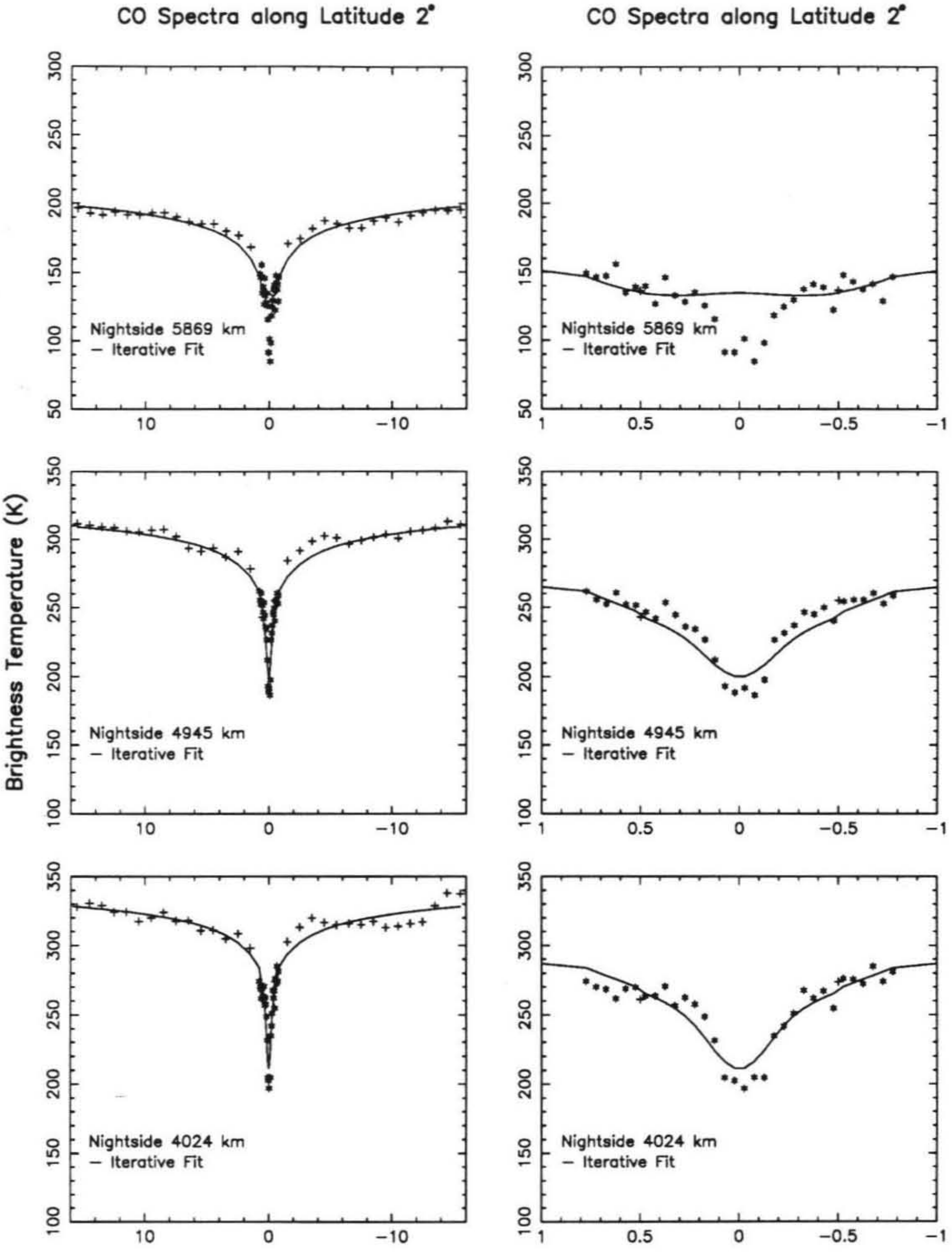

Figure 53a. Comparison of the inversion's synthetic lines to the observed lines. The 1 MHz channels are again denoted by crosses and the 50 kHz channels by asterisks.

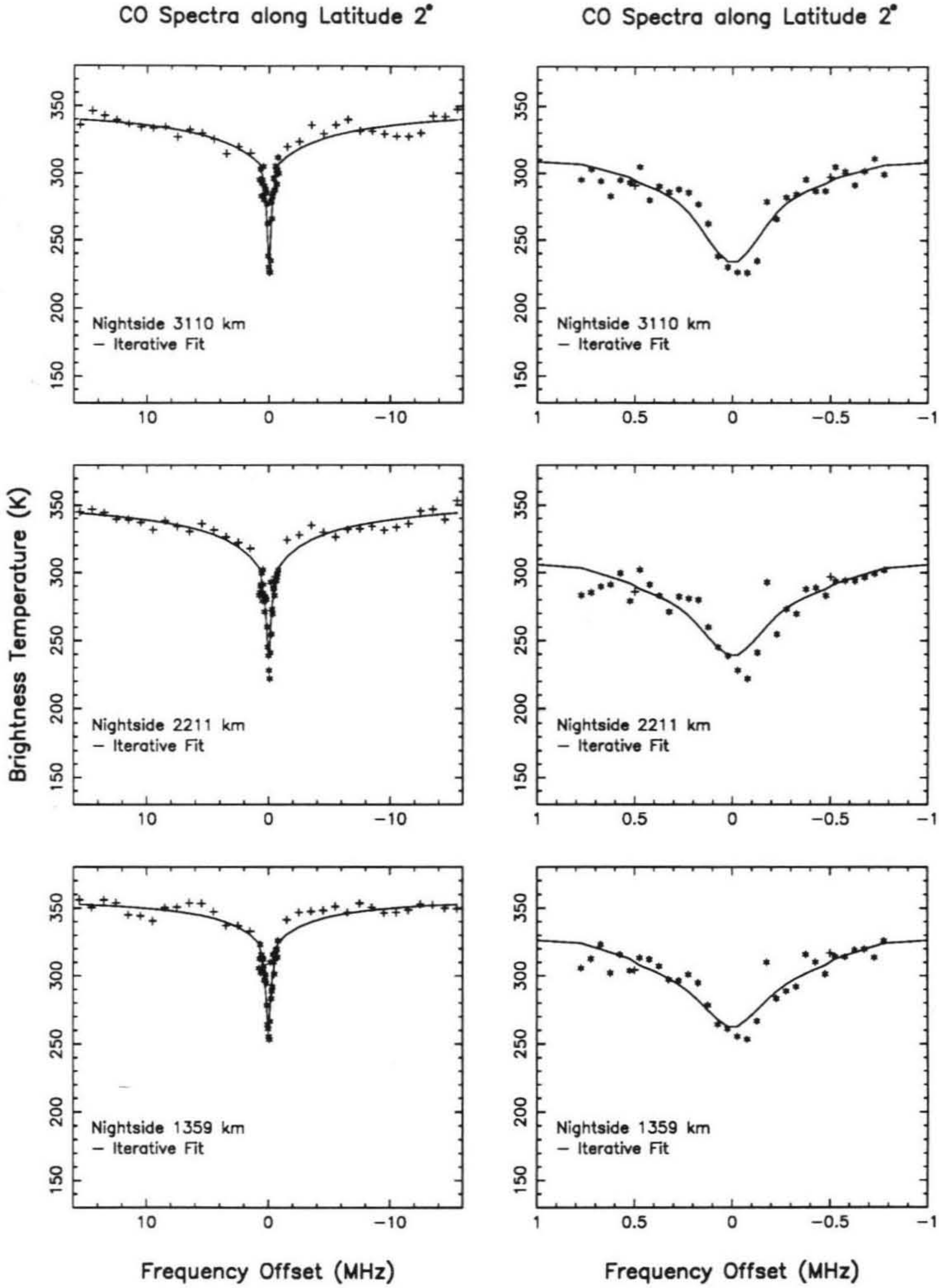
CO Spectra along Latitude 2°
CO Spectra along Latitude 2°
Brightness Temperature (K)
150
200
250
300
350
Nightside 3110 km
– Iterative Fit
Nightside 2211 km
– Iterative Fit
Nightside 1359 km
– Iterative Fit
10
0
−10
1
0.5
0
−0.5
−1
Frequency Offset (MHz)
Frequency Offset (MHz)

Figure 53b.

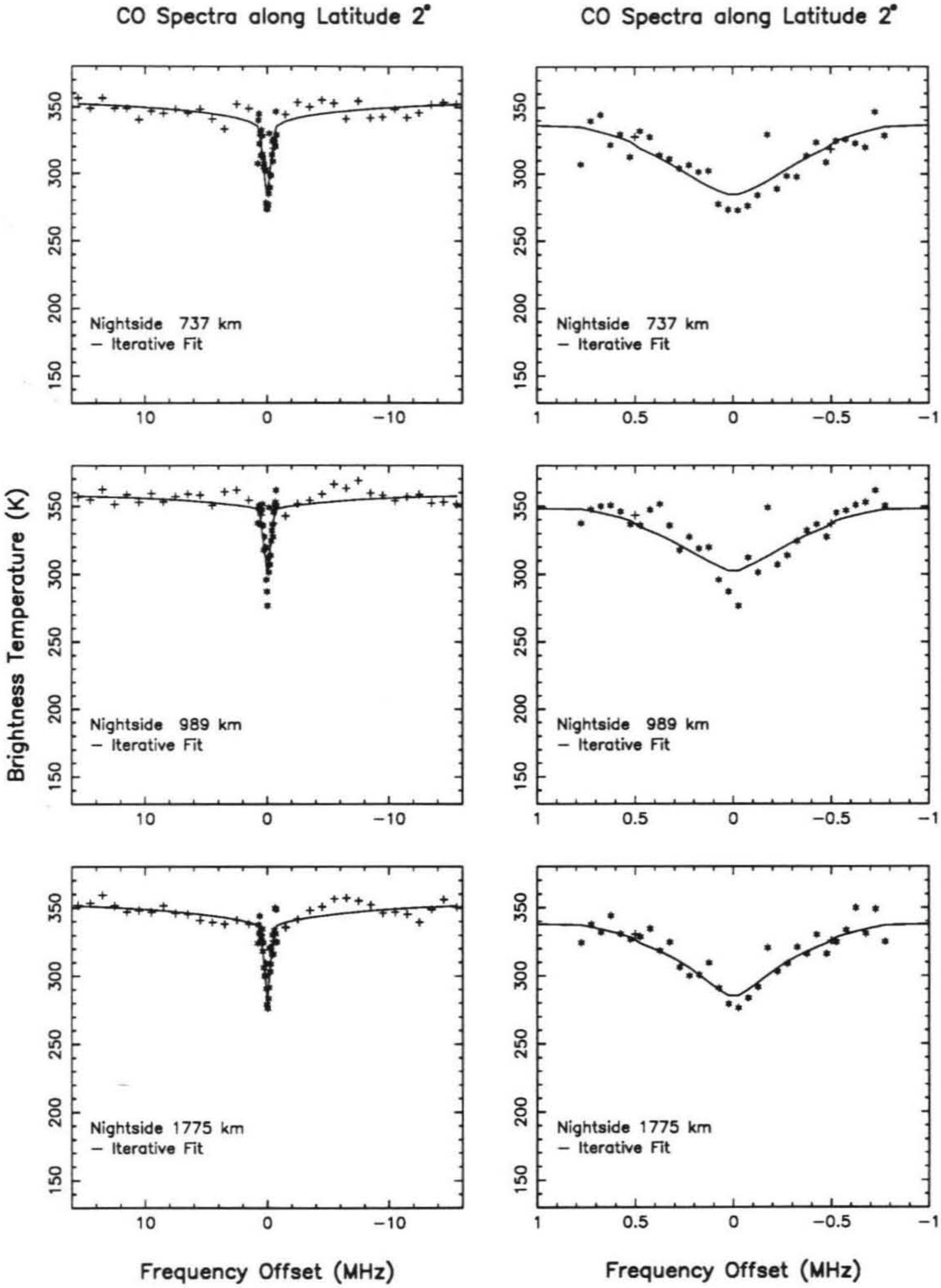
CO Spectra along Latitude 2°
CO Spectra along Latitude 2°
Brightness Temperature (K)
Nightside 737 km
– Iterative Fit
Nightside 989 km
– Iterative Fit
Nightside 1775 km
– Iterative Fit
150
200
250
300
350
10
0
−10
1
0.5
0
−0.5
−1
Frequency Offset (MHz)
Frequency Offset (MHz)

Figure 53c.

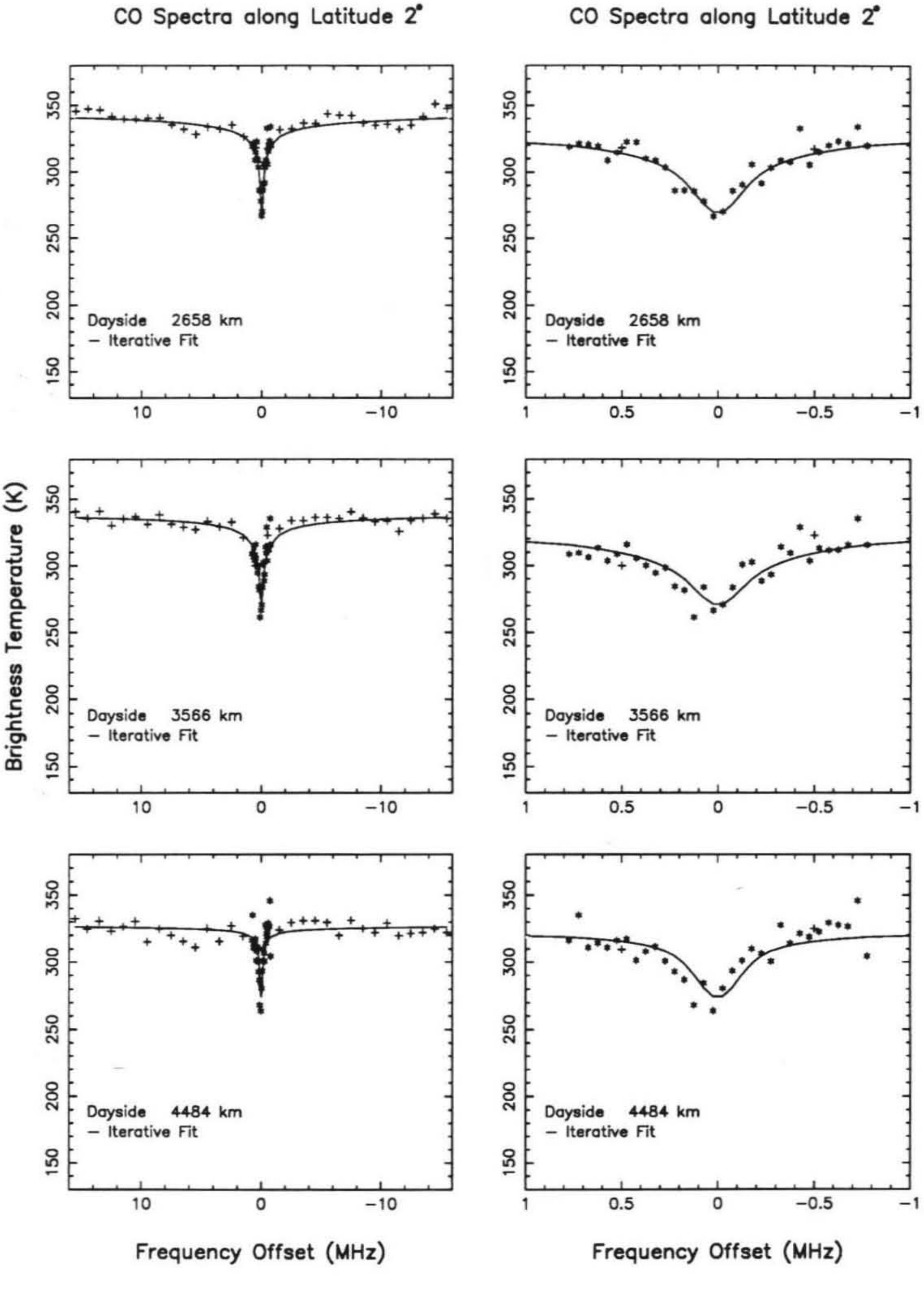
CO Spectra along Latitude 2°
CO Spectra along Latitude 2°
Dayside 2658 km
— Iterative Fit
Dayside 3566 km
— Iterative Fit
Dayside 4484 km
— Iterative Fit
Brightness Temperature (K)
150
200
250
300
350
10
0
−10
1
0.5
0
−0.5
−1
Frequency Offset (MHz)
Frequency Offset (MHz)

Figure 53d.

real or caused by noise. Corresponding channels of the 50 kHz data were merged with the 1 MHz data at ±0.5 MHz from $\nu_\circ$. The resultant CO lines are extremely narrow and have incongruous values between ±0.5 MHz from $\nu_\circ$ and ±1.5 MHz from $\nu_\circ$. This is an unavoidable weakness of the method employed to combine the data from the two filterbanks.

The 121 spatially resolved spectra were first converted from line-to-continuum ratios to brightness temperatures using appropriate continuum temperatures from the beam-weighted limb-darkening curve shown in Figure 52. Then the spectra were inverted with an initial CO profile of $10^{-3.4}$, 26 multi-levels and a CO smoothing constraint of 0.01 at radii $\geq$5500 km and 0.03 for radii closer to the disk center. Iterations were continued until the residuals between the model's line and the observed line were under ±8°K. Figure 53 shows the agreement between a typical final iteration synthetic line and the observed line for one latitude. The left panels compare the entire observed line to the final iteration synthetic line. The right panels compare observed absorptions close to the line center to the final iteration synthetic line. Because the inversion algorithm does not try to include doppler shifting due to winds in Venus' upper mesosphere, the synthetic lines are not shifted and some are displaced off the observed line by $\leq \pm 100$ kHz.

The CO profiles from the 121 inversions of the 1988 OVRO spectra are presented and discussed in section 6 of this chapter. But first, consideration must be given to how these CO solutions depend upon the continuum scaling temperature, the frequency resolution of the model and the temperature profile, assumed to be "known" for the inversions. The last subsection estimates uncertainties for a few CO profiles from inversions of typical equatorial afternoon, evening and nightside spectra and looks at a typical covariance matrix associated with an inversion.

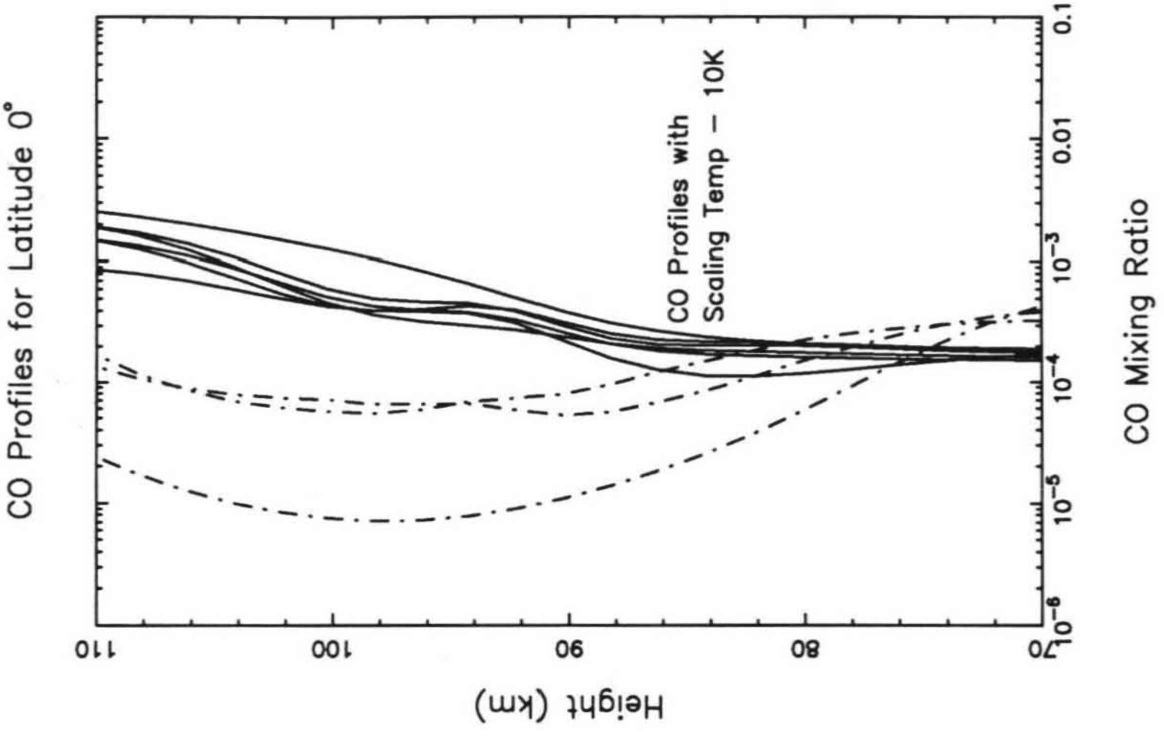

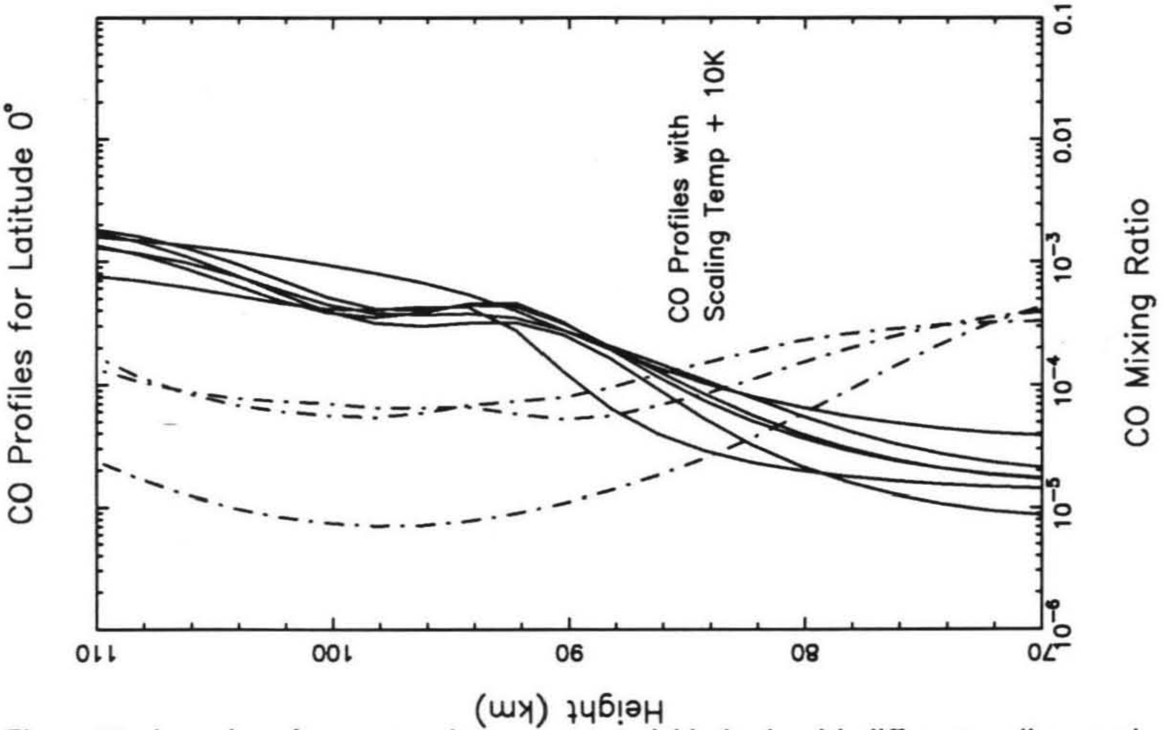

Figure 54. Inversions for spectra along an equatorial latitude with different scaling continuum temperatures. Night profiles are drawn with solid lines and afternoon profiles with solid-dot-solid lines.

5.1 Dependence on Scaling Temperature

Figure 54 shows the difference in CO profiles due to different continuum scaling temperatures for inversions of afternoon and night spectra centered about the equator. The CO profiles found in the afternoon hours are drawn with solid-dot-solid lines and the CO profiles found in the night hours with solid lines. The clustering of CO profiles into an afternoon branch and a nightside branch in Figure 54 is characteristic of all of the CO solutions. This diurnal separation of CO profiles is not the focus of this subsection and will be discussed later in the chapter. Here focus is upon the uncertainty associated with model's scaling brightness temperatures of 5-10 K. The scaling continuum temperature physically acts as a fixed lower boundary brightness temperature at 65 km. This lower boundary temperature dictates the amount of upwelling radiation which can be absorbed by the higher altitudes' CO molecules.

The left panel of Figure 54 shows CO solutions found with scaling temperatures 10 K more then the standard scaling temperatures shown in Figure 52. The right panel shows CO solution found with scaling temperatures 10 K less then the standard scaling temperatures shown in Figure 52. These changes to the scaling temperature influenced CO profiles below 85 km and only CO profiles with low abundances, $\leq 1 \times 10^{-4}$, below 85 km. When the lower boundary brightness temperature was increased by 10 K, the CO abundance fell in order to reproduce the same small degree of absorption in the line wings. The higher lower boundary temperature provided more upwelling radiation. So the inversion algorithm matched the observed absorption for altitudes between 65 and 85 km by decreasing its CO solution for these altitudes. When the lower boundary brightness temperature was decreased, the CO abundance similarly increased to reproduce the small line wing absorption. The deep, nightside CO lines corresponding to these scaling temperature-dependent CO abundances at low altitudes are more sensitive to the larger CO abundances at the high altitudes.

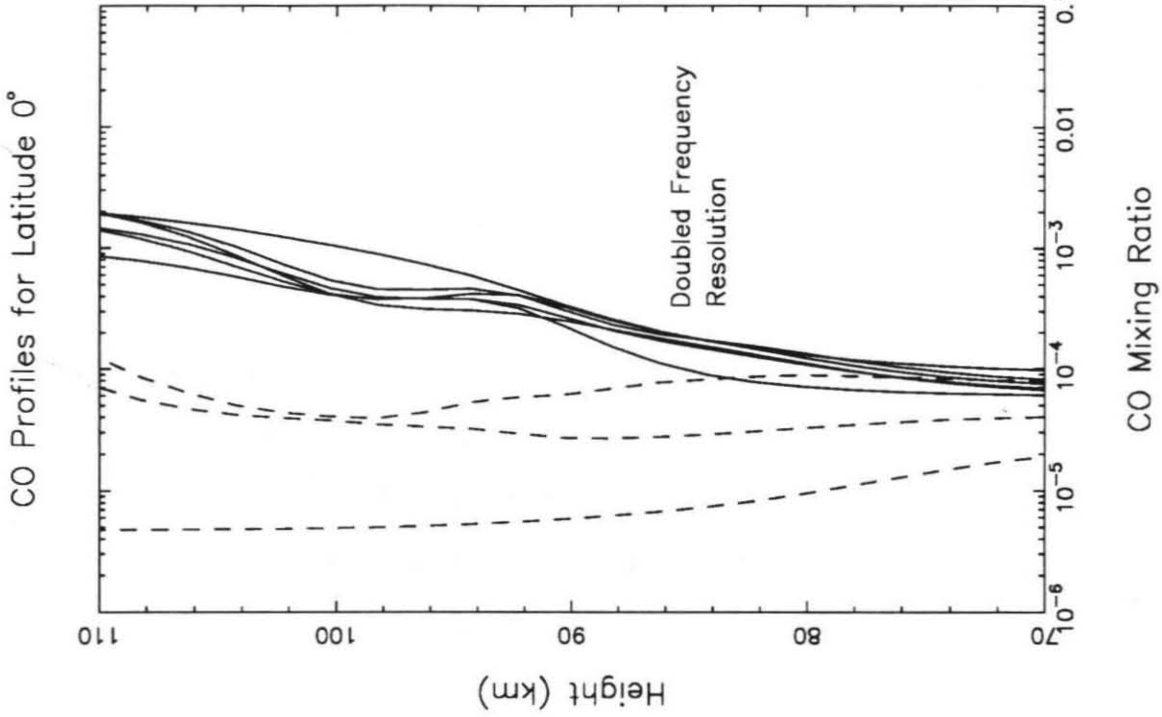

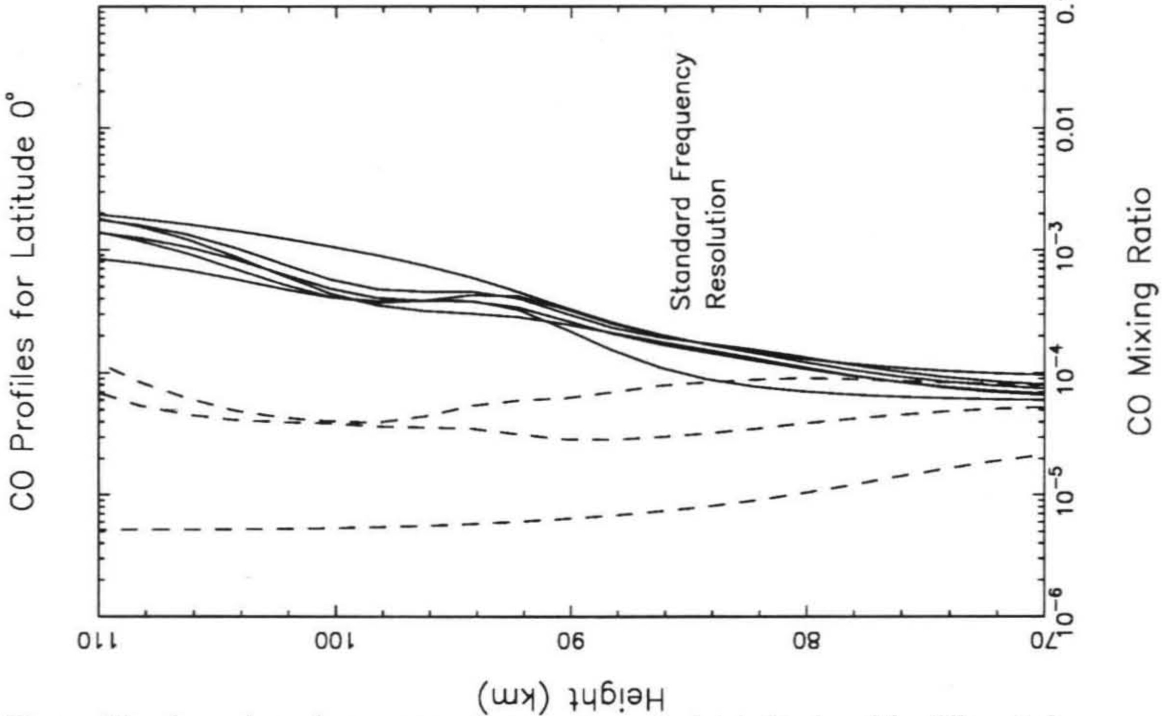

Figure 55. Inversions for spectra along an equatorial latitude with different frequency resolutions. Night profiles are drawn with solid lines and afternoon profiles with solid-dot-solid lines.

For observed dayside CO lines with nontrivial amounts of absorption in the line wings, changes to the scaling temperature could not influence the CO solution greatly. These CO lines are sensitive to the CO abundance in the lower mesospheric altitudes (see section 1 of this chapter). It will also be shown in a later subsection that the scaling temperature's influence on nightside CO profiles below 85 km, moving abundances from a few 10^{-5} to 10^{-4}, falls within the error bars on the CO solution.

5.2 Dependence on Frequency Resolution of the Model

The observed OVRO spectra were inverted with model calculations of brightness temperatures and partial derivatives of brightness temperature with CO mixing ratio parameters at 32 steps over frequency. These 32 frequency steps correspond to the centers of the 16 1 MHz channels from 15.5 MHz to 0.5 MHz and the centers of the 16 50 kHz channels from 0.775 MHz to 0.025 MHz from $\nu_\circ$. An average of brightness temperatures and partial derivatives over the frequency channels would have been preferable. However, increasing the frequency resolution of the model would have increased the computational time of each inversion considerably. Figure 55 shows the effects of doubling the model's frequency resolution on the equatorial CO solutions. The left panel shows the CO profiles found with a frequency resolution of one step per channel or 32 total frequency steps. The right panel show the CO profiles found with a frequency resolution of two steps per channel or 64 total frequency steps.

Figure 55 shows that the final CO profiles changed imperceptibly when the frequency resolution of the model was doubled. By calculating model brightness temperatures at two frequency positions within a channel and then averaging, the model brightness temperature for a given channel decreased. Accordingly, the CO abundance at altitudes sampled by this channel decreased in order to reproduce the observed absorption in this channel. The final CO profiles, therefore, decreased by 4-5% above approximately 96 km with increased model frequency resolution. These higher altitudes are sampled by the 50 kHz channels closest to ν_o, as shown by the weighting functions in Figure 44b and the frequency-binned partial derivatives in Figure 57b. The widths of these weighting functions and the 1 MHz weighting functions (Figure 44a) are broad enough to decrease the effects of increased frequency resolution to only 4-5% at a given altitude.

5.3 Dependence on Temperature Profiles

The main assumption of the CO inversions was that the temperature profile was "known". Undoubtedly, the vertical temperature profile of Venus' mesosphere varies as a function of latitude and local time. Such temperature information is, however, unavailable. Therefore, simplified forms of the temperature profiles measured during the descent of the Day and Night Pioneer Venus probes in late 1978 were used (Figure 43). To gain perspective on how the CO solutions will change with different temperature profiles, un-binned equatorial spectra were inverted with these standard temperature profiles (referred to as "smooth" temperature profiles) and also with the temperature profiles ("fluctuating" temperature profiles) shown in Figure 34. The latter temperature profiles contain a 5 km-wide inversion layer of roughly 10 K in the dayside profile at an altitude of about 96 km. The "fluctuating" temperature profiles also have 5 K cooler temperatures on the nightside above 100 km and have a 15-20 K diurnal difference in temperatures between 85 and 92 km.

Figure 56a shows the CO solutions found with the different pairs of diurnal temperature profiles. In both panels, the branch of clustered night CO profiles has a mixing ratio of roughly 10^{-3} at 110 km. The branch of clustered afternoon CO profiles has a mixing ratio of roughly 10^{-4} at 110 km. As discussed in section 1, the spectra appear to be more sensitive to CO abundance than to temperature at a given altitude. This comment is based on the general similarity between the CO profiles of the left panel (from smooth T(z)) and the right panel (from fluctuating T(z)) in

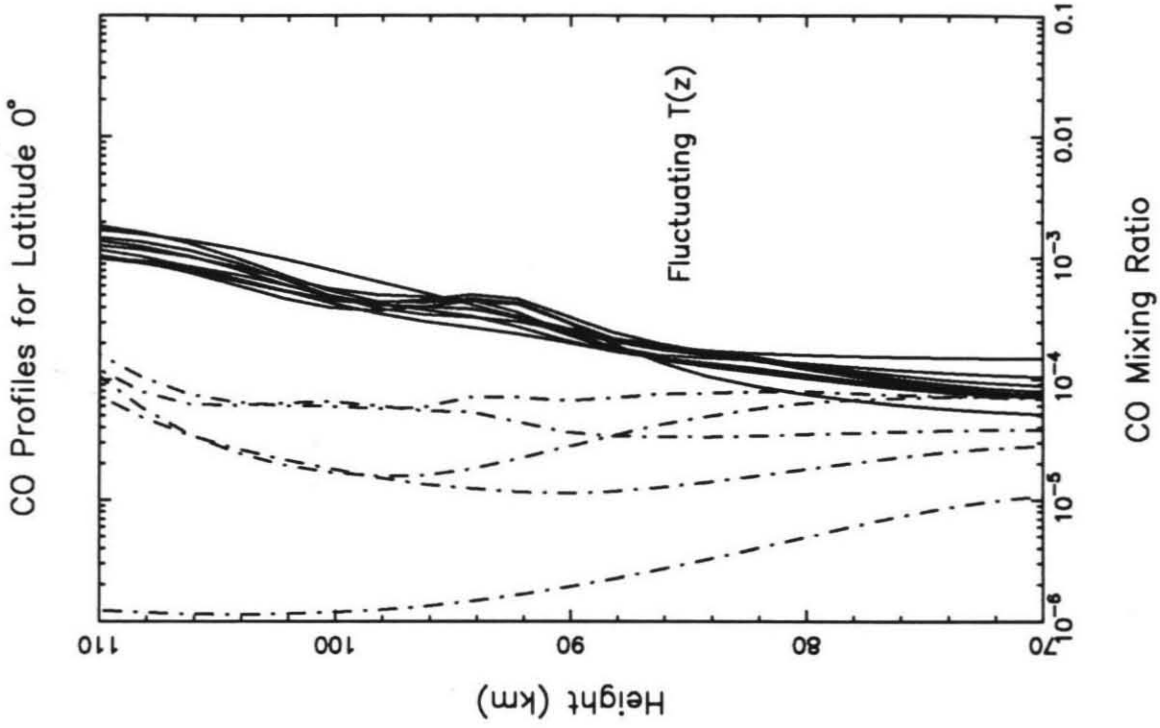

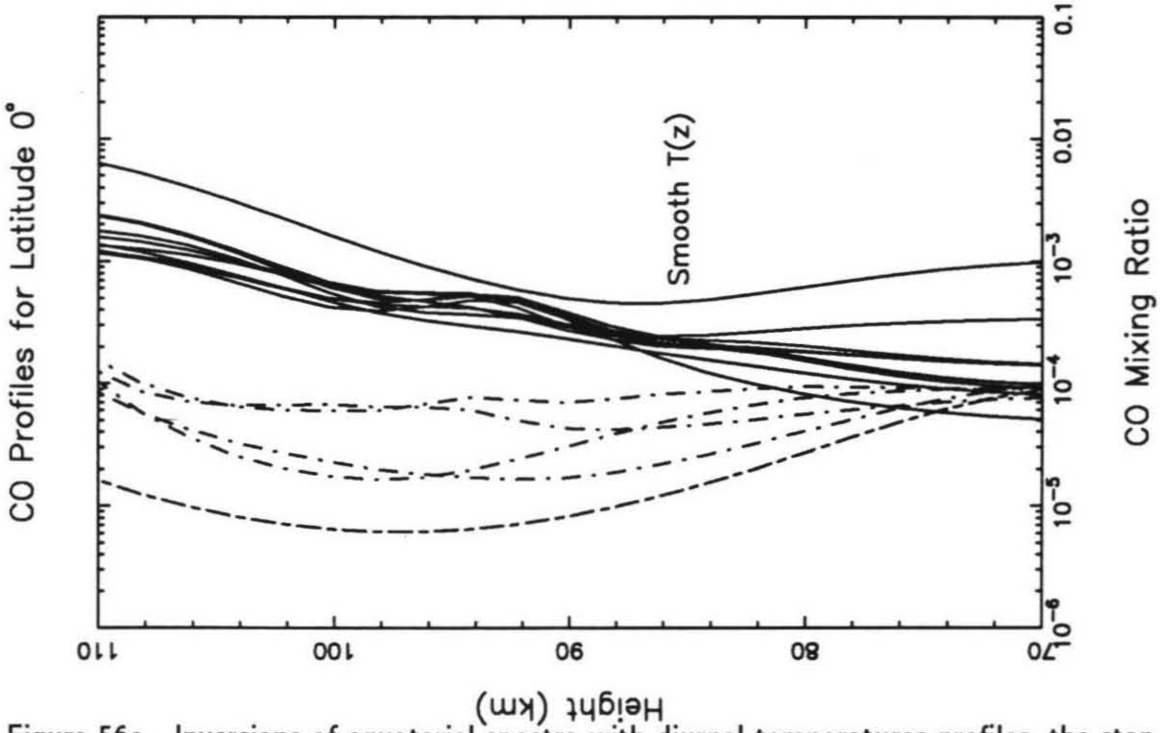

Figure 56a. Inversions of equatorial spectra with diurnal temperatures profiles, the standard "smooth" profiles of Figure 43 and "fluctuating" of Figure 34. Night CO profiles are noted by solid lines and afternoon profiles by solid-dot-solid lines.

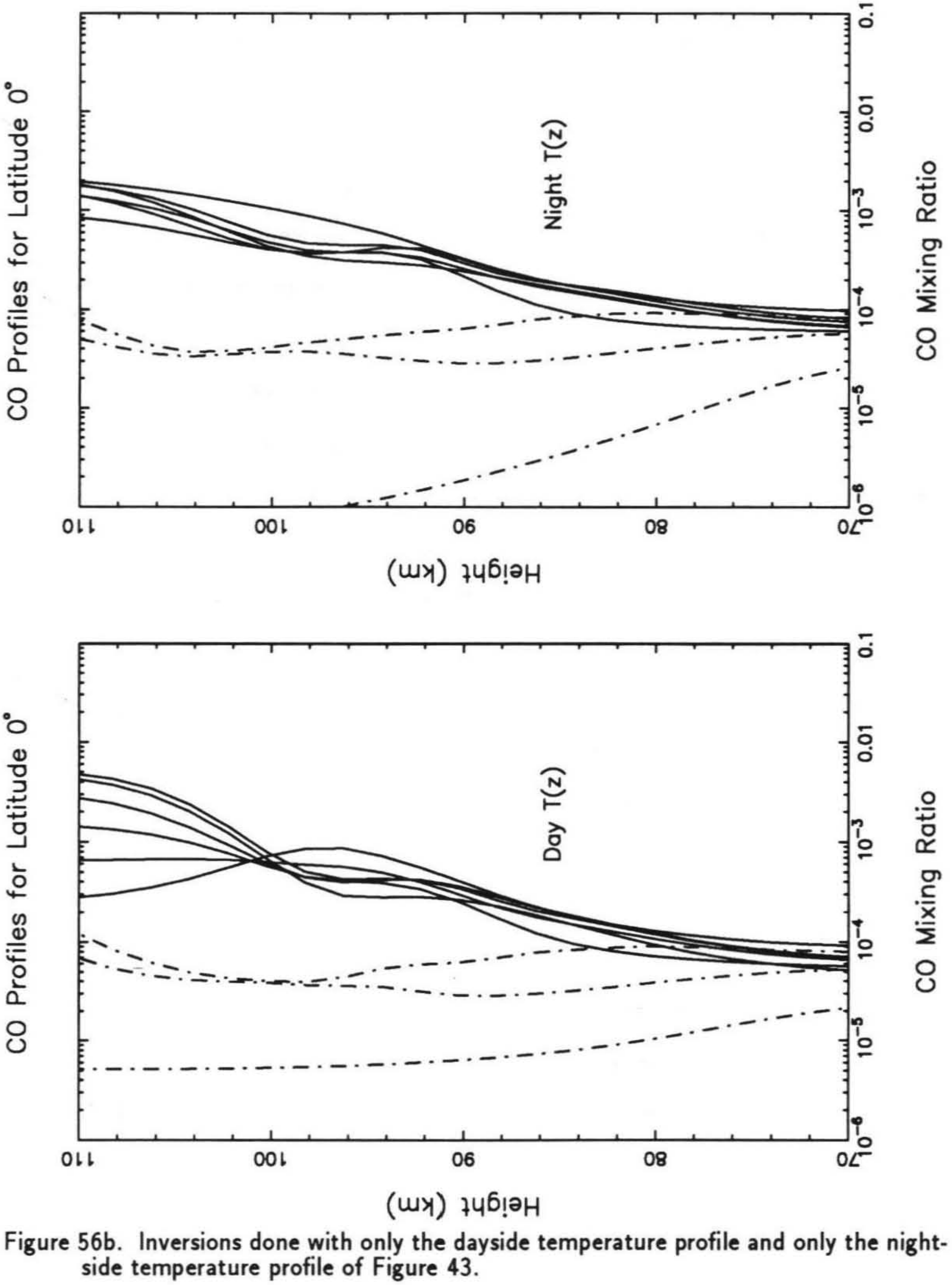

Figure 56b. Inversions done with only the dayside temperature profile and only the nightside temperature profile of Figure 43.

Figure 56a. The inversion layer in the dayside, fluctuating temperature profile has not created any corresponding small-scale structure to the dayside CO profiles of the right panel.

The broad changes to the CO profiles due to the different pairs of diurnal temperature profiles are less easily understood. The few CO profiles obviously different between the two panels are from either a very deep nightside spectrum or slight afternoon spectra. The afternoon spectra were formed with low vertical distributions of CO abundances. Such weak CO lines will have large uncertainties. Consequently, the algorithm, less constrained by a weak CO line, is influenced by the different temperature profile and can produce different synthetic lines characterized by low residuals. The changed nightside CO profile, on the other hand, will have relatively low uncertainties and requires consideration. This profile decreased overall when the associated temperature profile had lower temperatures between 85-92 km and above 100 km. The cooler populations of CO molecules appear to absorb efficiently enough so that the necessary number of molecules is reduced. The true temperature field of the upper mesosphere during the 1988 spring observations is not known. Therefore, the CO solutions from the inversions are simply best estimates of the true CO distribution.

The second test concerning the assumed temperature profiles did inversions of all the equatorial spectra with one temperature profile. Figure 56b shows the resultant CO profiles inverted with the "smooth" dayside temperature profile in the left panel and inverted with the "smooth" nightside temperature profile in the right panel. The structure of the CO profiles changes above 100 km. Above 100 km, the "smooth" diurnal temperature profiles differ as shown in Figure 43. So, reasonably, the inverted CO profiles are only affected above 100 km by whether a nightside or a dayside temperature profile is assumed.

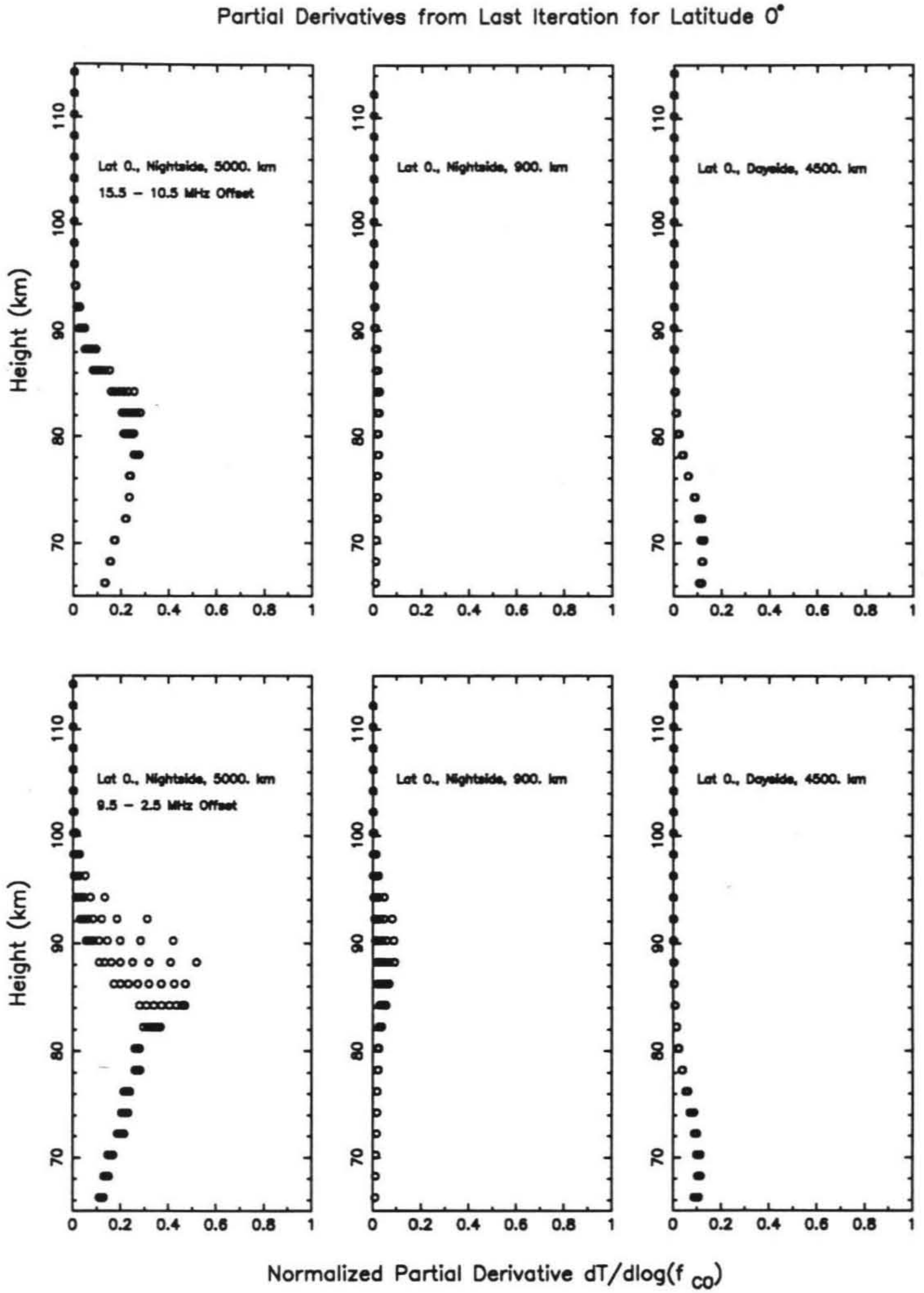

Figure 57a. $\delta T/\delta c$ for each channel are shown from the final iterations of night, evening and afternoon lines at specified radii and within the noted frequency ranges.

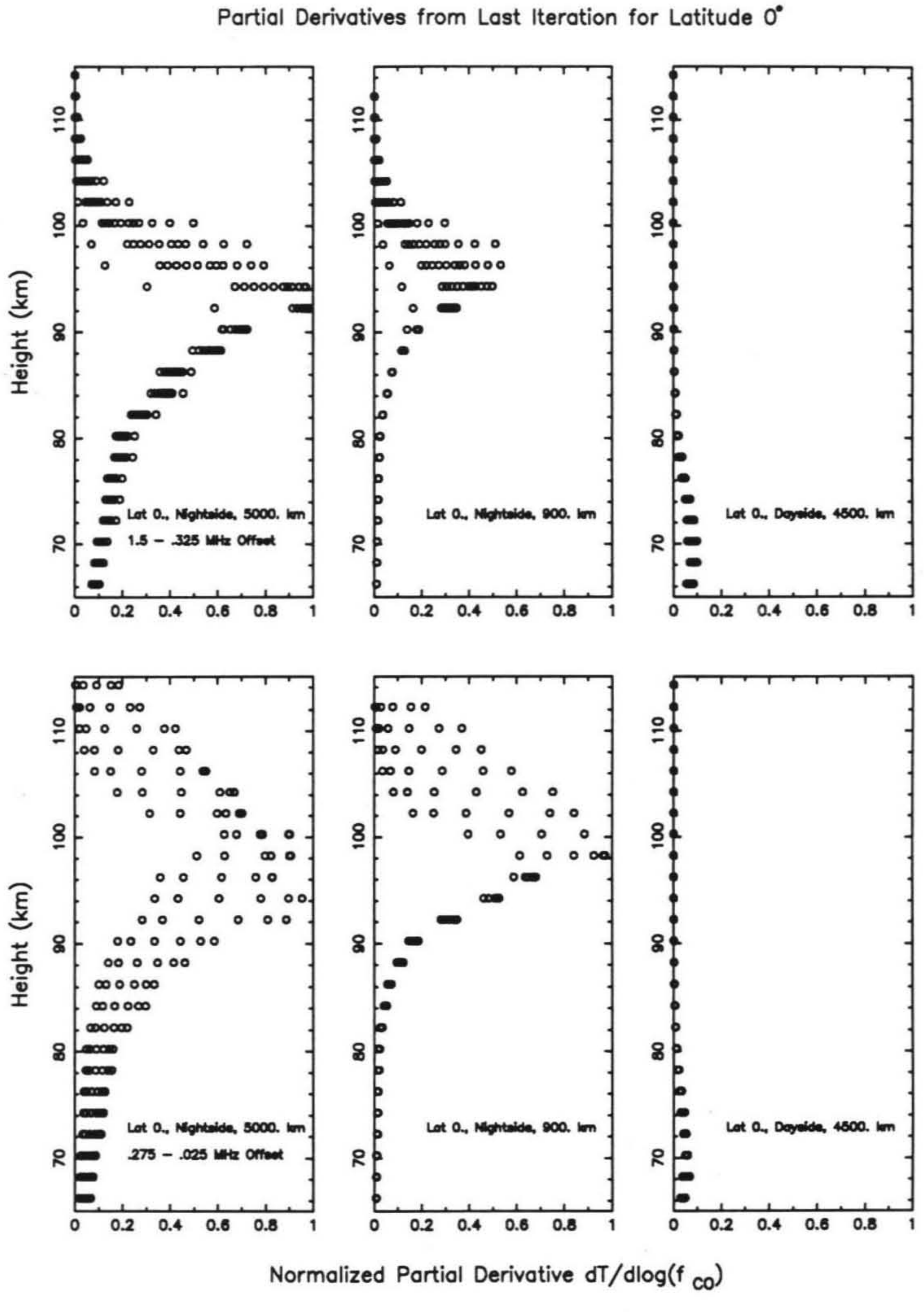
Partial Derivatives from Last Iteration for Latitude 0°
Height (km)
Height (km)
70
80
90
100
110
0
0.2
0.4
0.6
0.8
1
Lat 0., Nightside, 5000. km
1.5 – .325 MHz Offset
Lat 0., Nightside, 900. km
Lat 0., Dayside, 4500. km
Lat 0., Nightside, 5000. km
.275 – .025 MHz Offset
Lat 0., Nightside, 900. km
Lat 0., Dayside, 4500. km
Normalized Partial Derivative dT/dlog(f CO)

Figure 57b.

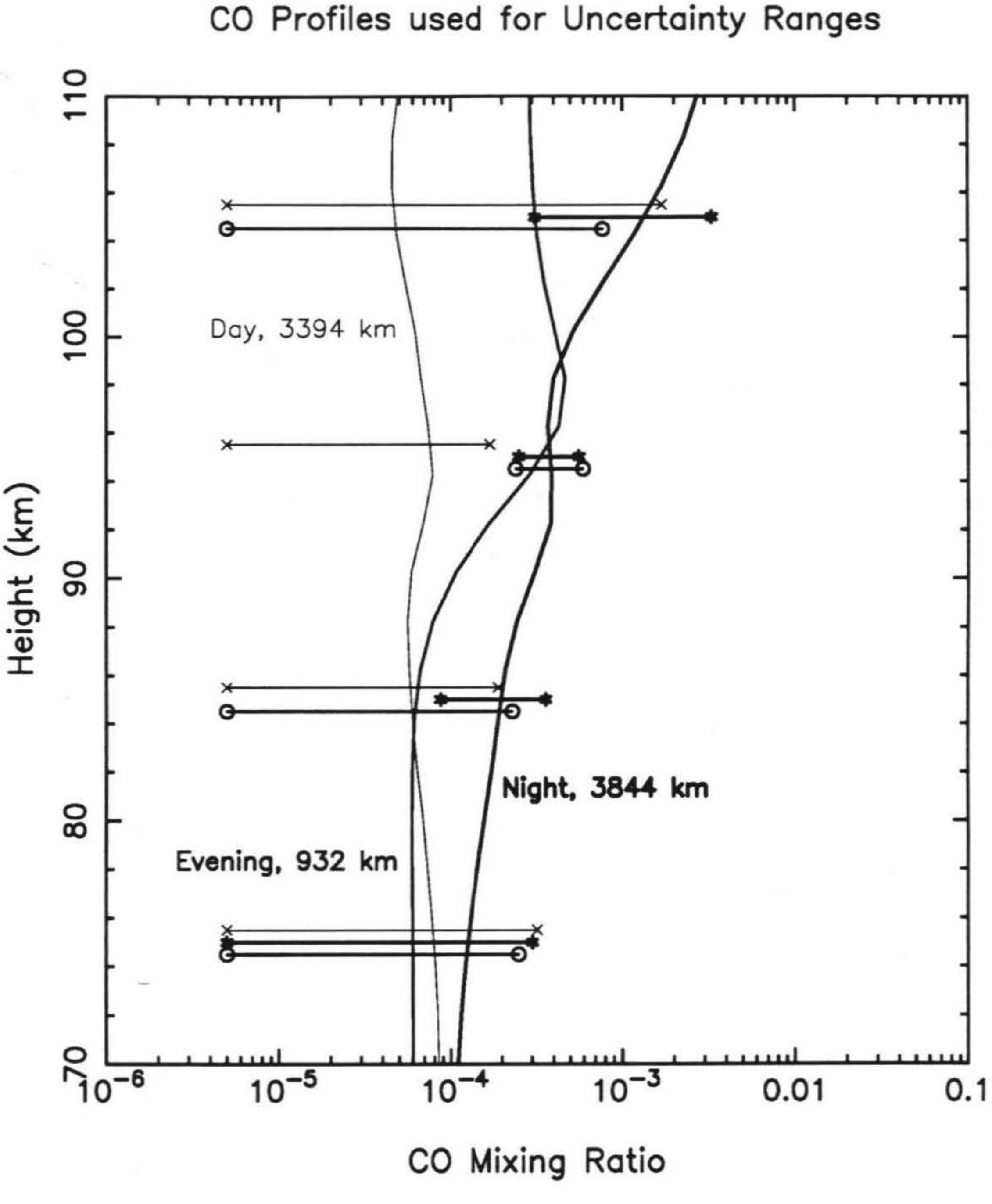

Figure 58. CO Solutions at night, evening and afternoon radii which were perturbed to find the uncertainties overlaid and listed in Table VI. The line widths become thicker progressively from day to evening to night values.

5.4 CO Uncertainties and Correlation Coefficients

Uncertainties for typical night, evening and afternoon CO solutions were determined at several altitudes by perturbing the CO solution until the final residuals were doubled. The CO solutions were perturbed in 10 km-wide layers centered about 75, 85, 95, and 105 km. Such layers correspond to peaks of weighting functions for frequency channels between 15.5-10.5 MHz from ν_o, 9.5-2.5 MHz from ν_o, 1.5-0.325 MHz from ν_o, and 0.275-0.025 MHz from ν_o. This correspondence can be seen in Figure 57 which show the partial derivative of temperature with respect to the CO mixing ratio parameter c_n for each channel in the specified frequency range and for typical night, evening and afternoon CO lines. These partial derivatives are the weights of the least-squares problem and move upwards in altitude for frequencies closer to ν_o. Unlike the night and evening lines, the afternoon temperature partial derivatives are small and remain centered about low heights. This happens because the observed afternoon lines are shallow and can be created with slight amounts of vertical CO abundance. If an altitude does not have much CO present, the 2.6 mm radiation will not interact with the atmosphere and the partial derivative at this altitude, consequently, will be small. As mentioned earlier, some of the innermost channels for nightside lines do show sensitivity at altitudes as high as 110 km. This is shown by the night and evening partial derivatives of Figure 57 for the frequency range of 0.275-0.025 MHz from ν_o.

The best-fit CO solution was perturbed by an amount σ in 10 km-wide layers until the residuals between the resultant synthetic line and the observed line were doubled. These uncertainties are listed in Table VI for the typical night, evening and afternoon lines and the four perturbation layers. The uncertainties in the CO solutions are largest at 75 km, smaller at 85 km, smallest at 95 km and then large again at 105 km. The CO solutions perturbed to determine these uncertainties are

TABLE VI

Uncertainty Range on the Inverted CO Mixing Ratios

	Night		Evening		Day	
H (km)	$10^{-\sigma}$	10^{σ}	$10^{-\sigma}$	10^{σ}	$10^{-\sigma}$	10^{σ}
75	no limit	$10^{.40}$	no limit	$10^{.62}$	no limit	$10^{.58}$
85	$10^{-.38}$	$10^{.23}$	no limit	$10^{.45}$	no limit	$10^{.50}$
95	$10^{-.20}$	$10^{.15}$	$10^{-.23}$	$10^{.17}$	no limit	$10^{.33}$
105	$10^{-.68}$	$10^{.35}$	no limit	$10^{.41}$	no limit	$10^{.55}$

Note. The CO mixing ratio parameter c is the CO solution from the inversion. The σ is the additional amount of CO in log exponent which doubles the solution's residuals. "no limit" indicates that the CO abundance could be perturbed indefinitely without doubling the residuals at the associated height.

shown in Figure 58. The night uncertainties are denoted by an asterisk, the evening uncertainties by a circle and the day uncertainties by a cross. If the CO abundance was almost negligible at an altitude, such as the afternoon profile at every altitude, then the CO solution's exponent could be decreased by -σ indefinity without doubling the residuals. These altitudes contained little CO so decreasing the CO abundance did not perturb the best-fit solutions greatly. This occurrence is expressed in Table VI by the comment "no limit". On Figure 58, these "no limit" uncertainties are assigned a value of 5.0e-6 for convenience.

A normalized covariance matrix for the typical night CO profile was calculated from the definition of covariance

$$\mathbf{Cov}(\Delta CO_n) \; = \; \left[\mathbf{P^T P}\right]^{-1} \sigma^2_{data}/\sigma_i\sigma_j, \tag{52}$$

with

$$\mathbf{P} \; = \; \begin{bmatrix} Partials \\ Constraints \end{bmatrix}_{mn} \tag{53}$$

as obtained from equation (50), σ_{data} the average ±8 K noise on the CO lines, and $\sigma_{i,j}$ the i,j standard deviations in the matrix (see equation (B2) of Appendix B). This calculation acts as a check on correlation coefficients between multi-levels in the constrained least-squares inversion and, equivalently, a check on the quality of the inversion's results. Correlation coefficients in a least-squares problem vary between -1.0 and 1.0 and should be near 0.0 for the least-squares results to be uncorrelated. A value of 1.0 (-1.0) indicates complete positive (negative) correlation and high interdependency between the least-squares' results.

The correlation coefficients for the CO results were smallest and most satisfactory between 90 and 100 km. For example, this inversion, using a standard constraint of 0.01, had a correlation coefficient of -0.04 for the multi-levels at 92 km and at 94 km. The correlation coefficients were largest $\leq$ 80 km and $\geq$ 100 km with values around 0.6 and 0.3 respectively. When the constraint on the inversion was loosened, the correlation coefficient became quite large. For example, for the multilevels at 92 and 94 km, the correlation between the neighboring multi-levels grew to -0.49 with the looser constraint of 0.1.

6. CO Abundance Results

The CO profiles determined by inversion of the 1988 OVRO 2.6mm CO spectra, with the standard parameters described in detail in previous sections of this chapter, are presented in Figure 59 and Figure 60. Figure 59 shows the CO profiles from the night and afternoon spectra and Figure 60 shows the CO profiles from spectra at all local hours in panels at the specified latitude. Latitudinal coverage ranged from -58° to 55°. Local time coverage ranged from roughly 3 PM to midnight with the profiles divided into night (8PM-midnight), evening (6PM-8PM), and afternoon (3PM-6PM) profiles. The evening profiles correspond to spectra measured at nearly-normal incidence radii on the planet (0-2000 km) while the night and afternoon profiles correspond to spectra measured at larger projected radii (2000-6000 km). Average uncertainties from Table VI are overlaid on the night CO results of latitude 2° for reference. The night and evening spectra were inverted with the "known"

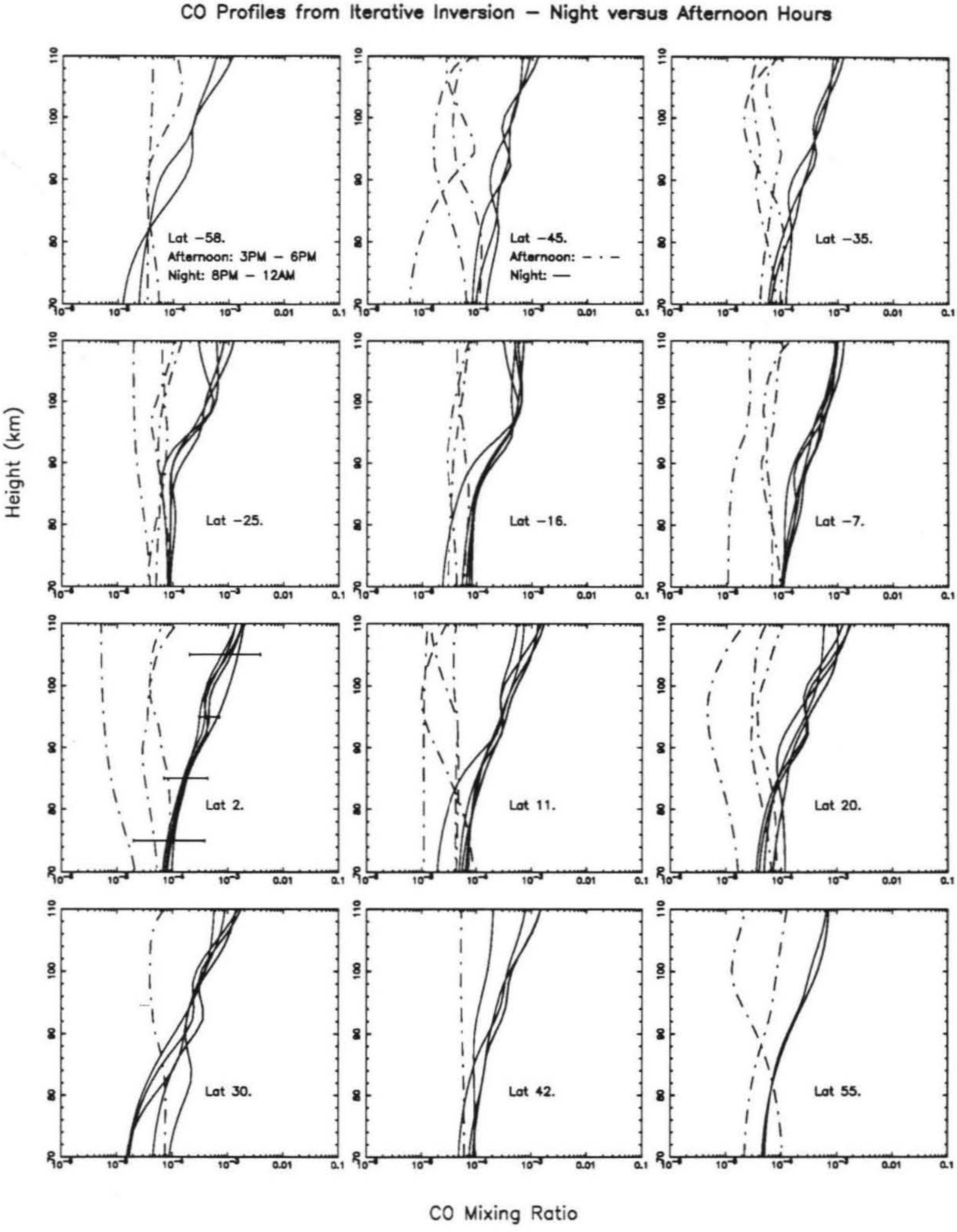

Figure 59. CO profiles from the inversion of 1988 OVRO 2.6mm spectra at specified latitudes during local night (8PM-Midnight) and afternoon (3PM-6PM) hours. Night profiles are solid lines while afternoon profiles are solid-dot-solid lines.

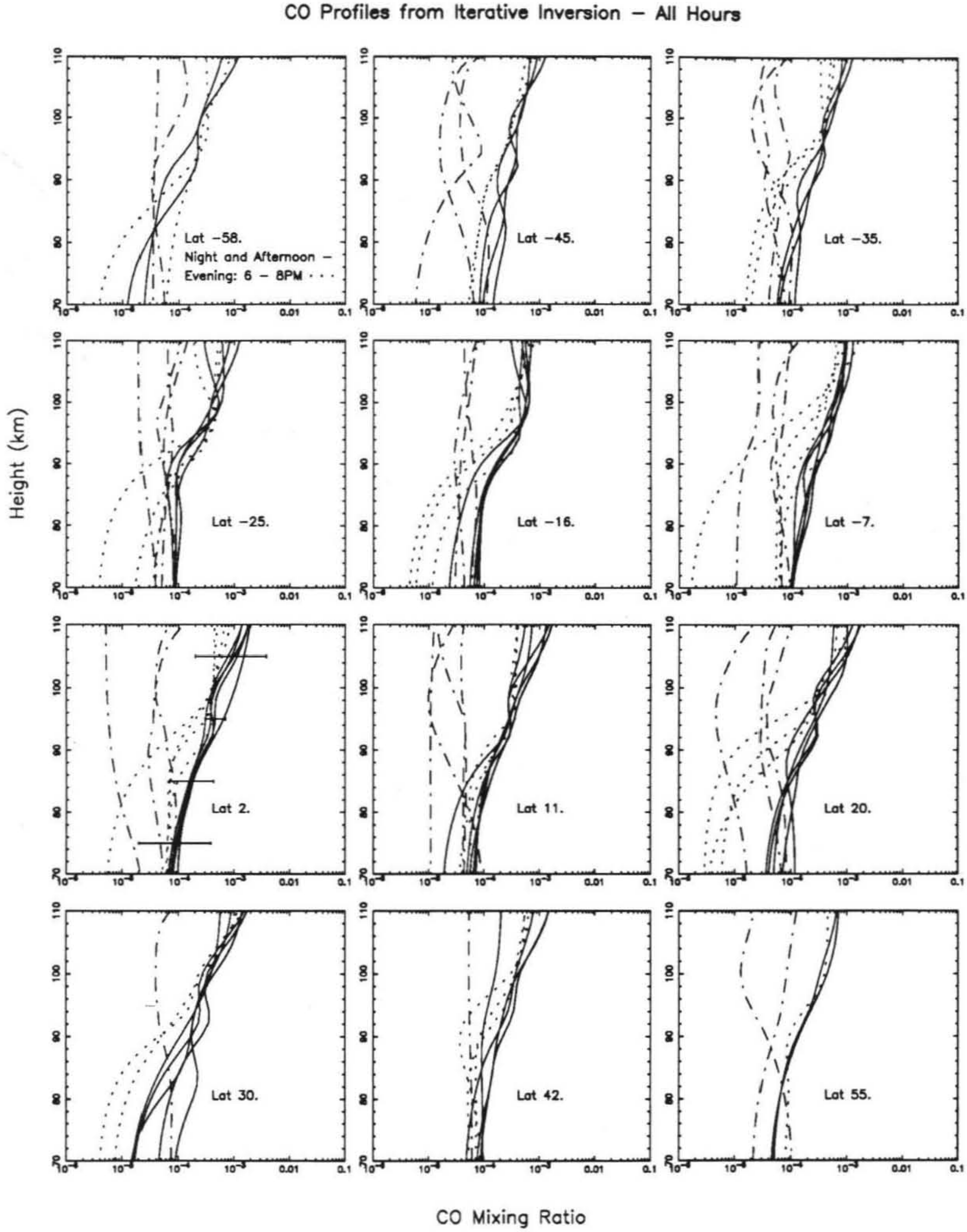

Figure 60. CO profiles from the inversion of 1988 OVRO 2.6mm spectra at specified latitudes are plotted with solid and solid-dot lines for the night and afternoon profiles and with dotted lines for the evening (6PM-8PM) profiles.

nightside temperature profile of Figure 43. The afternoon spectra were inverted with the "known" dayside temperature profile of Figure 43.

The CO profiles from the inversions of the 1988 spectra exhibit a strong local time dependency. Between roughly 85 and 110 km, the night and afternoon profiles separate. The afternoon CO distribution remains essentially constant over height at several 10^{-5} while the night CO distribution increases from 10^{-4} to 10^{-3} with height. The evening CO profiles exhibit a third vertical structure, having low abundances, several 10^{-5}, below 90-95 km and then large abundances at higher altitudes similar to the night profiles. The evening CO profiles are the result of inverting normal incidence spectra, noted earlier for their narrowness relative to the night and afternoon spectra. Narrow spectra would produce a vertical distribution of CO having a steep gradient, changing from much CO at high altitudes to little CO at lower altitudes. The high altitude CO population produces a sufficient linedepth and experiences only narrow doppler broadening. However, the evening spectra may also be partly affected by the assumed nightside temperature profile. The inversions' diurnal temperature profiles differed only at altitudes above 98 km where the nightside cooled in contrast to the dayside's warming. Nonetheless, the divergence of the night and afternoon CO profiles is *not* forced by differences between the assumed diurnal temperature profiles as the divergence begins around 85 km.

Finer details within the CO distribution can be seen in maps of CO abundance at 102, 98, 94, 90 and 86 km as shown in Figures 61, 62, 63, 64, and 65 respectively. At these selected heights, the uncertainties on the CO mixing ratio results are known to be relatively small compared to the uncertainties at lower and higher altitudes (see Table VI). These maps of CO abundance are shaded black for a mixing ratio $\geq 6 \times 10^{-4}$ and white for a mixing ratio $\leq 1 \times 10^{-5}$. Also, thin contours are drawn at mixing ratios of 1×10^{-5} and 5×10^{-5} and thick contours at 1×10^{-4} and 5×10^{-4}.

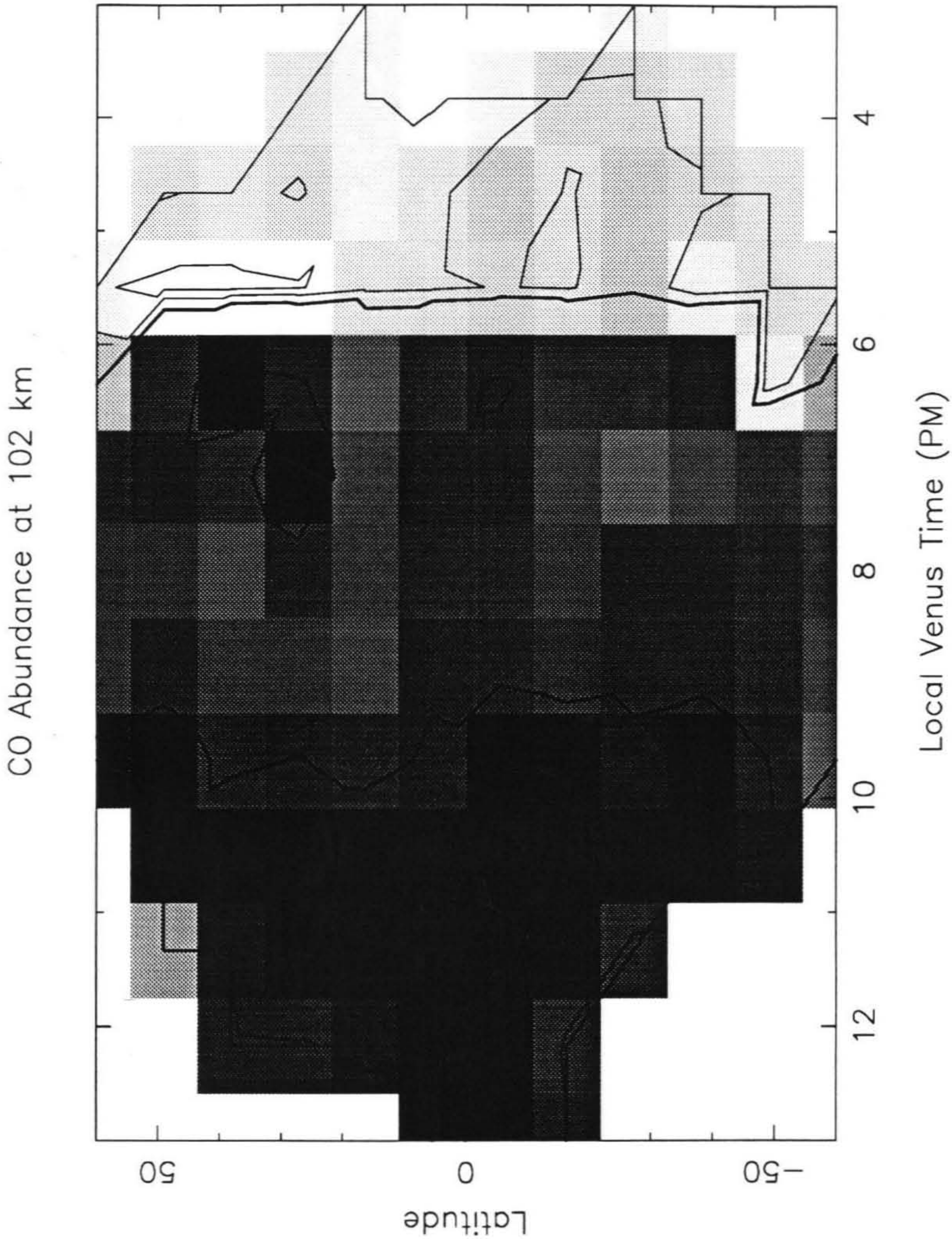

Figure 61. A map of the CO distribution with dark (light) shades corresponding to high (low) abundances, thin contours at 1×10^{-5} and 5×10^{-5}, and thick contours at 1×10^{-4} and 5×10^{-4} mixing ratios.

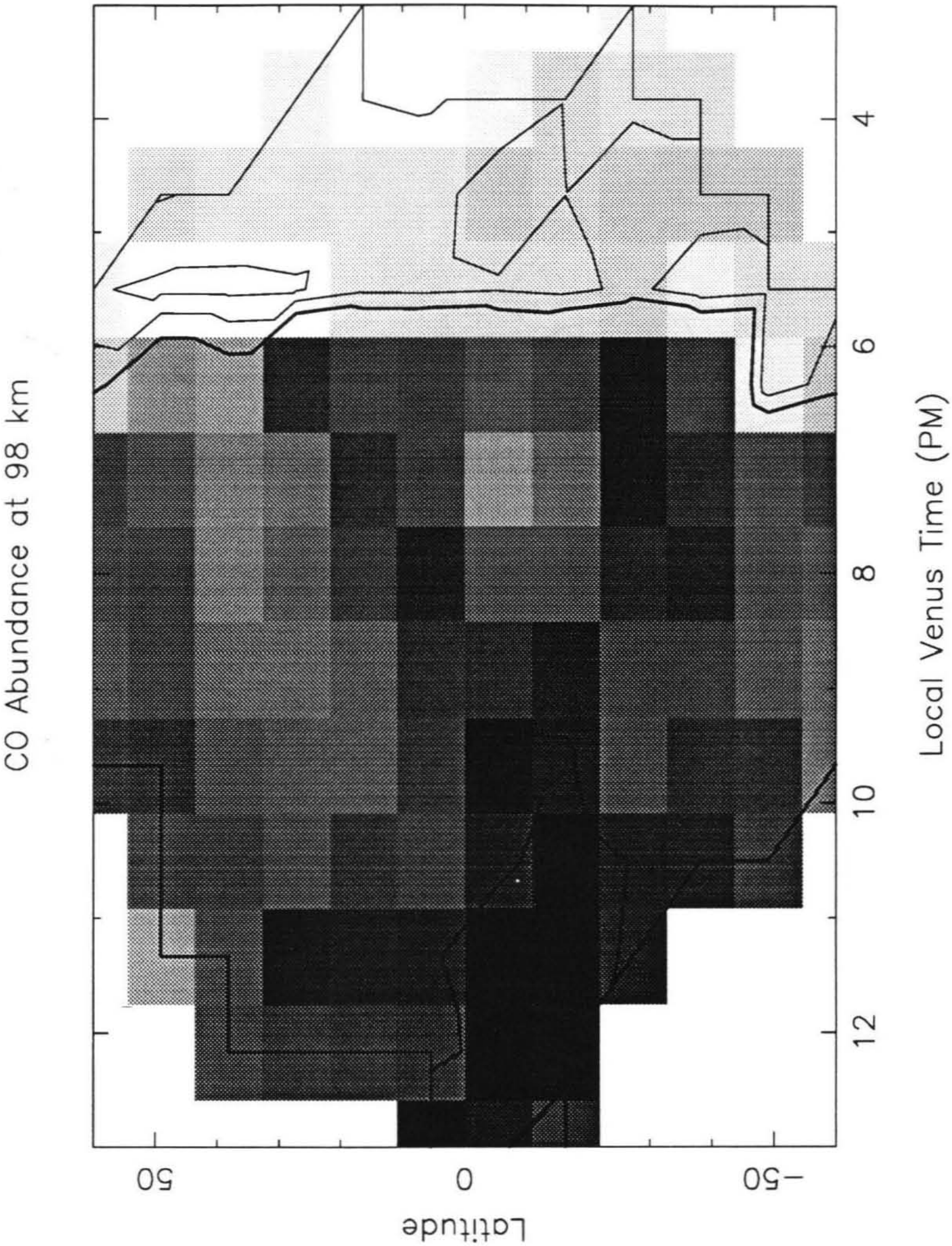

Figure 62. See Figure 61's caption.

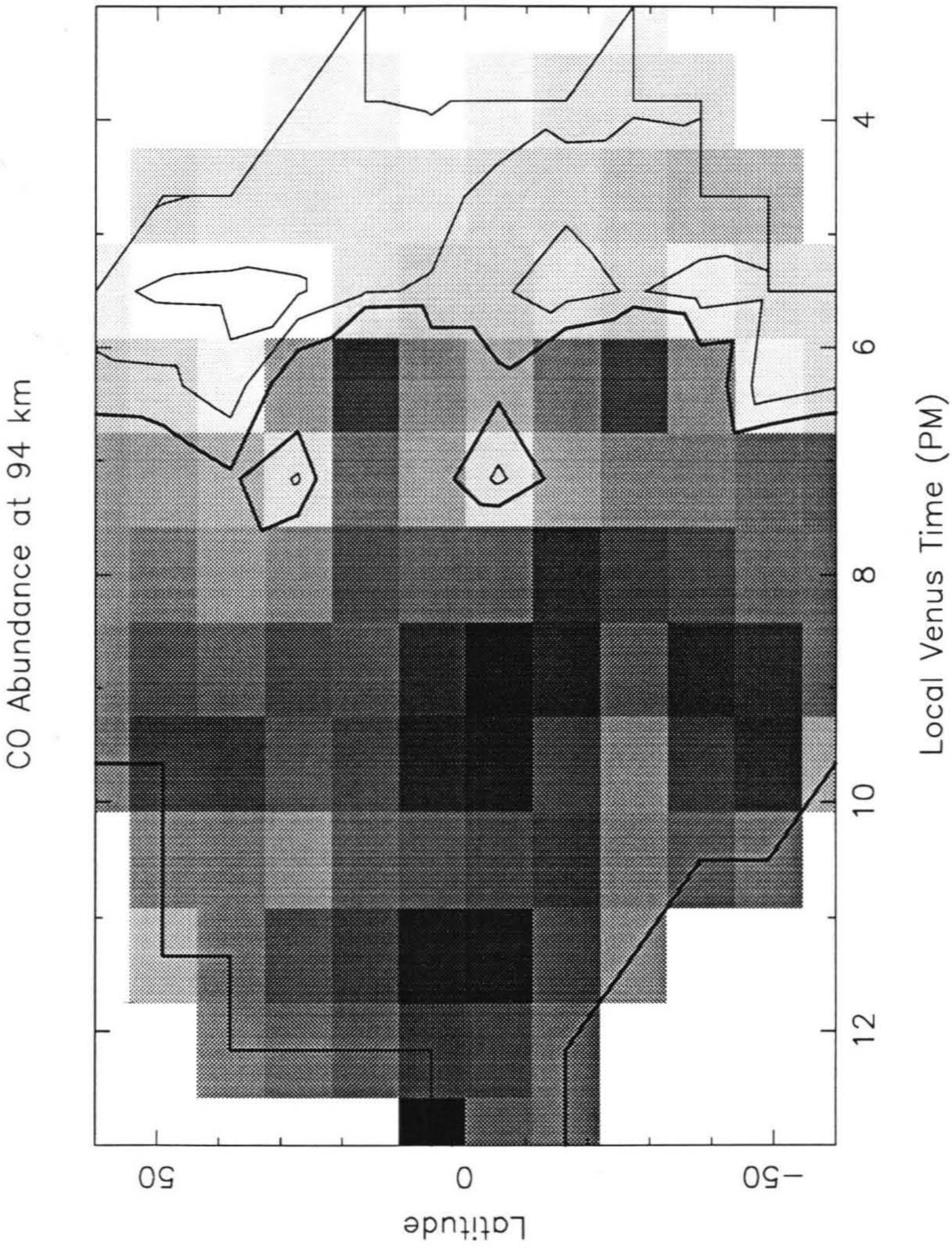

Figure 63. See Figure 61's caption.

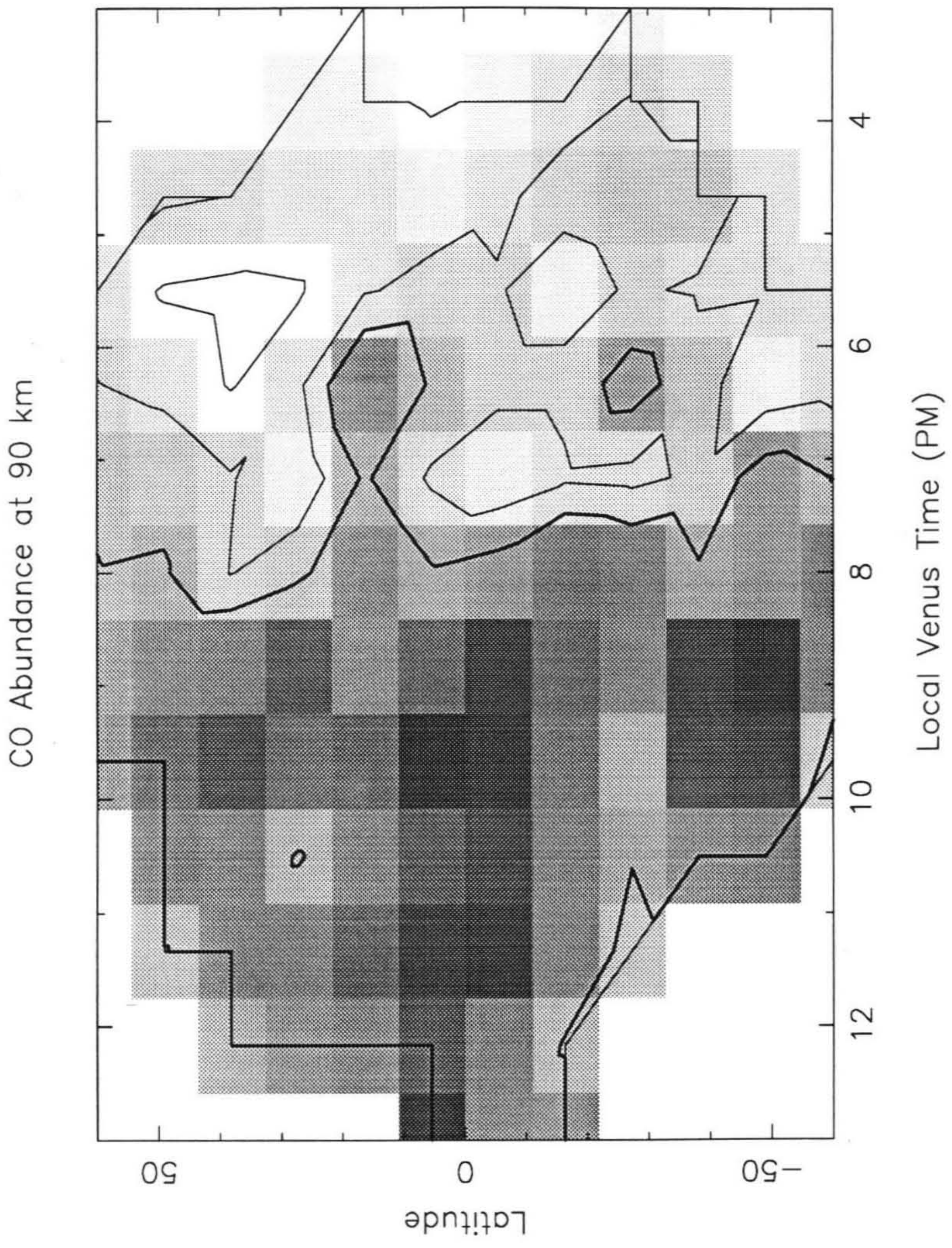

Figure 64. See Figure 61's caption.

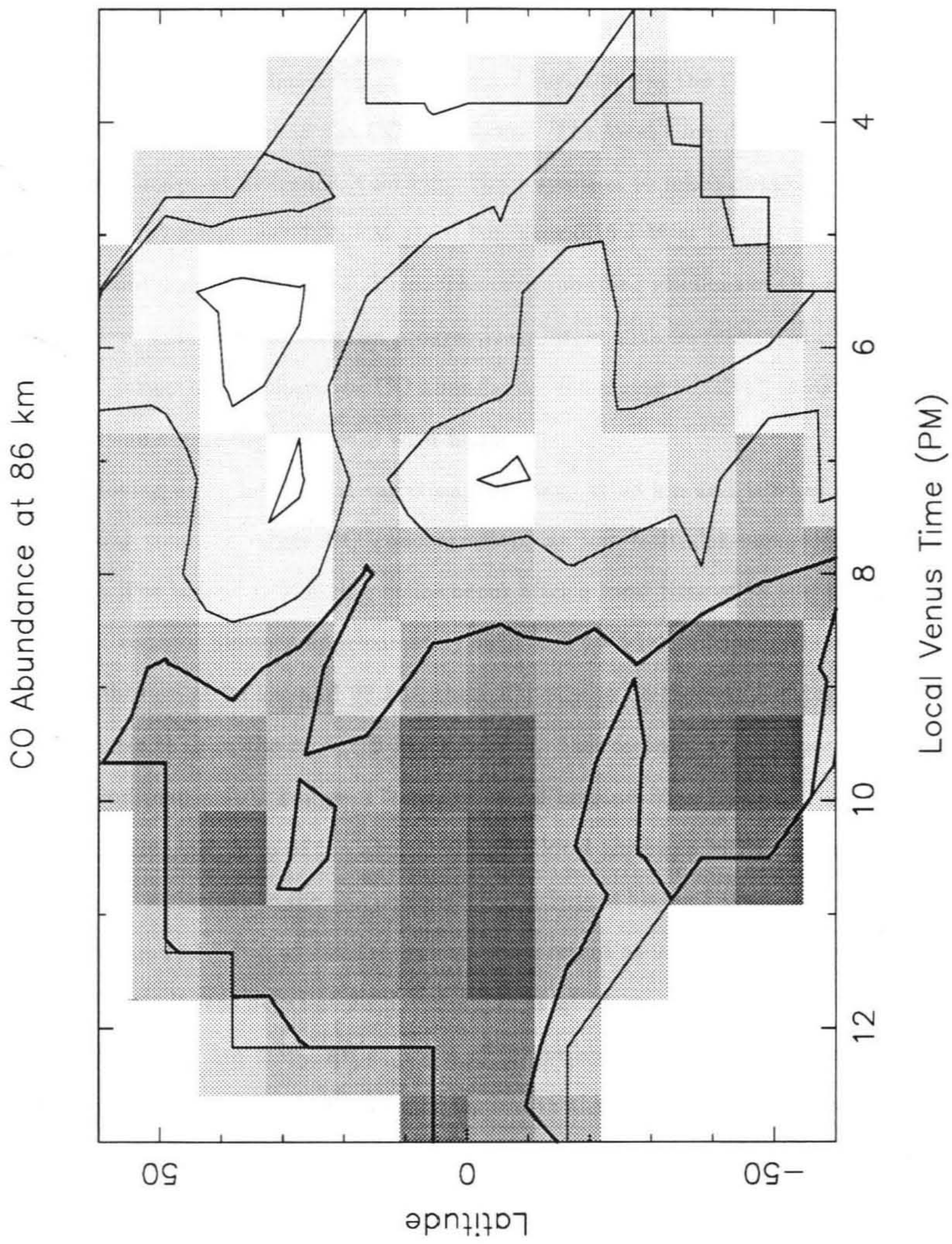

Figure 65. See Figure 61's caption.

Several aspects become apparent in the CO mixing ratio maps: a height variation to the local time dependency, latitudinal variations in the CO abundance, and smaller spatial variations in the CO abundance. The local time dependency is most apparent in maps at altitudes $\geq$ 90 km. The transition to mixing ratios $\geq 1 \times 10^{-4}$ begins at local times near 7:30 PM at 90 km, near 6:15 PM at 94 km, near 6:00 PM at 98 km and near 5:45 PM at 102 km. The corresponding gradient of CO abundance with respect to local time becomes progressively larger with increasing altitude. This is a consequence of the afternoon CO abundances remaining relatively constant while the nightside abundances increase with height.

Moving on to latitudinal variation, the maps at 98 km and 102 km best show the general trend of larger CO concentrations at low latitudes compared to high latitudes. The largest CO mixing ratios occur after a local time of 10 PM and center about the equator between approximately 40°N and 40°S latitude. In the maps of the CO distribution at 94 km and 98 km, there appears to be more CO in the southern low latitudes than in the northern low latitudes. This feature is not apparent in the distribution map at 102 km or in the maps at 90 km and 86 km.

Finally, each map of the abundance over local time and latitude shows small-scale spatial variations to the CO population. Pockets of higher CO abundances occur near 30°N around 7 PM at 102 km but are not present at 98 km. To a lesser degree, high CO abundances occur at 30°S around 7PM at 98 km and around 9 PM at the equator in the 94 km map. An example of the reverse phenomena, a "hole" in the CO distribution, occurs at 30°N around 10 PM in the 90 km and 86 km maps. Also CO "holes" can be seen at 30°N and 5°S in the 94 km, 90 km and 86 km maps near 7 PM. This feature of small abundance pockets and holes existing over approximately 4 km-wide vertical layers in the mesosphere is new to the understanding of Venus' CO distribution. Its validity is dependent upon uncertainties in the CO mixing ratio and will be discussed further in the following section.

7. Discussion

A discussion of this chapter's results is given here. Chapter VI will give a succinct summary of the CO abundance results from the spectral analysis and attempt to integrate them with results from the other chapters.

7.1 CO Abundance Variation With Local Time

The CO mixing ratios obtained from inversion of the 1988 OVRO spectra do show a decided variation with local time which agrees with results from previous analyses. Previous observers of CO rotational transitions in the mesosphere of Venus found that the shape and depth of the 2.6 mm absorption line varied diurnally (Kakar *et al.* 1976; Gulkis *et al.* 1977; Schloerb *et al.* 1980; Wilson *et al.* 1981; Clancy and Muhleman 1985ab; Clancy and Muhleman 1991). At low altitudes in the mesosphere, the CO abundance was determined to be larger on the dayside than the nightside. The reverse was true above 90 km with larger CO abundances on the nightside than the dayside. The spatially resolved CO profiles found with the OVRO spectra do have large abundances above 90 km in the night and evening hours as predicted. The size of the night CO mixing ratios also agrees with previous results, being $\sim 10^{-4}$ at 80 km and $\sim 10^{-3}$ at 100 km. This result is supported by the mixing ratio profiles shown in Figure 42 of the Kitt Peak CO results and the profiles shown in Figures 59 and 60 of the OVRO night CO results.

However, the OVRO CO mixing ratio profiles in the afternoon hours have surprisingly little CO and do not agree with conclusions of previous analyses. The afternoon abundances have values of several 10^{-5} and remain essentially constant over height. The profiles do not show the predicted higher-than-nightside CO abundances below 90 km and do not show effects of the CO_2 photodissociation expected on the dayside. Clancy and Muhleman (1985a) used a sinusoidal expression to describe the variation of the CO profile with local time when modelling their disk- averaged spectra. The sinusoidal function included phase offsets to produce CO profiles that changed smoothly over time of day between maximum CO mixing ratios at local midnight and minimum mixing ratios at both 6 AM and 6 PM local time. Based on such a functional description of the CO distribution and the consequent profiles in Figure 42 for 1988, the OVRO afternoon profiles should be different. The profiles were expected to show CO abundances greater than abundances in the night profiles below 90 km. Furthermore, the afternoon profiles were expected to show CO abundances greater than abundances in the evening profiles at *all* heights. The latter expectation was based upon the pattern of the subsolar-to-antisolar flow which is believed to carry CO from local noon across the evening terminator to local midnight above $\sim$ 80 km and, thus, create the high nightside CO abundance. The "iso-abundant" afternoon profiles from the 1988 OVRO spectra stir up questions on the assumptions made during the inversions and on current photochemical models.

Perhaps the assumed temperature profile for the dayside model is substantially inaccurate? Certainly the assumed dayside temperature profile of Figure 43 is reasonable based on available data. The disk-averaged temperature profile from the Kitt Peak CO lines is roughly 20 K warmer between 90 and 100 km (see Figure 41). Yet, section 5.3 showed CO profiles from inversions done with different assumed temperature profiles. The dayside profile from the "fluctuating" diurnal temperature pair is warmer then the dayside profile of the "smooth" pair over most altitudes (see Figures 34 and 43) but the resultant CO profiles are not significantly changed given the associated CO uncertainties (see section 5.4 and Table VI). Furthermore, the observed OVRO spectra are relatively shallow and narrow in the afternoon cells. This indicates that the absorption lines are optically thin and would have been more responsive to the ambient CO abundance than the ambient temperature in Venus' mesosphere during the observations. The low CO abundances from the inversions, therefore, appear to be accurate estimates of mesospheric CO during the afternoon hours.

Perhaps CO forms more closely about the subsolar point or local noon than the available one-dimensional models predict? Perhaps CO forms at higher altitudes than expected in these models and is quickly transported by subsolar-to-antisolar flow to the nightside without diffusion to the afternoon hours? Perhaps the estimated eddy diffusion, solar cycle position or atmospheric profiles used in the previous one-dimensional photochemical models could be re-examined to improve the local time constraints on production and diffusion of CO? If observational results do not agree with model predictions, then the model must be re-examined. Photochemical models lies outside the scope of this research. Hopefully future work will answer the questions posed here.

7.2 CO Abundance Variation With Latitude

Previous researchers assumed latitudinal variations wherein CO abundance bulges were centered about the equator. In modelling of disk-averaged spectra, Clancy and Muhleman (1991) had CO mixing ratios decrease from equator-to-pole by a factor of 2 at 95 km. This assumed latitudinal variation is not in disagreement with current one-dimensional photochemical models of Venus' mesosphere (Yung and DeMore 1982) or recent three-dimensional general circulation models of coupled dynamics and composition in Venus' thermosphere (Bougher *et al.* 1988). The latter uses model inputs for the photodissociation rate of CO_2, J_{CO_2}, and solar heating over latitude and longitude which are symmetric about the equator and local noon. Bougher *et al.* did not discuss the resultant CO distribution over latitude besides mentioning agreement with observed CO thermospheric densities. At their lower boundary of 136 km, though, the input CO_2 photodissociation rates do decrease from a noon maximum of 1.9×10^{-5} $\sec^{-1}$ at the equator to 0.7×10^{-5} $\sec^{-1}$ at latitudes of ±60°. Similarly, the input EUV and IR solar heating falls from a noon maximum of 2200 K/Earth day at the equator to 1000 K/Earth day at latitudes of ±60° for an altitude of 136 km. Solar heating rates at lower altitudes in the mesosphere are attributed with comparable latitudinal variation. For example, Crisp (1986) used diurnally averaged solar heating rates which were 50 K/Earth day at the equator and 35 K/Earth day at 60°N for an altitude of 100 km.

The maps of CO distribution resulting from analysis of the 1988 OVRO spectra do show abundances roughly centered about the equator (see Figures 61-65). Also, these maps do show larger CO abundances at low latitudes then at latitudes poleward of approximately ±40°. Furthermore, the high CO abundances during hours after 10 PM LVT do change by roughly a factor of 2-3 from equator to pole at altitudes $\geq$ 94 km as expected (see Figure 59). These results are in agreement with the assumed symmetry in the Bougher *et al.* (1988) thermospheric model and the Clancy and Muhleman (1991) mesospheric CO spectral work.

It should be stressed, however, that the temperature profiles used in the current inversions were not varied over latitude. As mentioned before, various equator-to-pole temperature gradients are possible for the upper mesosphere. Pioneer Venus radio occultation measurements in 1985 found negative temperature gradients in the mesosphere above 80 km. In 1987, the reverse was true with PV radio occultation measurements finding positive temperature gradients above 80 km (see Table V). The recent work by Clancy and Muhleman (1991) combining results of disk-averaged spectra from 1982, 1985, 1986, 1988 and 1990 also found strong interannual temperature variations in the mesosphere. The available data are too sparse to dictate the correct temperature gradients over latitude for the inversion of the high latitude OVRO spectra. These near-limb spectra have lineshapes created by the convolved effects of the CO abundance above 95 km, the ambient temperature field and the increased pathlength μ at the limb. Cooler CO molecules absorb upwelling thermal radiation more efficiently. Therefore, to first order, decreasing (increasing) the temperatures from the equator to the poles in the upper mesosphere will most likely lower (raise) the CO mixing ratios results at high latitudes. Following this simple argument further, if the temperature profile is cooler (warmer) at the poles, then the high latitude CO abundance will be even less (more) than the abundances shown in the maps of Figures 61-65.

7.3 CO Abundance Variations with Local Weather

The last noteworthy aspect of the CO distribution is the phenomena of small spatial fluctuations to the CO abundance on top of the broader variation with local time and latitude. Pockets of higher CO abundances occur in the maps of calculated mixing ratios at 102 km and at 98 km over ~4 km- wide layers (Figure 61 and Figure 62). Unlike the "holes" in the CO distribution mentioned in section 6, a few of the pockets of high CO abundance do not fall within the estimated CO uncertainty ranges of Table VI and may be "real" features in the CO distribution. One high abundance feature occurs just past the evening terminator between 6:30-7:30 PM around 30°N latitude at 102 km with CO enhanced by roughly a factor of 2-3 in two spatial cells (Figure 60 and Figure 61). What, then, is the mechanism which built up the CO abundance in a layer comparable in size to the 4-5 km pressure scale height at these altitudes and in horizontal cells approximately 1000 km wide?

Not the average atmospheric conditions over a period of months or years, i.e., the climate, but rather the "weather" on Venus, atmospheric conditions over shorter period of time, may have influenced the mean CO distribution and created small abundance features. The OVRO observations took place within a period of nine days in the spring of 1988 which places a timescale on the possible "weather". Recent dynamical studies of Venus' upper mesosphere which go beyond simple cyclostrophic balance have investigated the influence of atmospheric waves (Fels and Lindzen 1974; Covey and Schubert 1982; Del Genio and Rossow 1982; Fels *et al*. 1984; Crisp 1986; Rossow 1985; Seiff and Kirk 1991). No solid understanding has emerged yet from these dynamical studies. Without spatially resolved temperature data, repeated observation of the CO distribution with an interferometer, and further research on small-scale dynamical forces appropriate at mesospheric pressures of tenths and hundredths of a millibar, this indirect observation of possible weather in Venus' upper mesosphere remains speculative.

Chapter VI Summary of Conclusions.

This final chapter summarizes the results from the analyses of the 2.6 mm continuum map, the merged CO spectra from the 1 MHz and 50 kHz filterbanks, and the doppler-shifted CO spectra from the 50 kHz filterbank. The upper mesospheric wind measurements based on the 50 kHz filterbank spectra are considered to be the focus of this work. The last section weaves aspects of the results into a broader scenario and comments on appropriate future observations and research.

1. Conclusions on Venus' Millimeter Continuum Brightness

A reliable brightness map of Venus' millimeter emission would have been timely as Crisp *et al.* (1989) has just repeated Allen and Crawford's near-infrared photometric observations of Venus' nightside (1984) and again found bright features moving with the cloudtop's zonal wind. These researchers had suggested that the high contrast features, 50 K difference in brightness temperature, originated in the hot lower atmosphere below 35 km and then passed through the cooler, higher atmosphere which had horizontal patchiness in opacity. Departures in a *millimeter* brightness map from the expected smooth, limb-darkened disk would have added support to the new idea of a horizontally-variable Venus clouddeck.

The continuum map did show deviations from a smooth limb-darkened disk. The planetary disk in the map had two separated high 40 Jy/beam ($\approx$ 408.8 K) peaks on top of a flat 35 Jy/beam ($\approx$ 357.7 K) non-circular plateau. However, the symmetrical placement of the brightness temperature features about the disk center indicated that the peaks may have been generated by residual beam effects caused by the large sidelobes on the synthesized beam.

The disk's limb-darkened continuum emission was asymmetric: the nightside limb experienced more limb-darkening than the afternoon limb of the planet. Weighting functions calculated for this 2.6 mm continuum emission found sampling of the upper troposphere and lower mesosphere in a wide layer between 40 and 60 km at normal incidence and between 55 and 75 km along the planet limb. A radiative transfer model could approximately reproduce the continuum map's nightside limb-darkening when given a temperature profile 40 K cooler than the standard Pioneer Venus nightside temperature profile between 60 and 85 km. Again, however, the strength of this result was undercut by the smallness of the OVRO millimeter array. Within four days of observations, the three antennas of the array could not gather the u-v coverage needed to produce a millimeter brightness map having reliable absolute intensities.

2. Conclusions on the CO Inversions

Local CO mixing ratio profiles were determined in 2.5" by 2.5" cells or, equivalently, ~1000 km square cells across the disk of Venus for the spring of 1988 with the observed local 2.6 mm CO absorption lines. The spatially-resolved CO spectra show strong variation with local time, becoming progressively deeper from the afternoon to the night hours. This variation in absorption lineshape with local time was expected based on previous observations of disk-averaged CO lines. A constrained least-squares inversion algorithm was used to solve for the corresponding CO mixing ratio profiles assuming temperature profiles for a nightside model and a dayside model. The resultant mixing ratio profiles, accordingly, vary with local time. CO profiles in the afternoon hours are essentially "iso-abundant" with constant mixing ratio values of several 10^{-5} over height. The CO profiles in the night hours, on the other hand, increase from $\sim 10^{-4}$ at 80 km to $\sim 10^{-3}$ at 100 km. Uncertainty ranges for these CO results are narrowest between 90 and 100 km at a factor of approximately two for a CO mixing ratio of 4.0e-4. The uncertainties on the CO results become larger with decreasing altitudes to below 80 km and with increasing altitude above 105 km.

Also the uncertainty ranges are typically larger for low CO abundances than high CO abundances.

The small amount of CO present seen in the afternoon mixing ratio profiles is surprising. Analyses of disk-averaged CO spectra and theoretical models had suggested that more CO would be present in the late afternoon given the photodissociation of CO_2 on the dayside. In particular, the afternoon hours should contain more CO than the evening hours – that does not occur in the 1988 calculated CO mixing ratio profiles. This raises questions concerning existing one-dimensional models of Venus mesosphere. In particular, if eddy diffusion, solar cycle position and atmospheric parameters can be improved to generate a two-dimensional photochemical dynamical model and examine the height and longitudinal extent of dayside production of CO.

The mixing ratio profiles show a latitudinal distribution for mesospheric CO abundance centered roughly about the equator. This result has never been directly observed before and supports assumptions made in previous research. The largest CO abundances occur after a local time of 10 PM and center about the equator in latitudes between 40°N and 40°S for altitudes above 95 km. CO abundance decreases by roughly a factor of 2-3 from equator to pole in the late night hours. The magnitude of the decrease to CO abundance from equator to pole is not absolute since the temperature profiles used in the inversions of observed spectra remained unrealistically constant over latitude. Mesospheric temperatures may either increase or decrease towards the pole based on the available sparse temperature data. Given an observed line at high latitudes, the calculated CO abundances can be expected to decrease (increase) in colder (warmer) mesospheric temperatures assuming constant upwelling radiation.

3. Conclusions on the Wind Measurements

We observed Venus within a nine day period in the spring of 1988 with the

OVRO millimeter interferometer tuned to the first rotational transition of ^{12}CO. Using aperture synthesis techniques and a 50 kHz filterbank, these observations yielded high spatial and spectral resolution of doppler shifts to the center of this absorption line produced by winds in the Venusian upper mesosphere. These doppler shifts changed across the disk of the planet consistent with a pattern of a strong, westward wind moving across the evening terminator into the evening hours of Venus. The shifts were strongly blue in afternoon hours, zero near the subearth point at 19.3 hours LVT, and strongly red in the late evening hours.

Measurements corrected for incidence angle along the planet limb revealed similar velocities along the afternoon and nightside limbs. These incidence corrected wind measurements ranged about a mean value 85 ± 8 ms^{-1} on the dayside limb and 106 ± 10 ms^{-1} on the nightside limb, giving an initial estimate of the dominant westward winds. It was necessary to smooth the radial wind measurements spatially to minimize small scale structure due to residual dirty beam effects in order to least squares fit the data to canonical forms of the zonal and subsolar-to-antisolar flows. The high geometrical correlation between the subsolar-to-antisolar wind and a zonal wind in the mid-to-low latitudes over the Venusian evening terminator did not allow a least-squares fit for a superposition of the flows at most latitudes. However, if a relatively small subsolar-to-antisolar wind was present, its cross terminator speed had a rough upper limit of 40 ms^{-1} based on model fits at high latitudes. The best least squares fits of the smoothed radial wind measurements were to a model zonal flow in latitudinal bins of 10°. The fitted zonal speeds range over latitude about a mean value of 132 ± 10 ms^{-1}. Temperature weighting functions for the 2.6 mm CO line showed approximate altitudes for the wind measurements which changed from 97 km at normal incidence in the evening, to 99 km on the dayside limb, and to 103 km on the nightside limb. The weighting functions sample in a layer roughly 12 km wide about these center altitudes and move upwards into higher altitudes with greater radii from the disk center. As the smoothed measurements exclude limb measurements, the roughly 25 ms^{-1} difference between the mean fitted zonal speed and the mean limb speeds may reflect an actual decrease as the upper mesospheric zonal flow with increasing altitude. The roughly 25 ms^{-1} difference between these mean speeds, however, is the same size as error bars on the unsmoothed radial winds speeds.

Current cyclostrophic models can produce wind fields to explain these measurements given low horizontal viscosity coefficients, strong cloud top speeds, and, crucially, negative or zero temperature gradients towards the poles. Recent results from PV radio occultation data and ground-based CO spectroscopic observations have found substantial evidence for strong temporal variation to the mesospheric temperature structure. Negative or zero temperature gradients at heights above 80 km, similar to those measured in 1985 by PV radio occultations, may have occurred. A temperature field associated with such negative or zero gradients would have then produced the observed upper mesospheric zonal winds via cyclostrophic balance in the spring of 1988.

4. Synthesis of the Upper Mesospheric Results

The following points discuss the connections between the weak continuum map results, the CO distribution estimates and, most importantly, the zonal wind measurements, drawing in outside research at times. This is designed to intertwine the results presented in the thesis and to inspire future work by others.

The first point connects the 1988 Kitt Peak temperature profile, the 1988 OVRO continuum map and the OVRO CO profiles. The Kitt Peak disk-averaged temperature profile for spring 1988 was warmer than the Pioneer Venus temperature profiles by roughly 10-15 K. The only result from the OVRO continuum map was that the disk experienced asymmetric limb-darkening. So, perhaps the dayside limb of the continuum map experienced less limb-darkening rather than, as assumed in Chapter III, the nightside limb experiencing more limb-darkening than expected. The expected limb-darkening was based on models using the nominal Pioneer Venus temperature profiles. If the continuum map's dayside limb experienced less limb-darkening, then the dayside temperature profile was warmer than the PV temperature profile in 1988. If a warmer dayside temperature profile had been used in the inversions of the OVRO spectra, then higher CO mixing ratios would have been found in the afternoon hours. This possibility, though, is undermined by the uncertainties on the absolute flux densities in the continuum map and by the lack of correct normalization for the continuum map.

The second point connects the zonal winds measured with the OVRO data to the temperature field and the CO distribution present during the spring of 1988. The OVRO narrow-channel spectra were doppler shifted by zonal winds having speeds on the order of 100 ms^{-1}. If these observed winds were created by cyclostrophic balance, then the temperature field in the upper mesosphere probably decreased from the equator to the poles. If temperatures were cooler at higher latitudes, then even less CO abundance existed at higher latitudes than estimated by the inversion work in Chapter V.

The third point again connects the zonal winds to the CO distribution present during 1988 but draws upon thermospheric modelling by Bougher *et al.* (1988) and dynamical interpretations of disk-averaged CO spectra by Clancy and Muhleman (1985b). Bougher *et al.* (1988) had superimposed a 55 ms^{-1} retrograde superrotation upon the mean subsolar-to-antisolar circulation in their three-dimensional thermospheric model. The superimposed zonal flow increased evening cross-terminator speeds and decreased morning cross-terminator speeds and shifted the exospheric temperature minimum from midnight to 2 AM LVT in the model, without changing the magnitudes of calculated temperatures. They found, however, that a superimposed zonal flow did not change the CO distribution in the model – that is, in altitudes above 136 km and, equivalently, pressures below 5×10^{-3} microbars. But, Clancy and Muhleman (1985b) used a 50 ms^{-1} zonal wind in the upper mesosphere, at higher pressures of 1.0 to 0.10 millibars, to shift the expected midnight CO bulge to 8 AM LVT. What, then, are the effects of 100 ms^{-1} zonal winds on the CO distribution in 1988? If the simple displacement of the CO bulge of Clancy and Muhleman (1985b) is viable, could the CO midnight bulge be displaced into the late afternoon hours by a 100 ms^{-1} flow? The answers to these questions are complicated by the wide weighting functions associated with the 2.6 mm CO line, by the possible presence of a subsolar-to-antisolar flow, and by the possible presence of atmospheric waves passing through or breaking within the upper mesosphere. Future two- and three-dimensional models of photochemistry and dynamics in the upper mesosphere will hopefully address these questions.

The fourth point continues on the repercussions of a strong zonal wind in the upper mesosphere. It looks at the effects upon the temperature distribution over local time. In the inversions of the CO spectra, the assumed diurnal temperature profiles were identical below 100 km. Such diurnally-invariant temperature profiles are supported by balance equations found in the Bougher *et al.* thermospheric model. In their model's thermodynamic equation, the change in temperature with time at a given point in the atmosphere is directly proportional to the zonal speed. The full equation for the change in temperature with respect to time at a given altitude and latitude is

$$\frac{\delta T}{\delta t} = \frac{g e^{z}}{p_{\circ} C_p} \frac{\delta}{\delta z} \frac{k}{H} \frac{\delta T}{\delta z} - a(T - \overline{T}) - \left[\frac{u}{r}\frac{\delta T}{\delta \theta} + w\left(\frac{\delta T}{\delta z} + \frac{R^{*} T}{C_p \overline{m}}\right)\right] + \frac{Q}{C_p}, \qquad (54)$$

with k the coefficient of thermal conductivity, $\overline{T}$ the global mean equilibrium temperature, a a radiative damping constant, Q the rate of heat addition per unit mass and C_p the specific heat at constant pressure. Looking at just the advection term, the proportionality of change in temperature to the zonal flow is then

$$\frac{\delta T}{\delta t} \propto -\frac{u}{r}\frac{\delta T}{\delta \theta}, \tag{55}$$

wherein θ is the solar zenith angle, r the radius from the planet center, and u the horizontal velocity (Dickinson and Ridley 1975). Therefore, zonal winds may decrease any diurnal asymmetry in mesospheric temperatures in 1988 assuming the relationship (54) holds. Again, future models of the upper mesosphere will hopefully investigate this problem in detail.

The last point connects the CO and wind results from the OVRO data to the interannual variations in the mesosphere found by Clancy and Muhleman (1991) and the cyclical variations by the zonal winds of the cloudtop region found by Del Genio and Rossow (1989). The latter analysis found a 5- to 10-year cycle to the cloudtop's dynamics, measuring a decline to the mean zonal flow and disappearance of a Kelvin wave in 1982-83 PVO ultraviolet images in contrast to 1979-80 and 1985-86 ultraviolet images. The former analysis found a maximum perturbation in upper mesospheric temperatures and CO abundances from nominal Pioneer Venus 1978-79 conditions during the period of 1985-1986. Clancy and Muhleman's CO and temperature results for 1982, 1988 and 1990 were in better agreement with the PV results. They suggested that the interannual variations by the mesospheric atmospheric profiles might be related to the cloudtop's cycle. Given the existence of a mesospheric cycle as outlined by Clancy and Muhleman's results, then the 1988 OVRO CO and wind results are perhaps measurements of a midway state of the mesosphere between the 1985-1986 extreme state and a future or current Pioneer Venus state.

Further observations of CO absorption lines are needed, using the aperture synthesis technique to achieve high spatial resolution and using improved receivers for higher signal-to-noise ratios. A millimeter continuum brightness map of Venus should be made from data gathered with an array having at least five antennas. In order to best constrain the latitudinal, local time, and interannual variations of the CO distribution in the upper mesosphere, observations of more than one rotational transition should be done. This requires receivers operating at 230 GHz besides 115 GHz on the array. Such receivers are currently being incorporated at OVRO though coincident observations of two transitions is as yet far from standard practice. Finally, observations with narrow channel filterbanks – especially of Venus' morning terminator – will constrain latitudinal variation of the zonal flow in the upper mesosphere, determine whether a subsolar-to-antisolar component may be present and provide more insight into temporal variation of the circulation. This last goal for future observations hopefully will be accompanied by further three-dimensional photochemical modelling of the mesosphere and study of dynamical forces appropriate at millibar pressures as found in the upper mesosphere of Venus.

Appendix A: Beam Weighting

The beam convolution aspect of the radiative transfer model was work begun by Shugi Deguchi and Duane Muhleman. A beam equivalent to rotating a gaussian (0, σ) about an origin will have an area beneath it given by

$$A_{beam} = \int_0^{2\pi} \int_0^R e^{-r^2/2\sigma^2} r dr d\theta \tag{A1}$$

using polar coordinates centered about the origin. The half-width-half-maximum angular size of the beam is the radius where the magnitude of the gaussian beam has fallen by e^{-1} and is related to σ by

$$r_{HWHM} = \frac{r_{FWHM}}{2} = d = \sigma (2\, ln2)^{1/2}, \tag{A2}$$

Therefore, the integral for the area under a gaussian beam is

$$A_{beam} = \int_0^{2\pi} \int_0^R e^{-(r/d)^2 ln2} r dr d\theta. \tag{A3}$$

A brightness temperature at a radius r is weighted by its area under the gaussian beam and normalized by the total area under the beam.

Two beams effected the OVRO maps and spectra: the 3" full-width-half-maximum CLEAN beam and the 70" diameter primary beam of the OVRO 10-meter dishes. The normalized weighting by the primary beam (centered on the subearth point on the planet) of the model brightness temperature curve over radius was given by

$$\begin{aligned} b(r) &= \frac{2ln2\,(\frac{r}{d})^2}{1 - exp(-ln2(\frac{r}{d})^2)} \int_0^1 \mu exp(-(1-\mu)^2(\frac{r}{d})^2 ln2) d\mu \\ &= \frac{ln2\,(\frac{r}{d})^2}{1 - exp(-ln2(\frac{r}{d})^2)}, \end{aligned} \tag{A4}$$

where d is the size of the primary beam, μ the cosine of the angular distance from the subearth point and r is the angular radius of the planet in arcseconds. For Venus' diameter of 33" and a full angular size of 70" for the primary beam, this weighting of the model brightness temperatures amounts to a factor of 0.93 at the planet limb.

The planet-resolving CLEAN beam weights had to be calculated with the 3" beam centered on each resolution cell of the model across the planet. The weights applied to the model brightness temperatures $T_b(r_i)$ along a radial grid with index i are given by

$$b(r_i) = \frac{\Delta A_i \, e^{-(r_i/HPBW)^2 ln2}}{\Sigma_i \Delta A_i \, e^{-(r_i/HPBW)^2 ln2}}, \qquad (A5)$$

where ΔA_i is the area corresponding to the radial grid point r_i and is calculated as $r_i dr d\theta$. The spacing of the beam centers over radius was 0.625" and 0.200", selected based on the data were binned (the 2.5" spacing of the merged CO lines of Chapter V) or not (the 1.25" spacing of continuum map of Chapter III) respectively. The radial grid of r_i was the same for each radial position of the beam center. It is described in section 2 of Chapter III as a grid with spacing from the center of the disk to 5700 km by 200 km, from 5700 km to 6085 km by 100 km and, at the limb, from 6085 to 6180 km by 10 km. Also an angular grid was employed to calculate the area associated with a radial grid position, ΔA_i, over an angle of 2π with respect to the beam center's radial position.

Appendix B: Cross-Correlation Method

This brief derivation of least squares estimation of a parameter and its variance follows Appendix VI of Cuzzi (1972) and chapter four of Hamilton (1964). A linear dependence is assumed between the observed values f (in this case, the observed CO absorption line) and a set of parameters x (frequency offsets or frequency lags from line center)

$$\mathbf{F} = \mathbf{A}\mathbf{X} + \mathbf{e}, \qquad (B1)$$

where the vector **e** holds errors on the data **F**. Given a nonsingular covariance matrix for the data, **C**, with correlation coefficients ρ_{ij} and standard deviations σ_i as

$$\mathbf{C} = \begin{pmatrix} \sigma_1^2 & \sigma_1\sigma_2\rho_{12} & \dots & \sigma_1\sigma_n\rho_{1n} \\ \sigma_1\sigma_2\rho_{12} & \sigma_2^2 & \dots & \sigma_2\sigma_n\rho_{2n} \\ \vdots & \vdots & \ddots & \vdots \\ \sigma_1\sigma_n\rho_{1n} & \sigma_2\sigma_n\rho_{2n} & \dots & \sigma_n^2 \end{pmatrix} \qquad (B2)$$

then the solution to the set of equations (B1) is given by

$$\mathbf{X} = \left[\mathbf{A}^{\mathbf{T}}\mathbf{C}^{-1}\mathbf{A}\right]^{-1}\mathbf{A}^{\mathbf{T}}\mathbf{C}^{-1}\mathbf{F}. \qquad (B3)$$

If the errors on the data are independent so the correlation coefficients ρ_{ij} are zero, then it can be shown that a simple least squares analysis is equivalent to the above matrix solution (B3). This equivalence avoids the problem of knowing the matrices **A** and **C** in order to solve (B3).

From least squares analysis, the sum of residuals between an observed value $\mathbf{F_o}$ (the observed CO line) and a theoretical value $\mathbf{F_j}$ (the Lorentzian line) can be expressed as

$$S_j = \sum_i \frac{(F_{oi} - F_{ji})^2}{\sigma_i^2} \qquad (B4)$$

and weighted by the errors σ_i on observed values. By the description of (B1) the theoretical values can be given by

$$F_{ji} = A_{ji}x_j \qquad (B5)$$

so

$$S_j = \sum_i \frac{F_{oi}^2 - 2F_{oi}A_{ji}x_j + A_{ji}^2x_j^2}{\sigma_i^2}. \qquad (B6)$$

Then, since $\sigma_i^2 = C_{ii}^{-1}$, the sum of the residuals can be expressed as

$$S_j = \sum_i F_{oi}^2C_{ii}^{-1} - 2x_j\sum_i F_{oi}A_{ji}C_{ii}^{-1} + x_j^2\sum_i A_{ij}^2C_{ii}^{-1} \qquad (B7)$$

which has the form of a parabola over x_j

$$S_j = a_0 + a_1x_j + a_2x_j^2 \qquad (B8)$$

(here, the constants a are *not* the constants used in Appendix C or Chapter IV to refer to maximum wind flow speeds).

Hence, following least squares analysis, the minimization of the squared residuals for the best value of x (to fit the Lorenzian line to the observed CO line) occurs at the minimum of the parabola

$$\frac{\delta S_j}{\delta x_j} = 0 = a_1 + 2a_2 x_{min}, \tag{B9}$$

so

$$x_{min} = -\frac{a_1}{2a_2}. \tag{B10}$$

Identifying the a constants of (B8) to the constants of (B7) it can be seen that

$$x_{min} = \frac{\sum_i Foi C_{ii}^{-1} A_{ji}}{\sum_i A_{ji}^2 C_{ii}^{-1}}, \tag{B11}$$

which is simply the matrix solution

$$\mathbf{X} = \left[\mathbf{A^T C^{-1} A}\right]^{-1} \mathbf{A^T C^{-1} F} \tag{B3}$$

if the covariance matrix is diagonal as stated earlier. The x_{min} from fitting a parabola to the curve of the squared residuals is the frequency offset solution. This frequency offset or lag from the cross correlation residuals of an observed CO line and the Lorenzian lineshape corresponds to the best match of frequency positions of the two lines. The value of x_{min} is, therefore, the doppler shift of the observed CO line.

This estimated parameter has an associated formal error given by the diagonal elements of the covariance matrix

$$\mathbf{C_x} = \begin{pmatrix} Variance\, x_1 & Covariance\, x_1 x_2 & \dots & Covariance\, x_1 x_m \\ Covariance\, x_1 x_2 & Variance\, x_2 & \dots & Covariance\, x_2 x_n \\ \vdots & \vdots & \ddots & \vdots \\ Covariance\, x_1 x_n & Covariance\, x_2 x_n & \dots & Variance\, x_n \end{pmatrix} \tag{B12}$$

which at the best estimate x_{min} is the expectation value

$$C_{xmin} = \left\langle (x_{min} - x_{true})(x_{min} - x_{true})^T \right\rangle, \tag{B13}$$

where x_{true} is the unknown, exact value of the solution. To find an expression of the formal error associated with x_{min} in terms of the parabola coefficients above, let

$$\mathbf{F_{true}} = \mathbf{A x_{true}} \tag{B14}$$

and

$$\mathbf{B} = \mathbf{A^T C^{-1} A} = \mathbf{B^T}. \tag{B15}$$

Then the expectation value C_{xmin} can be expressed as

$$\mathbf{C_{xmin}} = \left\langle \mathbf{B^{-1} A^T C^{-1} (F - F_{true})} \left[\mathbf{B^{-1} A^T C^{-1} (F - F_{true})} \right]^T \right\rangle \tag{B16}$$

using the identities (B1), (B14) and (B15). This can be simplified within the averaging brackets since, **C** is a diagonal matrix, to

$$\mathbf{C_{xmin}} = \mathbf{B^{-1} A^T C^{-1}} \left\langle \mathbf{(F - F_{true})(F - F_{true})^T} \right\rangle \mathbf{C^{-1} A B^{-1}}. \tag{B17}$$

Since **C** is the matrix for the variance on the data set then

$$\mathbf{C} = \left\langle \mathbf{(F - F_{true})(F - F_{true})^T} \right\rangle \tag{B18}$$

and so

$$\mathbf{C_{xmin}} = \mathbf{B^{-1}(A^T C^{-1} A) B^{-1}} = \mathbf{B^{-1}}. \tag{B19}$$

Using relation (B15) and letting a new matrix $\mathbf{P} = \sigma^2 \mathbf{C^{-1}}$ (where the elements C_{ii} are unequal but uncertain by a factor σ^2) then

$$\mathbf{C_{xmin}} = \sigma^2 \mathbf{(A^T P A)^{-1}}. \tag{B20}$$

Hamilton (1964) shows that the best unbiased estimate of σ^2 is σ^2_{xmin} and is proportional to the matrix of the lowest residuals

$$\sigma^2_{\mathbf{xmin}} = \frac{\mathbf{(F - A x_{min})^T P (F - A x_{min})}}{n - m}, \tag{B21}$$

wherein m is the number of parameters (equal to one) and n the number of independent data points (equal to sixteen, the number of channels used in the cross-correlation). Thus

$$\mathbf{C}_{\mathbf{xmin}} = \frac{(\mathbf{F} - \mathbf{A}\mathbf{x}_{\mathbf{min}})^{\mathbf{T}}\mathbf{P}(\mathbf{F} - \mathbf{A}\mathbf{x}_{\mathbf{min}})(\mathbf{A}^{\mathbf{T}}\mathbf{P}\mathbf{A})^{-1}}{n - m}. \tag{B22}$$

By using the matrix identities for the parabola coefficients a of (B7) and (B8) and reducing the matrix relation of (B22) to a single parameter case, it can be seen that

$$C_{xmin} = Variance\, of\, xmin = \frac{S(xmin)}{(n-1)a_2}, \tag{B23}$$

which is related to the parabola minimum by

$$\sigma^2_{xmin} = \frac{(a_0 + a_1 x_{min} + a_2 x^2_{min})}{(n-1)a_2} \tag{B24}$$

with the notation as above in expressions (B4) through (B10).

If non-linear dependencies exist between F_{ji} and x in (B5), then these higher order terms will create a non-parabolic residual curve. The parabolic approximation about x_{min} will be valid if a small region of the residual curve is fitted. Consequently, only the three smallest squared residuals from the cross correlation were used to define a parabola and determine x_{min}. Figure 23 shows an example of such a parabolic fit and section 1 of Chapter IV cites the steep range in size for squared residuals with frequency lag.

Appendix C: Geometry for Model Wind Flows

A similar derivation of this geometry is presented in Appendix 2.5.2 of Goldstein (1989). The basic right-handed cartesian coordinate system (x_o, y_o, z_o) for the measurements are shown in Fig. C1. These axes are defined by an origin at the planet center, the y_o-axis on the equator, and the x_o-axis passing through the sub-earth point or along the line-of-sight. The next cartesian coordinate system (x, y, z)

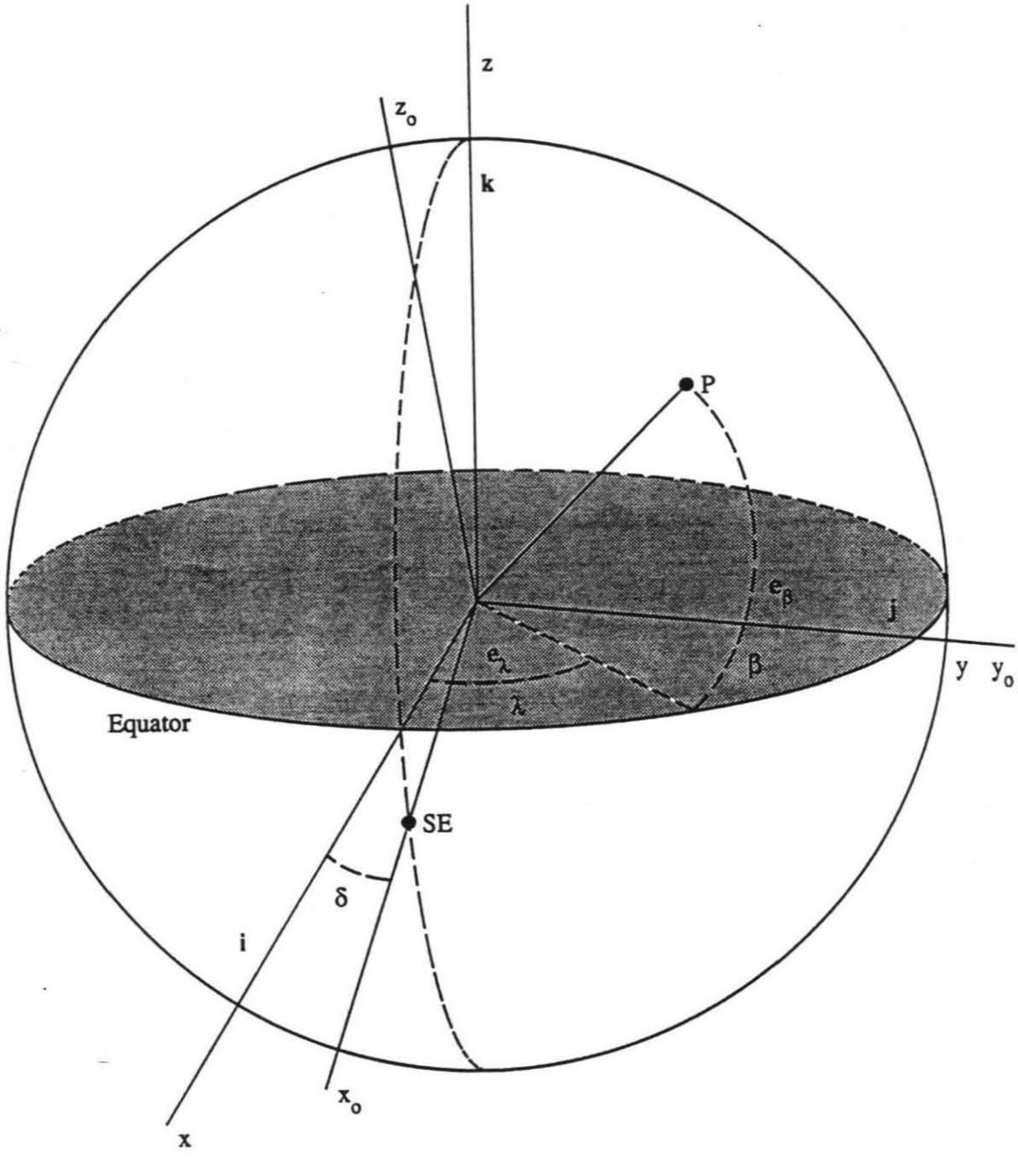

Figure C1. Coordinate systems, unit vectors and angles used to model the wind flows on a planetary disk orientated similar to Venus in the spring of 1988. Point SE marks the subearth point and point P a wind measurement position.

is rotated by the angle δ, the subearth point's planetary latitude, about the $y_\circ$-axis so the x-y plane contains the planet's equator. The unit vectors (**i**, **j**, **k**) lie along the axes of this second coordinate system. In this cartesian system, the planetary latitude β and planetary longitude from the subearth point λ can be used to define a measurement position P and have associated spherical coordinate unit vectors $\mathbf{e}_\beta$ and $\mathbf{e}_\lambda$. The usual transformations exist between these two cartesian systems and the spherical coordinates

$$\begin{aligned} x_\circ &= x cos\delta + z sin\delta \\ y_\circ &= y \\ z_\circ &= z cos\delta - x sin\delta \\ x &= cos\lambda cos\beta \\ y &= sin\lambda cos\beta \\ z &= sin\beta \end{aligned} \tag{C1}$$

as shown in Fig. C1.

The zonal winds were assumed to follow a constant westward pattern so

$$\mathbf{u_Z} = a_1 \mathbf{e}_\lambda, \tag{C2}$$

wherein a_1 is an unknown constant speed. Moving into cartesian coordinates

$$\mathbf{u_Z} = a_1 \Big[\frac{y\mathbf{i} - x\mathbf{j}}{(x^2 + y^2)^{1/2}} \Big] \tag{C3}$$

which, using the planetary angles available to position the wind measurements, is only

$$\mathbf{u_Z} = a_1 \Big[sin\lambda \mathbf{i} - cos\lambda \mathbf{j} \Big] \tag{C4}$$

using the identities of (C1). The actual wind measurements are components of the flow along the line-of-sight so a dot-product with the x-axis was applied

$$u_Z = a_1 \mathbf{e}_\lambda \cdot \mathbf{i} = a_1 sin\lambda \tag{C5}$$

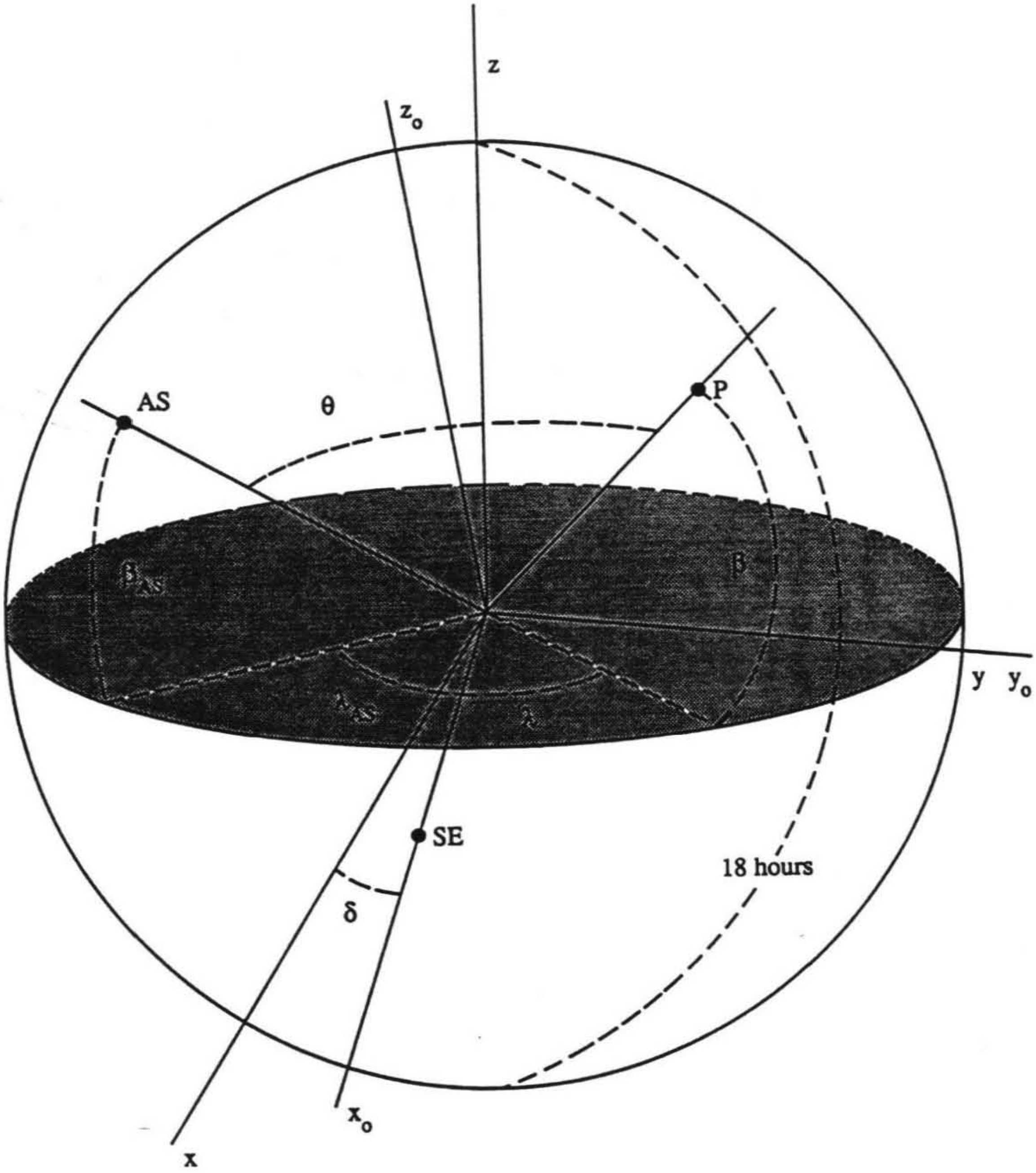

Figure C2. Additional angles and unit vectors used to describe the subsolar-to- antisolar flow with AS marking the antisolar point and a dashed longitude line the evening terminator.

and then transformed to the x_o-axis

$$u_Z = a_1 sin\lambda cos\delta, \tag{C6}$$

which gives equation (C2) in the text for the model zonal flow.

Modelling of the subsolar-to-antisolar flow requires additional variables to describe this flow's axisymmetric movement from the subsolar point to the antisolar point (Fig. C2). The antisolar point AS and a measurement position P can be represented in the vector forms

$$\mathbf{AS} = cos\lambda_{AS} cos\beta_{AS}\mathbf{i} + sin\lambda_{AS} cos\beta_{AS}\mathbf{j} + sin\beta_{AS}\mathbf{k}$$

$$\mathbf{P} = cos\lambda cos\beta\mathbf{i} + sin\lambda cos\beta\mathbf{j} + sin\beta\mathbf{k} \tag{C7}$$

using the coordinate systems described. Between the noon and midnight points on Venus a canonical form for the amplitude of the subsolar-to- antisolar winds is, to first order,

$$u_{SA} = a_2\left[1 - \frac{|90^\circ - \theta|}{90^\circ}\right], \tag{C8}$$

where a_2 is the maximum speed of the flow as it crosses the evening terminator and θ is the angle between the antisolar point and a measurement point P along a circle passing through both the subsolar (SS) and antisolar (AS) points and positioned about the planet center. This equation (C8) describes a horizontal velocity which is tangent to a circle defined by vectors **P** and **AS** and shown as vector **T** in Fig. C3. The angle θ can be defined by

$$cos\theta = \mathbf{P} \cdot \mathbf{AS}. \tag{C9}$$

Using the identities of (C7) for these vectors leads to

$$cos\theta = cos(\lambda - \lambda_{AS}) cos\beta cos\beta_{AS} + sin\beta sin\beta_{AS} \tag{C10}$$

in which λ, β, λ_{AS} and β_{AS} are all known parameters for a given measurement point P.

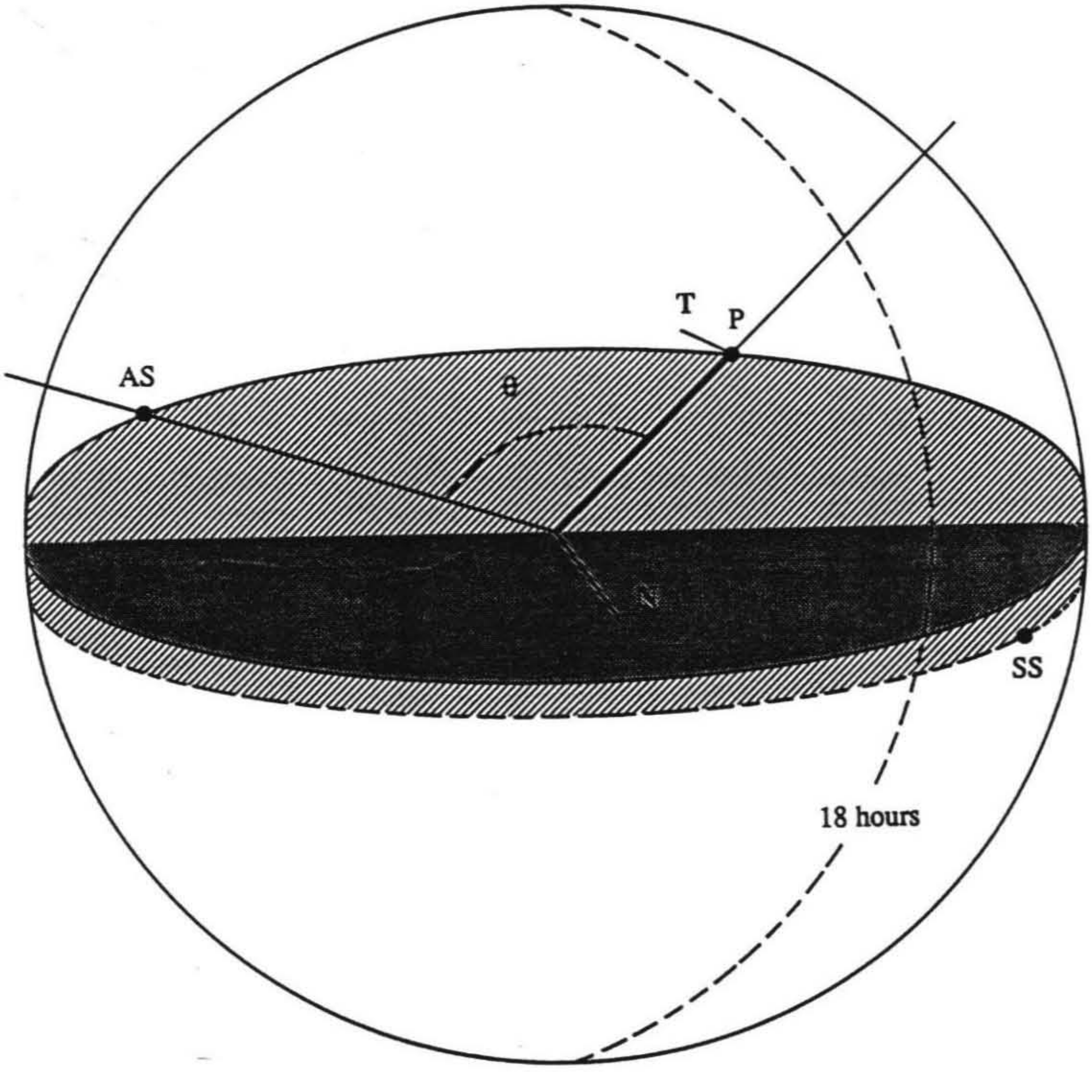

Figure C3. Additional vectors needed to describe the axisymmetric nature of the subsolar-to-antisolar flow with SS marking the subsolar point and further defining the circular plane containing vectors **AS**, **T**, and **P**.

However, the desired quantity is the component of the subsolar-to-antisolar flow vector along the x_o-axis. A first step towards this goal is the component of **T** along the x- and z- axes. This tangent vector **T** can be specified by creating a normal unit vector **N** to the circle passing through points AS, P and SS (see Fig. C3) where

$$\mathbf{N} = \frac{\mathbf{P} \times \mathbf{AS}}{sin\theta}. \tag{C11}$$

Then any tangent vector to such a circle can be defined by

$$\mathbf{T} = \mathbf{N} \times \mathbf{P} = \frac{\mathbf{P} \times \mathbf{AS}}{sin\theta} \times \mathbf{P}, \tag{C12}$$

and will satisfy the requirements that the flow be directed towards the antisolar point and be orthogonal to both **P** and **N**. Using the vector identity

$$(\mathbf{A} \times \mathbf{B}) \times \mathbf{C} = (\mathbf{A} \cdot \mathbf{C})\mathbf{B} - (\mathbf{B} \cdot \mathbf{C})\mathbf{A} \tag{C13}$$

then for evaluating **T**

$$(\mathbf{P} \times \mathbf{AS}) \times \mathbf{P} = (\mathbf{P} \cdot \mathbf{P})\mathbf{AS} - (\mathbf{P} \cdot \mathbf{AS})\mathbf{P}. \tag{C14}$$

Given that **P** is a unit vector and relation (C9) then

$$\mathbf{T} = \frac{1}{sin\theta}\Big[\mathbf{AS} - \mathbf{P}cos\theta\Big] \tag{C15}$$

and the x and z components of the vector **T** are

$$\begin{aligned} T_x &= \frac{1}{sin\theta}\Big[AS_x - P_x cos\theta\Big] \\ T_z &= \frac{1}{sin\theta}\Big[AS_z - P_z cos\theta\Big] \end{aligned} \tag{C16}$$

and the x and z components of the flow are

$$\begin{aligned} u_{SA_x} &= a_2\Big[1 - \frac{|90^\circ - \theta|}{90^\circ}\Big]T_x \\ u_{SA_z} &= a_2\Big[1 - \frac{|90^\circ - \theta|}{90^\circ}\Big]T_z. \end{aligned} \tag{C17}$$

So, the component of the subsolar-to-antisolar winds along the x_o- axis or line-of-sight is, with substitution of relations (C7) and (C10) and transformations with (C1), given by

$$\begin{aligned} u_{SA} &= a_2\left[1 - \frac{|90^\circ - \theta|}{90^\circ}\right] \\ &\quad \Big[(cos\delta/sin\theta)[cos\lambda_{AS}cos\beta_{AS} - cos\lambda cos\beta cos\theta] \\ &\quad + (sin\delta/sin\theta)[sin\beta_{AS} - sin\beta cos\theta]\Big] \end{aligned} \qquad (C18)$$

which is equation (C4) in the text on wind modelling.

Appendix D: 1988 OVRO CO Spectra

This appendix presents all of the merged CO spectra from the 1988 OVRO observations which were inverted for CO mixing ratio profiles as discussed in Chapter V.

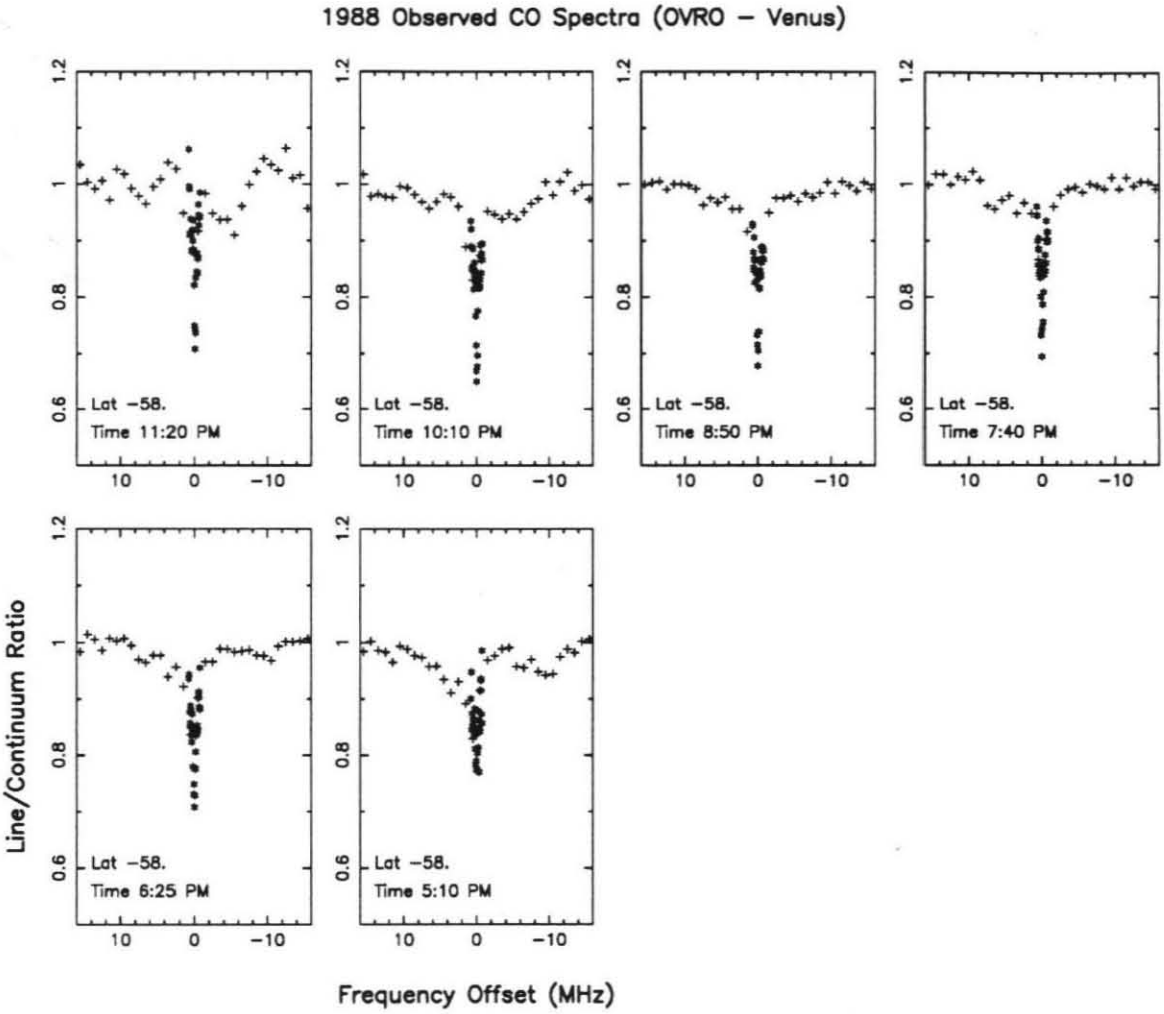

Figure D1a. The OVRO CO spectra in bins across Venus centered about the specified latitude and specified local times. The line-to-continuum ratios measured in the 1 MHz channels are denoted by crosses and the 50 kHz channels by asterisks.

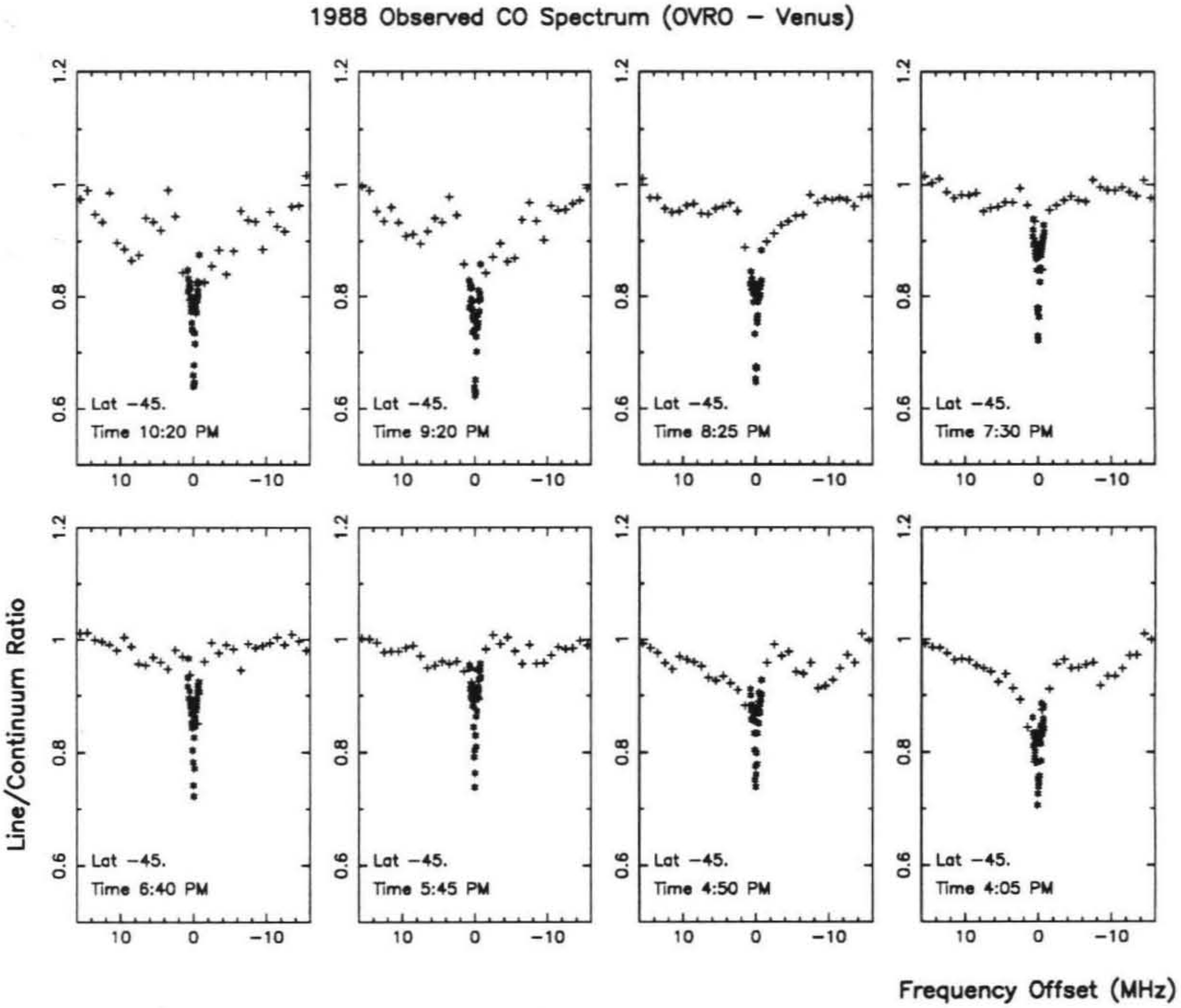
1988 Observed CO Spectrum (OVRO – Venus)
Line/Continuum Ratio
Frequency Offset (MHz)
1.2
1
0.8
0.6
10
0
−10
Lat −45.
Time 10:20 PM
Time 9:20 PM
Time 8:25 PM
Time 7:30 PM
Time 6:40 PM
Time 5:45 PM
Time 4:50 PM
Time 4:05 PM

Figure D1b.

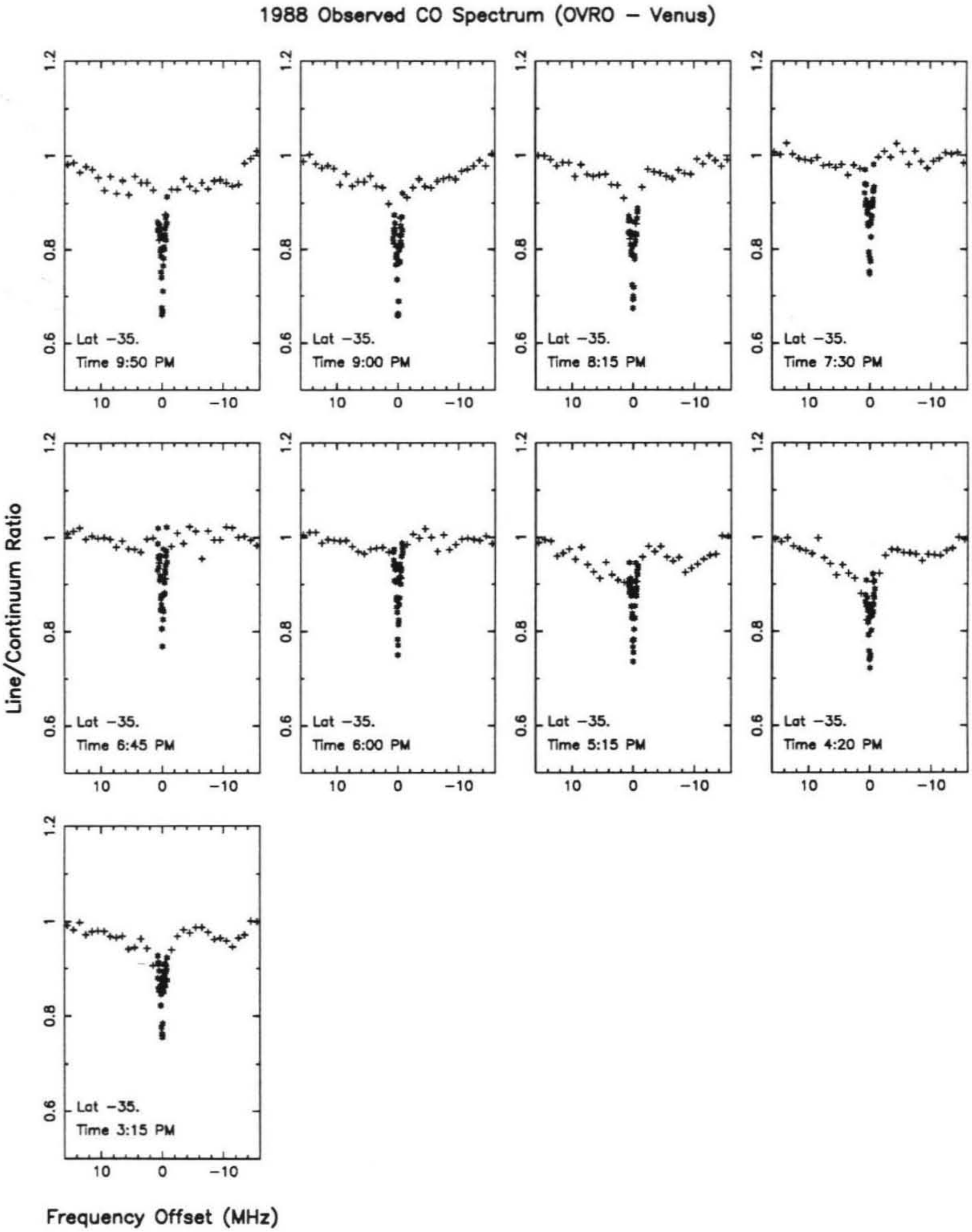
1988 Observed CO Spectrum (OVRO – Venus)
Line/Continuum Ratio
1.2
1
0.8
0.6
Lat −35.
Time 9:50 PM
Time 9:00 PM
Time 8:15 PM
Time 7:30 PM
Time 6:45 PM
Time 6:00 PM
Time 5:15 PM
Time 4:20 PM
Time 3:15 PM
10
0
−10
Frequency Offset (MHz)

Figure D1c.

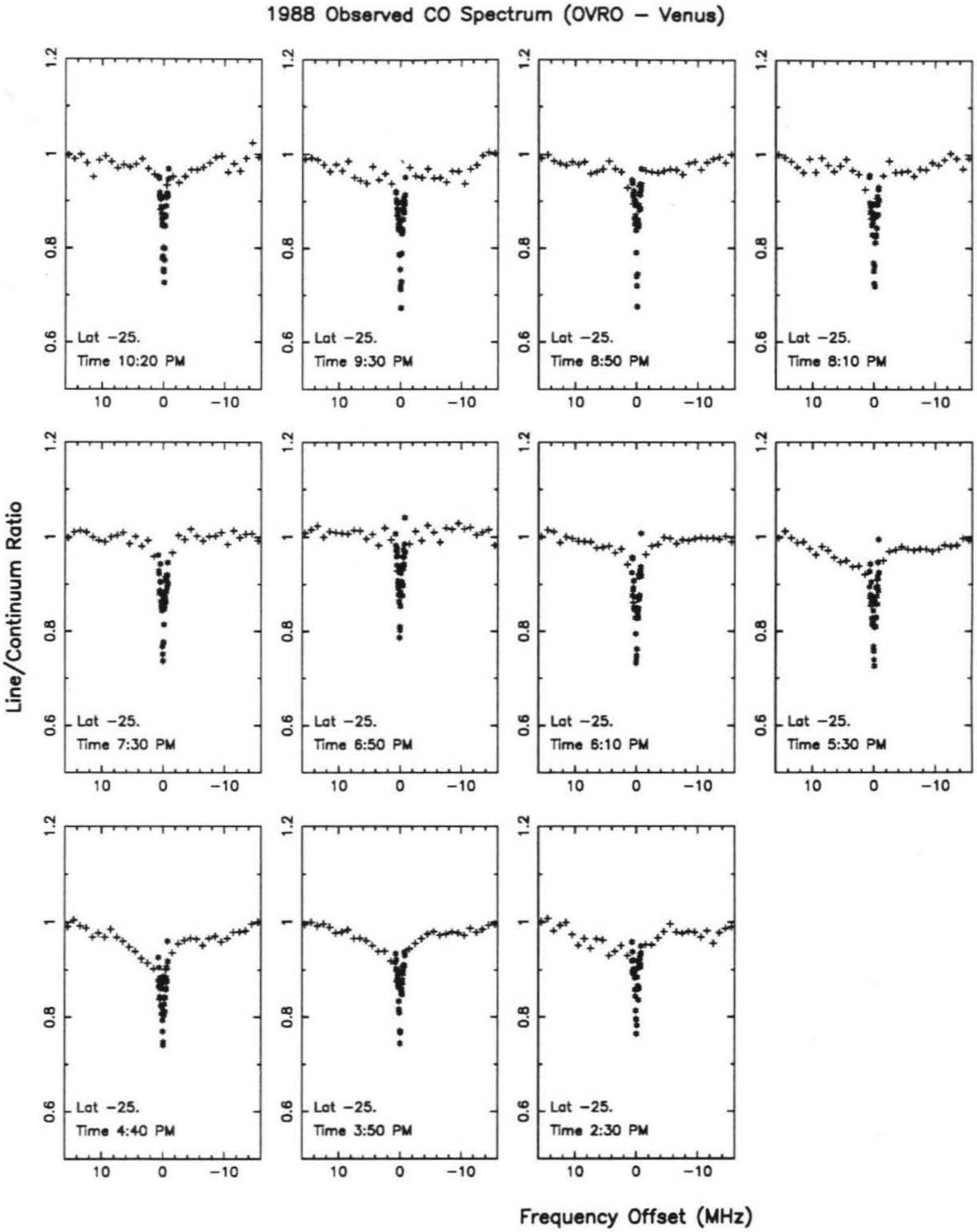
1988 Observed CO Spectrum (OVRO – Venus)
Line/Continuum Ratio
Frequency Offset (MHz)
1.2
1
0.8
0.6
10
0
−10
Lat −25.
Time 10:20 PM
Time 9:30 PM
Time 8:50 PM
Time 8:10 PM
Time 7:30 PM
Time 6:50 PM
Time 6:10 PM
Time 5:30 PM
Time 4:40 PM
Time 3:50 PM
Time 2:30 PM

Figure D1d.

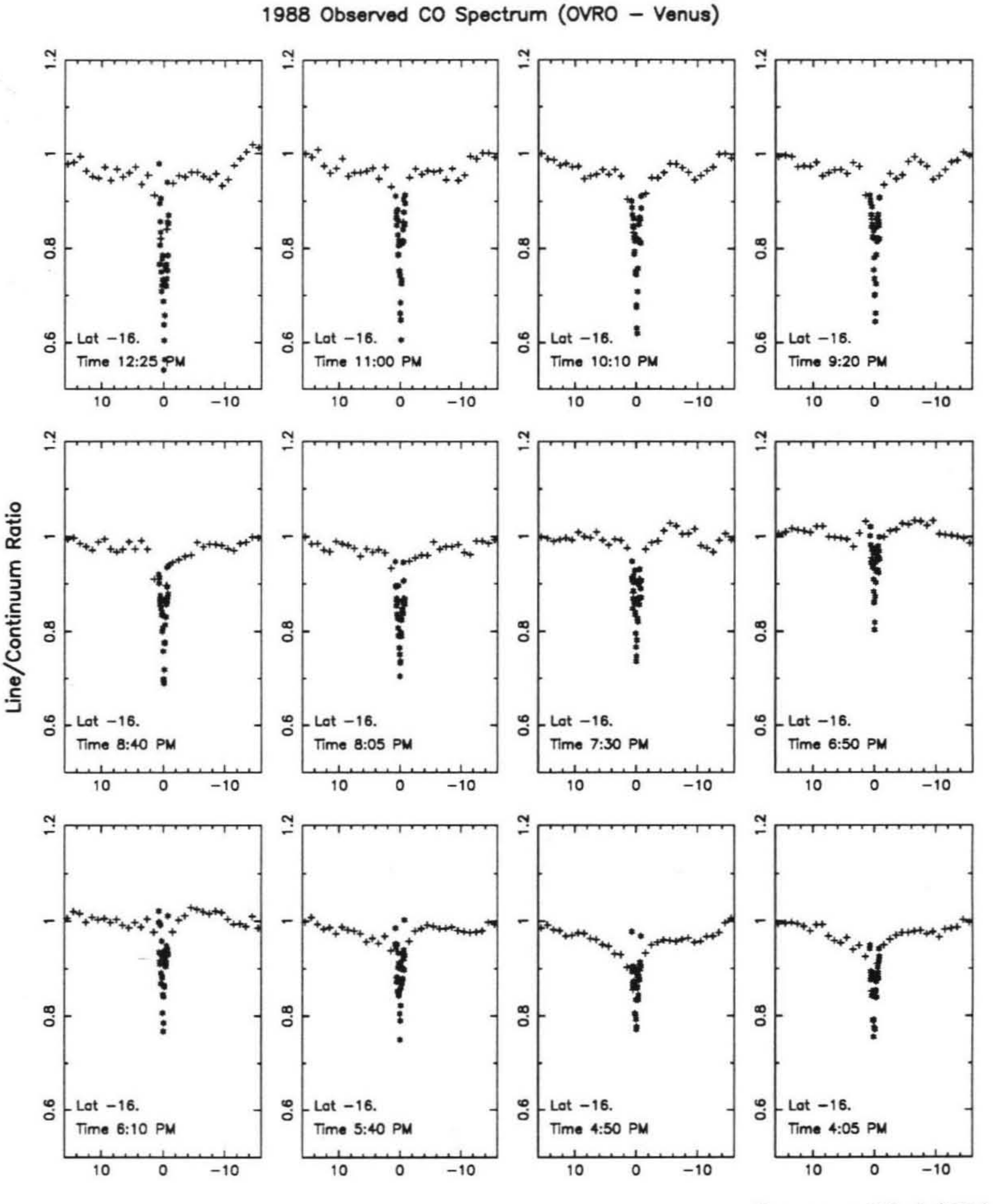
1988 Observed CO Spectrum (OVRO – Venus)
Line/Continuum Ratio
Frequency Offset (MHz)
1.2
1
0.8
0.6
10
0
−10
Lat −16.
Time 12:25 PM
Time 11:00 PM
Time 10:10 PM
Time 9:20 PM
Time 8:40 PM
Time 8:05 PM
Time 7:30 PM
Time 6:50 PM
Time 6:10 PM
Time 5:40 PM
Time 4:50 PM
Time 4:05 PM

Figure D1e.

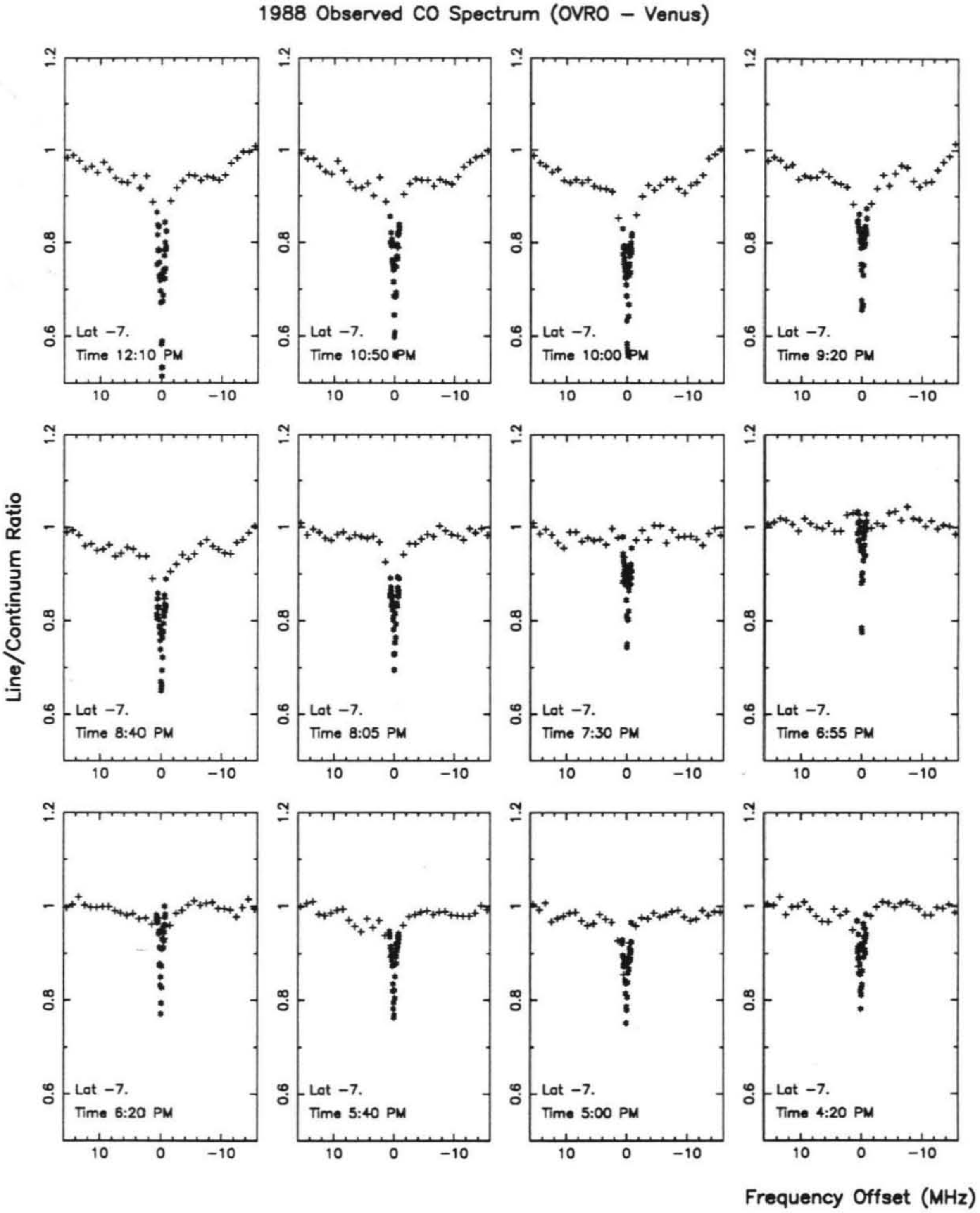
1988 Observed CO Spectrum (OVRO – Venus)
Line/Continuum Ratio
Frequency Offset (MHz)
1.2
1
0.8
0.6
10
0
−10
Lat −7.
Time 12:10 PM
Time 10:50 PM
Time 10:00 PM
Time 9:20 PM
Time 8:40 PM
Time 8:05 PM
Time 7:30 PM
Time 6:55 PM
Time 6:20 PM
Time 5:40 PM
Time 5:00 PM
Time 4:20 PM

Figure D1f.

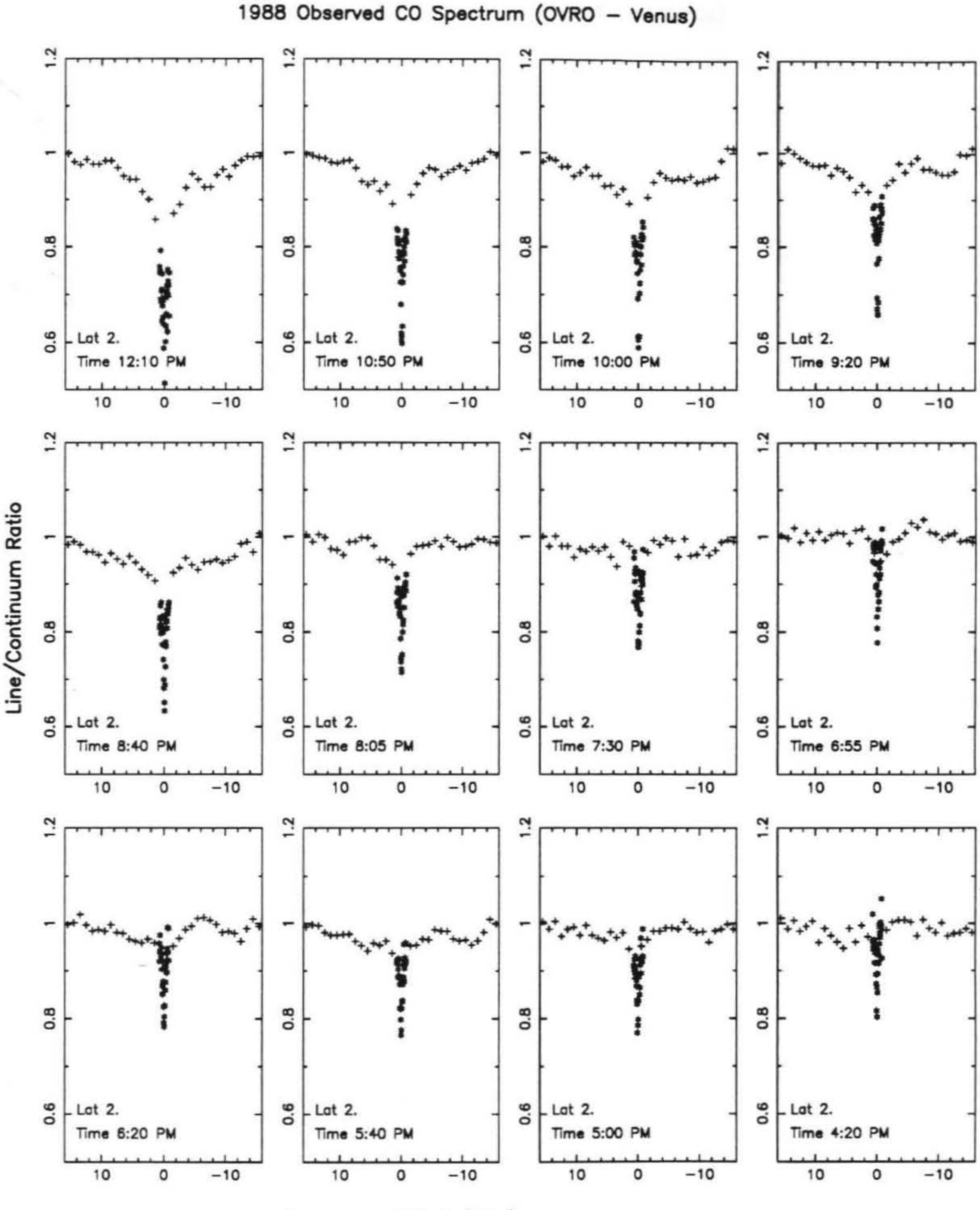
1988 Observed CO Spectrum (OVRO – Venus)
Line/Continuum Ratio
Frequency Offset (MHz)
1.2
1
0.8
0.6
10
0
−10
Lat 2.
Time 12:10 PM
Lat 2.
Time 10:50 PM
Lat 2.
Time 10:00 PM
Lat 2.
Time 9:20 PM
Lat 2.
Time 8:40 PM
Lat 2.
Time 8:05 PM
Lat 2.
Time 7:30 PM
Lat 2.
Time 6:55 PM
Lat 2.
Time 6:20 PM
Lat 2.
Time 5:40 PM
Lat 2.
Time 5:00 PM
Lat 2.
Time 4:20 PM

Figure D1g.

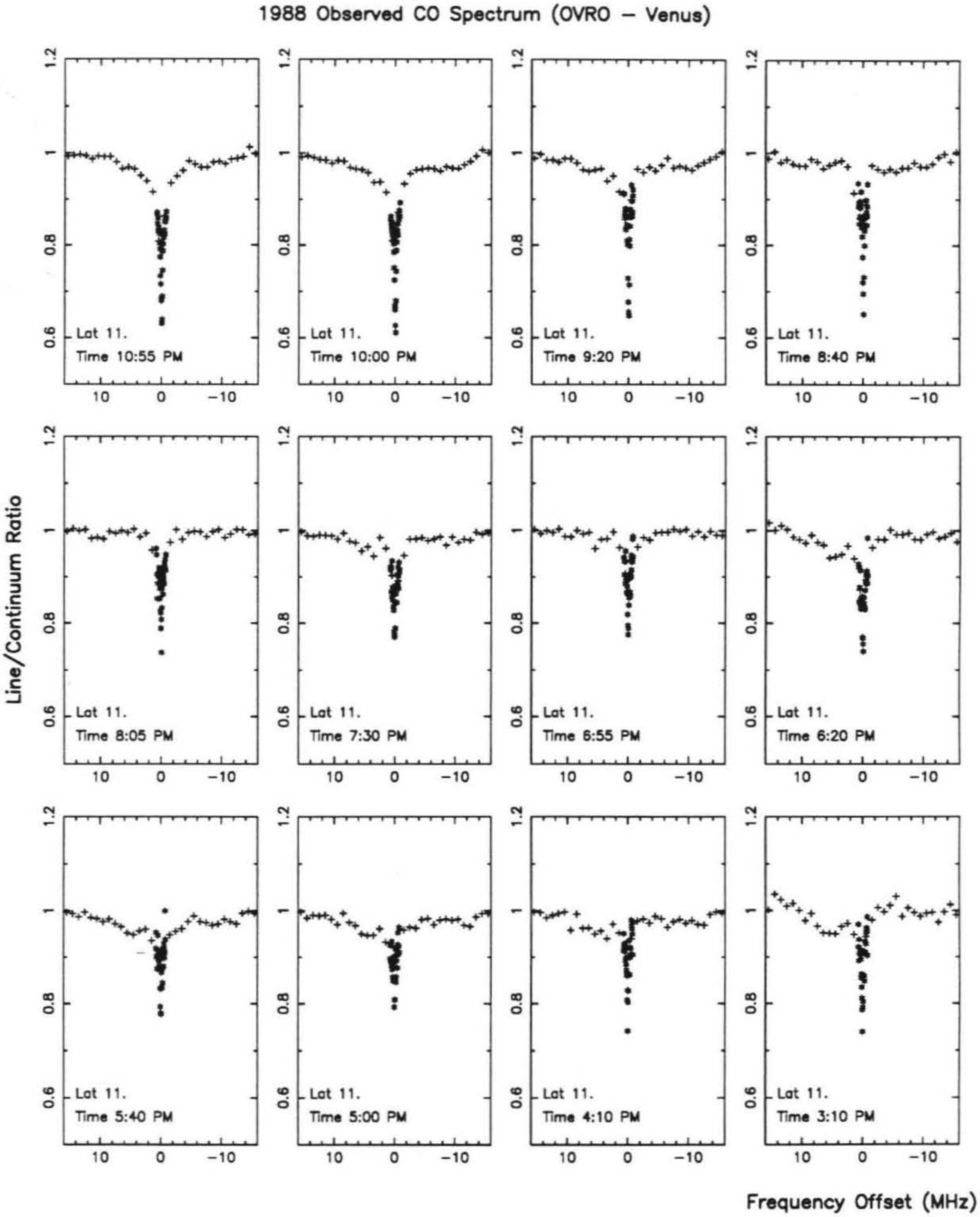
1988 Observed CO Spectrum (OVRO – Venus)
Line/Continuum Ratio
1.2
1
0.8
0.6
Lat 11.
Time 10:55 PM
Lat 11.
Time 10:00 PM
Lat 11.
Time 9:20 PM
Lat 11.
Time 8:40 PM
Lat 11.
Time 8:05 PM
Lat 11.
Time 7:30 PM
Lat 11.
Time 6:55 PM
Lat 11.
Time 6:20 PM
Lat 11.
Time 5:40 PM
Lat 11.
Time 5:00 PM
Lat 11.
Time 4:10 PM
Lat 11.
Time 3:10 PM
10
0
−10
Frequency Offset (MHz)

Figure D1h.

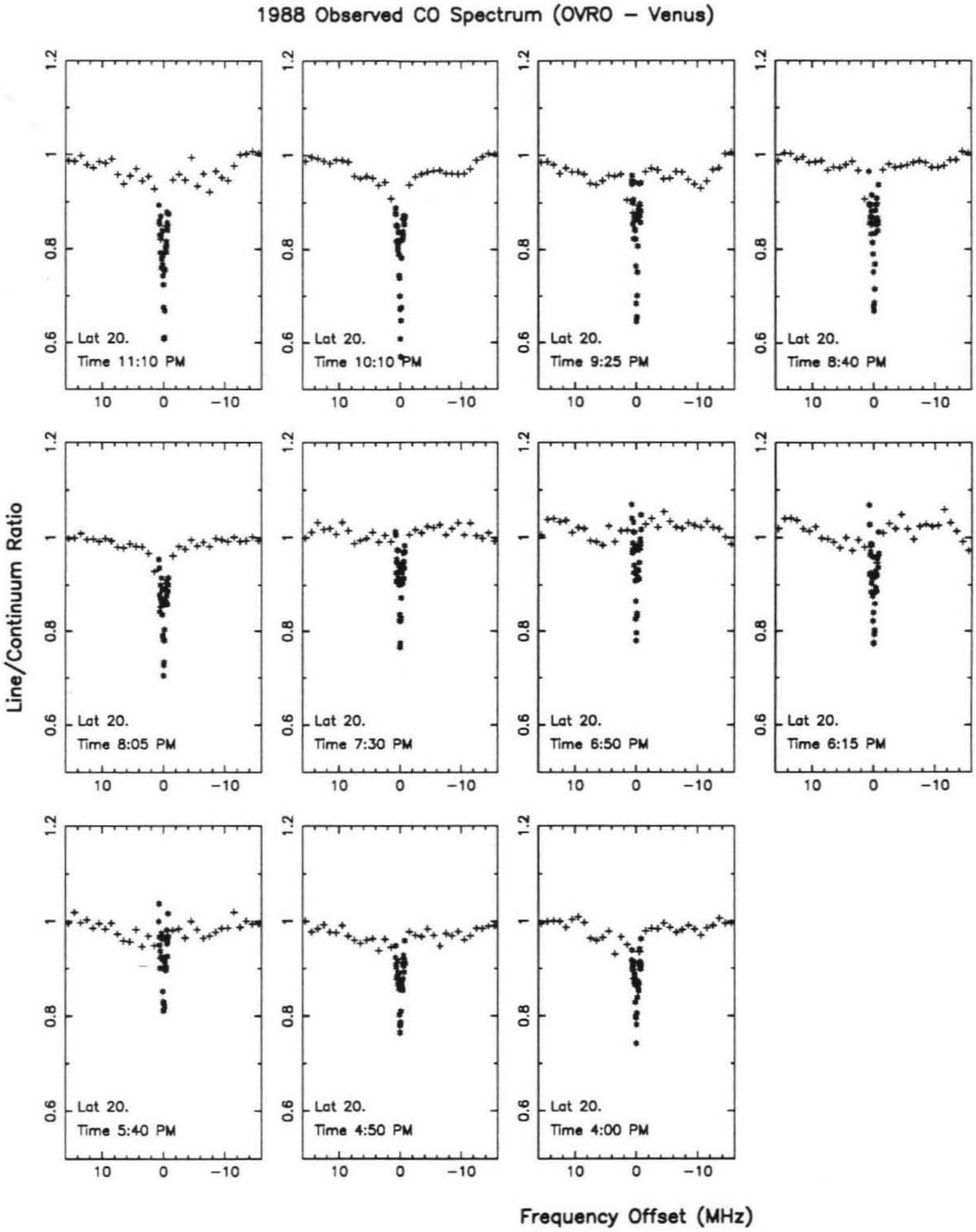
1988 Observed CO Spectrum (OVRO – Venus)
Line/Continuum Ratio
Frequency Offset (MHz)
1.2
1
0.8
0.6
10
0
−10
Lat 20.
Time 11:10 PM
Lat 20.
Time 10:10 PM
Lat 20.
Time 9:25 PM
Lat 20.
Time 8:40 PM
Lat 20.
Time 8:05 PM
Lat 20.
Time 7:30 PM
Lat 20.
Time 6:50 PM
Lat 20.
Time 6:15 PM
Lat 20.
Time 5:40 PM
Lat 20.
Time 4:50 PM
Lat 20.
Time 4:00 PM

Figure D1i.

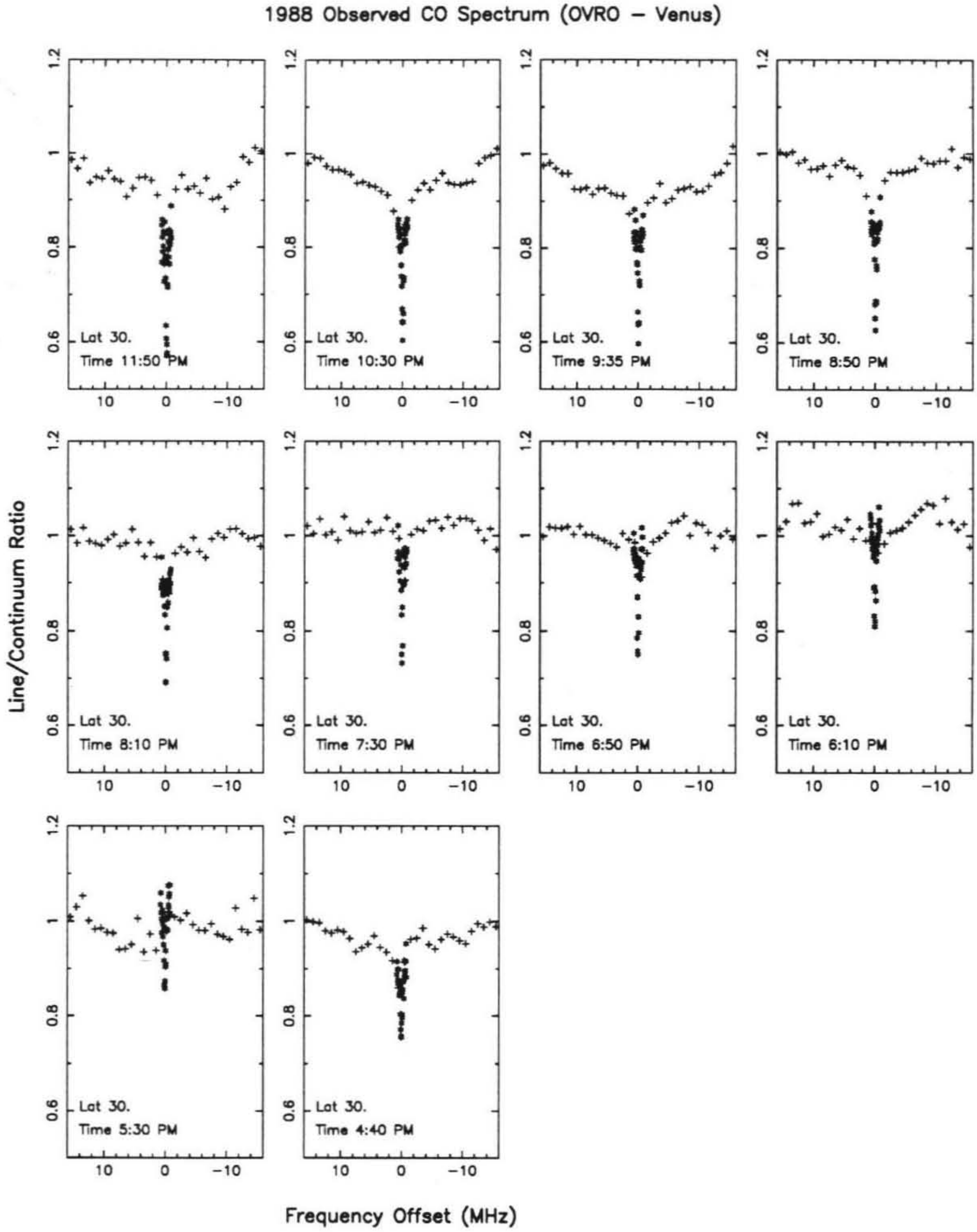
1988 Observed CO Spectrum (OVRO – Venus)
Line/Continuum Ratio
Frequency Offset (MHz)
1.2
1
0.8
0.6
10
0
−10
Lat 30.
Time 11:50 PM
Time 10:30 PM
Time 9:35 PM
Time 8:50 PM
Time 8:10 PM
Time 7:30 PM
Time 6:50 PM
Time 6:10 PM
Time 5:30 PM
Time 4:40 PM

Figure D1j.

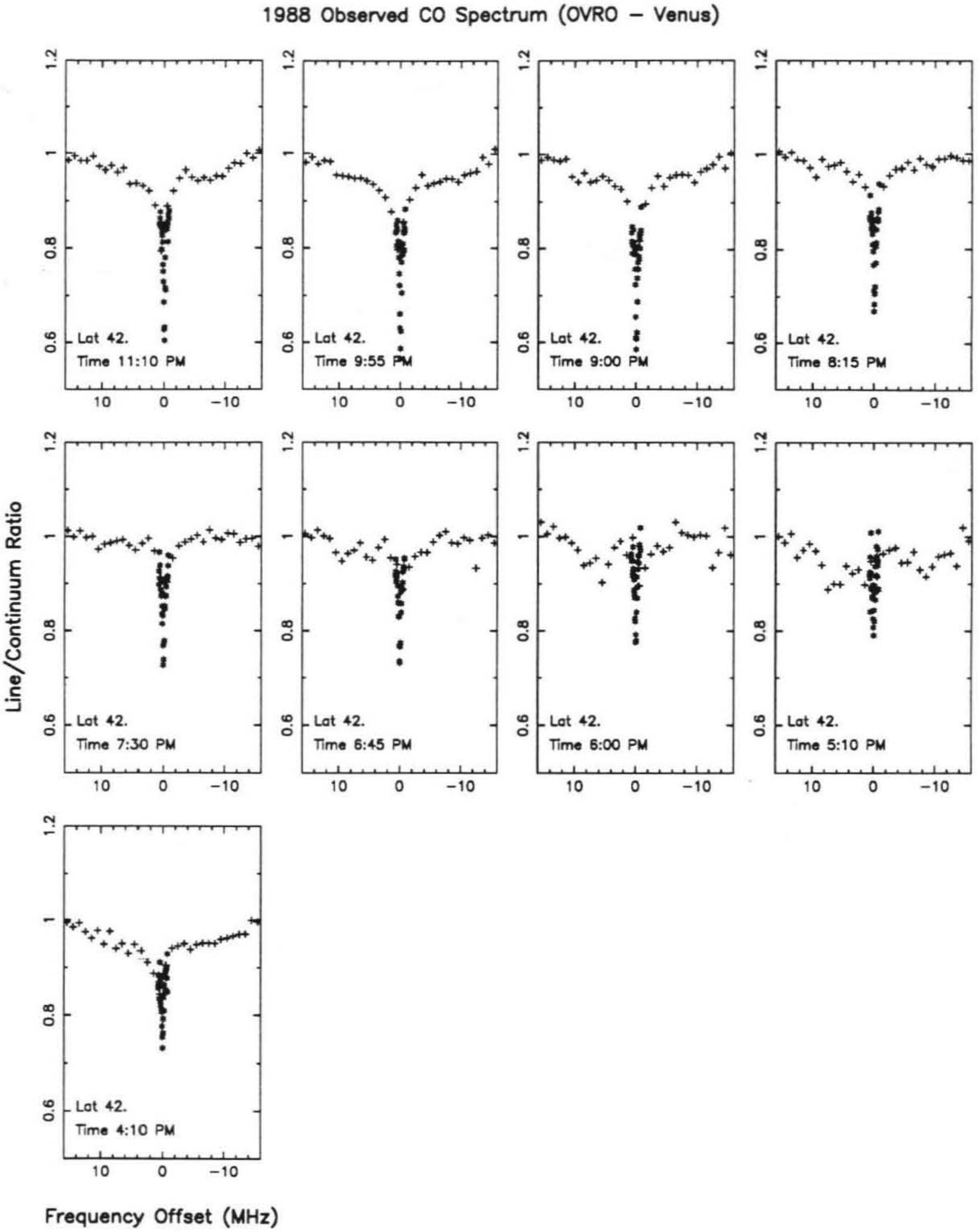
1988 Observed CO Spectrum (OVRO – Venus)
Line/Continuum Ratio
0.6
0.8
1
1.2
10
0
−10
Lat 42.
Time 11:10 PM
Lat 42.
Time 9:55 PM
Lat 42.
Time 9:00 PM
Lat 42.
Time 8:15 PM
Lat 42.
Time 7:30 PM
Lat 42.
Time 6:45 PM
Lat 42.
Time 6:00 PM
Lat 42.
Time 5:10 PM
Lat 42.
Time 4:10 PM
Frequency Offset (MHz)

Figure D1k.

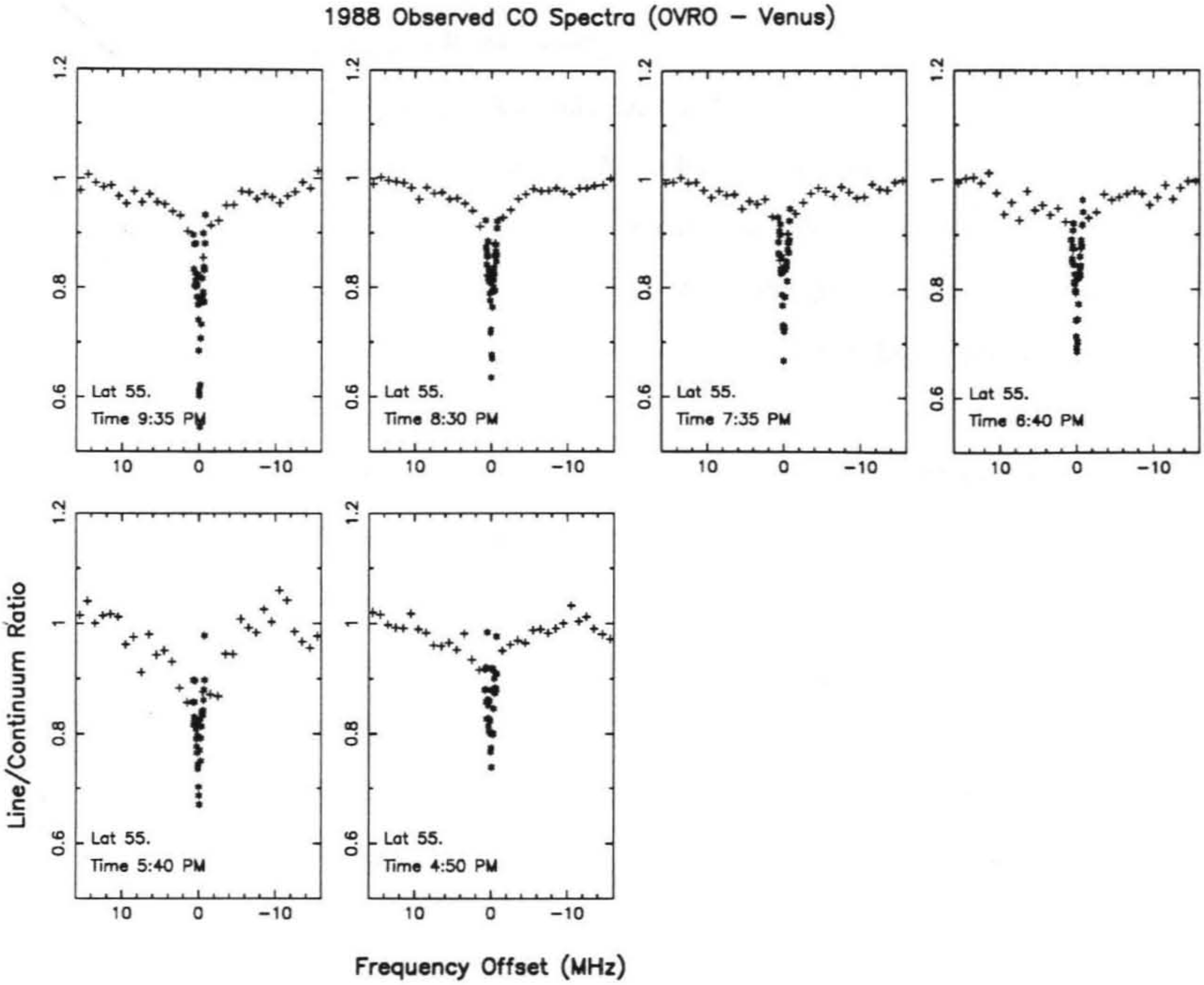
1988 Observed CO Spectra (OVRO – Venus)
Line/Continuum Ratio
Frequency Offset (MHz)
1.2
1
0.8
0.6
10
0
−10
Lat 55.
Time 9:35 PM
Lat 55.
Time 8:30 PM
Lat 55.
Time 7:35 PM
Lat 55.
Time 6:40 PM
Lat 55.
Time 5:40 PM
Lat 55.
Time 4:50 PM

Figure D1l.

References

Allen, D. A. and J. W. Crawford 1984. Cloud structure on the dark side of Venus. *Nature* **307**, 222-224.

Apt, J., R. A. Brown, and R. M. Goody 1980. The character of the thermal emission of Venus. *J. Geophys. Res.* **85**, 7934-7940.

Avduevskiy, V. S., M. Ya. Marov, Yu. N. Kulikov, V. P. Shari, A. Ya. Gorbachevskiy, G. R. Uspenskiy, and Z. P. Cheremukhina 1983. Structure and parameters of the Venus atmosphere according to Venera probe data. In *Venus* (D. M. Hunten, L. Colin, T. M. Donahue, and V. I. Moroz, Eds.), pp. 280-298. Univ. of Arizona Press, Tucson.

Ayers, G. P., R. W. Gillett, and J. L. Gros 1980. On the vapor pressure of sulfuric acid. *Geophys. Res. Lett.* **7**, 433-436.

Baker, N. L., and C. B. Leovy 1987. Zonal winds near Venus' cloud top level: A model study of the interaction between the zonal mean circulation and the semidiurnal tide. *Icarus* **69**, 202-220.

Berge, G. L., D. O. Muhleman and R. P. Linfield 1988. Very Large Array observations of Uranus at 2.0 cm. *Astron. J.* **96**, 388-395.

Betz, A. L., M. A. Johnson, R. A. McLaren and E. C. Sutton 1977. Heterodyne detection of CO_2 emission lines and wind velocities in the atmosphere of Venus. *Astrophys J.* **208**, L141-L144.

Born, M. and E. Wolf 1980. *Principles of Optics*, sixth edition. Pergamon Press, Oxford.

Bougher, S. W., R. E. Dickinson, E. C. Ridley and R. G. Roble 1988. Venus mesosphere and thermosphere: III. Three-dimensional general circulation with coupled dynamics and composition. *Icarus* **73**, 545-573.

Boyer, C. 1973. The 4-day rotation of the upper atmosphere of Venus. *Planet. Space*

Sci. **21**, 1559-1561.

Boyer, C. and P. Guerin 1969. Etude de la rotation retrograde, en 4 jours, de la couche exterieure naugeuse de Venus. *Icarus* **11**, 338-355.

Brinton, H. C., H. A. Taylor, H. B. Niemann, and H. G. Mayr 1979. Venus nighttime hydrogen bulge. *Bull. Amer. Astron. Soc.* **11**, 538.

Chahine, M. T. 1970. Inverse problems in radiative transfer: Determination of atmospheric parameters. *J. Atmos. Sci.* **27**, 960-967.

Chandrasekhar, S. 1960. *Radiative Transfer.* Dover, New York.

Imino, J. 1982. The composition and vertical structure of the lower cloud deck on Venus. *Icarus* **51**, 334-357.

Clancy, R. T. and D. O. Muhleman 1985a. Chemical-dynamical models of the Venus mesosphere based upon diurnal microwave CO variations. *Icarus* **64**, 183-204.

Clancy, R. T. and D. O. Muhleman 1985b. Diurnal CO variations in the Venus mesosphere from CO microwave spectra. *Icarus* **63**, 157-182.

Clancy, R. T. and D. O. Muhleman 1991. Long term (1979-1980) changes in the thermal, dynamical, and compositional structure of the Venus mesosphere as inferred from microwave spectral line observations of ^{12}CO, ^{13}CO and C^{18}O. *Icarus* **89**, 129-146.

Clancy, R. T., D. O. Muhleman, and G. L. Berge 1990. Global changes in the 0 – 70 km thermal structure of the Mars atmosphere derived from 1975–1989 microwave CO spectra. *J. Geophys. Res.* **95**, 14543-14554.

Clancy, R. T., D. O. Muhleman, and B. M. Jakosky 1983. Variability of carbon monoxide in the Mars atmosphere. *Icarus* **55**, 282-301.

Colin, L. 1983. Basic facts about Venus. In *Venus* (D. M. Hunten, L. Colin, T. M. Donahue, and V. I. Moroz, Eds.), pp. 10-26. Univ. of Arizona Press, Tucson.

Connes, P., J. Connes, L. D. Kaplan and W.s. Benedict 1968. Carbon monoxide in the Venus atmosphere. *Astrophys. J.* **152**. 731-743.

Counselman, C. C. III., S. A. Gourevitch, R. W. King and G. B. Loriot 1980. Zonal and meridional circulation of the lower atmosphere of Venus determined by radio interferometry. *J. Geophys. Res.* **85**, 8026- 8030.

Covey, C. and G. Schubert 1982. Planetary-scale waves in the Venus atmosphere. *J. Atmos. Sci.* **39**, 2397-2413.

Covey, C., E.J. Pitcher, and J. P. Brown 1986. General circulation model simulations of superrotation in slowly rotating atmospheres: Implications for Venus. *Icarus* **66**, 380-396.

Crisp, D. 1986. Radiative forcing of the Venus mesosphere. *Icarus* **67**, 484-514.

Crisp, D., W. M. Sinton, K.-W. Hodapp, B. Ragent, F. Gerbault, J. H. Goebel, R. G. Probst, D. A. Allen, K. Pierce, and K. R. Stapelfeldt 1989. The nature of the near-infrared features on the Venus night side. *Nature* **246**, 506-509.

Cruikshank, D. P. 1983. The development of studies of Venus. In *Venus* (D. M. Hunten, L. Colin, T. M. Donahue, and V. I. Moroz, Eds.), pp. 1-9. Univ. of Arizona Press, Tucson.

Cuzzi, J. N 1972. *The Subsurface Nature of Mercury and Mars From Thermal Microwave Emission*, Ph.D. thesis, California Institute of Technology.

De Pater, I., F. P. Schloerb and A. Rudolph 1991. Venus imaged with the Hat Creek interferometer in the J=1-0 CO line. *Icarus* **90**, 282-298.

De Pater, I., F. P. Schloerb and A. Rudolph 1987. High resolution observations of the J = 1-0 line on Venus, *Bull. Amer. Astron. Soc.*, **19**, 846.

Del Genio, A. D. and W. B. Rossow 1989. Planetary scale waves and the cyclic nature of cloud top dynamics on Venus. *J. Atmos. Sci.* **47**, 293-318.

Del Genio, A. D. and W. B. Rossow 1982. Temporal variability of ultraviolet cloud features in the Venus stratosphere. *Icarus* **51**, 319-415.

Del Genio, A. D. and R. J. Suozzo 1987. A comparative study of rapidly and slowly rotating dynamical regimes in a terrestrial general circulation model. *J. Atmos. Sci.* **44**, 973-986.

Dickinson, R. E. and E. C. Ridley 1975. A numerical model for the dynamics and composition of the Venusian thermosphere. *J. Atmos. Sci.* **32**, 1219-1231.

Dickinson, R. E. and E. C. Ridley 1977. Venus mesosphere and thermosphere temperature structure II. Day-night variations. *Icarus* **30**, 163-178.

Diner, D. J., J. Apt, and L. S. Elson 1982. Comparison of ground-based and spacecraft observations of the infrared emission from Venus: The nature of thermal contrasts. *Icarus* **52**, 301-319.

Dollphus, A. 1968. Synthesis on the ultraviolet survey of clouds in Venus' atmosphere. In *The Atmospheres of Venus and Mars* (J . C. Brandt and M. E. McElroy, Eds.), pp 133-146. Gordon and Breach, New York.

Elson, L. 1979. Preliminary results from the Pioneer Venus Orbiter Infrared Radiometer: Temperature and dynamics in the upper atmosphere. *Geophys. Res. Lett.* **6**, 720-722.

Esposito, L. W., M. Copley, R. Eckert, L. Gates, A. I. F. Stewart, and H. Worden 1988. Sulfur dioxide at the Venus cloud tops, 1978–1986. *J. Geophys. Res.* **93**, 5267-5276.

Esposito, L. W., R. G. Knollenberg, M. Ya. Marov, O. B. Toon, and R. P. Turco 1983. The clouds and hazes of Venus. In *Venus* (D. M. Hunten, L. Colin, T. M. Donahue, and V. I. Moroz, Eds.), pp. 484-564. Univ. of Arizona Press, Tucson.

Fels, S. B. and R. S. Lindzen 1974. The interaction of thermally excited gravity waves with mean flows. *Geophys. Fluid Dyn.* **6**, 149-191.

Fels, S. B., J. T. Schofield and D. Crisp 1984. Observations and theory of the solar semidiurnal tide in the mesosphere of Venus. *Nature* **312**, 431-434.

Gierasch, P. J. 1975. Meridional circulation and the maintenance of the Venus atmospheric rotation. *J. Atmos. Sci.* **32**, 1038-1044.

Gierasch, P. J. 1987. Waves in the atmosphere of Venus. *Nature* **328**, 510-512.

Gmitro, J. I. and T. Vermeulen 1964. Vapor-liquid equilibrium for aqueous sulfuric acid. *Amer. Inst. Chem. Eng. J.* **10**, 740-746.

Goldstein, J. J., M. J. Mumma, T. Kostiuk, D. Deming, F. Espenak and D. Zipoy 1988. Direct measurements of lower thermospheric circulation on Venus using doppler-limited infrared spectroscopy. *Bull. Amer. Astron. Soc.* **20**, 833-834.

Goldstein, J. J. 1989. *Absolute Wind Measurements in the Lower Thermosphere of Venus Using Infrared Heterodyne Spectroscopy*, Ph.D. thesis, University of Pennsylvania.

Goldstein, J. J. 1990. Absolute winds measurements in the lower thermosphere of Venus using infrared heterodyne spectroscopy. *Pub. Astro. Soc. Pac.* **102**, 493.

Gulkis, S., R. K. Kakar, M. J. Klein, E. T. Olsen, and W. J. Wilson 1977. Venus: Detection of variations in stratospheric carbon monoxide. In *Proc. of the Symp. on Planetary Atmospheres* (A. V. Jones, Ed.), pp. 61-65. Roy. Soc. Canada, Ottawa.

Hamilton, W. C. 1964. *Statistics in Physical Science*, Ronald Press, New York.

Hansen, J. E. and J. W. Hovenier 1974. Interpretation of the polarization of Venus. *J. Atmos. Sci.* **31**, 1137-1160.

Ho, W. I. A. Kaufman, and P. Thaddeus 1966. Laboratory measurement of microwave absorption in models of the atmosphere of Venus. *J. Geophys. Res.* **71**, 5091-5108.

Hobbs, R. W. and S. L. Knapp 1971. Planetary temperatures at 9.55 mm wavelength.

Icarus **14**, 204-209.

Holton, J. R. 1979. *An Introduction to Dynamic Meteorology*, 2nd ed., 391 pp. Academic, New York.

Hou, A. Y. and B. F. Farrell 1987. Superrotation induced by critical-level absorption of gravity waves on Venus: An assessment. *J. Atmos. Sci.* **44**, 413-432.

Janssen, M. A. and M. J. Klein 1981. Constraints on the composition of the Venus atmosphere from microwave measurements near 1.35 cm wavelengths. *Icarus* **46**, 58-98.

Janssen, M. A. and R. L. Poynter 1981. The microwave absorption of SO_2 in the Venus atmosphere. *Icarus* **46**, 51- 57.

Jennison, R. C. 1953. *The measurement of the fine structure of the cosmic radio sources*, Ph. D. thesis, University of Manchester.

Jennison, R. C. 1958. A phase sensitive interferometer technique for the measurement of the fourier transforms of spatial brightness distributions of small angular extent. *Mon. Not. Roy. Astron. Soc.* **118**, 276-284.

Kakar, R. K., J. W. Waters, and W. J. Wilson 1976. Venus: Microwave detection of carbon monoxide. *Science* **191**, 379-380.

Kawabata, K. D., D. L. Coffeen, J. E. Hansen, W. A. Lane, M. Sato, and L. D. Travis 1980. Cloud and haze properties from Pioneer Venus polarimetry. *J. Geophys. Res.* **85**, 8129-8140.

Keating, G. M., J. Y. Nicholson and L. R. Lake 1980. Venus upper atmosphere structure. *J. Geophys. Res.* **85**, 7941-7956.

Kliore, A. J. and L. Mullen 1988. Solar cycle variability of upper atmosphere temperatures on Venus. *EOS Transactions* **69**, 1287.

Knollenberg, R. G. and D. M. Hunten 1980. Microphysics of the clouds of Venus: Results of the Pioneer venus particle size spectrometer experiment. *J. Geophys.*

Res. **85**, 8039-8058.

Knollenberg, R. G., L. Travis, M. Tomasko, P. Smith, B. Ragent, L. Esposito, D. McCleese, J. Martonchik, and R. Beer 1980. The clouds of Venus: A synthesis report. *J. Geophys. Res.* **85**, 8059-8081.

Kolbe, W. F., H. Buscher, and B. Leskovar 1977. Microwave absorption coefficients of atmospheric pollutants and constituents. *J. Quant. Spectrosc. Radiat. Transfer* **18**, 47-64.

Krasnopolsky, V. A. and V. A. Parshev 1981. Chemical composition of the atmosphere of Venus. *Nature* **292**, 610.

Kuczkowski, R. L., R. D. Suenram and F. J. Lovas 1981. The microwave spectrum, structure, and dipole moment of sulfuric acid. *J. Amer. Chem. Soc.* **103**, 2561-2566.

Kuz'min, A. D. and A. E. Salomonivich 1962. Observations of the radio emission of Venus and Jupiter at wavelength 8 cm 1962. *Astron. J.* **39**, 660-668.

Leovy, C. B. 1973. Rotation of the upper atmosphere of Venus. *J. Atmos. Sci.* **30**, 1218-1220.

Limaye, S. S. 1977. *Venus Stratospheric Circulation: A Diagnostic Study*, Ph.D. thesis, the University of Wisconsin.

Limaye, S. S. and V. E. Suomi 1981. Cloud motion on Venus: Global structure and organization. *J. Atmos. Sci.* **38**, 1220-1235.

Limaye, S. S., C. J. Grund and S. P. Burre 1982. Zonal mean circulation at the cloud level on Venus: Spring and fall 1979 OCPP observations. *Icarus* **51**, 416-439.

Limaye, S. S., C. Grassotti and M. J. Kuetemeyer 1988. Venus: Cloud level circulation during 1982 as determined from Pioneer cloud photopolarimeter images. *Icarus* **73**, 193-211.

Lowenstein, R. F., D. A. Harper, S.H. Moseley, C. M. Telesco , H.A. Thronson, R.H.

Hildebrand, S. E. Whitcomb, R. Winston and R. F. Steining 1977. Far-infrared and submillimeter observations of the planets. *Icarus* **31**, 315-324.

Maryott, A. A. and G. Birnbaum 1962. Collision-induced microwave absorption in compressed gases, 1, Dependence on density, temperature, and frequency in CO_2. *J. Chem. Phys.* **36**, 2026-2032.

Mayr, H. G., I. Harris, H. B. Niemann, H. C. Brinton, N. W. Spencer, H. A. Taylor, Jr., R. E. Hartle, W. G. Hoegy and D. M. Hunten 1980. Dynamic properties of the thermosphere inferred from Pioneer Venus mass spectrometer measurements. *J. Geophys. Res.* **85**, 7841-7847.

Mayr, H. G., I. Harris, D. R. Stevens-Rayburn, H. B. Niemann, H. A. Taylor, Jr., and R. E. Hartle 1985. On the diurnal variations in the temperature and composition: A three- dimensional model with superrotation. *Adv. Space. Res.* **5**, 109- 112.

McElroy, M. B. and T. M. Donahue 1972. Stability of the Martian atmosphere. *J. Geophys. Res.* **74**, 1720-1739.

Moroz, V. I., B. E. Moshkin, A. P. Ekonomov, N. F. San'ko, N. A. Parfent'ev, and Y. M. Golovin 1979. Spectrometric experiment on board the Venera 11, 12 descenders: Some results of the analysis of the Venus dayside spectrum. *Space Res. Inst. Publ. Engl. Trans.* **117**, USSR Acad. of Sci., Moscow.

Muhleman, D. O. and G. L. Berge 1991. Observations of Mars, Uranus, Neptune, Io, Europa, Ganymede and Callisto at a wavelength of 2.66 millimeters. *Icarus* **92**, 263-272.

Muhleman, D. O., A. Grossman, E. Smith and G. Berge 1987. Synthetic aperture CO map of Venus. 22nd General Assembly of URSI, Tel Aviv, Israel.

Muhleman, D. O., G. S. Orton and G. L. Berge 1979. A model of the Venus atmosphere from radio, radar and occultation observations. *Astrophys. J.* **234**, 733-745.

Newman, M., G. Schubert, A. J. Kliore and I. R. Patel 1984. Zonal winds in the middle atmosphere of Venus from Pioneer Venus radio occultation data. *J. Atmos. Sci.* **41**, 1901-1913.

Niemann, H. B., W. T. Kaprzak, A. E. Hedin, D. M. Hunten and N. W. Spencer 1980. Mass spectrometric measurements of the neutral gas composition of the thermosphere and exosphere of Venus. *J. Geophys. Res.* **85**, 7817-7827.

Orton, G. S., M. J. Griffin, P. A. R. Ade, I.G. Nolt and J. V. Radostitz 1986. Submillimeter and millimeter observations of Uranus and Neptune. *Icarus* **67**, 289-304.

Oyama, V. I., G. C. Carle, F. Woeller, J. B. Pollack, R. T. Reynolds, and R. A. Craig 1980. Pioneer Venus gas chromatography of the lower atmosphere of Venus. *J. Geophys. Res.* **85**, 7891.

Padin, S., D. P. Woody and S. L. Scott 1988. A local oscillator system for millimeter wave interferometry. *Radio Science* **23**, 1067-1074.

Pechmann, J. B. and A. P. Ingersoll 1984. Thermal tides in the atmosphere of Venus: Comparison of model results with observations. *J. Atmos. Sci.* **41**, 3290-3313.

Perley, R. A., F. R. Schwab and A. H. Bridle, Eds 1989. *Synthesis Imaging in Radio Astronomy.* Astronomical Society of the Pacific Conference Series **6**, San Francisco.

Pollack, J. B. 1991. Kuiper prize lecture: Present and past climates of the terrestrial planets. *Icarus* **91**, 173-198.

Poynter, Robert L. 1989. Private communication.

Poynter, Robert L. 1990. Private communication.

Prinn, R. G. 1971. Photochemistry of HCl and other minor constituents in the atmosphere of Venus. *J. Atmos. Sci.* **28**, 1058-1068.

Rather, J.D.G., B. L. Ulich and P. A. R. Ade 1974. Planetary brightness temperature measurements at 1.4 mm wavelength. *Icarus* **22**, 448-453.

Rossow, W. B. 1983. A general circulation model of a Venus-like atmosphere. *J. Atmos. Sci.* **40**, 273-302.

Rossow, W. B. 1985. Atmospheric circulation of Venus. *Adv. Geophys.* **28A**, 347-379.

Rossow, W. B., A. D. Del Genio, S. S. Limaye, L. D. Travis, and P. Stone 1980. Cloud morphology and motions from Pioneer Venus images. *J. Geophys. Res.* **85**, 8107-8128.

Rossow, W. B., A. D. Del Genio and T. Eichler 1990. Cloud- tracked winds from Pioneer Venus OCPP images. *J. Atmos. Sci.* **47**, 2053-2084.

Rowan-Robinson, M., P. A. R. Ade, E. I. Robson, and P.E. Clegg 1978. Millimeter observations of planets, galactic and extragalactic sources. *Astron. Astrophys.* **62**, 249-254.

Rossow, W. B. and G. P. Williams 1979. Large-scale motion in the Venus stratosphere. *J. Atmos. Sci.* **36**, 377-389.

Rudy, D. J., D. O. Muhleman, G. L. Berge, B. M. Jakosky and P. R. Christensen 1987. Mars: VLA observations of the northern hemisphere and the north polar region at wavelengths of 2 and 6 cm. *Icarus* **71**, 159-177.

Rudy, D. J. 1987. *Mars: High resolution VLA observations at wavelengths of 2 and 6 cm and derived properties*, Ph.D. thesis, California Institute of Technology.

Schloerb, F. P., D. O. Muhleman and G. L. Berge 1979. An aperture synthesis study of Saturn and its rings at 3.71-cm wavelength. *Icarus* **39**, 232-250.

Schloerb, F. P., S. E. Robinson and W. M. Irvine 1980. Observations of the CO in the stratosphere of Venus via its J = 0 - 1 rotational transition. *Icarus* **42**, 121-128.

Schubert, G. 1983. General circulation and the dynamical state of the Venus atmosphere. In *Venus* (D. M. Hunten, L. Colin, T. M. Donahue, and V. I. Moroz, Eds.), pp. 681-765. Univ. of Arizona Press, Tucson.

Schubert, G., C. Covey, A. Del Genio, L. S. Elson, G. Keating, A. Seiff, R. E. Young, J. Apt, C. C. Counselman III, A. J. Kliore, S. S. Limaye, H. E. Revercomb, L. A. Sromovsky, V. E. Suomi, F. Taylor, R. Woo and U Von Zahn 1980. Structure and circulation of the Venus atmosphere. *J. Geophys Res.* **85**, 8007-8025.

Schubert, G. and J. Whitehead 1969. Moving flame experiment with liquid mercury: Possible implications for the Venus atmosphere. *Science* **163** 71-72.

Scott, A. H. and E. J. Reese 1972. Venus: Atmospheric rotation. *Icarus* **17**, 589-601.

Seiff, A. 1983. Thermal structure of the atmosphere of Venus. In *Venus* (D. M. Hunten, L. Colin, T. M. Donahue, and V. I. Moroz, Eds.), pp. 215-279. Univ. of Arizona Press, Tucson.

Seiff, A. and D. B. Kirk 1982. Structure of the Venus mesosphere and lower thermosphere from measurements during entry of the Pioneer Venus probes. *Icarus* **49**, 49-70.

Seiff, A. and D. B. Kirk 1991. Waves in Venus' middle and upper atmosphere: Implications of Pioneer Venus probe data above the clouds. *J. Geophys. Res.* **96**, 11021-11032.

Seiff A., D. B. Kirk, R. E. Young, R. C. Blanchard, J. T. Findlay, G. M. Kelley and S. C. Sommer 1980. Measurements of the thermal structure and thermal contrasts in the atmosphere of Venus and related dynamical observations: Results from the Pioneer Venus probes. *J. Geophys. Res.* **85**, 7903-7933.

Seling, Ted. 1989. Private communication.

Smith, W. L. 1970. Iterative solution of the radiative transfer equation for the temperature and absorbing gas profile of an atmosphere. *Applied Optics* **9**, 1993-1999.

Steffes, P.G. 1985. Laboratory measurements of the microwave opacity and vapor pressure of sulfuric acid vapor under simulated conditions for the middle atmosphere of Venus. *Icarus* **64**, 576-585.

Steffes, P. G. and V. R. Eshleman 1982. Sulfuric acid vapor and other cloud-related gases in the Venus atmosphere: Abundances inferred from observed radio opacity. *Icarus* **51**, 322-333.

Steffes, P. G. M. J. Klein, and J. M. Jenkins 1990. Observations of the microwave emission of venus from 1.3 to 3.6 cm. *Icarus* **84**, 83-92.

Stewart, A. I. F. and C. A. Barth 1979. Ultraviolet night airglow of Venus. *Science* **205**, 59-62.

Suomi, V. E. 1974. Cloud motions on Venus. In *The Atmosphere of Venus* (J. Hansen, Ed.), pp. 42-58. NASA SP-382.

Taylor, F. W., R. Beer, M. T. Chahine, D. J. Diner, L. S. Elson, R. D. Haskins, D. J. McCleese, J. V. Martonchik, P. E. Reichley, S. P. Bradley, J. Deiderfield, J. T. Schofield, C. B. Farmer, L. Froidevaux, J. Leung, M. T. Coffey and J. C. Gille 1980. Structure and meteorology of the middle atmosphere of Venus: Infrared remote sensing form the Pioneer orbiter. *J. Geophys. Res.* **85**, 7962-8006.

Thompson, A. R., J. M. Moran, and G. W. Swenson Jr. 1986. *Interferometry and Synthesis in Radio Astronomy*, first edition. John Wiley and Sons, New York.

Tolbert, C. W. and A. W. Straiton 1964. 35 Gc/s and 94 Gc/s cytherean radiation. *Nature* **204**, 1242-1245.

Twomey, S. 1963. On the numerical solution of Fredholm integral equations of the first kind by the inversion of the linear system produced by quadrature. *J. Assoc. Comput. Mach.* **10**, 97.

Ulich, B. L., J. R. Cogdell and J.H. Davis 1973. Planetary brightness temperature measurements at 8.6 mm and 3.1 mm wavelengths. *Icarus* **19**, 59-82.

Ulich, B. L. 1974. Absolute brightness temperature measurements at 2.1-mm wavelength. *Icarus* **21**, 254-261.

Ulich, B. L. and E. K. Conklin 1976. Observations of Ganymede, Callisto, Ceres, Uranus and Neptune. *Icarus* **27**, 183- 189.

Ulich, B. L. 1981. Millimeter-wavelength continuum calibration sources. *Astron. J.* **86**, 1619-1626.

Varanasi, P. 1975. Measurements of line widths of CO of planetary interest at low temperatures. *J. Quant. Spectrosc. Radiat. Transfer* **15**, 191-196.

Vetukhnovskaya, Yu. N., A. D. Kuz'min, B. G. Kutusa, B. Ya. Losovskiy, and A. E. Salomonovich 1963. Measurements of the spectra of the radio emission of the nightside of Venus. *Radiofisika* **6**, 1054-1056.

von Zahn, U., S. Kumar, H. Niemann, and R. Prinn 1983. Composition of the Venus atmosphere. In *Venus* (D. M. Hunten, L. Colin, T. M. Donahue, and V. I. Moroz, Eds.), pp. 299-430. Univ. of Arizona Press, Tucson.

Wark, D. Q. and H. E. Fleming 1966. Indirect measurements of atmospheric temperature profiles from satellites. *J. Geophys. Res.* **66**, 77.

Waters, J. W. 1976. Absorption and emission by atmospheric gases. In *Methods of Experimental Physics* **12**, Astrophysics Part B., pp. 142-176. Academic Press, New York.

Werner, M. W., G. Neugebauer, J. R. Houck, and M. G. Hauser 1978. One millimeter brightness temperatures of the planets. *Icarus* **35**, 289-296.

Whitcomb, S. E., R. H. Hildebrand, J. Keene, R. F. Stiening, and D. A. Harper 1979. Submillimeter brightness temperatures of Venus, Jupiter, Uranus, and Neptune. *Icarus* **38**, 75-80.

Wilson, W. J., M. J. Klien, R. K. Kakar, S. Gulkis, E. T. Owen, and P. T. P. Ho 1981. Venus. I. Carbon monoxide distribution and molecular-line searches. *Icarus* **45**, 624-637.

Woody, D. P., R. E. Miller and M. J. Wengler 1985. 85-115 GHz receivers for radio astronomy. *IEEE Transactions on Microwave Theory and Techniques* **MTT-33**, 90-95.

Yefanov, V. A., A. G. Kislyakov, I. G. Moiseyev, and A. I. Naurnov 1969. The radio emission of Venus at 2.25 and 8 cm. *Astron. J.* **46**, 147-151.

Young, R. E. and G. Schubert 1973. Dynamical aspects of the Venus 4-day circulation. *Planet. Space. Sci.* **21**, 1563-1580.

Yung, Y. L. and W. B. DeMore. 1982. Photochemistry of the stratosphere of Venus: Implications for atmospheric evolution. *Icarus* **51**, 624-637.